Analysis Of Disc Brake Squeal Using The Finite Element Method

by

Zaidi Bin Mohd Ripin

A thesis submitted in accordance with the requirements for the degree of

Doctor of Philosophy

Department of Mechanical Engineering

University of Leeds

Leeds, United Kingdom

September 1995

The candidate confirms that the work submitted is his own and that appropriate credit has been given where reference has been made to the work of others

Abstract

The problem of disc brake squeal has been examined by developing a finite element model of the coupled pad-disc system , conducting complex eigenvalue analysis and associating unstable modes with potential squeal problem areas. A key issue in this process is the representation of the contact pressure distribution at the frictional interface between the disc and the pad. Non-linear contact analysis using the finite element model of the pad revealed that contact is only partial at the pad-disc interface and that the contact pressure distribution depends on the friction coefficient, Young's modulus of the friction material and the way the applied pressure is distributed on the pad backplate. A new method is proposed in which interface contact stiffness is related to brake line pressure using a statistical approach based on the measured surface properties of the interface. Complex eigenvalue analysis of the coupled pad-disc system has shown that unstable modes exist within different ranges of contact stiffness thereby providing an explanation of the effect of varying line pressure on squeal. The two most unstable modes from the analysis show good correlation with experimental squeal results. The coupled model is then used for parametric studies the results of which indicate that high coefficient of friction and uniform contact pressure distribution increase instability whilst a trailing edge biased pressure distribution and a high support stiffness at the pad backplate reduce it. Limiting the disc symmetry by introducing equispaced slots was shown to be effective in reducing instabilities involving diametral modes of the disc with the same order of symmetry only. Other modes were stabilised by increasing the rigidity of the pad. The overall results suggest that either the pad or the disc can be mainly responsible for the instability depending on the mode thus unifying the different approaches to disc brake squeal and enabling the most appropriate component to be targeted for squeal abatement purposes.

Table of contents

Chapter Three - Methodology Of Present Study

Chapter Four - Modal Analysis of the Disc and Pad

Chapter Five - Contact Pressure Analysis Of The Brake Pad

Chapter Six - Contact Stiffness Determination

List of Figures

List of Tables

Acknowledgements

I would like to express my sincere thanks to my two supervisors , Professor D A. Crolla and Dr. D.C. Barton for their valuable guidance, support, encouragement and training given throughout this research work. I would also like to acknowledge the support from Dr P.C. Brooks for the time spent for teaching me ABAQUS and supporting ANSYS. I would also like to express my gratitude to the Government of Malaysia for the funding.

An acknowledgement is due to Mr R M. Martin, the Chief Technician and Mr. D. Readman for their great sense of humour and timely help. I would also like to thanks everyone in the Brake Group for the beneficial discussion.

I should like to show my deepest appreciation to my family for their endless help and encouragement given over such a long period of time especially my parent who has tried their best in providing me with the best education. A special appreciation to my beloved wife Norshamshida for all the care and understanding throughout these long and hard years and to my two daughters, Aminah and Maryam - all of whom has made life in this foreign country bearable.

Finally to everyone I knew, whose names are too many to be listed, thanks for the memory.

Declaration of Originality

The problem of disc brake squeal has been examined by developing a finite element model of the coupled pad-disc system , conducting complex eigenvalue analysis and associating unstable modes with potential squeal problem areas. A key issue in this process is the representation of the contact pressure distribution at the frictional interface between the disc and the pad. Non-linear contact analysis using the finite element model of the pad revealed that contact is only partial at the pad-disc interface and that the contact pressure distribution depends on the friction coefficient, Young's modulus of the friction material and the way the applied pressure is distributed on the pad backplate. A new method is proposed in which interface contact stiffness is related to brake line pressure using a statistical approach based on the measured surface properties of the interface. Complex eigenvalue analysis of the coupled pad-disc system has shown that unstable modes exist within different ranges of contact stiffness thereby providing an explanation of the effect of varying line pressure on squeal. The two most unstable modes from the analysis show good correlation with experimental squeal results. This therefore provides some explanation towards the reason why squeal tends to occur under low pressure actuation. This area of disc brake squeal modelling will add to the present body of knowledge on squeal and the parameters affecting it.

General Layout and Presentation

The thesis is presented in accordance with the regulations of the University of Leeds. All symbols and nomenclature, where possible, are in accordance with general and consistent usage and are fully defined at their first appearance. Equations, figures and tables are identified by the chapter number in which they occur and by a second number denoting the order in which they appear in the chapter. Figures and tables are bound into the thesis near the appropriate text. References cited in the work are listed at the end of the thesis and are numbered according to the order they appear in each chapter. Pages are numbered consecutively throughout the thesis including figures and tables.

CHAPTER ONE

INTRODUCTION

1.1 Background

The problem of brake noise is in general related to comfort and refinement rather than to safety or performance. Increased refinement in other parts of the car such as suspension, passenger compartment acoustics and transmission has turned attention to noise emanating from the brake. Legislation relating to noise level however is limited to continuous noise sources and therefore does not cover the intermittent nature of brake noise. Nevertheless the ideal solution in the form of a silent brake would help to bring about a better environment and reduce noise level particularly in places where stopping frequently occurs - the ubiquitous noise from bus brakes for example.

The vibration problem of a disc brake can in general be divided into two categories. The first is judder which is felt rather than heard as it occurs typically at frequency below 100 Hz. The second is noise which occurs as a result of self-excited oscillation or dynamic instability. This second type of noise is generally described as

'squeal' or 'squeak' or 'moan' [1]. Squeal is commonly associated with noise involving transverse modes of the disc which in general exists at above 1 kHz.

In economic terms the general problem of persistent brake noise may lead to high warranty costs and disc brake noise contributed to the majority of the brake faults in a recent survey [1]. In another study disc brake squeal tends to occur more frequently in European cars [2]. The most recent survey carried out by a consumer magazine 'Which' [3] where over 100 different brands of cars were tested indicated that squeal still exists as a potential fault for consumers to watch out for when buying used cars. The report also confirms that the major of brake noise problems can be found in continental cars.

As the market for mass produced cars becomes ever more competitive, profit margins reduce resulting in manufacturers venturing into the luxury car market in which the margin is higher. This market requires much higher levels of refinement. However one of the best selling luxury cars is still facing a disc brake squeal problem even though research into the problem has been going on for quite sometime [4].

For the above reasons there is every impetus to reduce disc brake squeal. In particular research into understanding and modelling disc brake squeal may prevent costly post-production modifications. Mathematical modelling of the squeal problem has indeed been identified as one of the major means by which understanding and solution of the problem could be further advanced [1]. A recent article by Smales [5] recognised the fact that it is uneconomic in terms of cost and time to fix problems which occur at the prototype stage rather than to design 'right first time'. Further fixes are usually developed retrospectively by empirical processes which are again expensive in terms of manpower and the manufacturer's reputation. Thus Smales proposed the use of predictive modelling based on the finite element method rather than the alternative lumped parameter approach which is difficult to apply to actual brake design since it is unable to model flexural effects.

The advent of powerful digital computers facilitates the application of the finite element method in modelling the disc brake squeal problem as exemplified by Liles [6] who employed the MSC Nastran finite element software and used the real part of the

complex eigenvalues of a coupled pad-disc finite element model as a measure of squeal propensity. Introducing friction into a finite element model causes asymmetry of the stiffness matrix which causes problems as most proprietary finite element codes do not have the capability to solve eigenvalue problems which involves unsymmetric matrices. The friction effect itself is very complex and forms its own discipline of study. Modelling of friction in the finite element analysis of disc brake squeal is still based on the relatively simple Amonton's Law as this has been proven to provide good correlation with experimental trends [7]. Incorporating non-linear friction based on the Oden-Martin friction model [8] is more realistic but costly in computational terms.

1.2 Present Work

In the present work disc brake squeal propensity is evaluated by examining the complex eigenvalues of a finite element model developed for a particular pad-disc combination. The primary objectives of the research were to :

- Develop finite element models of the disc and the pad which display acceptable correlation with the available experimental results.
- Study the contact pressure distribution at the pad-disc interface under normal sliding conditions.
- Establish a relationship between the applied pressure and the interface contact stiffness.
- Determine the effect of applied pressure on squeal propensity based on the relationship thus established and the results of the complex eigenvalue analysis.
- Compare the results of the stability analysis with experimental trends by varying certain parameters over a realistic range.
- Suggest realistic and coherent strategies for eliminating squeal at the design stage using the results of the above studies.

The finite element models of the brake pad and disc are iteratively developed using the ANSYS Revision 5.0A [9] software package until the free-free modal analysis results compare well with experimental results published by Fieldhouse and Newcomb

[10] The finite element model of the pad is then used for contact pressure analysis using the ABAQUS [11] package as it is more suitable for the non-linear contact analysis required. The resulting contact pressure distribution is next linked to the distribution of interface contact stiffness using a random process approach which takes account of the material and surface roughness properties at the interface.

The disc and pad finite element models are then coupled with the contact stiffness distribution at the interface based on the predicted contact pressure distribution under steady state sliding conditions. Contacts between the pad and external bodies such as the piston and abutments are approximated with stiff springs. With the inclusion of friction at the sliding interface, the stiffness matrix becomes unsymmetric which results in complex eigenvalues, the positive real part of which is used as a measure of squeal propensity. Parameters relating to the brake system are varied in order to determine the overall effect of pressure on squeal propensity and also to determine methods by which the parameters responsible for squeal can be isolated. The trends from this parameter study are compared with other published work.

1.3 Thesis Organisation

This thesis is divided into eight further chapters as follows

Chapter Two comprises a literature review on the subject of brake noise in general and disc brake squeal in particular.

Chapter Three discusses the methodology of disc brake squeal modelling and provides the overall framework of the present analysis.

Chapter Four concentrates on the free-free modal analysis of the two major components of the disc brake system (the pad and the disc) with the results compared with reconstructed experimental holographic images from experiments.

Chapter Five discusses analysis of the contact pressure distribution between the pad and the disc using the finite element method and the parameters affecting it.

Chapter Six covers the random process approach used to link the applied pressure to contact stiffness via the surface material and roughness properties.

Chapter Seven discusses the stability analysis of the coupled pad-disc system using complex eigenvalues and concentrating on the effect of applied pressure on squeal propensity.

Chapter Eight reports the parametric studies of the coupled pad-disc system to determine the extent to which each parameter investigated affects the system squeal propensity.

Chapter Nine summarises the results and conclusions of the present work. Recommendations for further work are also presented in this chapter.

CHAPTER TWO

LITERATURE REVIEW

2.1 Introduction

Brake noise has been a problem since the introduction of friction brakes. In motor vehicle applications , the increase of passenger comfort resulting from systematic studies on the transmission , the handling and suspension systems and the acoustics of the passenger compartment has brought the brake noise problem to the fore due to the risks of increased warranty costs and reduced product marketability as discussed in Chapter One.

In the present chapter , a series of studies on disc brake noise are discussed , in particular the understanding of disc brake squeal mechanisms using various mathematical models from relatively simple one degree-of-freedom models to multi degree-of-freedom models. Some of the work is based on the simple strut on disc apparatus in order to make the system more amenable to analysis and to explain the more general problem of friction excited vibration. Past work on the full disc brake system which provides more

insight into realistic situations is also discussed. This in total provides an overall picture of disc brake squeal mechanisms and the underlying explanations.

2.2 Definitions

The noise emanating from a disc brake covers the whole range of audible frequency and different mechanisms and components may be responsible for each type of noise. Although the present study is aimed at disc brake squeal, it is important to see squeal as a sub-problem of the wider more general brake noise problem. Therefore brief definitions of the various types of disc brake noise based on the work of Lang and Smales [12] are listed below :-

a) Judder - very low frequency non-resonant vibration caused by disc rubbing path non-uniformity resulting from circumferential thickness variation.

b) Groan - semi-resonant vibration with frequency typically less than 100Hz. May involve rigid body rotational modes of the caliper and local suspension parts.

c) Hum - frequency typically in range of 200Hz - 400Hz with rigid body motions as for groan.

d) Squeal - Vibration involving transverse disc modes. If the squeal mode frequency is lower than the first bending mode frequency of the pad , it is considered as low frequency squeal. Higher frequency modes are sometimes referred to as squeak.

e) Squelch - amplitude modulated version of squeak.

f) Wire brush - periodic and at squeak frequency but with random amplitude modulation.

Squeal is sometimes defined as any brake noise of over 1 kHz frequency. This is generally true as usually the transverse disc modes begin at about 1 kHz. In the present work squeal is considered as defined in (d).

2.3 Squeal Models

2.3.1 Early work

The problem of brake squeal was studied as early as 1935 when Lamarque [13] collected the experience of manufacturers and operators on the causes and prevention of squeal in drum brakes. A catalogue of preventive methods were listed , including the clamping of steel bands lined with woven asbestos around the drum periphery supposedly to damp the vibration of the drum.

Fosberry and Holubecki [14] began a systematic attempt to understand the nature of brake squeal in 1955 and started with the idea of squeal as a result of oscillation caused by increasing friction coefficient with decreasing speed. The hypothesis was tested by roughening the surface of a brake lining artificially treated with graphite and mineral oil to alter the friction-velocity characteristics. The results did not show any clear relationship between the friction-velocity characteristics and squeal. Measurements using short linings, however, showed an increase in brake torque at the near stop conditions for a squealing brake. Due to the unavailability at that time of friction material with static friction coefficient equal to or less than the kinetic friction coefficient, they suggested improved damping of either the drum or shoes as one way to remedy squeal.

The suggestion above resulted in the subsequent work reported in 1957 [15] where friction dampers attached to the drum proved to be effective in reducing squeal on buses.The extension of this work to brake shoes followed [16] even though the friction damper on the shoe was found to be effective only for low frequency squeal occuring at less than 3 kHz. The work also began to classify general brake noise into the various frequency classifications of judder , hum ,squeal and wire brush. At this time discussion had already begun on the energy input into the system due to the friction-velocity characteristic of the lining. In 1961 , Fosberry and Holubecki suggested that disc brake squeal was also caused by either static friction that was higher than the kinetic friction or kinetic friction which increased with decreasing speed [17]. The disc brake squeal

frequency was found to be the same as the frequency of the disc in the clamped condition and a "fix" in the form of dished laminations between the pad backplate and the caliper piston was proposed as a means to alleviate squeal. However, there was no explanation as to how the fix actually worked.

2.3.2 Variable friction model

Sinclair [18] put forward a model based on his experiment in which a rigid block of mass m and applied load N is pulled along a plane using a spring of stiffness k with friction force F acting against the sliding motion (figure 2.1). The free end of the spring moves with constant velocity, V and the kinetic friction coefficient μ_k is less than the static friction μ_s.

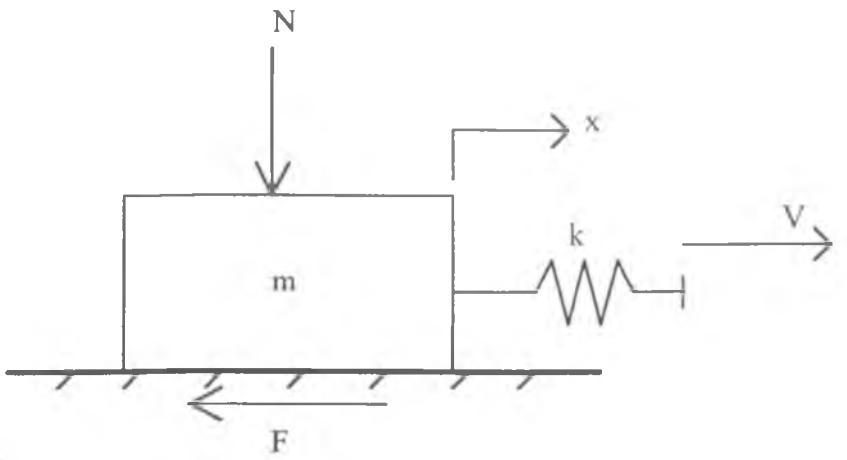

Figure 2.1 - Sliding block on plane [18]

Under this condition ,stick-slip motion can occur. The equation of motion during slip is

$$m\ddot{x} + kx = L(\mu_s - \mu_k) + kVt \qquad (2.1)$$

where $L = N + mg$, $\ddot{x}$ is the acceleration and t is time.The solution of equation (2.1) is

$$x = A\sin(\omega t + \Phi) + \frac{L}{k}(\mu_s - \mu_k) + Vt \qquad (2.2)$$

where the amplitude A is given by

$$A = \left(\frac{L^2}{k}(\mu_s - \mu_k)^2 + \frac{V^2}{\omega^2}\right)^{1/2} \qquad (2.3)$$

and the natural frequency ω and the phase angle Φ are given by

$$\omega = \sqrt{\frac{k}{m}} \qquad \text{and} \qquad \tan\Phi = \frac{\omega L}{kV}(\mu_s - \mu_k) \qquad (2.4)$$

From equation (2.3) the amplitude of oscillation increases with the difference between the static and kinetic friction , the applied velocity and the normal force. Considering the special case when the static and kinetic friction coefficients are equal , this would result in steady oscillation without sticking which in practice will disappear due to damping. From equation (2.4) the natural frequency of the system is shown not to be influenced by the friction coefficient, however, the associated phase angle is very much affected by the difference between the static and kinetic friction coefficient. The experimental observation showed that stick-slip motion only occurred when the applied velocity was reduced to a few hundredths of a meter per second and the response changed to uniform sliding as the velocity was increased. Wetting the surface resulted in a decrease of kinetic friction coefficient causing the amplitude to increase as predicted by equation (2.3). From this model , Sinclair concluded that the tangential oscillatory motion of the brake lining was caused primarily by $\mu_s > \mu_k$ and that decrease of μ_k with speed is the reason for brake squeal. The model proposed, however, predicted squeal amplitude increasing with the rubbing speed as shown in equation (2.3), which is generally not true for squeal.

Measurement of the coefficient of friction and velocity characteristics of lining materials was carried out by Basford and Twiss [19]. They found cyclic vibrations of the apparent friction with the amplitude and frequency of the oscillations dependant on the mass and stiffness of the sample and mounting system. From this they suggested a squeal model as shown in figure 2.2a.

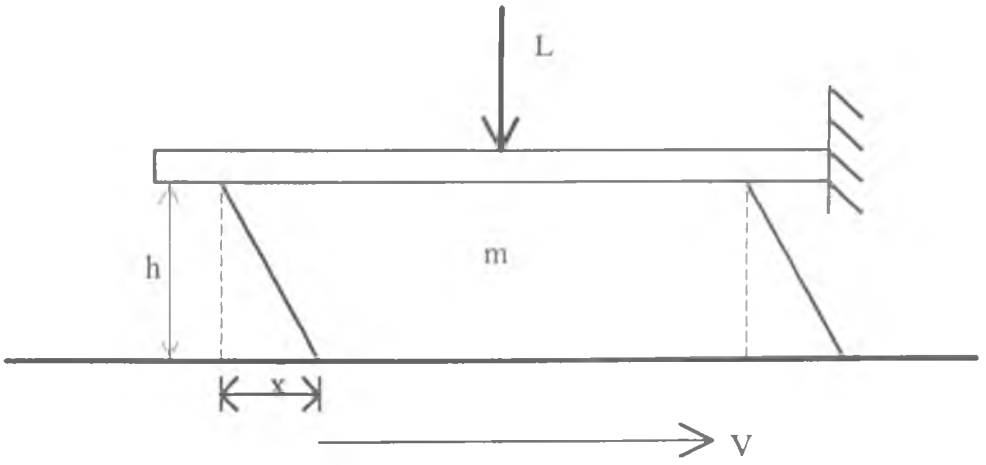

Figure 2.2a - Block on sliding plane [19]

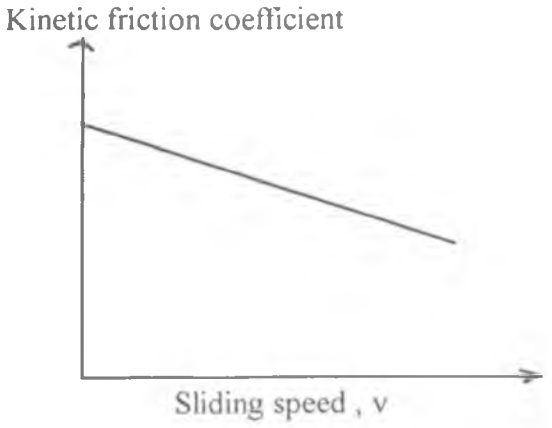

Figure 2.2b - Kinetic friction coefficient as a linear function of sliding speed

Figure 2.2a shows an elastic block of mass m is rigidly held with load L acting normal to the sliding plane moving at a constant sliding speed of V and held against a moving surface with the friction force causing shear and displacing the block friction face by x, measured positive in the direction of sliding. The thickness of the friction block is given by h. In the model the kinetic friction is assumed to decrease linearly with the rubbing speed,

$$\mu_k = \mu_s - a(V - \dot{x}) \tag{2.5}$$

where a is the gradient of the friction-relative velocity curve as shown in figure 2.2b. The equation of motion of the friction surface is ;

$$m\ddot{x} - \mu_k L\dot{x} + G\frac{x}{h} = L(\mu_s - aV)..... \quad (2.6)$$

where m=block mass per contact area

G=elastic shear modulus

L=normal load

Equation (2.6) is derived by assuming that shear angle due to the displacement of the pad surface x can be approximated (at small angle) using the elastic shear modulus of the friction material.

The solution of this equation when neglecting the particular integral is

$$x = A\exp[(aLht/2m)\sin((4Gm/h - a^2L^2)^{0.5}\frac{t}{2m} + B)] \quad (2.7)$$

where A and B are integration constants. From equation (2.7) , squeal occurs when x increases with time indicating oscillations with growing amplitude. This happens when the exponential term is positive i.e. the coefficient a is positive. Therefore from equation (2.5) the kinetic friction coefficient must decrease with increasing relative velocity in order to produce instability.

Equation (2.7) was then used by Bassford and Twiss [19] to determine an expression for the probability of noise from a lining as below :

$$p = c\left(\frac{aL}{2m}\right)\exp\left\{\frac{1}{2\sigma^2}\left(\omega_d - \frac{1}{4\pi m}\left(\frac{4Gm}{h} - aL^2\right)^{1/2}\right)\right\} \quad (2.10)$$

where c - constant

ω_d - drum natural frequency

σ - width of frequency band which induces drum resonance

Experiments using four linings partially verified the above equation with the squeal occurrence increasing with the noise probability p and the elastic shear modulus G. The model developed by Basford and Twiss has a definite advantage over the Sinclair model because it takes into account the slope of the friction coefficient-velocity curve and therefore allows for different noise behaviour for similar values of static friction.

Wagenfuhrer [20] introduced a very similar model to Sinclair but which allowed a non-linear variation of the friction coefficient-velocity curve. In this model (figure 2.3) , a block is loaded against a sliding plane and restrained by a spring and damper.

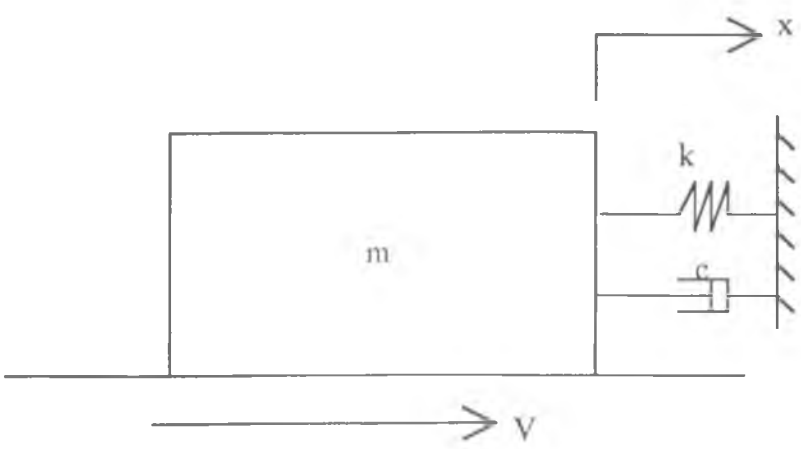

Figure 2.3 Block on sliding plane [20]

Oscillations of the block were considered to be stick-slip due to $\mu_s > \mu_k$. The expression for kinetic friction was found from experiment to be :

$$\mu_k = \left(\frac{\mu_s - \mu_h}{1+dV}\right) + \mu_h \qquad (2.11)$$

where d and μ_h are constants for a given friction material. The equation of motion for the system is

$$m\ddot{x} + c\dot{x} + kx = \pm L\left(\frac{\mu_s - \mu_h}{1 + d(V - \dot{x})} + \mu_h\right) \tag{2.12}$$

the (+) sign being for $V > \dot{x}$ and the (-) sign for $V < \dot{x}$. The analysis showed that increasing the damping stabilised the system. The condition for continuous oscillation is fulfilled when the total energy of the system increases with time (i.e. dE/dt > 0). This condition then reduces to

$$c < \frac{Ld(\mu_s - \mu_h)}{(1 + dV)(1 + d(V - V_i))} \tag{2.9}$$

where V_i is the initial velocity of the block. The above expression shows that large differences between the static and kinetic friction coefficient , large normal loads and low sliding speeds will all enhance squeal.

2.3.3 Sprag-slip model

Up to this point in time , all squeal models proposed were single degree of freedom blocks with a common instability mechanism of decreasing friction coefficient with increasing sliding speed and with squeal favouring a large normal load.

The introduction of the sprag-slip model by Spurr [21] gave brake squeal an added instability mechanism. The model is shown in figure 2.4.

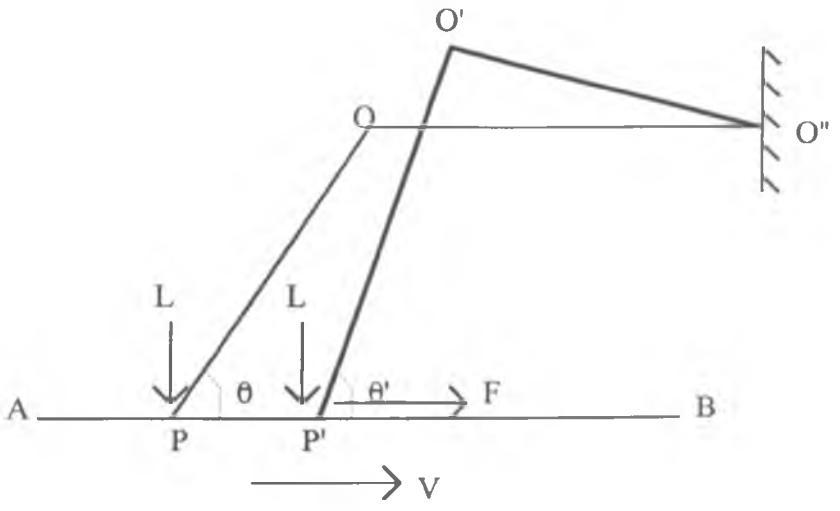

Figure 2.4 - Sprag-slip model [21]

OP is a rigid strut pivoted at O and loaded at P against a sliding surface AB. The friction force for a rigid pivot O is:

$$F = \frac{\mu_k L}{(1 - \mu_k \tan\theta)} \tag{2.14}$$

Thus the friction force will approach infinity as $\cot\theta$ approaches μ_k. At the sprag angle $\theta = \text{arc}\cot(\mu_k)$, further motion is impossible.

For the motion to continue, the pivot at O is elastically displaced to O' causing an increase of the angle θ to θ'. This will cause the friction force F to fall thus allowing the strut to return to its initial position due to its elasticity. The motion then repeats itself and as long as the sliding motion is available to energised the system the strut OP will continue to oscillate. With this model variation of friction coefficient with sliding speed is unnecessary for instability. Various experimental evidence was used by Spur to support this theory ; in relation to disc brake squeal , a contact area forward of the piston support (pivot) was achieved by grinding a double taper on the pad and squeal was achieved when the imaginary line joining the contact area and the pivot was at the sprag angle. The great advantage of Spur's model is that it is relatively easy to understand.

2.3.4 Pin-on-disc models

2.3.4.1 Friction induced self-excited oscillations.

In this section the focus is on friction induced self excited vibration which has been mostly studied using pin-on-disc experiments. The models derived therefrom form much of the basis of the present understanding of disc brake squeal.In general friction induced vibrations can be divided into two major categories :-

a) stick-slip vibration where the displacement versus time curve is of a saw tooth form

b) quasi-harmonic vibration where the displacement versus time curve is of sinusoidal form.

The idea of friction as uniform and steady throughout any vibratory process was shown to be untrue by Lienkewicz [22]. He demonstrated the effect of vibration in reducing the static friction coefficient and damping out stick-slip motion. Lo and Brockeley [23] showed the need to take into account the vibration effect during the measurement of kinetic friction coefficient since an averaging technique does not indicate the true friction coefficient. For the quasi-harmonic friction induced vibration , they used a model similar to Sinclair [18]. The phase-plane analysis indicated a stable limit cycle and adequate damping was shown to eliminate the vibration.

A study by Aronov et. al. [24] showed both low and high frequency friction induced vibration depended upon the system rigidity. There is a critical normal load when self excited oscillations occur. A higher system rigidity would require higher critical normal load. The oscillation frequency also increases with the system rigidity. Low frequency oscillations occur only in the friction direction while high frequency oscillations occur due to the coupling between the frictional and normal degrees of freedom.

Soom and Kim [25] proposed a very useful concept of variable friction coefficient. They began with the argument that normal vibrations could be excited either

by external oscillatory forces or by surface roughness including waviness of the surface. They measured the frequency domain transfer function between the frictional (output) and normal (input) forces and found good coherence around the contact resonance. The instantaneous coefficient of friction with time could then be written as

$$\mu(t) = \frac{F_F(t)}{F_N(t)} = \frac{F + f_F(t)}{N + f_N(t)} = \bar{\mu} + \tilde{\mu}(t) \tag{2.15}$$

where $\bar{\mu}$ is the average value of the friction coefficient and $\tilde{\mu}(t)$ is the fluctuating component. Also $\bar{\mu} = \mu_K$ where μ_K is the kinetic coefficient of friction. The instantaneous oscillatory friction coefficient could then be defined as

$$\mu_D(t) = \frac{f_F(t)}{f_N(t)} = \mu_K + \frac{\tilde{\mu}(t)}{f_N(t)/N} \tag{2.16}$$

If $\tilde{\mu}(t)$ is proportional to and in phase with $f_N(t)$, the dynamic coefficient of friction μ_D will be higher than the averaged kinetic coefficient of friction μ_K.

Continuing the same work , Soom and Kim [26] analyzed a slider model as shown in figure 2.5. The contact stiffness k_s was calculated from Hertzian theory The equation of motion in the y-direction could be written as

$$m\ddot{y} + c_s(\dot{y} - \dot{y}_{ic}) + k_s(y - y_{ic}) = 0 \tag{2.17}$$

In the case of the weight loaded condition ,

$$f_N(t) = -m\ddot{y} \tag{2.18}$$

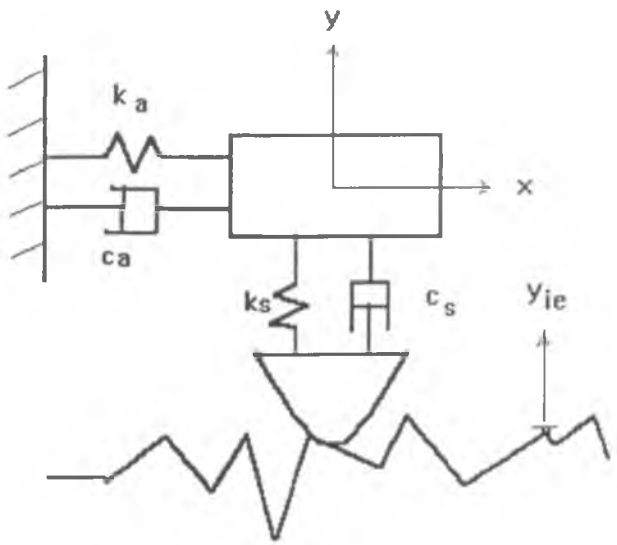

Figure 2.5 - Slider model for analysis of dynamic coefficient of friction [26].

In this case the dynamic coefficient of friction was found to be approximately 1.4 times higher than the steady kinetic coefficient of friction and independent of average load (weight loaded only) , sliding speed and surface roughness. The normal and frictional forces were found to be in phase and the amplitude ratio was found to be independent of frequency.

In their experimental work Dweib and D'Souza [27] found 4 distinctive regions of friction behaviour as the normal load was increased , namely :

1. Linear region - μ_K constant , F linear with N
2. Non-linear region - F non-linear with N , tangential natural frequency dominant
3. Transient region - irregular and brief self-excited oscillations
4. Self-excited region - periodic self-excited vibrations , amplitudes are much higher , average value of friction force F remains constant.

In the self-excited region , the slider vibrates in the various directions (lateral , normal and rotating) at the same fundamental frequency which is close to its torsional natural frequency. Dweib and D'Souza estimated the contact stiffness of the non-Hertzian contact experimentally by deducting the no-contact natural frequency from the in-contact natural frequency , the difference between which was assumed to come from the added stiffness from the contact. In subsequent work [28] they analyzed the effect of various parameters on the critical normal load for instability. In general , higher normal or torsional stiffness required higher critical normal load which indicated coupling of normal and torsional modes as the cause of instability. Therefore separation of these modes would increase the stability of the system.

A series of studies on frictional noise was carried out by Yokoi and Nakai using a rod pressing on the circumferential face of a steel disc. In the first study [29] , the noise generated came from bending vibration of the rod only because of the relatively thick disc used. Scanning electron micrography showed that , in the case of ordinary rubbing noise , the surface of the rod is relatively rough and as it wears and squeal occurs the surface becomes smooth. Measurements of the friction coefficient-velocity curve of the pair showed a shallow trough and squeal noise could even be generated with friction coefficient increasing with velocity. This was explained using an instantaneous value of friction coefficient μ_i dependant on the relative sliding speed v_r which in turn has a relationship of the form $v_r = v - u^*$, where v is the tangential speed of the disk circumferential face and u^* is the instantaneous velocity of the rod tip. The instantaneous friction coefficient versus relative sliding speed curve was shown to form a loop the negative gradient part of which would cause squeal to occur.

A subsequent study [30] used a longer rod to produce higher modes of squeal noise. Higher squeal modes were shown to be generated when the real area of contact between the disk and the rod is relatively large with the axial vibration of the rod increasing with the noise and the fundamental bending mode being damped out.

The effect of surface roughness was studied in a further paper [31] which showed that sound pressure level increased with roughness to the power of 0.8. The effect of angle of inclination was studied in [32] and the frequency of the noise generated was found to increase with the angle for positive angle i.e. the rod inclined towards the direction of rotation. For negative angles , an unstable condition develops resulting in chatter as digging-in occurs.

Tworzydlo et al [33] analysed the friction induced dynamic instability of a pin-disc system.This included a very comprehensive study of dynamic friction which is shown to be a function of the properties of the interface and the dynamic characteristics of the system. The friction coefficient was calculated on the basis of the Oden-Martin model [8] which took into account the normal approach indentation (and thus the stiffness) and its time derivative (damping) and the approaching phase of the normal motion. Obviously the approach used here is non-linear. A matter of interest was the squeal problem which was categorized under the group of instabilities where the dynamic characteristics are important. Using a model of the pin-disc system , the stability of the system was determined by transient analysis and by linearized equations of motion reduced to the form of an eigenvalue problem. The eigenvalue analysis showed coalescence of rotational and translational modes of the pin when moving into the self-excited region and divergence into two separate modes when the system stabilizes which occured with increase in normal load. Higher friction coefficient would initiate instability at a lower normal load. There were also other unstable modes for the different components (pin and block) which occurred independently and at different frequencies.

The transient analysis of [33] showed that sufficiently large disturbances can cause self-excited oscillation of the system , which may initially be shown to be stable from a linearized eigenvalue analysis.The transient analysis of the non-linear equations of motion of the system also indicated an apparent drop in the kinetic friction (predicted from the angular displacement) after the self-excited oscillations reached a certain amplitude. Tworzydlo et al listed two important mechanisms which limit the unstable growth of the oscillation in the self-excited zone :

a) micro stick-slip motion of the pin which tends to alter the rotational frequency of the slider

b) normal jump of the slider which tends to alter the normal frequency.

The system was also shown to be sensitive to the angle of inclination , instability favouring the digging-in position (an acute angle measured from the direction of sliding plane).

Swayze and Akay [34] studied a two degree of freedom pin on a slider using phase-plane analysis. The results showed that an increase in friction coefficient would move the equilibrium point further away from the origin until , at a critical value of friction coefficient , the origin of the phase plane is no longer the equilibrium point. Higher torsional stiffness and damping increases the stability of the system. Interestingly the analysis demonstrated how the critical friction coefficient could be obtained from the moment equilibrium condition , and that it is inversely proportional to the aspect ratio of the pin.

2.3.4.2 Geometrically constrained instability

The work covered in this section evolves mainly around the use of pin-on-disc apparatus to understand the mechanism of disc brake squeal. It differs from the above section where in general the study of friction induced noise was the main objective. The relatively simple geometry of the pin-on-disc system makes it more amenable to analysis and the results obtained can be compared to the general characteristics of squeal.

Jarvis and Mills [35] proposed a model where flexibility of the rubbing components is taken into account. This simplified model is explained using a cantilever tipped with friction material loaded at various angles against the flat surface of a rotating disc. The cantilever and the disc were assumed to vibrate in one of their principal modes and with different phases in time and space for the disc modes. Expressing the displacement of the cantilever and the disc by the product of their normal functions and normal co-ordinates and frictionally coupling the two components with the geometric constraints (the axial displacement of the disc surface is set equal to the axial

displacement of the cantilever) , the Langrange's equations of the system could then be derived , the solution of which indicated the system stability.Overall stability of the system was found to be dependant on the damping , geometric configurations (length of cantilever and slope angle) and friction coefficient. The authors predicted a stability radius for a given configuration but the experimental agreement was poor. Later Hales [24] showed how the agreement could be improved by taking account of the radii of both the cantilever tip and the area of contact in the analysis. The Jarvis and Mills model showed how instability can arise from the geometry of the coupling of the rubbing surfaces and showed how instability could be avoided by the use of favourable configurations.

Earles and Soar [37] began a series of experiments with the pin-on-disc apparatus. They observed during squeal that the pin support beam always oscillated in a torsional mode. The fundamental frequency of the squeal did not coincide with the natural frequencies of the components but varied with radius of contact and angle of inclination of the pin. They rejected the variation of friction coefficient with velocity as the cause of squeal because squeal was found to be independent of speed. They therefore deduced that the kinematic-constraint instabilities were the principal cause of squeal.

Further work by [38] on the same apparatus was done by limiting the analysis to linear equations while the system was considered to be continuous. The model predicted squeal frequencies for the system in good agreement with experiment. Different modes of the pin were found to excite different modes of the disc with the translational mode of the pin exciting the second diametral mode of the disc and the rotational mode exciting the third diametral mode.

The complexity of the analysis increased in the subsequent work by Earles and Lee [39] where the degees of freedom of the model were increased to three (translational x and y , rotational). Deriving the equations of motion of the system resulted in a set of equations of the form of $a\beta^2 + b\beta + d = 0$, from which instability could be predicted. Again the predicted region of instability correlated well with

experiment , with the different shape of the region attributed to the higher experimental friction coefficient of 0.6 compared to the coefficient of 0.4 that was modelled. It is interesting to note that this work predicted a narrow range of preferred stiffness of the beam and disc for squeal to occur.

The work continued with the added complexity of a double pin and disc system [40]. Each pin had two degrees of freedom (translation and rotation) with a single degree of freedom for the disc. The equations of motion derived were used to obtain the characteristic equations and the Routh-Hurwitz criterion was applied to determine the stable boundary. The predicted envelope agreed well with experiment. The primary parameters found to affect the system stability were friction coefficient, disc stiffness and pin support torsional stiffness. The complex relationship between the system parameters was cited as the reason for the fugitive nature of brake squeal.

The above series of experiments by Earles et al using the pin-on-disc system did not reveal any new mechanism for disc brake squeal. The approach confirmed the earlier work of Spurr [21] on the sprag-slip model and kinematically constrained instability with the pin required to be at an angle of $0 < \theta < \tan^{-1}\mu$ to produce squeal (a necessary but not sufficient condition). Nevertheless the difficulties of translating these results to actual disc brake squeal remained due to the dissimilar geometry.

2.3.5 Lumped parameter models

Departing from the pin-on-disc model , North [41] produced a lumped parameter model which more closely resembled a disc brake assembly , in this case a single piston swinging caliper design. The model consisted of two pads clamping a disc supported by a caliper (see figure 2.6). Each component has translational and rotational degrees of freedom which are connected by springs and dampers.

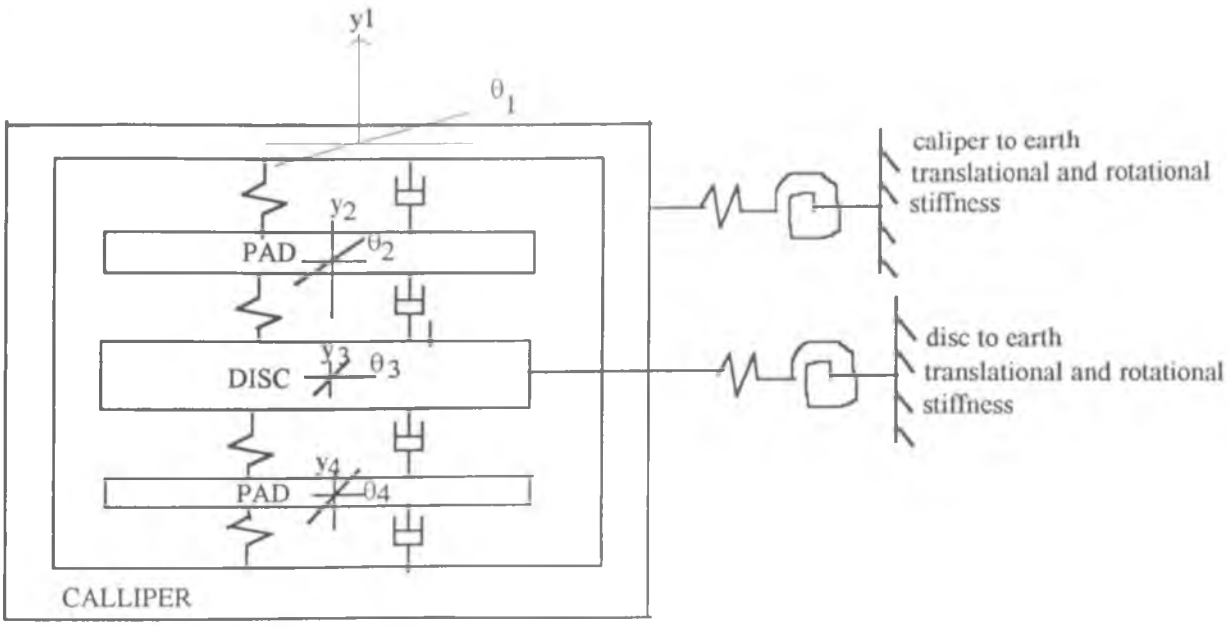

Figure 2.6 - Eight degrees of freedom lumped parameter model of a disc brake system [41]

This approach is based on the assumption that for a pad which is relatively short compared with the nodal spacings of the diametral modes of the disc, the centre of mass of the pad is subjected to lateral movement with the disc cosine mode and rotation with the disc sine mode , the disc presumably having two modes of the same order with different amplitude and phase as assumed by Jarvis and Mills in their geometrically coupled model [35]. The eight coupled equations of motion were then arranged in matrix form , the problem being essentially an eigenvalue problem , the solutions of which may come in the form of complex conjugates , with the positive real part indicating system instability and the imaginary part the system frequency. The instability mechanism of this model is explained by the convergence of two different modes to form one common mode due to favourable parameters - similar to a binary flutter instability. The model predicted increase in squeal propensity with increasing friction coefficient. The pad thickness and the magnitude of the normal force however were found to have no effect on the system stability. The model was able to give good agreement with

experiment because of the wide range of parameter values used , for example the pad stiffness was assumed to lie anywhere between zero and a maximum value. The fugitive nature of disc brake squeal was explained by the model requiring certain values of stiffness and effective pad length to allow proper interaction between the lateral and rotational modes. This model however contradicts the observation that squeal occurs over a range of applied hydraulic pressure (typically 40 - 60 psi) in that the model was insensitive to normal load.

Millner [42] used the same approach as North to produce a lumped parameter model of a fixed caliper assembly with the action of the two pads simplified by considering a single pad acting on the disc. The pad abutted rigidly against the caliper. The equations of motion of the assembly were then reduced to an eigenvalue problem and the squeal propensity of the system is again based on the positive real parts of the roots. The general trend from the study is the same as [41] but with the additional observations that squeal favours leading edge contact of the piston with respect to the pad and also that the friction material modulus could affect the system stability since the system becomes stable for a modulus greater than 350 MPa. The instability also occurs over a very narrow range of caliper mass and stiffness. The model is insensitive to normal load and backplate-caliper friction and this has been considered as unrealistic as the modulus of the friction material apparently varies with the brake actuating pressure. The effect of temperature on squeal behaviour was argued on the basis that thermal distortion shifted the centre of pressure. Compared to North's work , Millner's model added piston-backplate contact point as one of the variables.

Increases in model complexity to allow closer approximation to real disc brake systems led to the lumped parameter model of Murakami et al [7]. Modeling a pin-slider fist type caliper and backed by extensive experimental data , they produced a lumped parameter model to explain the effect of parametric changes on squeal. Again the positive real parts of the roots of the eigenvalues were used as a squeal propensity measure. The model showed increased squeal propensity with increase in friction coefficient and friction-coefficient velocity gradient and that positioning of the piston-pad contact towards the leading edge of the pad is more amenable to squeal than trailing

edge contact. Various other geometric parameters were studied in order to determine least squeal conditions and the analytical findings agreed well with experiment. This demonstrated the effectiveness of lumped parameter models in disc brake squeal analysis. The work also showed that squeal is more likely to happen when the natural frequencies of the components are about the same. The model explained squeal as an unstable condition which occurs when the friction force available to the system excites the component modes resulting in coupled vibrations of the system which under favourable conditions may become unstable. Therefore this interpretation comes under the category of geometrically induced instability with the friction coefficient - velocity negative gradient merely assisting in destabilizing the system.

Brooks et al [43] uses eigenvalue sensitivity analysis to study the effect of changing various parameters on their 12 degrees of freedom model of a fixed caliper , four opposed piston disc brake system. The eigenvector plots of the analysis clearly illustrate how the phase angles between the translational and rotational modes of the disc and pads develop from a stable to unstable condition , i.e. changing from 0 to 90 degrees. This highlighted the coupling of translational and rotational modes as the mechanism by which energy is fed to the system - a binary flutter mechanism. The authors suggested that maximum separation of the frequency of each mode (thereby preventing them from converging) would provide minimisation of squeal in a real system.

2.3.6 Analysis of squeal using the finite element method

With the advent of powerful digital computers , more complicated models can now be analyzed taking account of the flexibility of the components , in particular using the finite element method. Berndt and Schweiger [44] analysed the disc brake squeal of rail vehicle installations. They used the finite element method in a substructure analysis of the components to derive the modal matrix in terms of generalised co-ordinates which were then coupled by both the normal and friction forces at the interface. The normal coupling forces N and the friction coupling forces F were represented as below , where the superscript (1,2) represents the different components and the subscripts n and t

represent tangential and normal direction of motion and superscript 1 and 2 represents the two components:

$$N = c({}^{1}X_n - {}^{2}X_n) + N_0 \tag{2.19}$$

$$F = \mu N \,\text{sign}\,(V_0 - {}^{1}\dot{X}_t + {}^{2}\dot{X}_t) \tag{2.20}$$

where

	c	is the coupling stiffness
	X_n	normal displacement of the component
	X_t	tangential displacement of the component
	N_0	steady state normal force
	V_0	steady state sliding velocity
	$\dot{X}_t$	tangential velocity of the component

In real case where the sliding velocity V_o is high , the sign would always be positive. Berndt and Schweiger used a time varying friction coefficient to introduce a self-excitation mechanism into the system which could be represented as

$$\mu = \bar{\mu} + \mu(t + T) \tag{2.21}$$

where T is the period.

The coupled second order equations of motion which included Rayleigh damping were then reduced to first order systems of the form :

$$\dot{y} + A(t)y = 0 \tag{2.22}$$

The solution of which would result in complex eigenvalues in the form :

$$y = C(t)\alpha_k \exp(\eta_k t) \tag{2.23}$$

where $\eta_k = \lambda_k + j\omega_k$ and $j = \sqrt{-1}$

The solution could therefore be written as

$$y = C(t)\alpha_k \exp(\lambda_k t)\{\cos(\omega_k t) + j\sin(\omega_k t)\} \quad (2.24)$$

The maximum value of λ_k was used as a stability measure for each parameter investigated. The analysis showed that the system could be stabilized with 3% damping ratio applied to all modes whilst with selective damping (3% applied to the selected mode , 1% to all other modes) only one mode was found to be stable. The coupling stiffness c has very strong effect on system stability with the real part increasing with the stiffness. The instability also increases with increasing coefficient of friction , with 0.2 as a critical coefficient. The analysis of Berndt and Schweitzer was the first to include the flexible modes of the various components in disc brake squeal analysis.

Liles [6] showed how automotive disc brake squeal could be predicted by complex eigenvalue analysis with the positive real part of the eigenvalue used as a squeal propensity measure. He began by constructing a finite element model of each component and refining the models until good correlation existed with measured modal frequencies. A modal model was then created for each component with the interaction location determined through an iterative procedure until similar frequency response functions to experiment was achieved. Finally the frictional coupling terms were added at the pad-disc interface. These frictional coupling terms form part of the stiffness matrix which now has off diagonal terms and is no longer symmetric. Thus the necessary but not sufficient condition for complex eigenvalues to exist was met. For each parameter studied , the spread of eigenvalues was obtained on the s-plane in which the real part of the eigenvalues is represented by the abscissa and the imaginary part represented by the ordinate. The standard deviation of the real parts from the spread was then used as a squeal propensity measure. Using this model , sensitivity studies were carried out for the disc brake system including the effect of coefficient of friction , pad geometry , caliper stiffness and structural damping. The results indicated an increase of instability with

increasing friction coefficient and lining length and that instability could be reduced by improved damping.

Ghesquire [45] analyzed disc-pad systems considering the static full contact condition and studied the evolution of the disc and pad modes when contact stiffness changes. For low contact stiffness the system was found to be relatively stable with the rigid body modes of the pads far lower than the third diametral mode of the disc. When the translational frequency of the pads are in the region of the disc third diametral mode , the system is coupled and the frequency rises rapidly with the increase in contact stiffness until it exceeds the pad translational frequency. The system then remains stable until the frequency approaches the pad rotational frequency then coupling again occurs causing a further rapid increase in the system frequency. The effect of friction is to make possible the coupling of the symmetry and anti-symmetric modes. Modes in close proximity could be made to converge to one unstable mode with the introduction of friction but this alone was shown to be insufficient to initiate instability.

In the work that followed [46] , Ghesquire examined a pad-disc system taking into account the static contact area and the contact between the pad and the support (caliper) boundary. By varying a parameter , the normal contact stiffness for example , the evolution of the system modes could be tracked ; this showed convergence of 2 separate and initially stable modes to one unstable mode which is essentially a binary flutter instability. The caliper-pad contact stiffness was found to affect stability only for high stiffness values. The work of Ghesquire demonstrates the need to include all the modes within the frequency range of the instability for the analysis of disc brake squeal and that modal proximity alone is not enough to initiate squeal.

Lee [47] studied disc brake noise using component modal matrices and coupling them with a friction interface formulation which links a normal direction degree of freedom to the corresponding lateral degree of freedom. He measured brake noise and showed that regardless of the noise frequency , the rising portion of the amplitude envelope could be fitted very well by an exponential curve , thus proving that a

mathematical expression for the amplitude of brake squeal could be written in the form of a pair of exponential functions of complex conjugate order:

$$x = Ae^{(\alpha \pm i\beta)t} \tag{2.25}$$

The above equation could be the general solution of a set of undamped equations of motion , $[m]\{\ddot{x}\} + [k]\{x\} = 0$. For example by using the Hilbert transformation a measurement of single squeal noise amplitude revealed the rising amplitude in the form $x = A_o e^{\alpha t} = 2.3x10^{-8} e^{917t}$. The method was used to analyze moan , a low frequency disc brake noise using a single pin on a flexible disc to model the phenomenon ; the brake noise was shown to be dependant on both caliper length and friction coefficient.

Mottershead and Chan [48] analyzed the effect of disc symmetry on disc flutter instability. The analysis used finite elements of the disc only which deform under frictional follower loads acting as surface tractions which are active only in the direction opposing the rotation of the disc. The equations were arranged to form a friction matrix which was then added to the stiffness matrix and the ensuing eigenvalue problem solve. For flutter modes , the eigenvalues occur in complex conjugate pairs with the mode shapes of the real and imaginary modes differing in phase by 90 degrees , referred to as sine and cosine modes. These modes are capable of supporting flutter instability as they are already in a state of coalesce and require a small but finite load to be applied to drive the instability. Therefore the doublet modes are considered to be susceptible to squeal. The numerical results showed that singlet modes are unaffected by the brake pressure and show no tendency to become unstable. Thus the symmetry of the disc is considered the primary mechanism of flutter instability and the frictional mechanism considered as only secondary based on this approach.

Hulten [49] used an interface friction relationship which he termed the counter-coupled friction model where the motion in the x-direction causes changes in the normal force acting in the y-direction. The reverse action applies for the corresponding normal motion in the y-direction. The friction element formulation with this nodal relationship was then used to evaluate the eigenvalues for a brake shoe model and a brake pad model

on a rigid plane. The solution indicated instability with a non-synchronous motion for the brake shoe and also for the brake pad. Thus Hulten concluded that the brake shoe or pad acted as a motor to generate squeal.

2.3.7 Other theoretical work

Nishiwaki [50] derived a generalised theory of brake noise to explain low frequency groan and also high frequency squeal problems. The kinetic and potential energy terms of each component were calculated and , using Lagrange's equation , the kinetic energy per cycle of the coupled system was determined. Increase of kinetic energy of the system over a cycle indicates instability. The integration of kinetic energy over the cycle excludes symmetric terms (i.e. the component stiffness and mass matrices) thus leaving the anti-symmetric term of the friction matrix. The system equations of motion were also used to determine the eigenvalues the positive real parts of which indicate instability. The approach indicated that all the brake problems considered , i.e drum and disc brake squeal and groan , are essentially instability problems which can be analyzed by determining the complex eigenvalues.

2.4 Experimental Work

2.4.1 General experimental techniques

Apart from experiments carried out in conjunction with modeling work , experiments have also been conducted primarily in order to quantify the nature of squeal and the various operating conditions affecting it.

Bracken and Sakioka [51] proposed a list of methods to overcome the subjective nature of disc brake squeal evaluation. This included a period of bedding-in of the brake system (whereby the intially high rate of wear is allowed for) and the measurement of the frequency spectrum and the rotor surface temperature for discrete increments in brake pressure.

Tarter [52] used the same burn-in technique as [41] and added a temperature-pressure matrix for the average sound pressure level as a method to determine the preferred temperature and pressure for squeal to occur. His experiments with the brake pad central area milled to reduce the pad stiffness showed a lowering of the squeal frequencies and , for different friction materials , different squeal frequencies were found. His work on radially slotted rotors indicated a stable condition , with no audible squeal detected. The test procedures were then updated to include accelerated conditioning of the brake studied [53].

2.4.2 Experiments to determine the effect of component dynamics on squeal

Lewis and Shah [54] used an experimental method to isolate the source and mechanism of disc brake squeal. Their measurements indicated the fifth diametral mode of disc vibration and the outboard pad deflected in-phase with the disc for a squeal frequency of 7250 Hz. Frequency measurement of the disc brake system under static condititons showed the natural frequency of the assembled system to be 6500 Hz which is near to the squealing frequency. Removing the disc and clamping the brake assembly to a work table , the frequency measurement was repeated , the results of which showed that the subsystem of the pad and caliper alone had a resonance near the squeal frequency , with the system resonance at higher frequency becoming more pronounced with increase in line pressure. Free-free modal analysis showed the first bending mode of the pad to be at 6250 Hz and the 5th diametral mode of the disc to be at 6500 Hz. From the measured dynamics of the system the authors deduced that , at appropriate line pressure , localized resonances of the pads coincide with the localized resonance of the disc to form the global system resonance of squeal. They also proved that altering the natural frequency of the pad by adding mass eliminated squeal. Added a constrained layer of damping material to the brake pad backplate in order to damp out the bending motion of the pad proved to be successful in suppressing squeal.

Hoffman [55] reported the development of a new constrained layer damping material and laid down the requirements for the constrained layer damping to be effective within the operating temperature and vibration frequency range of a squealing disc brake.

2.4.3 Experiments on the effect of contact stiffness on squeal

Hany et al [56] analyzed squeal noise with the squeal generated relatively continuously using a glass disc apparatus which allowed direct observation of the whole assembly. They found that roughening of the glass disc surface is a necessary condition for squeal. The effect of normal load was found to be :

a) to increase the sound pressure level within the 30-100N range

b) to increase squeal frequency within the above range (e.g. 9024 Hz at 30N and 9216 Hz at 90N) whilst , above this range of load , higher modes were excited.

High rigidity in the normal direction of the disc obtained by higher modulus friction material or increased contact radius was shown to reduce the sound pressure level. It was observed that during squeal the friction force increased compared to the no squeal condition and this was attributed to the simultaneous increase in tangential and normal contact stiffness.

Working on the above assumption that the increase of tangential and normal contact stiffness is the cause of squeal , Hany [57] used this effect to analytically design out longitudinal vibration that lead to squeal. The normal and tangential contact stiffness arising from the contact of asperities at the pad-disc interface were modelled as massless springs. The Routh-Hurwitz criterion was then used to derive the characteristic equations to determine the stable boundary. The numerical results indicated several parameters which tended to reduce squeal namely short , thick and wide pads , a more rigid caliper , higher Young's modulus and loss factor of the friction material. Nevertheless the longitudinal vibration predicted by the model remained dependant on the slope of the friction coefficient - velocity relationship.

2.4.4 Experiments on the effect of separation of doublet modes

Nishiiwaki et al [58] studied the effect of mass added to the disc in order to separate the doublet modes of the disc. The initially stationary mode would then rotate thus changing the excitation area continously throughout the rotation with the effect of preventing squeal. However when the effect of added stiffness from the pad-disc contact area was taken into account , high brake pressure with consequently high contact stiffness reduced the mode separation effect. Further mode separation (by increasing the added mass) was found to be an effective way of overcoming the added stiffness effect. Experimental work evidently showed the effectiveness of this approach in reducing the squeal propensity.

Lang et al [59] used doublet mode decoupling by added mass to achieve stability of a drum brake and studied the effect of added stiffness when a practical mass was added to the drum. Their study showed the cyclic decoupling effect when the mass rotated with the drum producing cyclic squeal. Added stiffness along the drum periphery was found to be effective in separating the doublet modes with the arc length having great influence on the separation ; a longer arc length was more effective for separation of the lower modes.

This method of removing the symmetry of the rotor and separating the doublet modes was used by Kim [60] in his analytical work to eliminate squeal from a S-cam drum brake installation. Added mass located at the drum peripheral was shown to enhance the decoupling effect of the doublet modes and concentrated added mass was more effective than distributed mass. The trends from his analysis matched well with experiment.

2.4.5 Experiments using double-pulsed laser holographic

Imaging techniques using holography allows the equal displacement line of the flexing surface of the vibrating body to be captured. Double pulsed laser interferometry allows the visualisation of the vibration pattern by generating onto it a system of

interference fringes which are loci of equal displacement occuring between the first and second pulses with the timing between the pulses controlled to match the frequency of the body by sensing the maximum amplitude of the cycle.

Felske and Happe [61] used this technique to analyze general vibration of automotive interest - the chasis , gearbox and also disc brake squeal. The study of disc brake squeal in particular revealed the pad to be vibrating with a mode shape similar to the first bending free-free mode when squeal occured at 6.5 kHz with low pressure application. At higher pressures , the mode shape changed to the fixed-free first bending mode. In subsequent work Felske, Hoppe and Matthai [62] specifically studied disc brake squeal. The study showed that squeal (for a different brake type) was strongest at 2.5kHz , when the squealing frequency coincided with the caliper resonance frequency. For the short pad used in the study , this was attributed to the contact areas between the caliper and the nodes of the vibrating backplate. The mode shapes of the pad included bending and also twisting with anti-nodes at every corner of the pad. For the long brake pad studied , the anti-nodes of the disc reinforced the vibration with the displacement of the paws considered reactionary. Measurement of the sound pressure level emitted during squeal was compared to that of the disc when excited artificially. This showed that the higher sound pressure level came from the squealing brake system rather than from the artificially excited disc , indicating that the major part of the noise came from the caliper. They suggested the following remedial actions based mainly on reduction of the amplitude of the coupled vibrations:

a) increased damping to limit amplitude during resonance

b) increased stiffness of the pad

c) caliper paws to coincide with the antinodes of the pad

d) increased stiffness of the caliper

e) mismatching the natural frequencies of the components.

The work proceeded to analyse drum brake squeal [63] in which the squeal was hypothesised to be initiated at the lining interface causing a bending-twisting vibration of the shoe which was transmitted to the drum and the backplate. Similar remedial actions

as listed above were suggested , for example stiffening of the flange of the backplate to reduce the amplitude of the anti-node vibration.

Fieldhouse and Newcomb [10] used the holographic interferometry technique to study the effect of the abutment on disc brake squeal. They produced a clear reconstructed holographic image of the free-free vibration of the disc and the pad and also of the squealing brake assembly. For combined trailing and leading edge abutments the mode shape of the disc and the outboard pad were transformed from the sixth diametral and bending modes respectively at low pressure to the sixth diametral and twisting mode respectively at a higher pressure range , with a quiet zone inbetween the two pressure ranges. For a trailing edge abutment , the system was relatively quiet and squeal obtained only with difficulty ; and the disc mode was of high-order (eighth diametral mode) at pressures in the range of 0.14-0.27 MPa and of low order mode (the third diametral mode) at pressures in the range of 0.20 - 0.41 MPa. Higher pressures tended to quieten the system. The leading edge abutment was shown to be the most unstable , with a relatively wide range of pressure (0.14 - 0.8 MPa) and of temperature (20 - 114 degrees Celsius) for which squeal was recorded. The mode shape of the disc was of the fifth diametral mode with the anti-node position under the pad shifted to the node position at a pressure above 0.68 MPa. The overall results demonstrated the importance of the line pressure and abutment configuration in disc brake squeal.

Fieldhouse and Newcomb [64] extended their analysis to study the disc mode shape waveform and the effect of piston-pad contact position on disc brake squeal. From the holographic image , they discovered that the disc waveform moves not only relative to the disc but also relative to ground and the variation in amplitude indicated the possibility of an additional waveform of a similar order displaced in space and time - similar to a complex wave of real and imaginary parts. The effect of piston-pad contact position was studied by inserting a wire in various positions between the piston and pad with the resulting squeal favouring a leading edge position up to a certain distance beyond which the effective sound pressure level was reduced.

2.5 Discussion

Progress in the understanding of disc brake squeal mechanisms has been assisted in recent years by the increased complexity of the experimental and computational techniques available.

Early work [14,15,16,17,18,19,20] suggested disc brake squeal was an instability problem primarily caused by the friction coefficient increasing as the sliding velocity decreases. The difference between each model was of a geometrical nature and either inclusion or exclusion of damping. Later longitudinal instability of a brake pad was also demonstrated to be caused by the same effect [57]. With this understanding , remedial action has been centred around increasing the damping of components to reduce the resonant amplitude.

Kinematic instability [21,28,32,35,37,38,39,40] due to the geometric disposition of the rubbing component provided new insight into the squeal problem. With this mechanism , instability may occur with an invariant coefficient of friction above a critical value when a suitable geometry configuration is achieved. This is analytically demonstrated by mapping the stability boundary either using the Routh-Hurwitz criterion or by solving the characteristics equation and assessing the real part of the complex eigenvalues obtained. Upto this point the models considered were of pin -on-disc type only , differing only in the degrees of freedom considered and the complexity.

Lumped parameter modelling [10,41,42,43] has allowed closer approximation of the true brake system. The friction effect has been modelled as a function of variable normal force i.e. proportional to the displacement between the pad and the disc. This approach however is limited to one particular frequency of squeal and only rigid body modes of pad translation and rotation can be considered ; this in particular is valid for short brake pads. However the approach is less valied for long brake pads (which is the trend for modern disc brake design) since flexible modes of the pad cannot be included in the model. Moreover the disc squeal modes need to be predetermined to allow accurate representation of the equivalent ground stiffness of the disc ; this works well for

exisiting brake designs but remains indeterminate for new brake systems at the design stage.

With the finite element method [6,44,45,46,47,48,49] the flexible modes of the brake components can modelled but the complexity increases as more components and modes are considered. The friction effect included is still similar to that used in lumped parameter modelling where the friction force is a function of normal force which itself is proportional to the normal displacement between the pad and the disc. This representation has been successfully used in eigenvalue sensitivity analysis [46]. The advantage of the finite element method lies on the fact that geometrical representation of the components is not lost in the analysis.

Study of the disc brake components in isolation indicated two different mechanisms of disc brake squeal. Firstly study of the disc [58,59,60] has shown that it is the symmetry of the rotor that is responsible for squeal. A symmetric rotor produces doublet modes , the term used to describe two modes of the same order occurring at the same frequency but with phase difference. Doublet modes which have a phase difference of 90 degrees are very susceptible to squeal. Similarly the disc doublet modes can be regarded as stationary [58] thus being continuously excited at the contact area. This approach advocates the separation of the doublet modes in order to achieve stability ; this can be achieved by adding mass but is only partially successful in overcoming the effect of increased pressure or added stiffness. Analysis of the pad alone [40] has shown that , above a critical coefficient of friction , the pad could be excited producing asynchronous motion hammering the disc to produce squeal. This approach advocates that a stable pad should not create squeal. Experimental evidence is available to support both ideas.

The representation of friction in the models studied can be categorized into two major types. The first is the relatively complex representation based on the Oden-Martin model [8] which accounts for the normal approach indentation (the displacement), its time derivative (the velocity of the contact) and the approach phase. This is a very realistic representation as shown in the two degree of freedom model by Tworzydlo et al

[33]. The main disadvantage of this approach is the high cost of computation which prohibites its use in multi degree of freedom models. The second approach gives a variable friction force proportional to the variable normal force which is represented as a function of relative displacement between the pad and the disc. This approach has been used in numerous models [6,41,42,43,44,45,46,47,48,49]and has proven successful in producing complex eigenvalues the real parts of which are used as an index for squeal propensity.

Experimental evidence using holographic interferometry [9,61,62,63,64] suggests that flexible modes of the pad are involved in squeal and that changes in abutment type and pressure application points do affect squeal considerably.

From the papers studied , there are various steps that can be taken to overcome squeal with different techniques to suit different stages of production. Some methods are very suitable at the design stage. Although no universal solution has yet been found ; some of the remedies for squeal are listed below:

1) Prevention of global resonance of the disc brake system by mismatching the natural frequencies of the components.

2) Limiting the amplitude during resonance by either

   a) increased damping of the brake components , usually the pad by constrained layer damping at the backplate

   b) increased stiffness of the pad support - this can occur naturally when high pressure is applied to the system

   c) suppressing the anti-nodes of the pad by appropriate location of the paw.

3) Separation of the doublet modes of the rotor by added mass or by unsymmetric stiffness of the disc by means of slotted rotor.

4) The use of a shorter brake pad.

5) Reduced friction by using a friction material with low coefficient of friction.

There are other techniques at the post-production stage in particular where, by measuring component frequencies and comparing them with squeal frequencies , the

individual components responsible for the squeal can be identified and the natural frequencies altered.

2.6 Conclusions

From the literature review of the previous experimental and theoretical work on disc brake squeal , the following conclusions can be drawn :

(a) Increasing friction coefficient with decreasing velocity is one of the mechanisms whereby friction energy is fed into the disc brake system causing the amplitude of the motion to increase with time when instabilities are present leading to squeal.

(b) Dynamic instability resulting in squeal of the disc brake system can arise from favourable dynamic and geometric conditions , even when the coefficient of friction does not vary with the sliding velocity. Thus (a) is not a necessary condition for squeal to occur.

(c) The friction force can be modelled as a function of variable normal force. The variable normal force is proportional to the relative displacement between the disc and the pad and also proportional to the contact stiffness.

(d) The real part of the complex eigenvalues can be used as an index for squeal propensity.

e) The finite element method is a very suitable technique to investigate disc brake squeal since multiple flexible modes of the contributing components can readily be modelled.

f) The important operating parameters of applied pressure or temperature have not yet been considered in the squeal models reviewed.

CHAPTER THREE

METHODOLOGY OF PRESENT STUDY

3.1 Introduction - The Need for A New Approach

Previous models of squeal as discussed above range from relatively simple lumped-parameter models to geometrically representative finite element models. Squeal in general does not occur throughout the full operating range of pressure and temperature but favours low pressure and low brake temperature applications. Sakioka and Bracken [51] identified the favoured combination of pressure and temperature for brake squeal by comparative display of the squeal sound pressure level over the pressure-temperature matrix. Experiments by Fieldhouse and Newcomb [64] also showed that pressure is an important factor in squeal.

None of the models reviewed so far have considered the effect of the pressure applied on the brake pad, squeal being represented as an instability resulting only from favourable dynamic parameters (mass ,damping and stiffness) or geometric parameters

(point of force application). The pressure distribution and contact area between the disc and the pad is influenced not only by the Young's modulus of the friction material and the position of the piston force application to the brake pad backplate but also the friction coefficient at the interface of the sliding pair as shown by Harding [65] in which different points of application of piston force will produce different contact pressure distributions. Again this will cause a shift of the centre of pressure and based on the sprag-slip model a favourable sprag angle may occur resulting in disc brake squeal. Experimental evidence by Fieldhouse & Newcomb [64] suggested that, upto a certain distance of the point of application of the pressure forward of the piston centre-line, the disc brake can readily be made to squeal and that stability can be achieved by moving the centre of pressure toward the rear of the piston centre-line.

Alteration of the backplate thickness will not only change the natural frequencies of the pad but also the contact pressure distribution [66]. Therefore a favourable contact pressure distribution can be achieved by proper matching of friction material modulus and backplate thickness. Even though Ghesquire [46] does consider the actual area of contact under static pressure in his model , the measurements with ink paper were done without any sliding friction, thus giving a symmetric pressure distribution During sliding, friction has been shown to shift the centre of the interface contact reaction force toward the leading edge [67], depending on the modulus of the friction material and its coefficient of friction. This will influence the sprag angle and therefore the overall stability of the disc brake system Mismatching the free-free natural frequencies of the components has been suggested as a means of avoiding squeal [7,54] but this is not entirely satisfactory as the boundary conditions in the real contact situations differ markedly. Therefore a stability analysis which considers the pressure distribution and magnitude of the coupled system would provide a more detailed explanation of the contribution of each effect to squeal.

Another parameter which has not been considered in previous models is the surface condition of the friction face. Experiments by Sherif [56] showed that a glazed surface is a necessary condition for squeal to occur and experiments with pin-on disc apparatus by Yokoi & Nakai [29] showed that a worn and relatively smooth pin surface

would make the system readily squeal. The surface condition therefore is another factor governing squeal and the continuously changing surface condition may explain the fugitive nature of squeal.

In short , by including the effect of interfacial pressure on disc brake squeal , a more sophisticated model which considers in particular the magnitude of pressure applied and contact pressure distribution and the surface properties of the friction interface could be achieved , thus bringing the representation of squeal nearer to the true physical situation. This model would hopefully provide some explanation as to why squeal is pressure dependent and why it tends to occur under low actuation pressure situation. However any such model must be carefully validated against experiment before it can be used with confidence to predict the effect of parameter changes.

3.2 Selection of Experimental Results for Validation

Experiments concerning the pressure effect on squeal of a fist-type slider caliper disc brake system have been carried out by Fieldhouse and Newcomb [10]. The holographic interferometry technique was used to determine the mode shapes of the squealing disc brake system and the effect of varying line pressure was studied. The same technique was also used for free-free natural frequency analysis of the two most important components of the disc brake system : the pad and the disc. In the free-free analysis , piezo-electric crystals were mounted on the surface of the disc and also on the pad to provide the excitation forces needed for the analysis. Double-pulsed laser holography was used to capture an image of the deformed pad or disc (the mode shape) presented in the form of a reconstructed holographic image. This in turn provided excellent data for the present finite element analysis , where validation of the free-free natural frequency analysis is essential for the subsequent stability analysis to be successful.Therefore the published work of Fieldhouse and Newcomb [10] allows correlation between the experimental data and the finite element analysis in respect of :

1) free-free modal analysis of the disc and the brake pad

2) stability of the coupled disc brake system.

3.3 Operation of A Fist-Type Sliding Caliper

In order to analyse the effect of pressure on squeal , a brake system similar to the one used in the experiments by Fieldhouse and Newcomb [10] was selected The fist-type sliding caliper system has three major components , the disc , the caliper assembly and two pads. The caliper assembly as shown in figure 3.1 consists of the caliper carrier bracket (B) and the caliper (H) itself which houses the piston (G). The caliper (H) is able to slide on the two guide bolts (A) of the fixed caliper bracket allowing movement in the wheel axis direction with respect to the disc. There are two corresponding pin holes on the caliper with two rubber bushes , lightly oiled to allow the whole caliper to slide on the two guide bolts. The caliper carrier bracket is bolted to the car suspension.

The operation of this disc brake system begins with the driver applying pressure to the brake pedal , thereby increasing the hydraulic line pressure and causing the piston push the inner pad against the disc. When the inner pad comes into contact with the disc, the reaction force from the disc will cause the caliper to slide along the two guide bolts in the direction B as shown in figure 3.2. The fist (or paw) will now press on the backplate of the outer pad to move it into contact with the disc. Therefore both pads are now in contact with the disc , resisting the disc rotation by the friction force generated at the pad-disc interfaces. The abutments at ends of the caliper bracket would provide the reaction force necessary to prevent the pad from rotating with the disc as shown in figure 3.3. There is a clearance between the pad backplate and the abutment slot on the caliper bracket which therefore can only sustain compression forces (as tension will produce a no contact condition) except when shims are used to fill in the gaps as in the experiments of Fieldhouse and Newcomb. The contact areas at each abutment area are shown shaded in figure 3.3.

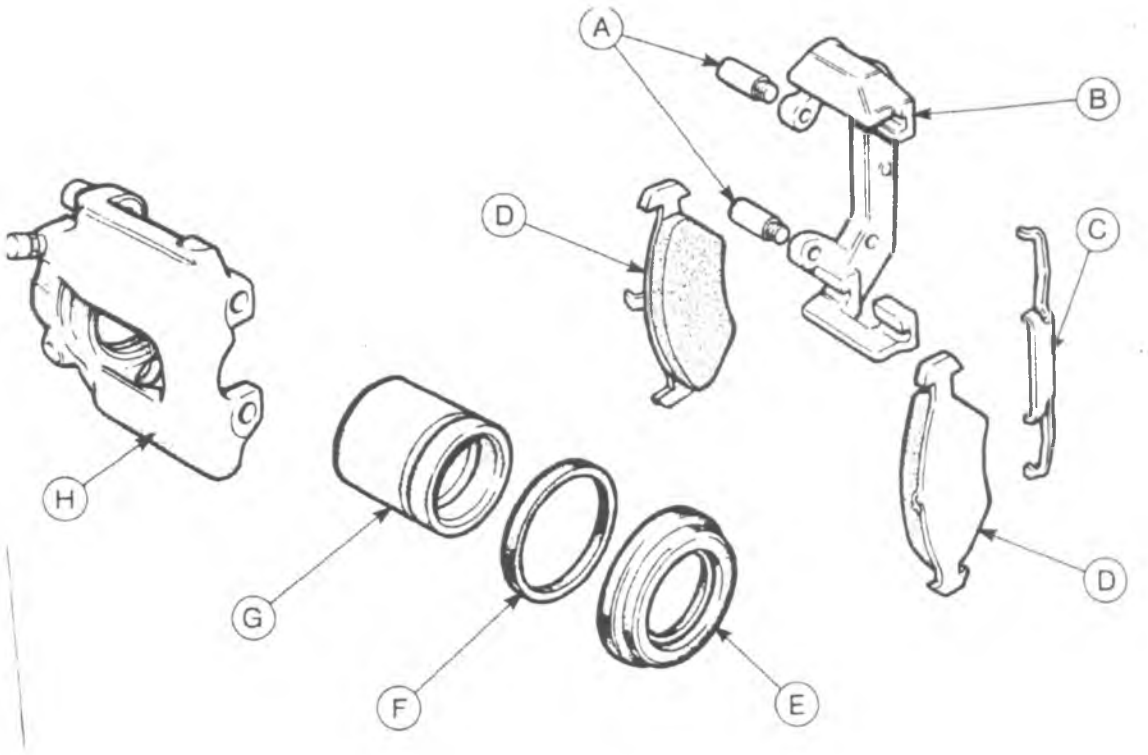

A Guide bolts
B Caliper carrier bracket
C Caliper retaining clip
D Disc pads
E Dust excluding seal
F Piston seal
G Piston
H Caliper

Figure 3.1 Exploded view of the caliper assembly [68]

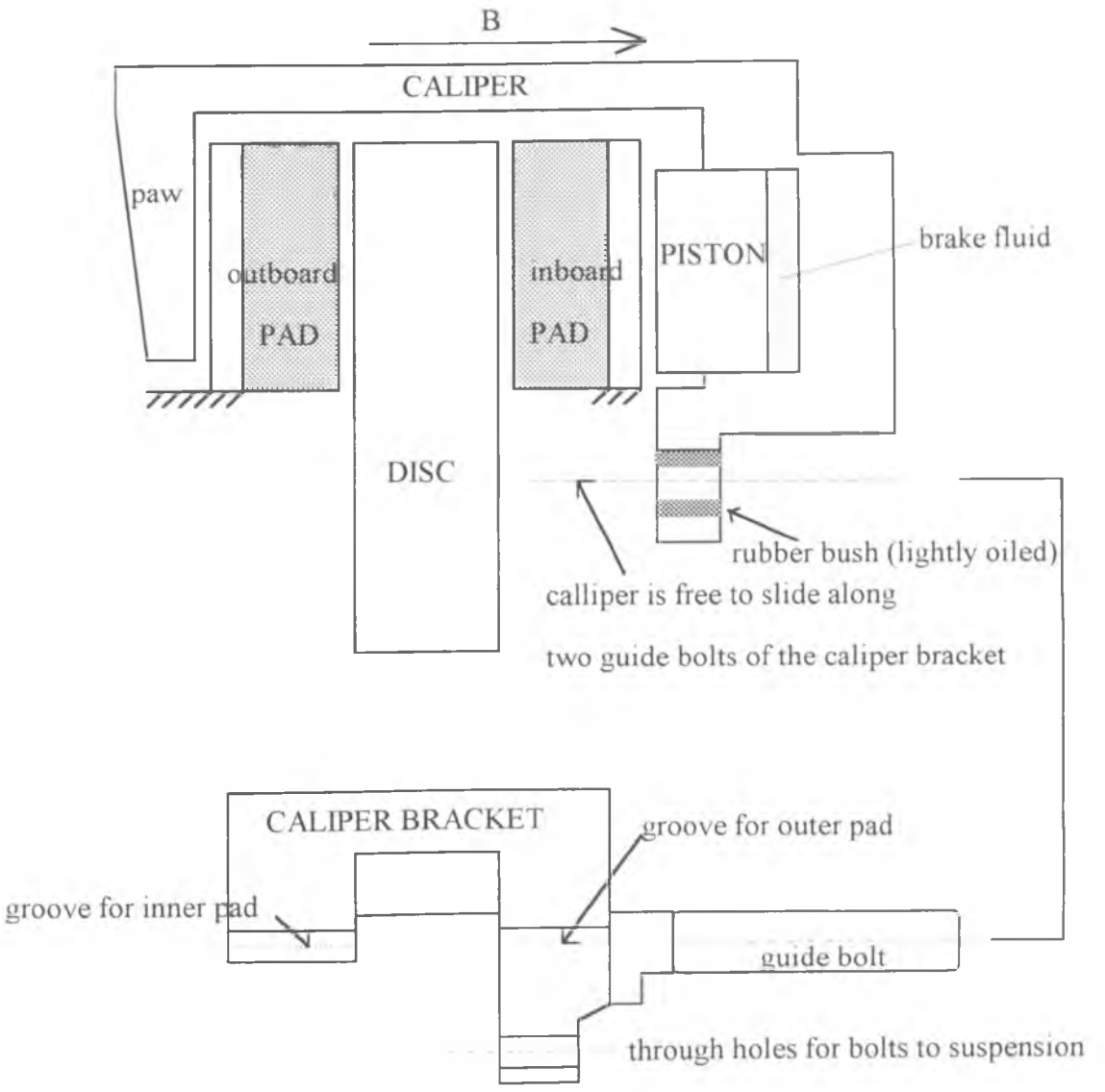

Figure 3.2- Schematic diagram of the operation of the sliding caliper disc brake.

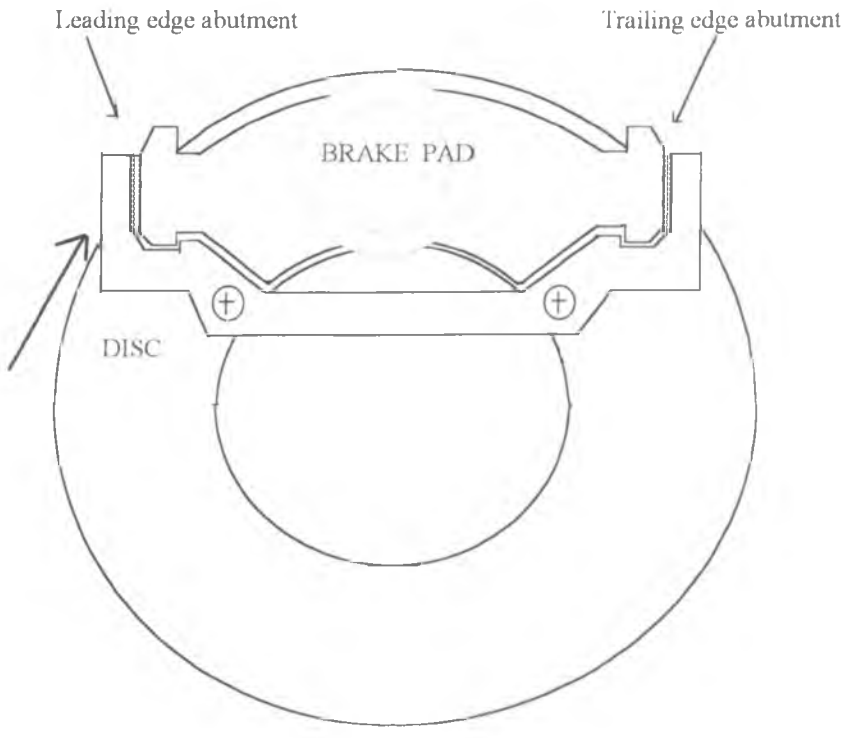

Figure 3.3 - The brake pad and the abutment arrangement. (dotted lines showing relative position of the piston on the pad backplate)

3.4 Pressure Representation

In previous analyses of disc brake squeal , the components involved are usually assumed to be in full contact and the contact stiffness is represented as massless stiff springs. The contact would often be modelled as a single-point contact as in lumped parameter models [7,41,42,43] whilst in finite element models the contact is represented as stiff springs connecting the disc face nodes with the adjacent pad nodes with equal stiffness at all the connected nodes. Previous work on brake contact pressure analysis has shown that the contact pressure distribution at the pad-disc interface is not uniform with the normal pressure maximum at about the centre of pressure application on the brake pad backplate [65,66,69] and that full contact over the pad area could only be achieved with the most compliant friction material [66]. Modern friction materials are

often of the semi-metallic type with good thermal conductivity and wear properties but relatively high modulus. This latter must result in only partial contact.

Therefore for more realistic modelling of the interface contact , two conditions must be established. Where there is no contact , there should be no coupling between the sliding faces but where contact is established , the surfaces should be connected with a contact stiffness k_c. Most lumped parameter models quote a constant figure of k_c based on the compliance of the friction material given as below :

$$k_c = t/(AE) \tag{3.1}$$

where t=thickness of friction material

A= contact area

E = Young's modulus of friction material

Alternatively , if the compliance of the friction material is modelled separately as in the finite element method the contact stiffness k_c could be made a measure of the coupling strength of the interface. Stiff joints with high values of k_c would indicate strong coupling of the components since unit relative displacement of the interface node would generate high reaction forces. Similarly low values of k_c would indicate weak coupling of the components as unit relative displacement would generate relatively low reaction forces. It is assumed at this point that contact stiffness could be made a function of the normal force applied , with the general effect of increase in normal force being to increase the contact stiffness. The effect of the brake pad pressed against the disc could be modelled in a similar fashion to a beam on elastic foundation with the contact stiffness taken as the foundation modulus. In other words, the contact pressure of the pad-disc interface can be represented as massless springs with the contact stiffness k_c distributed along the interface as shown in figure 3.4.

As the reaction force at each node is different , a different contact stiffness is specified for each spring connecting a node pair. Thus, the contact stiffness at each node pair k_i is a function of the reaction force at that node pair F_i (figure 3.4).

Force equilibrium dictates that :

$$F = \text{total force} = \sum_{i}^{i=n} F_i \qquad (3.2a$$

where n is the number of nodes in contact

and for springs in parallel $K = \text{total contact stiffness} = \sum_{i}^{i=n} k_i$ (3.2b

$$\text{where } K=f(F) \quad \text{and } k_i = \frac{F_i}{F} K \qquad (3.3)$$

Therefore the effect of pressure is implicit in the system equations of motion by means of the stiffness representation.

In order to estimate the correct contact reaction force distribution at the pad-disc interface , a static contact pressure analysis is required prior to the dynamic stability analysis of the coupled system. Node pairs which have zero reaction force predicted from the contact pressure analysis will have no contact stiffness in the stability analysis whilst other node pairs will have contact stiffness in direct proportion to the predicted reaction force.

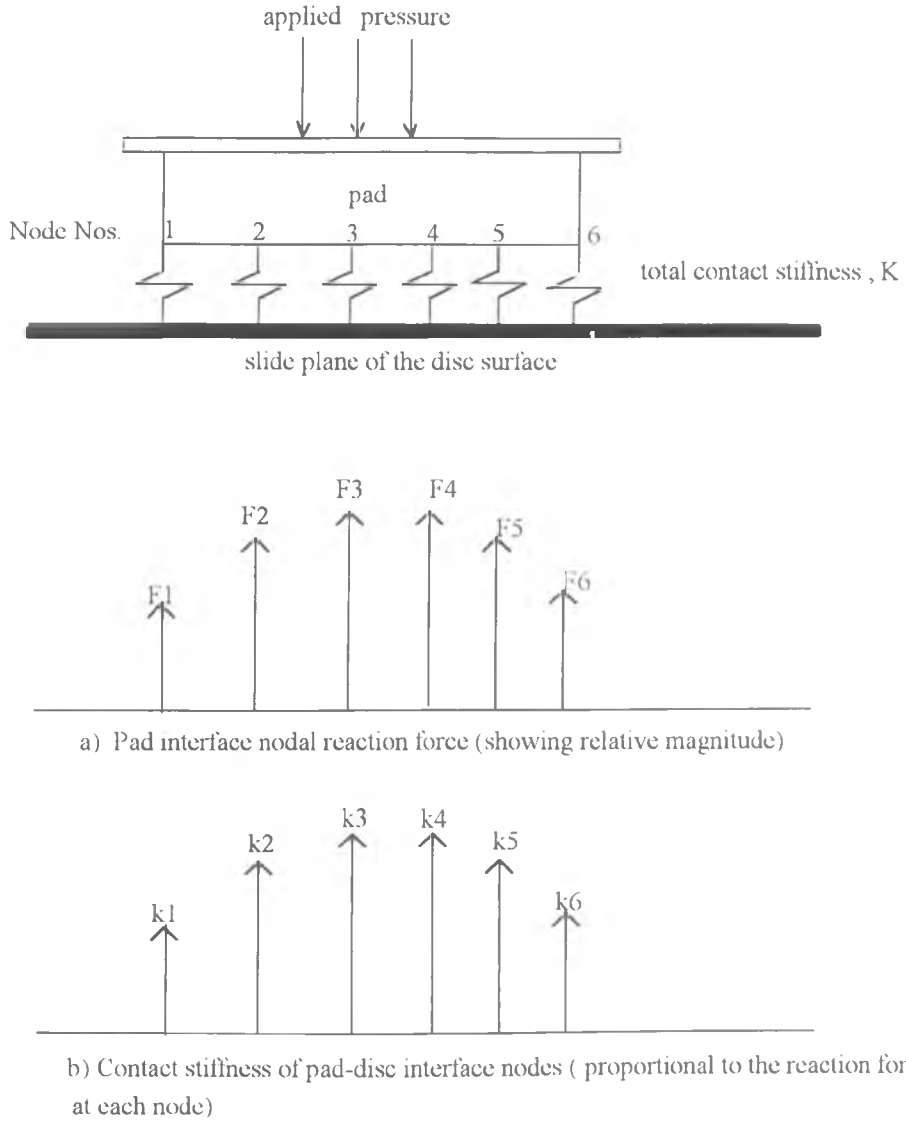

Figure 3.4 - Representation of contact pressure effect using distributed contact stiffness.

3.5 Interface Element

3.5.1 Variable friction force with variable normal force

The contact stiffness derived from the interface contact pressure analysis is to be used in the friction element which defines the interaction between adjacent nodes including the effect of friction. This friction element must be able to model :

i) the steady state friction force acting at the interface of the components

ii)the steady state reaction force acting in the normal direction

iii)the varying part of the normal force which is to be proportional to the stiffness of the element and the relative displacement of the adjacent nodes

iv)the varying part of the friction force which is to be related to the varying normal force according to Amonton's law ($F=\mu N$).

Such an interface is represented graphically in figure 3.5.

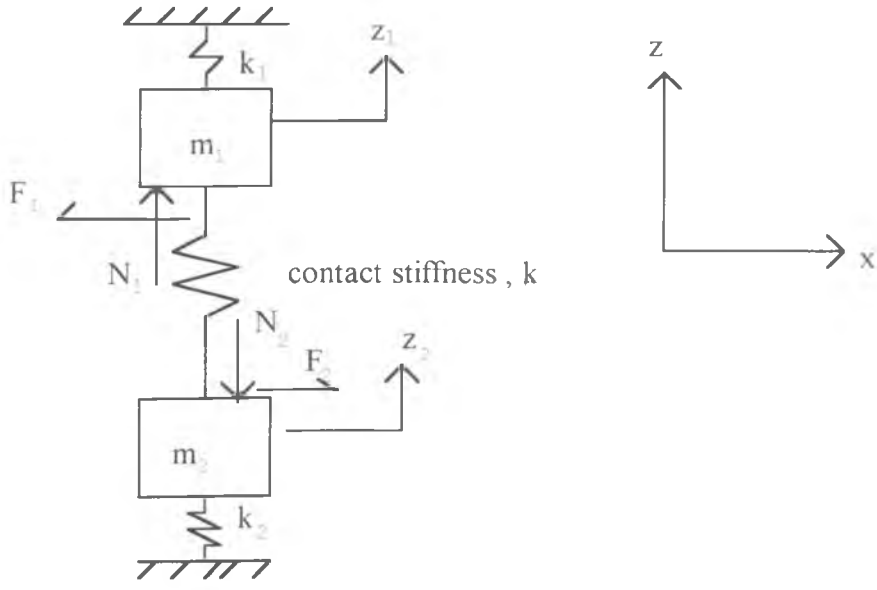

Figure 3.5 - Interaction of two masses with friction effect included

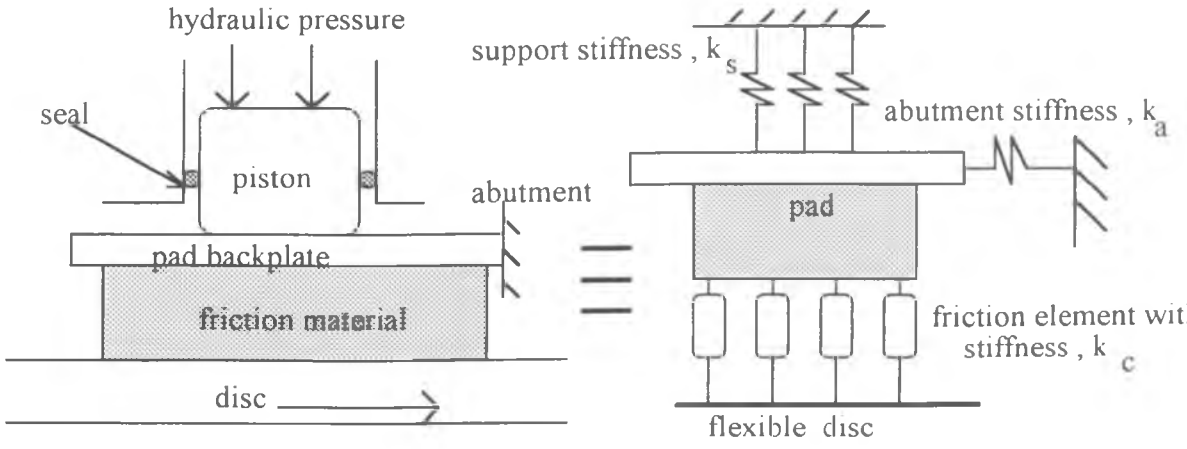

a) Schematic pad on disc system

b) Equivalent model with interface element

Figure 3.6- A pad model coupled to the disc face with friction elements

From figure 3.5 ,

The steady state normal force on mass 1 = N_1

The steady state friction force acting on mass 1 , $F_1 = \mu N_1$

Variable normal force acting on mass 1 due to the relative displacement :

$$\Delta N_1 = k_c(z_2 - z_1) \tag{3.4}$$

Variable friction force due to variable normal force on mass 1 :

$$\Delta N_1 = \mu \Delta N_1 = \mu k_c(z_2 - z_1) \tag{3.5}$$

For the disc brake system studied , sliding is uni-directional and the total normal force is assumed constant acting normal to the slide plane (figure 3.6). The interface nodes only 'see' the effect of the gross friction force acting against the direction of relative motion.

Assume that node 1 represents one of the nodes on the disc face and node 2 is the adjacent node on the brake pad friction face as shown in figure 3.7. When perturbed, nodes 1 and 2 move relative to each other causing a variable normal force on node 2 which is a function of the relative displacement between the two nodes and the contact stiffness (i.e. $dN_2 = k_c (y_1 - y_2)$). In the case where both nodes move further apart:

$$\Delta N_2 = k_c [(-y_1) - (+y_2)] = -ve \tag{3.6}$$

as shown in figure 3.7(ii). This would reduce the total effective normal force acting on node 2 (i.e. total effective normal force = steady state normal force + variable normal force)

$$N_{eff2} = N_2 + (- dN_2) \tag{3.7}$$

This in effect superimposes the variable normal force on to the steady state normal force.

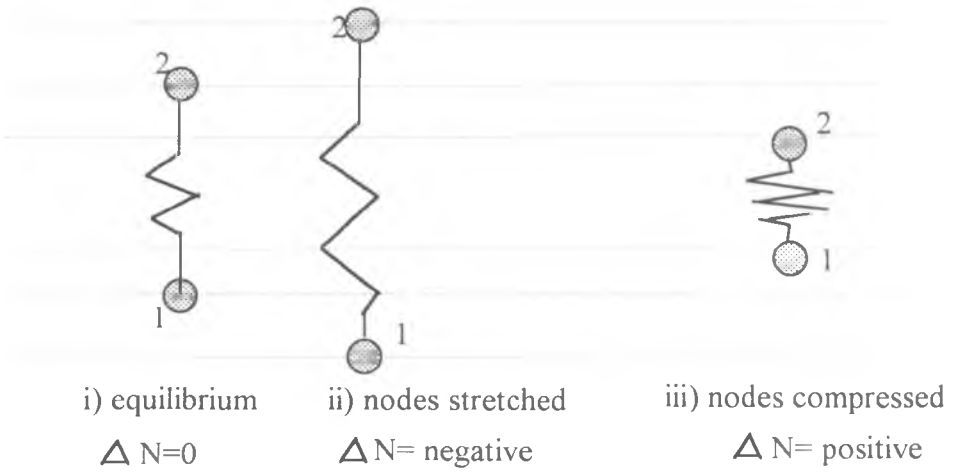

Figure 3.7- The effect of normal displacement to the variable normal force.

When the nodes move closer together as in figure 3.7(iii), the displacement of node 1 from the equilibrium position would be y_1 (+ve) and node 2 would be y_2 (-ve) and therefore :

$$dN_2 = k_c[\,(+y_1) - (-y_2)\,] = +ve \tag{3.8}$$

$$N_{eff2} = N_2 + (+dN_2) \tag{3.9}$$

which increases the effective normal force.

The varying part of the friction force is related to the normal force as below :

$$(F_2 + dF_2) = \mu(N_2 + dN_2) \tag{3.10}$$

and since $F_2 = \mu N_2$

$$dF_2 = \mu\, dN_2 \tag{3.11}$$

From the above equation the dynamically varying friction force dF_2 is proportional to the dynamically varying normal force dN_2. For node 1 a similar relation is obtained by

taking into consideration the direction of the forces. This effect would be realised in the model as alternately reducing and increasing the effective normal force as the displacement varies harmonically about the mean value and as a consequence the effective friction force would also vary in a similar manner. This provides the necessary mechanism for energy to be fed into the vibrating system , creating self-excited oscillations and making the system potentially unstable.

The equation of motion representing the interaction of nodes 1 and 2 can therefore be used as the basis of the interface element in a stability analysis. In order to make the friction element compatible with the finite element software used , in this case ANSYS Revision 5.0A [9] developed by the Swanson Analysis System Incorporation , the direct input method using the MATRIX 27 element is most suitable. The MATRIX 27 element allows direct input in matrix form of the relationship between two nodes using any one of the node variables - displacement , velocity or acceleration; in this case the displacement is chosen as the variable. From the equations of motion of the two nodes , the MATRIX 27 element is written in matrix form as follows.

Referring to figure 3.5 :

at node 1 (pad friction face) $$F_{x1} = \mu\, k_c(y_1 - y_2) \qquad (3.12a)$$

and $$F_{y1} = k_c\,(y_1 - y_2) \qquad (3.12b)$$

at node 2 (disc friction face) $$F_{x2} = -F_{x1} \quad \text{and} \quad F_{y2} = -F_{y1} \qquad (3.13)$$

Thus arranging the nodal stiffness relationship in matrix form :

$$\begin{bmatrix} 0 & -\mu k_c & 0 & \mu k_c \\ 0 & k_c & 0 & -k_c \\ 0 & -\mu k_c & 0 & -\mu k_c \\ 0 & -k_c & 0 & k_c \end{bmatrix} \begin{bmatrix} x_1 \\ y_1 \\ x_2 \\ y_2 \end{bmatrix} = \begin{bmatrix} F_{x1} \\ F_{y1} \\ F_{x2} \\ F_{y2} \end{bmatrix} \qquad (3.14)$$

or $$[K_f^e]\{u\} = \{F\} \tag{3.15}$$

where $$K_f^e] = \begin{bmatrix} 0 & -\mu k_c & 0 & \mu k_c \\ 0 & k_c & 0 & -k_c \\ 0 & -\mu k_c & 0 & -\mu k_c \\ 0 & -k_c & 0 & k_c \end{bmatrix} \tag{3.16}$$

In the above element interface friction matrix , only 2 degrees of freedom for each node are considered whilst in the MATRIX27 element all six degrees of freedom for each node must be included (3 translational and 3 rotational freedoms). However since friction is assumed to act in the circumferential direction only the full matrix is sparse.

In order to apply the above approach to the disc-pad interface, some minor modifications are necessary. The coupled pad-disc system can be represented as in figure 3.6 where k_c is the interface contact stiffness coupling the mating surfaces of the disc and the outboard and inboard pads. The normal and friction forces arising from small displacement of the components as shown in figure 3.6 can be written as follows. For the disc-outboard pad :

Normal force on the disc, $F_{z1} = -k_c (z_1 - z_2)$

Normal force on the outboard pad, $F_{z2} = k_c (z_1 - z_2)$

Friction force on the disc = $F_{y1} = \mu F_{z1} = -\mu k_c (z_2 - z_1)$

Friction force on the outboard pad = $F_{y2} = \mu F_{z2} = \mu k_c (z_1 - z_2)$

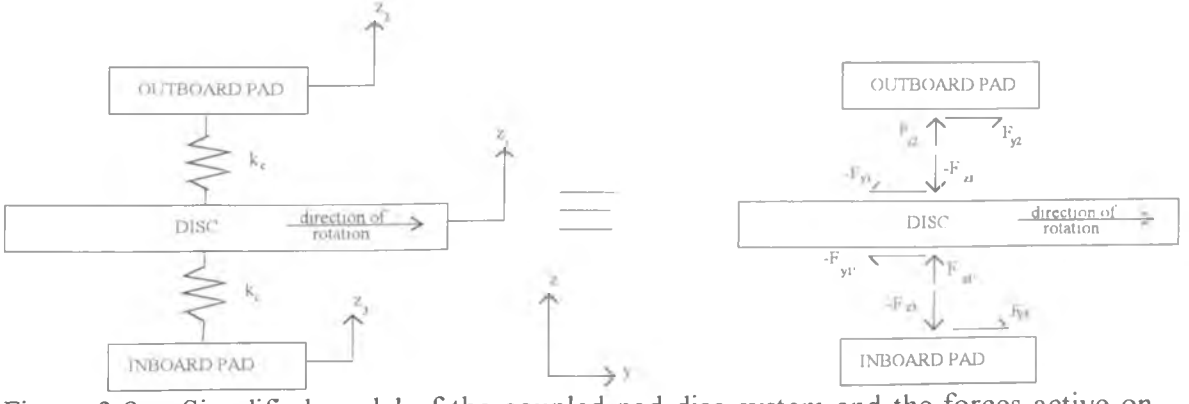

Figure 3.8 - Simplified model of the coupled pad-disc system and the forces active on the interface with friction.

For the disc-inboard pad :

Normal force on the disc, $F_{z1'} = -k_c(z_1 - z_3)$

Normal force on the outboard pad, $F_{z3} = k_c\ (z_1 - z_3)$

Friction force on the disc = $F_{y1'} = -\mu F_{z1'} = \mu k_c\ (z_3 - z_1)$

Friction force on the outboard pad = $F_{y3} = -\mu\ F_{z3} = -\mu k_c\ (z_1 - z_3)$

In the above equations, the negative sign applied to the friction force on the disc-inboard pad cluster is due to the friction force F_v acting in the negative y-direction relative to the positive normal and friction force direction as applied to the disc-outboard pad cluster. The above equations can be arranged in matrix form as follows.

For the outboard pad-disc cluster:

$$\begin{bmatrix} F_{y1} \\ F_{z1} \\ F_{y2} \\ F_{z2} \end{bmatrix} = \begin{bmatrix} 0 & -\mu k_c & 0 & \mu k_c \\ 0 & -k_c & 0 & k_c \\ 0 & \mu k_c & 0 & -\mu k_c \\ 0 & k_c & 0 & -k_c \end{bmatrix} \begin{bmatrix} y_1 \\ z_1 \\ y_2 \\ z_2 \end{bmatrix} = [K_f]\{u\} \qquad (3.17)$$

For the inboard pad -disc cluster:

$$\begin{bmatrix} F_{y1'} \\ F_{z1'} \\ F_{y3'} \\ F_{z3'} \end{bmatrix} = \begin{bmatrix} 0 & \mu k_c & 0 & -\mu k_c \\ 0 & -k_c & 0 & k_c \\ 0 & -\mu k_c & 0 & \mu k_c \\ 0 & k_c & 0 & -k_c \end{bmatrix} \begin{bmatrix} y_{1'} \\ z_{1'} \\ y_3 \\ z_3 \end{bmatrix} = [K_f']\{u\} \qquad (3.18)$$

The above interface stiffness matrices are ready for direct input in order to couple the finite element model of the pad and disc at the interface nodes. This is explained in more detail in section 3.8.

3.5.2 Follower friction force effect

Another effect of friction on a deformable surface is the frictional follower force model proposed by Mottershead and Chan [48] which can be explained as follows. Consider a small area dA on the contact surface as shown in figure 3.9.

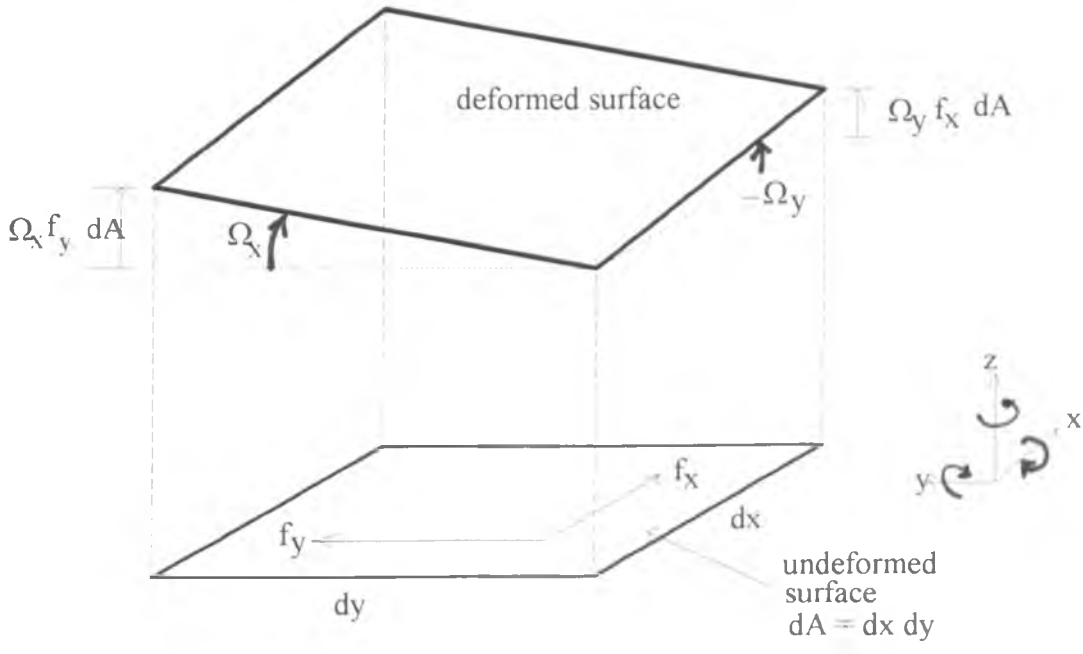

Figure 3.9 - Non-conservative follower forces on deformable surface

Using a local rectangular axis system with x,y in the tangent plane and z normal outward the general friction force could be written in vector form as :

$$\mathbf{f}dA = (\mathbf{i}f_x + \mathbf{j}f_y)dA \tag{3.19}$$

Assuming that the surface is flexible in the transverse direction but stiff in the friction plane and that as it undergoes a small rotation

$$\Omega = \mathbf{i}\Omega_x + \mathbf{j}\Omega_y \tag{3.20}$$

a simultaneous displacement occurs

$$\Delta = \mathbf{i}\Delta_x + \mathbf{j}\Delta_y + \mathbf{k}\Delta_z \tag{3.21}$$

This effect is followed by the surface tractions f , a non-conservative friction force acting upon the deformed surface and is given by :

$$(\Omega \times \mathbf{f})dA = (\Omega_x f_y - \Omega_y f_x)\mathbf{k}dA \tag{3.22}$$

where **i,j** and **k** represent unit vectors in the x,y and z direction respectively. When applied to the disc and pad interface , the friction force is acting in the tangential direction only and the force terms acting in the radial direction is zero (fx = 0). Thus equation (3.22) is reduced to

$$(\Omega \times \mathbf{f})dA = \Omega_x f_y \mathbf{k}dA \tag{3.23}$$

Equation (3.23) indicates that there will be an increase in follower force acting on the surface dA as the surface transverse deformation increases. In order to allow equation (3.23) to be included in the programme using the ANSYS Finite Element software , it needs to be reduced to a form of constraint equations between the nodes. This is achieved by further reducing the equation (3.23) to represent two adjacent nodes on the surface of the disc or the pad at the interface. The two nodes on the same surface, (nodes 1 and 2) are separated by distance d and are acted upon by a friction force F. As the surface deforms one of the nodes will be displaced relative to the other as shown in figure 3.10.

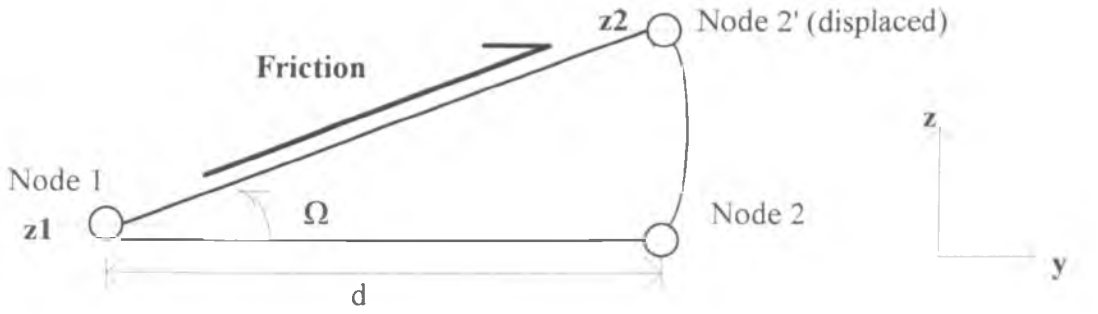

Figure 3.10 Follower friction force effect as applied to two nodes on the same surface

Therefore the increase in the force acting in the z-direction due to the deformation of the surface between node 1 and node 2 can be approximated for small angles as

$$f_z = F\sin\Omega \approx F(z2 - z1)/d \tag{3.24}$$

where z1 and z2 are the nodal displacement in z-direction. Equation (3.24) is the constraint equation used to represent follower forces effect in the stability analysis. The magnitude of the friction force F is determined from the contact pressure analysis. Equation (3.24) shows that the nodal follower friction force is related to the normal displacement of the node and this has been included in the variable normal force friction model described above. In order to use the follower friction force model for analysis of disc-pad interaction, friction force of equal magnitude but of opposite direction is applied with the interface nodes constrained to move together in the direction normal to sliding.

3.5.3 Comparison with the Hulten friction element

In the work of Hulten [49] , the friction element for a drum brake pad was presented as a counter-coupled motion as shown in figure 3.11.

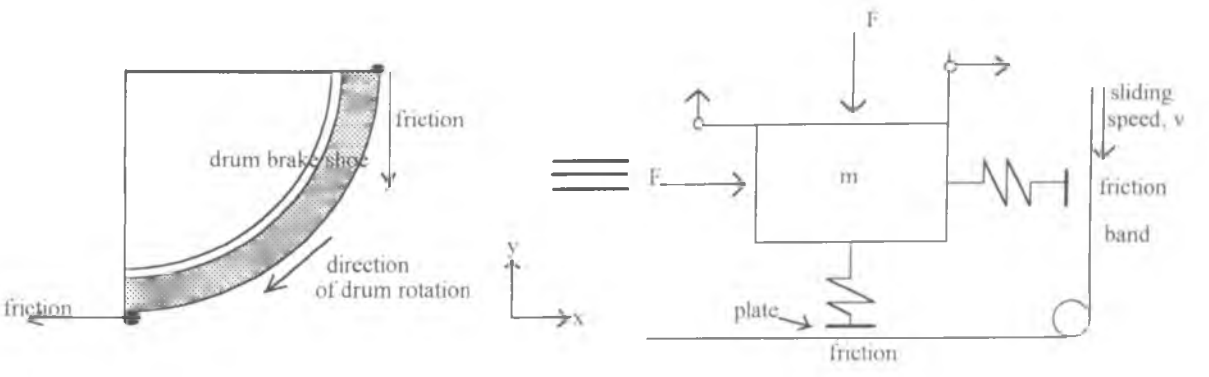

Figure 3.11 - Friction counter-coupled model [49]

The equation of motion for this system can be written in matrix form as :

$$[M]\{\ddot{q}\} + [K]\{q\} = \{0\} \tag{3.25}$$

where $\{q\} = \begin{Bmatrix} x \\ y \end{Bmatrix}$ = generalised displacement vector

$$[M] = \begin{bmatrix} m & 0 \\ 0 & m \end{bmatrix} = \text{mass matrix}$$

$$[K] = \begin{bmatrix} k_x & -\mu k_y \\ \mu k_x & k_y \end{bmatrix} = \text{stiffness matrix}$$

A stability analysis could be performed by solving the eigenvalue problem

$$\det([K] - \lambda[M]) = 0 \tag{3.26}$$

The eigenvalues , λ, can be used to indicate stable or unstable solutions and , if complex eigenvalues exist , they must occur as conjugate pairs. For self-excited problems such as squeal , it is the complex eigenvalues which are of major interest since the positive real parts can be used as an index for the growth of amplitude of the oscillations. In [49], a numerical example was used to demonstrate that the above stiffness matrix could give

rise to instability. However, there is a basic assumption that Hulten made in which the friction force acting on the lower plate must act in the opposite direction to the friction band motion which made the stiffness matrix not representative of the drum brake system modelled. If on the other hand the physical similarity in the friction force direction is maintained (that the friction force acting on the plate must always act in the direction of motion of the friction band) then the friction terms ($\mu k_x, \mu k_y$) will have the same sign in the stiffness matrix which will result in a symmetric matrix and instability will not occur since the eigenvalues will not be complex. However Hulten then used his approach to define the nodal relationship between a disc brake pad and an infinitely stiff rotor represented as a frictional stiffness matrix. For each node representing the interface , 3 degrees of freedom were considered , clearly illustrated in figure 3.12.

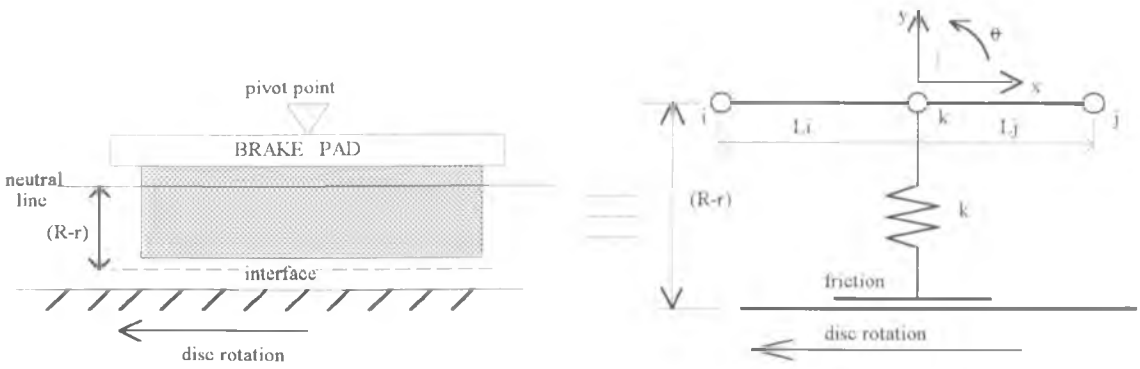

Figure 3.12 - Idealised pad model used by Hulten and the associated nodal relationship with friction effect included.

For the one node shown , x , y and θ are the degrees of freedom considered in the derivation of what Hulten termed a ' friction stiffness' matrix. Lk is the mean surrounding length where $Lk = \frac{Li + Lj}{2}$. The (R-r) term is used to represent the distance of the interface to the neutral plane for bending of the brake pad , thus the derived stiffness friction matrix is as below :

$$k\begin{bmatrix} 1 & 0 & 0 \\ -\mu & 0 & 0 \\ -\mu(R-r)/L_0 & 0 & 0 \end{bmatrix}\begin{bmatrix} y \\ x \\ \theta \end{bmatrix} = \begin{bmatrix} F_y \\ F_x \\ F_\theta \end{bmatrix} \tag{3.27}$$

where F_y is the normal force , F_x is the friction force and F_θ is the friction moment created by the friction force multiplying the distance (R-r) and compensated by the unit length L_0. The resultant friction matrix is then added to the global stiffness matrix to form an unsymmetric global stiffness matrix. In the numerical example of a disc brake pad , 50 elements were used and the results indicated instability. The problem with this approach is that the distance (R-r) must be non-zero to produce instability and that the degree of instability increases with this distance - physically it means that a thicker pad is more unstable than a thin pad which is not borne out in practice. Furthermore this led to the conclusion by Hulten that stability could be achieved if the distance between the neutral plane of the brake pad and the interface could be made which is unrealistic.

With the friction element proposed for the present study in section 3.5.1 above this problem is overcome and the distance from the neutral plane is no longer a necessary parameter in the formulation of the interface element.

3.6 Component Interaction

It is proposed in the present study to limit the component interaction to only the pad and disc. Interaction of the pads with the caliper via the piston and the paw is considered as passive with the interface modelled using stiff springs. Previous studies [6,7,43] show that the effect of caliper stiffness on disc brake squeal propensity is not as strong as the other parameters of friction coefficient , damping and pad length. Furthermore , the fist pin-slider type caliper is not a rigid assembly but several sub-assemblies of different materials ; for example the piston seal and the pin bushes are made of rubber thus introducing considerable flexibility to the assembly.The assumption that the contribution of the caliper to the system stability is small is not applicable to disc brake groan analysis where the noise is at a low frequency of less than 200 Hz and

involves the caliper body motion ; the caliper assembly must be included in analysis of such noise. The approach where only the pads and disc are considered has been used successfully in squeal analysis by Ghesquire [46]. Therefore the same approach is also adopted in the present study

The action of the piston and the paw on the inner and outer pads respectively is represented by stiff springs. For the disc , constraints are applied to represent the top hat portion near to the centre of the disc to the wheel hub.

3.7 Stability Analysis

There are several methods which could be used for the assessment of the stability of the disc brake system studied , namely :

a) the Routh-Hurwitz criterion

b) a transient solution of the equations of motion

c) by complex eigenvalues.

The work of Kuo [70] can be used to explain the concept of the Routh-Hurwitz criterion as a method for determining the right-hand or left-hand side location of zeros of polynomials with constant real coefficient on the s-plane without actually solving the equation. Consider the characteristics equations of a linear time-invariant system of the form

$$F(s) = a_0 s^n + a_1 s^{n-1} + a_2 s^{n-2} + \ldots\ldots + a_{n-1} s + a_n = 0 \qquad (3.28)$$

where all the coefficients are real numbers. The necessary but not sufficient conditions for the roots of this equation to have positive real parts are :

i) all of the coefficients of the polynomial have the same sign

ii) none of the coefficients vanishes (i.e zero).

For these conditions to be met , the polynomial of Hurwitz's determinants must all be positive which can be checked using Routh tabulation The Routh-Hurwitz criterion indicates the absolute stability of the system but does not give the relative stability. The advantage is that it does not require the solution of the characteristic equation

Transient solution of the equations of motion of the system would indicate the presence of an initially increasing amplitude or overshoot for a stable system as well as a true instability but does not indicate which mode is responsible. Moreover for high frequency vibrations such as squeal, the analysis may proved to be very computationally costly as the time steps need to be sufficiently small

For a damped system where the damping matrix is included in the equation of motion of the system , the eigenvalue problem [8] which can be stated in the form below :

$$[K]\{\Phi_i\} + \bar{\lambda}_i[C]\{\Phi_i\} + \bar{\lambda}_i^2[M]\{\Phi_i\} = 0 \qquad (3.29)$$

where [K] , [C] and [M] are the stiffness ,damping and mass matrices correspondingly which may be symmetric or unsymmetric and $\{\Phi_i\}$ is the i-th eigenvector corresponding to i-th eigenvalue λ_i. Solution of the above equation gives the complex eigenvalues λ_i in the form:

$$\bar{\lambda}_i = \sigma_i \pm j\omega_i$$

where σ_i = real part of the eigenvalue

ω_i = imaginary part of the eigenvalue

$j = \sqrt{-1}$

The dynamic response of a particular mode is

$$\{u_i\} = \{\Phi_i\} e^{(\sigma_i \pm j\omega_i)t} \tag{3.30}$$

where t is time.

For i-th eigenvalue , the system is stable if σ_i is negative and unstable if σ_i is positive.

Complex eigenvalue analysis can predict all the modes of the system with the real part of the eigenvalue indicating the stability of the mode and the imaginary part the frequency. This would allow correlation with experimental squeal results and the unstable modes could be made the focus of the attempt to eliminate squeal. In detail , the results when displayed on the complex plane (also known as the s-plane) clearly indicate the relative stability of modes and the root locus diagram may be used to track the progressive instability of the mode concerned.

Even when damping is ignored , the eigenvalue of a system may still be complex as the inclusion of a friction matrix causes the stiffness matrix which is comprised of real terms to be unsymmetric thus fulfilling one of the necessary condition for a system to have complex eigenvalues [71].

The advantages of complex eigenvalue analysis over the other methods of identifying instability are obvious , with the strength lying mainly in the ability to clearly identify the unstable modes responsible for squeal. Therefore the method of complex eigenvalue analysis was adopted for the present study.

3.8 Complex Eigenvalues Analysis Using The Finite Element Method

The theory of the finite element method in general is discussed in this section and in particular with respect to eigenvalue problems based mainly on two references [72,73].The finite element method can be broken into several major steps :

1) Transformation of the boundary value problem into a more general and simpler form for finite element approximation.

2) Discretization of the domain and functions in the weak form. This in practice entails the breakdown of the region into a finite number of small elements. The coordinates of each nodal point of the elements will define its geometry. The element connectivity of a finite element is the sequence consisting of its node numbers. A typical example of this is shown in figure 3.8.The shape functions N (or the element characteristic matrix) also need to be defined.

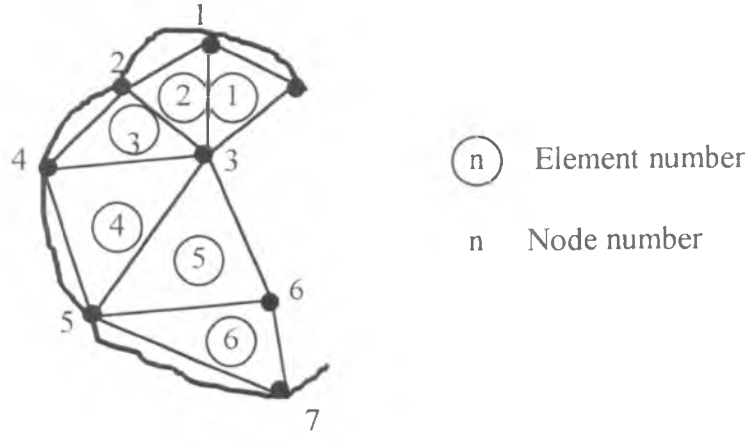

Figure 3.13 Discretization of the domain Ω by 3 nodes triangular elements [73]

3) Derivation of the stiffness and mass matrix. The stiffness matrix can be obtained by various approach (Galerkin , potential energy) but as the potential energy approach is physically more representative it is used here.

Figure 3.14 shows a three dimensional body occupying a volume V and having a surface S. The points on the body is located by x,y,z coordinates. The boundary is constrained in some region where displacement is specified. On some part of the body traction force **T** is applied. Under the force the body deforms in which the deformation of a point is given by the three components of its displacement :

$$\mathbf{u} = [\, u,v,w \,]^{T} \qquad (3.31)$$

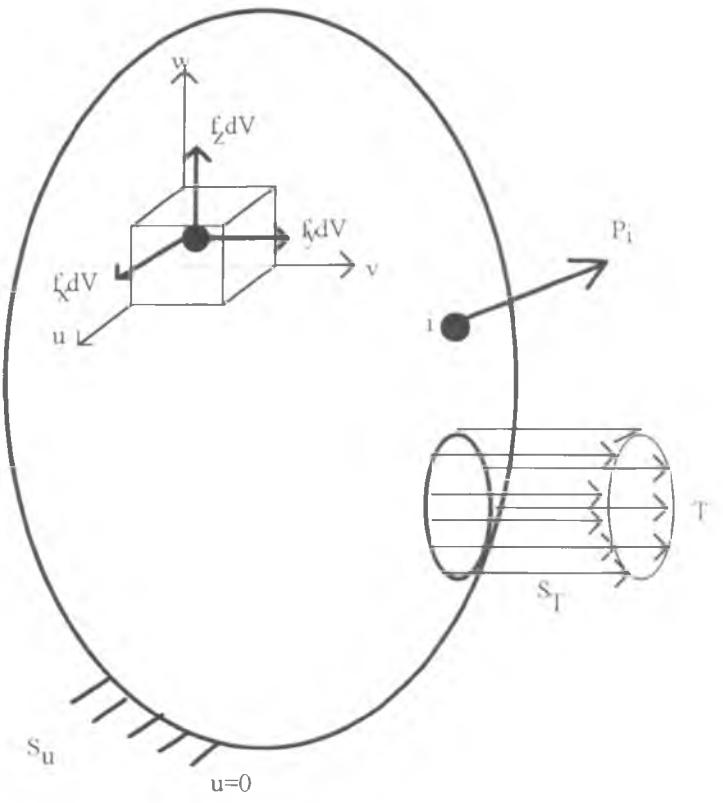

Figure 3.14 - Three dimensional body [73]

The distributed force per unit volume vector **f** is given by

$$\mathbf{f} = [\, f_x \;, f_y \;, f_z \,]^T \tag{3.32}$$

The surface traction T may be given by its component values at points on the surface

$$\mathbf{T} = [T_x, T_y, T_z]^T \tag{3.33}$$

A load P acting at point i is represented by its three components

$$\mathbf{P} = [P_x, P_y, P_z]^T \tag{3.34}$$

The stresses acting on the elemental volume dV can be represented by six independant components as follows:

$$\sigma = [\sigma_x, \sigma_y, \sigma_z, \tau_{yz}, \tau_{xz}, \tau_{xy}]^T \tag{3.35}$$

where σ_x , σ_y , σ_z are normal stresses and τ_{yz} , τ_{xz} , τ_{xy} are shear stresses.

The strain is represented in a vector form

$$\varepsilon=[\varepsilon_x , \varepsilon_y , \varepsilon_z , \gamma_{yz} , \gamma_{xz} , \gamma_{xy}]^T \tag{3.36}$$

The general expression for the potential energy Π of a continuum of a volume V of solid material (figure 3.9) is given by

$$\Pi = \frac{1}{2}\int_V \sigma^T \varepsilon dV - \int_V u^T f dV - \int_S u^T T dS - \sum_i u_i^T P_i \tag{3.37}$$

where the terms are as defined above and the last term P_i represents a force acting at point i (in this case the point i is assumed to be a node) and u is the displacement at that point. For a volume in which the area is constant (dV=Adx) and after discretization the expression for potential energy becomes

$$\Pi = \sum_e \int_e \sigma^T \varepsilon A dx - \sum_e \int_e u^T f A dx - \sum_e \int_e u^T T dx - \sum_i Q_i P_i \tag{3.38}$$

or simplified as

$$\Pi = \sum_e U_e - \sum_e \int_e u^T f A dx - \sum_e \int_e u^T T dx - \sum_i Q_i P_i \tag{3.39}$$

where U_e is the element strain energy given by

$$U_e = \frac{1}{2}\int_e \sigma^T \varepsilon dV \tag{3.40}$$

Using Hooke's Law $\sigma = E\varepsilon$ and by substituting $\varepsilon = \mathbf{Bq}$

$$\sigma = E\mathbf{Bq} \tag{3.41a}$$

where $\mathbf{B}$ = element strain displacement matrix and $\mathbf{q}$ = displacement vector and the subscript e indicates element. For one-dimensional element with linear shape function the matrix $\mathbf{B}$ is given by

$$\mathbf{B} = \frac{1}{x_2 - x_1}\begin{bmatrix} -1 & 1 \end{bmatrix} \tag{3.41b}$$

Thus $$\mathbf{U}_e = \frac{1}{2}\int_e q^T B^T \mathbf{E} Bq \, \mathbf{A}dx \tag{3.42}$$

or $$U_e = \frac{1}{2}\mathbf{q}^T \int_e [\mathbf{B}^T E \mathbf{B} A dx]\mathbf{q} \tag{3.43}$$

For a one-dimensional element with linear shape function , the natural or intrinsic coordinate system denoted by ξ and $-1 \leq \xi \leq 1$ can be used for the transformation

$$dx = \frac{x_2 - x_1}{2} d\xi \quad \text{or} \quad dx = \frac{l_e}{2} d\xi \tag{3.44}$$

where the subscript denotes the node number and l_e is the element length. The element strain energy is now written as

$$U_e = \tfrac{1}{2}\mathbf{q}^T \left[A_e \frac{l_e}{2} E_e \mathbf{B}^T \mathbf{B} \int_{-1}^{1} d\xi \right] \mathbf{q} \tag{3.45}$$

since the $\mathbf{B}$ matrix is constant and E_e is the Young's modulus of the element.

Substituting $\mathbf{B}$ from equation (3.35a and 3.35b) and noting that $\int_{-1}^{1} d\xi = 2$ results in

$$U_e = \frac{1}{2}\mathbf{q}^T \frac{A_e E_e}{l_e}\begin{bmatrix} 1 & -1 \\ -1 & 1 \end{bmatrix}\mathbf{q} \tag{3.46}$$

which is of the form $$U_e = \frac{1}{2}\mathbf{q}^T\mathbf{k}^e\mathbf{q} \tag{3.47}$$

where the element stiffness matrix $\mathbf{k}^e$ is given by

$$\mathbf{k}^e = \frac{E_e A_e}{l_e}\begin{bmatrix} 1 & -1 \\ -1 & 1 \end{bmatrix} \tag{3.48}$$

The expression in equation 3.42 gives the element stiffness matrix for a one-dimensional element with a linear shape function. In general the element stiffness matrix is given :

$$\mathbf{k}^e = \int_e [\mathbf{B}^T E \ \mathbf{B} dV] \tag{3.49}$$

The element stiffness matrices can then be assembled to form the global stiffness matrix $\mathbf{K}$ by preserving the element connectivity (for example $q = [\ Q_1, Q_2]^T$ for element 1 and $q = [\ Q_2, Q_3]^T$ for element 2 where Q_i is the displacement for node i) where the elements of each $\mathbf{k}^e$ are placed in the appropriate locations in the larger $\mathbf{K}$ matrix and the overlapping terms are then summed.

Similarly, using the individual terms in equation (3.39) , the element body force f^e , the element traction force term T^e and the point loads P_i can be evaluated. Therefore the potential energy can be written using matrix notation in the form

$$\Pi = \sum_e \frac{1}{2}\mathbf{q}^T\mathbf{k}^e\mathbf{q} - \sum_e \mathbf{q}^T\mathbf{f}^e - \sum_e \mathbf{q}^T\mathbf{T}^e - \sum_i P_i Q_i \tag{3.50}$$

or $$\Pi = \frac{1}{2}\mathbf{Q}^T\mathbf{K}\mathbf{Q} - \mathbf{Q}^T\mathbf{F} \tag{3.51}$$

where after assembly $\mathbf{K}$ denotes $\sum_e \mathbf{k}^e$ and $\mathbf{F}$ denotes $\sum_e (\mathbf{f}^e + \mathbf{T}^e) + \mathbf{P}$

The mass matrix can be derived from the kinetic energy term. For a solid body with distributed mass , the kinetic energy T is given by

$$T = \frac{1}{2}\int_v \dot{\mathbf{u}}^T \dot{\mathbf{u}} \rho dV \tag{3.52}$$

where ρ is the density , $\dot{u}$ is the velocity vector at point x with components $\dot{u}$, $\dot{v}$ and $\dot{w}$ as shown in figure 3.15.

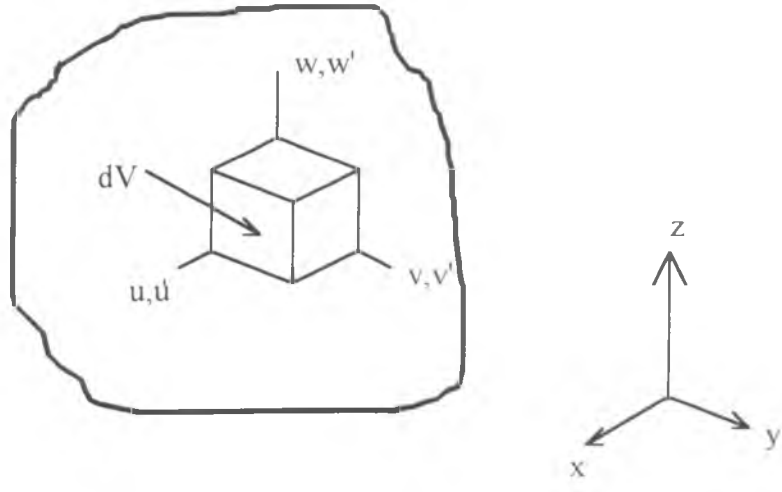

Figure 3.15 Schematic diagram of a body with distributed showing the velocity components [72].

In the finite element method , the displacement of each element is described in terms of the nodal displacement q and shape function N. Therefore

$$\mathbf{u} = \mathbf{N}\,\mathbf{q} \tag{3.53}$$

The velocity vector is then given by $\dot{\mathbf{u}} = \mathbf{N}\dot{\mathbf{q}}$

Substituting this into equation (3.52) , the element kinetic energy is given by

$$T_e = \frac{1}{2}\dot{\mathbf{q}}\left[\int_e \rho \mathbf{N}^T \mathbf{N}\, dV\right]\dot{\mathbf{q}} \tag{3.54}$$

or

$$\mathbf{m}^e = \left[\int_e \rho \mathbf{N}^T \mathbf{N}\, dV\right] \tag{3.55}$$

$\mathbf{m}^e$ is also known as the element mass matrix. Summing over all elements :

$$T = \sum_e T_e = \sum_e \frac{1}{2}\dot{\mathbf{q}}^T \mathbf{m}^e \dot{\mathbf{q}} = \frac{1}{2}\dot{\mathbf{Q}}^T \mathbf{M}\dot{\mathbf{Q}} \tag{3.56}$$

where **M** is the global mass matrix and **Q** is the global displacement matrix.

4) Statement of the Eigenvalue Problem. After obtaining the global stiffness and mass matrices **K** and **M** respectively , the Langrangian approach can be used to determine the Langrangian term L :

$$L = T - \Pi \tag{3.57}$$

or

$$L = \frac{1}{2}\dot{\mathbf{Q}}^T \mathbf{M}\dot{\mathbf{Q}} - \frac{1}{2}\mathbf{Q}^T \mathbf{K}\mathbf{Q} - \mathbf{Q}^T \mathbf{F} \tag{3.58}$$

and by using Hamilton's Principle

$$\frac{d}{dt}\left(\frac{\partial L_i}{\partial \dot{q}_i}\right) - \frac{\partial L_i}{\partial q_i} = 0 \tag{3.59}$$

Thus

$$\mathbf{M}\ddot{\mathbf{Q}} + \mathbf{K}\mathbf{Q} = \mathbf{F} \tag{3.60}$$

For steady-state conditions starting from equilibrium , $\mathbf{Q} = \mathbf{U} \sin \omega t$

and by rearranging equation 3.60 for $\mathbf{F} = 0$,

$$\mathbf{KU} = \omega^2 \mathbf{MU}$$

or alternatively $$\mathbf{KU} = \lambda \mathbf{MU} \tag{3.61}$$

which is a statement of the generalized eigenvalue problem where λ is the eigenvalue and U the eigenvector. In the above approach damping was neglected. However the friction force equation as stated in equations (3.17) and (3.18) is as reproduced below for each interface node pair :

$$\begin{bmatrix} 0 & -mk & 0 & mk \\ 0 & -k & 0 & k \\ 0 & mk & 0 & -mk \\ 0 & k & 0 & -k \end{bmatrix} \begin{bmatrix} y1 \\ z1 \\ y2 \\ z2 \end{bmatrix} = \begin{bmatrix} fy1 \\ fz1 \\ fy2 \\ fz2 \end{bmatrix} \tag{3.17}$$

or $$k_f^e]\{u\} = \{f\} \tag{3.18}$$

By summation over the elements $\mathbf{K}_f = \sum_e \mathbf{k}_f^e$ and $\mathbf{F}_f = \sum_e \mathbf{f}^e$

Therefore $$\mathbf{K}_f \mathbf{Q} = \mathbf{F}_f \tag{3.62}$$

The eigenvalue problem can then be rewritten to include the friction force acting at the interface nodes by substituting for F :

$$\mathbf{M}\ddot{\mathbf{Q}} + \mathbf{KQ} = \mathbf{K}_f \mathbf{Q} \tag{3.63}$$

By bringing the right hand side to the left hand side :

$$\mathbf{M}\ddot{\mathbf{Q}} + (\mathbf{K} - \mathbf{K}_f)\mathbf{Q} = 0 \tag{3.64}$$

The effect is to make the global stiffness matrix unsymmetric because of the inherently unsymmetric friction matrix. According to Wilkinson [71] for eigenvalues problem if A and B (read **K** and **M**) are real symmetric matrices but neither is positive definite then

the eigenvalues of AB need not be real and the same applies to the roots of det(A- λB) =0. In the present case the mass matrix **M** is symmetric but the stiffness matrix $(\mathbf{K} - \mathbf{K}_f)$ is unsymmetric.Therefore the eigenvalues may be complex.

3.9 Method of analysis

As the pressure effect is represented in the form of a varying contact stiffness distribution and the pad - caliper interaction represented by stiff springs , the proposed analysis of disc brake squeal using the finite element method can be broken down into the following steps :

1) Conduct free-free modal analysis of finite element models of the pad and the disc to determine the natural frequencies and the corresponding mode shapes and correlate these with the experimental results of Fieldhouse and Newcomb [10]

2) Carry out a static contact analysis using the finite element model of the pad as derived in step (1) under the applied loading from either the piston and the paw to estimate the contact pressure distribution for both the inboard pad (piston applied pressure) and outboard pad (paw applied pressure) with the effect of circumferential friction effect and abutment arrangement taken into consideration.

3) Determine the contact stiffness for each node pair at the pad-disc interface from the predicted reaction forces and the calculated contact stiffness- reaction force relationship

4) Carry out eigenvalue analysis of the coupled pad-disc system with the boundary conditions applied as stiff springs. As the inclusion of friction causes the stiffness matrix to become unsymmetric , the analyses will predict complex eigenvalues, the positive real parts of which would indicate the squeal propensity and the imaginary parts would indicate the frequency. The corresponding eigenvectors indicate the mode shape of the unstable modes.

Steps 2 - 4 above are repeated for different pressure magnitudes.

3.10 Summary

The need for a new approach to analyse the effect of contact pressure on disc brake squeal has been discussed. The novelty of the work lies in the fact that this effect has never been modelled before despite the experimental and operational evidence that squeal generally occurs at low applied pressures only. To understand this effect a new modelling approach is proposed whereby the pressure distribution and also the surface properties of the interface including the effect of friction is included in a stability analysis of the coupled disc-pad system.

It is argued that the coupling stiffness at each node should vary with the magnitude of the reaction force at that pair , providing some form of preloading to the system and that the friction effect should also be included in the node pair interaction. Since it is known that the reaction force distribution at the pad-disc interface is not uniform this approach will take this non-uniformity into account.The passive interaction between the pad and the caliper is modelled by the penalty formulation whereby approximate stiffness are used to model the boundary conditions. The effect of the interface friction on the system stiffness is derived from first principles and using the finite element method the resulting stiffness matrix when the interface friction element is included becomes unsymmetric. This when taken into the eigenvalue problem may result in complex eigenvalues. Stability analysis is carried out using complex eigenvalue analysis with the real part of the eigenvalue used as a measure of the squeal propensity and the imaginary part as the squeal frequency of the system studied A disc brake system has been selected which has been studied thoroughly using double pulsed laser holography , thus providing the necessary experimental results for comparison.

CHAPTER FOUR

MODAL ANALYSIS OF THE DISC AND PAD

4.1 Introduction

A major step in the proposed analysis of disc brake squeal using the finite element method as discussed in Chapter Three is the development and validation of finite element models of the major components , namely the disc and the pad. The models would then be coupled for stability analysis with the friction effect included at the interface.

In the present chapter all the work related to modal analysis of the components is discussed. This includes the development of the models , the results from the eigenvalue analysis for the free-free condition and comparison with the experimental results of Fieldhouse and Newcomb [10]. The chapter also describes substructuring , a technique by which the number of degrees of freedom of a finite element model can be reduced significantly resulting in a reduced wavefront for the problem.

4.2 General Method of Analysis

Finite element models of the disc and the pad are developed and modal analysis carried using the modal analysis option in the ANSYS Rev. 5.0A software [8] The natural frequencies and mode shapes obtained are compared with the experimental results of Fieldhouse and Newcomb [10]. The finite element model are then refined until acceptable difference levels are achieved between prediction and experiment. In this analysis, damping is neglected as in general structure analysis damping only affects the natural frequencies by 1-2% in most cases [75].

4.2.1 Limitations in the analysis

There are several limitations in the present analysis as discussed below :

1) The usual practice in the dynamic analysis of a system which consists of several components is to carry out the analysis of the components independently and finally to couple them together. This method implies the use of constraints equations to connect the nodes which are in contact and is adequate for passive node interactions (no friction effect involved). However , the use of a friction matrix to define the nodal interactions at the pad-disc interface as proposed in Chapter Three does not permit the use of constraint equations. Moreover the interface nodes of the disc and pads must have similar radial and circumferential co-ordinates if possible in order to closely preserve the contact condition.

2) The present finite element software used (ANSYS Rev. 5.0A Educational Version) has a maximum wavefront of 400, which limits the number of active degrees of freedom in the model and therefore also the degree of refinement of the model to get good correlation with the experiment. A simplified model with many of the degrees of freedom removed would help in reducing the wavefront and would also reduce the CPU time needed to solve the problem. In order to achieve this a technique known as substructuring is used and for the free-free natural frequency analysis the Reduced Householder [8] method is employed as it readily utilises the active degrees of freedom specified for the eigenvalue problem.

4.2.2 General substructuring theory

Substructuring analysis uses the technique of matrix reduction in order to reduce the number of active degrees of freedom [8]. The matrix reduction technique was first presented by Guyan [75]. As the technique is widely used in the present study ,the theory of substructuring [8] will be discussed in some detail here.

In static problems where the inertia is ignored , the finite element equation is reduced to :

$$[K]\{u\} = \{F\} \tag{4.1}$$

where [K] element stiffness matrix

{u} vector representing the total degrees of freedom

{F} force vector

The problem can be reduced by selecting active degrees of freedom , which are also known as masters degrees of freedom and are denoted here by subscript m, whilst the remaining degrees of freedom are considered as slave degrees of freedom , denoted by subscript s. The stiffness matrix can be partitioned into submatrices according to master and slave degrees of freedom as below :

$$\begin{bmatrix} [K_{mm}] & [K_{ms}] \\ [K_{sm}] & [K_{ss}] \end{bmatrix} \begin{Bmatrix} \{u_m\} \\ \{u_s\} \end{Bmatrix} = \begin{Bmatrix} \{F_m\} \\ \{F_s\} \end{Bmatrix} \tag{4.2}$$

It is usual to arrange that $\{F_s\}=0$ i.e. external forces are applied at master degrees of freedom only.

Expanding equation (4.2) :

$$[K_{mm}]\{u_m\} + [K_{ms}]\{u_s\} = \{F_m\} \tag{4.3}$$

$$[K_{sm}]\{u_m\} + [K_{ss}]\{u_s\} = \{F_s\} \tag{4.4}$$

Solving for the slave degrees of freedom in equation (4.4):

$$\{u_s\} = [K_{ss}]^{-1}\{F_{ss}\} - [K_{ss}]^{-1}[K_{sm}]\{u_m\} \tag{4.5}$$

Finally substituting equation (4.5) into equation (4.3):

$$[K_{mm}] - [K_{ms}][K_{ss}]^{-1}[K_{sm}]]\{u_m\} = \{F_m\} - [K_{ms}][K_{ss}]^{-1}\{F_s\} \tag{4.6}$$

or $$[\hat{K}]\{\hat{u}\} = \{\hat{F}\}$$

where $$[\hat{K}] = [K_{mm}] - [K_{ms}][K_{ss}]^{-1}[K_{sm}] \tag{4.7}$$

and $$\{\hat{u}\} = \{u_m\}$$

and $$\{\hat{F}\} = [F_m] - [K_{ms}][K_{ss}]^{-1}\{F_s\} \tag{4.8}$$

The same method can be extended to dynamic analysis :

$$[M]\{\ddot{u}\} + [C]\{\dot{u}\} + [K]\{u\} = \{F\} \tag{4.9}$$

or in the substructured form :

$$[\hat{M}]\{\ddot{u}\} + [\hat{C}]\{\dot{u}\} + [\hat{K}]\{\hat{u}\} = \{\hat{F}\} \tag{4.10}$$

where , by using Guyan's reduction technique [75] for mass reduction :

$$[\hat{M}] = [M_{mm}] - [K_{ms}][K_{ss}]^{-1}[M_{sm}] - [M_{ms}][K_{ss}]^{-1}[K_{sm}] + [K_{ms}][K_{ss}]^{-1}[M_{ss}][K_{ss}]^{-1}[K_{sm}] \quad (4.11)$$

The same approach can be used to derive the reduced damping matrix by simply substituting the mass terms with the damping terms in (4.11).

The terms derived for the reduced mass , damping , stiffness and force matrices are also known as the superelement coefficients , since in the finite element method the technique of reducing a component matrix is akin to forming a superelement with its own mass,damping and stiffness matrices. The reduced stiffness matrix is said to be complete since as shown in equation (4.7) all the elements of the original stiffness matrice contribute. In the case of the reduced mass matrix , combinations of stiffness and mass elements appear As a result the completeness in the eigenvalue-eigenvector problem is said to be closely but not exactly preserved [75].

4.2.3 Substructuring applied to eigenvalue problems

The eigenvalue problem in the reduced condition can be stated as follows:

$$([\hat{K}] - \omega^2[\hat{M}])\{\hat{u}\} = \{0\} \quad (4.12)$$

Thus the reduced eigenvalue problem is of order (p) instead of initial order (p+q) where p is the number of master degrees of freedom and q the number of slave degrees of freedom. The eigenvalues ω^2 obtained from the above equation are used to recover the global displacement vector or mode shape :

$$\begin{bmatrix} [K_{mm}] & [K_{ms}] \\ [K_{sm}] & [K_{ss}] \end{bmatrix} - \omega^2 \begin{bmatrix} [M_{mm}] & [M_{ms}] \\ [M_{sm}] & [M_{ss}] \end{bmatrix} \begin{Bmatrix} \{u_m\} \\ \{u_s\} \end{Bmatrix} = \{0\} \qquad (4.13)$$

where in this case the master degrees of freedom vector $\{ u_m \}$is known from equation (4.12). By solving (4.13) the slave degrees of freedom vector $\{u_s\}$ is recovered and the global vector or mode shape is obtained as

$$\{u\} = \begin{Bmatrix} \{u_m\} \\ \{u_s\} \end{Bmatrix} \qquad (4.14)$$

It is clear from equation (4.12) that the problem size can be greatly reduced by using the substructuring technique.

4.2.4 Selection of master degrees of freedom

As explained in the preceding sections , the substructuring technique requires the selection of master degrees of freedom from the complete model defination. The degrees of freedom selected are important as they define the dynamics of the reduced model ; this is usually achieved by selecting degrees of freedom which have a large ratio of mass to stiffness [8]. In the pad-disc stability stability, the nodal degrees of freedom which define the nodal interaction at the interface need to be preserved. This entails the following considerations :

a) All degrees of freedom in the z-direction (normal to the disc rubbing surface) at the pad-disc interface need to be retained as they are used in the friction matrix.

b) All degrees of freedom defining the interaction between the pad and the external environment (the piston pressure face, the paw pressure face and the abutments) need to be retained.

c)All degrees of freedom in the z-direction on the disc (normal to the disc rubbing surface) need to be retained in order to adequately capture the disc diametral modes. Any

asymmetry introduced in the definition of the disc master degrees of freedom might introduce separation of the doublet modes of the disc ; this should be avoided at the model definition stage.

d)The total number of master degrees of freedom must be less than the number allowed within the limited 400 wavefront. This is equivalent to a limit of about 310 master degrees of freedom.

4.3 Eigenvalue Analysis Of The Disc

4.3.1 Disc model definition

The brake analysed in the present work is similar to the one used in the experiments reported by Fieldhouse and Newcomb [10]. The disc is plain (i.e. unvented), made from grey cast iron and mounted to the wheel hub by four bolts on the top hat section of the disc. The disc cross section geometry and dimensions are shown in figure 4.1.

Various experimental work [7,10,58,60] has shown that only the diametral modes of the disc are involved in squeal. This fact allows for a simpler representation of the disc and for exclusion of the rigid body modes from the stability analysis. In a diametral mode it is the rubbing surface of the disc (shown dark grey in figure 4.1) which deforms at a particular squeal frequency ; this information has been used in the representation of the disc as a beam with two simultaneous modes (translational and rotational) as in the work of North [41] and others [7,42,43]. In the present eigenvalue analysis of the free-free disc , only the rubbing surface and the portion connecting it to the top hat part are therefore considered as shown by the dark grey shade in figure 4.1.

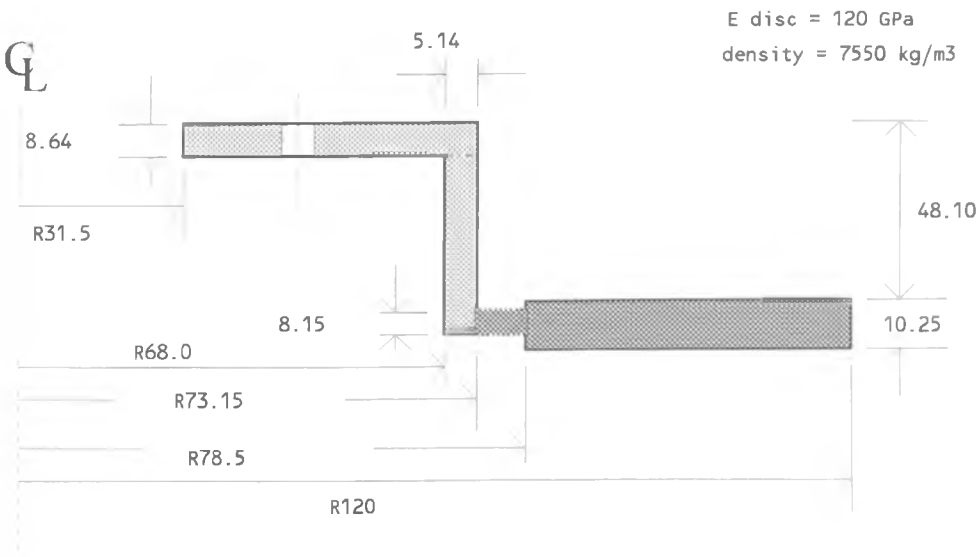

Figure 4.1 - The cross-section dimension of disc (all dimensions in mm)

The element type used in the analysis is a 4 noded three dimensional shell element , known as STIF63 in the ANSYS nomenclature. The advantage of using this element over an 8 noded isoparametric brick is obvious in terms of the relative amount of computational time involved as the 4-noded shell element has half the number of degrees of freedom. In order to investigate the optimum number of elements to be used in the definition of the disc model , a study was carried out in which the number of elements in the radial direction on the disc rubbing surface was fixed at four (which gives a width/thickness aspect ratio of about 1.0) and the circumferential angular definition (figure 4.2) is varied between 20 and 6 degrees.

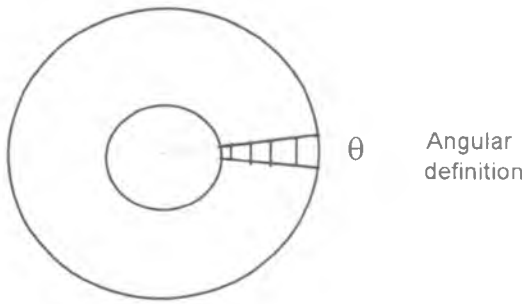

Figure 4.2 - Angular definition in the modeling of the disc

The reduced Householder method is used in the eigenvalue as it readily takes into account all the necessary master degrees of freedom and it is therefore suitable for the analysis of the substructured component. The master of degrees of freedom include all the degrees of freedom in z-direction on the rubbing surfaces of the disc. As the angular definition is reduced , more elements are defined and the problem size therefore increases. Modal analysis is then carried out for each model with the results as shown in figure 4.3.

In figure 4.3, the predicted frequencies of the diametral modes of each model are plotted together with the corresponding experimental results. The detail mode shape of the diametral modes is described in section 4.3.2.It can be seen from figure 4.3 that for modes that are below the fifth diametral mode (marked 5D) the frequencies for all the models are less than the experimental values whilst for modes above the fifth diametral mode the frequencies for all model are greater than the experimental values It is also clear that as the angular definition is decreased (i.e. more elements) the difference between the experimental values and finite element analysis results reduces. The least difference occurs for an angular definition of 6 degrees.

As mentioned above the wavefront limit also restricts the definition of the model. As the master degrees of freedom selected has to include all the nodes on the disc rubbing surface , the number of master degrees of freedom also increases with decreasing angular definition. The effect of angular definition on the maximum wavefront of the eigenvalue problem is shown in figure 4.4. It is clear that as the model becomes more detailed the wavefront size increases. The model with an angular definition of 6 degrees has a maximum wavefront size of 371 which is approaching the 400 wavefront limit of the present software.

It was also decided to investigate whether a full three dimensional model of the disc using 8 noded isoparametric elements (i.e. 'brick elements') would improve the correlation further. Based on this the previous results the angular definition of the full disc was set at 6 degrees but as there are abrupt dimensional changes at the connection between the disc

rubbing surface and the top hat extra elements have to be introduced. This resulted in the need for 23 elements per segment whilst the total number of elements for the model is 1380. The full model of the disc is shown in figure 4.5a. Modal analysis is carried out for this model using full subspace method where all the degrees of freedom of the disc are included. In comparison the simplified disc model using shell elements is shown in figure 4.5b.

The results from modal analysis of the full and simplified models are shown in figure 4.6 together with the experimental results. It is clear from the plot that the full model is in better agreement with the experimental results than the simplified disc. For the full disc model the maximum difference occurs at the eighth diametral mode with the model frequency 253 Hz (2.38%) higher than the experiment whilst the simplified disc model has a frequency of 11225 Hz which is 585 Hz (5.50%) higher than the experiment.

Although the full disc model provides better correlation than the simplified disc model, there is a time penalty associated with using the full disc model. The details of the problem size for both the full disc and simplified disc models are listed in Table 4.1. From the table the number of elements of the simplified model is 300 with 1800 degrees of freedom whilst the number of elements for the full model is 1380 with total 25920 degrees of freedom. More importantly is the time needed to solve the problem. The CPU time for the full model is 8124.5 seconds whilst for the simplified model it is 74.56 seconds. In real time the solution took 5 hours 28 minutes for the full model and 201 seconds for the simplified model. It is therefore obvious that while on one hand the full model gives better correlation it takes much longer to solve; on the other the simplified model is very much faster and has acceptable correlation. Therefore it is decided to adopt the simplified model for the subsequent coupled analysis as it is sufficiently accurate with very much reduced computational time.

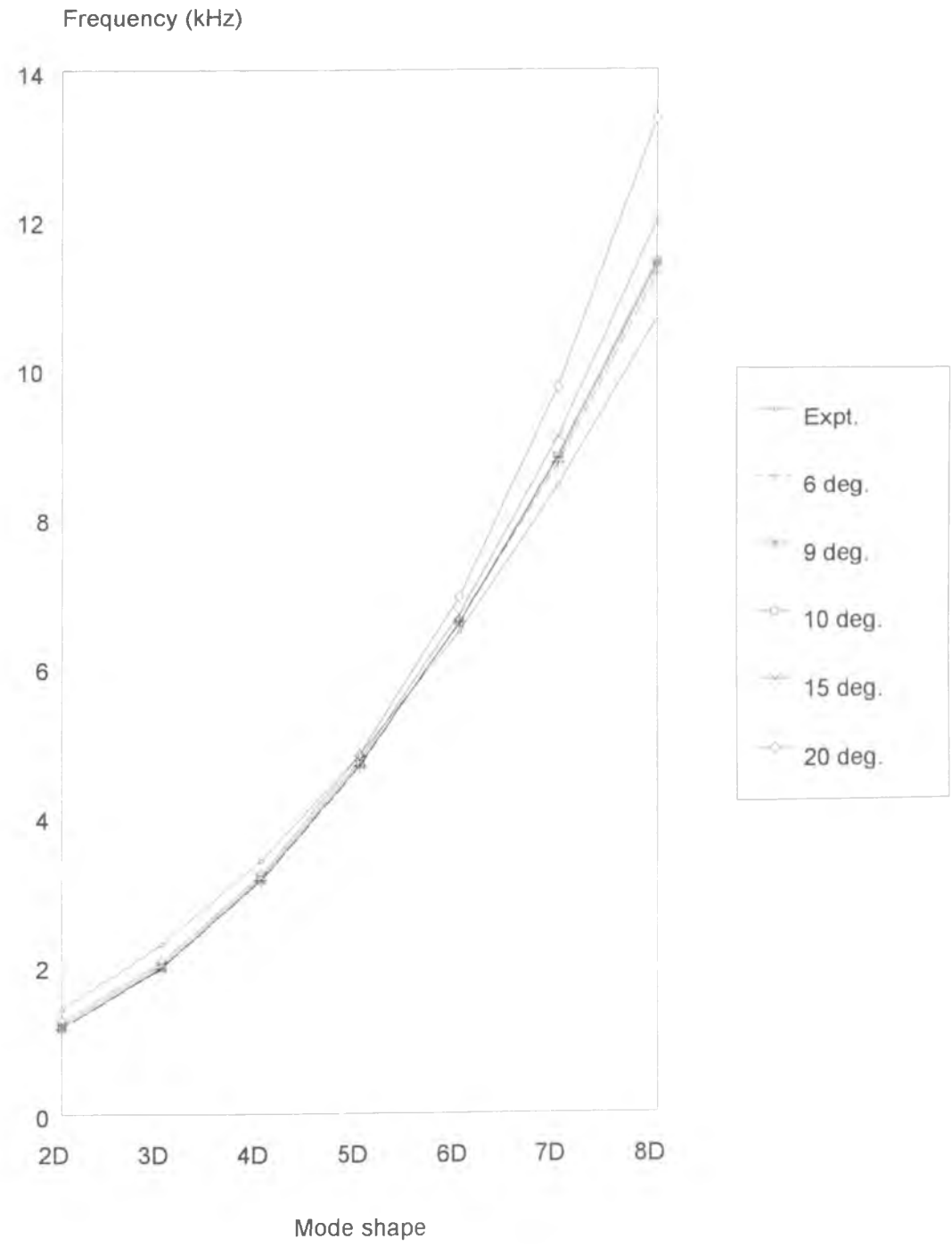

Figure 4.3 - The frequencies for the diametral modes of the disc for various angular definition of the disc model and experimental results.

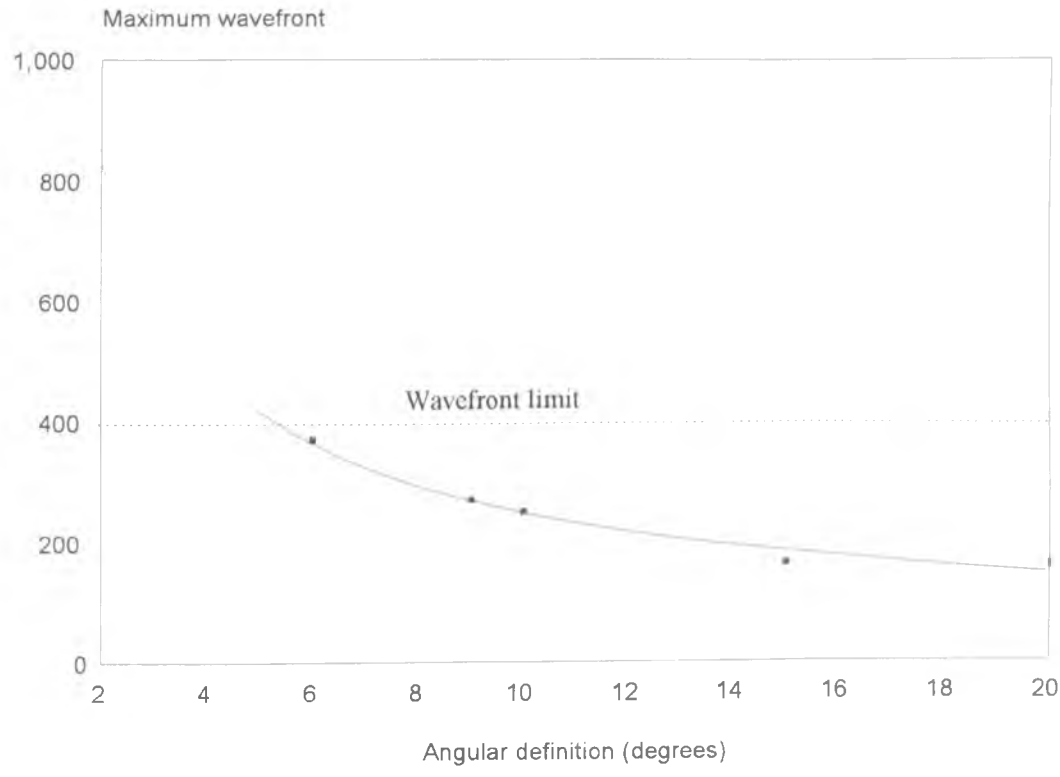

Figure 4.4 - The effect of the angular definition of the disc model on the wavefront size

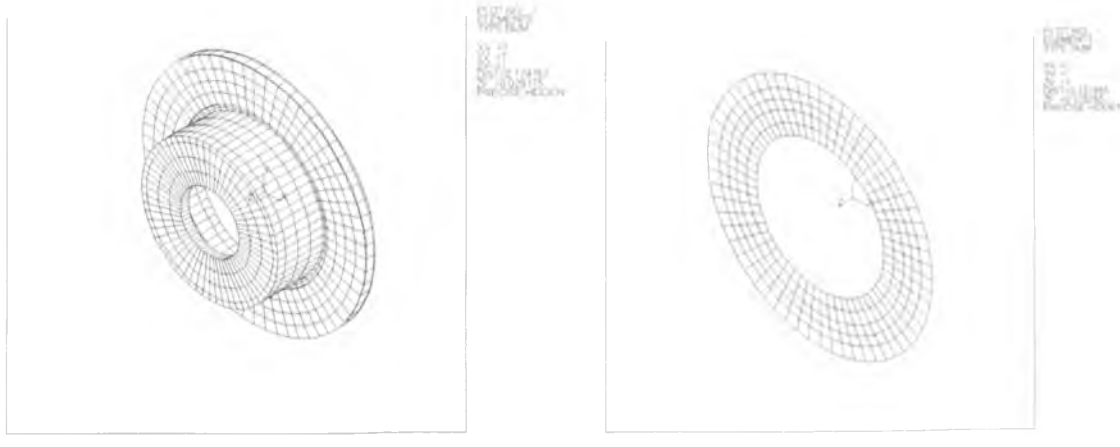

(a) (b)

Figure 4.5 - The finite element model of (a) full disc with 3D solid elements and (b) simplified disc using shell elements

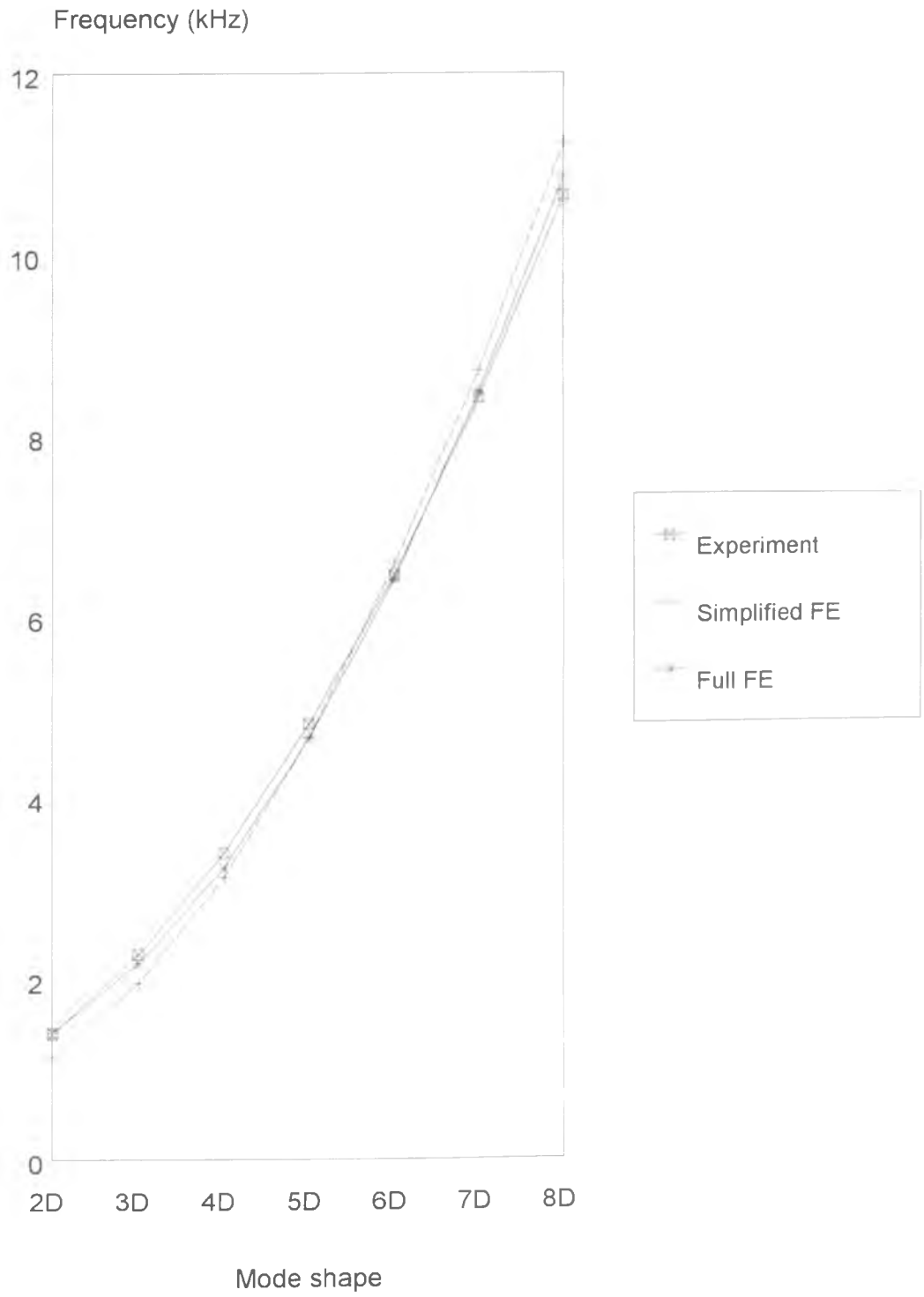

Figure 4.6 - Results for full and simplified disc model compared to experiment

Table 4.1 - Comparison between full model and simplified model of the disc

	Full model	Simplified model
Angular definition (deg.)	6	6
Type of element	8 noded isoparametric brick	4 noded shell
No. of elements	1380	300
Total no. d.o.f.	25920	1800
Method used	Full subspace	Reduced Householder
CPU time (s)	8124.5	74.56
Real time (s)	19690	201

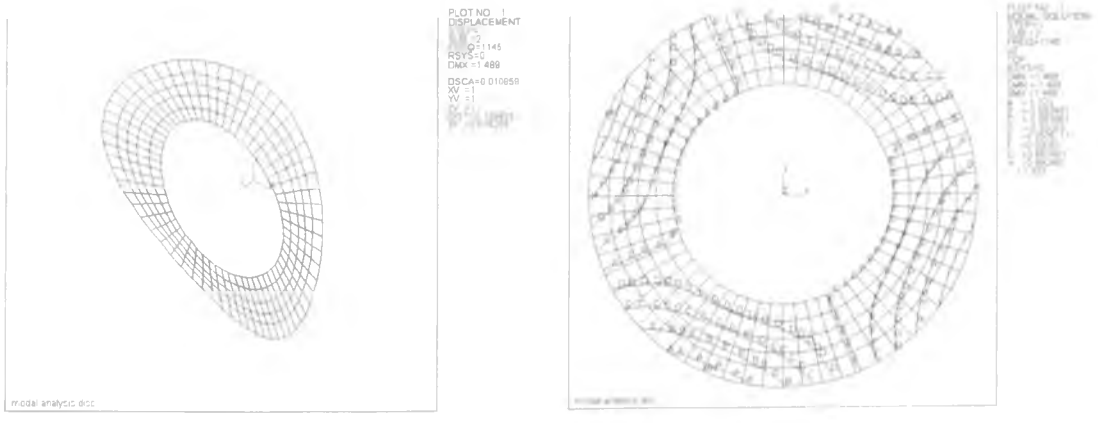

Figure 4.7a - 2nd diametral disc mode shape and equal displacement plot at 1145Hz.

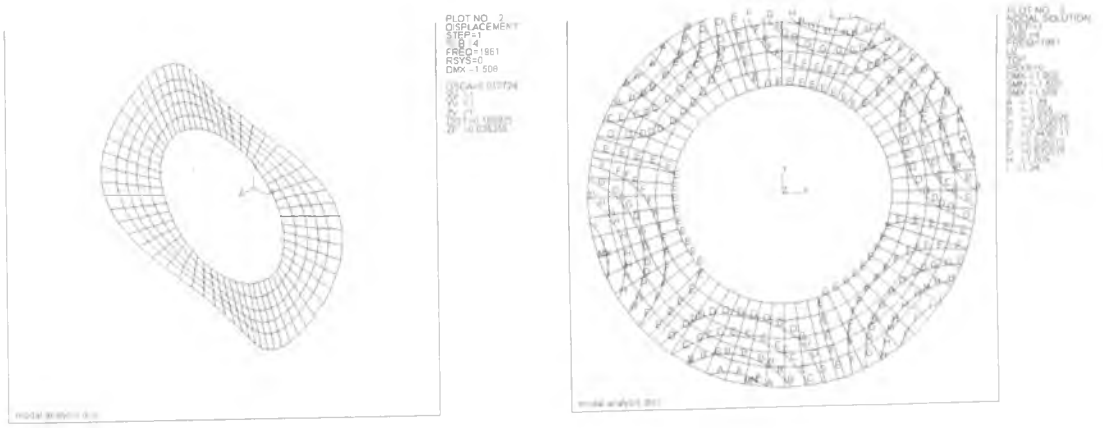

Figure 4.7b - 3rd diametral disc mode shape and equal displacement plot at 1961 Hz

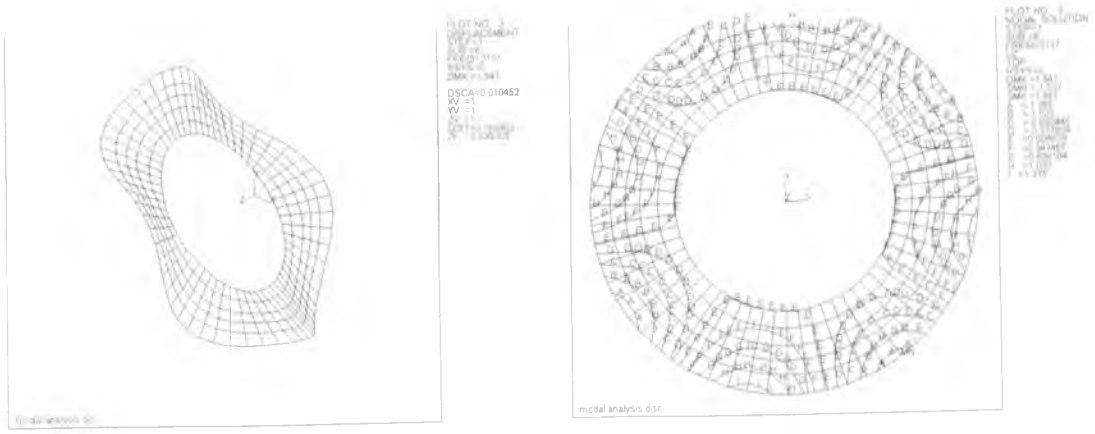

Figure 4.7c - 4th diametral disc mode shape and equal displacement plot at 3137Hz

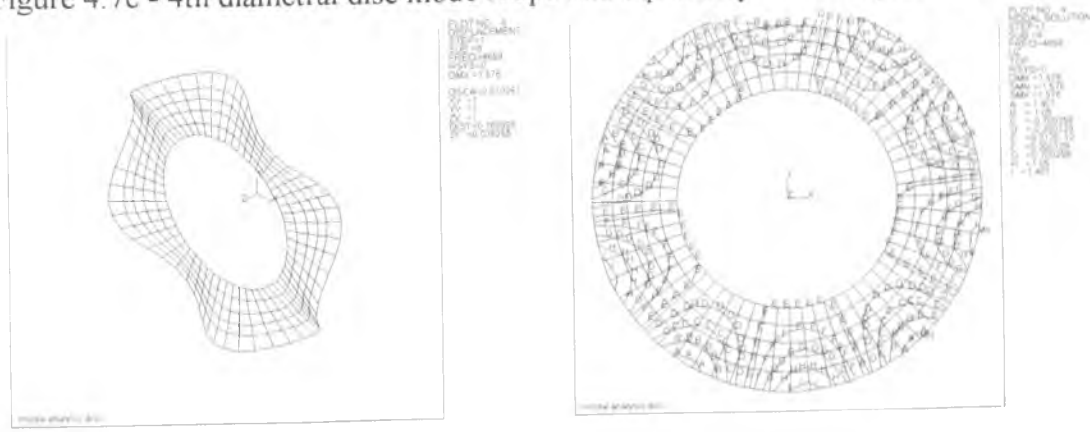

Figure 4.7d - 5th diametral disc mode shape and equal displacement plot at 4659 Hz

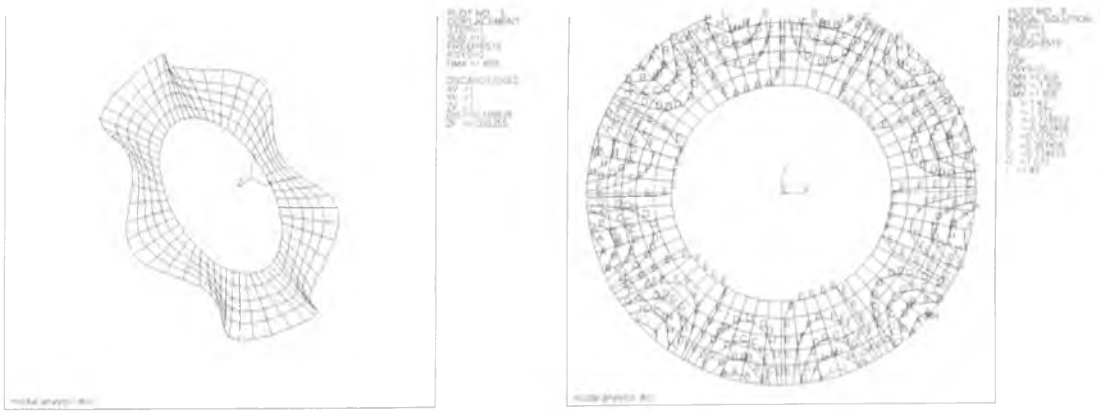

Figure 4.7e - 6th diametral disc mode shape and equal displacement plot at 6518 Hz

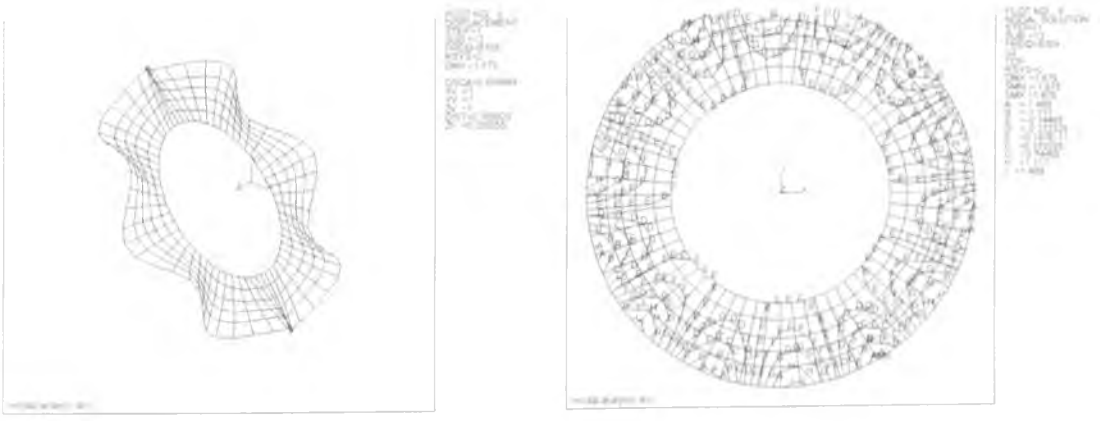

Figure 4.7f - 7th diametral disc mode shape and equal displacement plot at 8708 Hz

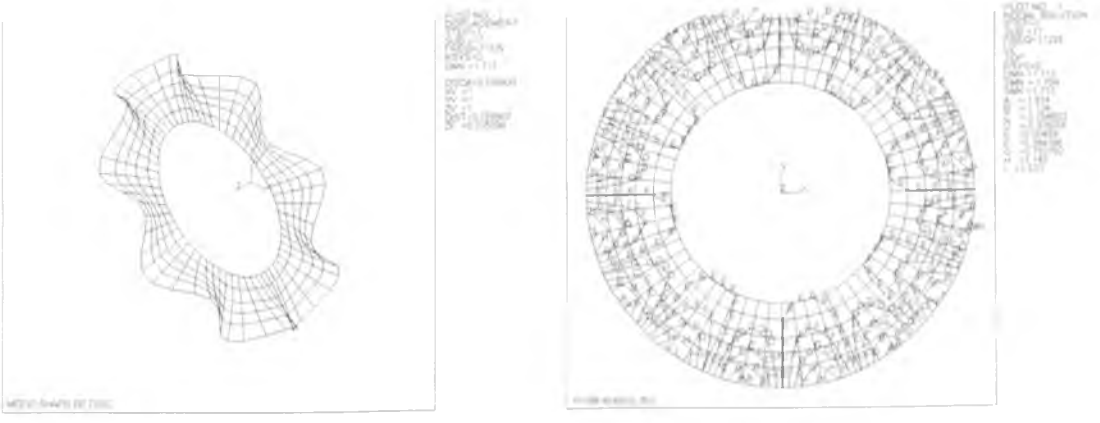

Figure 4.7g - 8th diametral disc mode shape and equal displacement plot at 11225 Hz

4.3.2 Results

The eigenvalue analysis of the simplified model of the disc showed a total of 7 diametral modes within the frequency range studied of 1 000 - 14 000 Hz. The mode shapes are presented in figures 4.7a-4.7g in the form of the displaced shape of the disc and also equal displacement contours in order to allow two important factors to be considered :

i) The results from the eigenvalue analysis using the finite element method in the form of equal displacement contours are compared with the experimental results in the form of fringe lines (which also indicate equal displacement contour).

ii) The reconstructed holographic images [10] show only the fringe lines and this when associated with the equal displacement contour plot provides a method to visualise the mode shape by referring to the corresponding displaced shape plot.

From the analysis of the simplified disc model the first mode occurs at a frequency of 1145 Hz. The equal displacement contour plot in figure 4.7a shows clearly the nodal lines (marked E) and the anti-node positions (contour lines marked A or I). There are four nodes and four anti-nodes around the circumference of the disc which indicate that it is the second diametral mode.

The second mode occurs at a frequency of 1961 Hz and figure 4.7b shows clearly six nodal lines (marked E) and six anti-node positions (lines marked A and I) which confirm that it is the third diametral mode.

The third mode occurs at a frequency of 3137 Hz and from the contour plot in figure 4.7c there are eight node lines (lines marked E) and eight anti-node position (lines marked A and I) which indicate that it is the fourth diametral mode.

The fourth mode occurs at a frequency of 4659 Hz with the displaced shape in figure 4.7d showing that it is the fifth diametral mode and the contour plot from figure 4.7d

therefore showing ten node lines (lines marked E) and ten anti-node positions (lines marked A and I).

The fifth mode occurs at a frequency of 6518 Hz and from the contour plot in figure 4.7e there are twelve node lines (lines marked E) and twelve anti-node position (lines marked A and I) which indicate that it is the sixth diametral mode

The sixth mode as shown in figure 4.7f occurs at a frequency of 8708 Hz with the displaced shape plot showing seven peaks and seven troughs and the contour plot showing fourteen node lines (lines marked E) and fourteen anti-nodes position (lines marked A and I) which confirm that it is the seventh diametral mode.

The seventh mode occurs at a frequency of 11 225 Hz. As shown in figure 4.7g, the displaced shape of the disc model shows eight troughs and eight peaks whilst the contour plot shows a total of sixteen nodal lines (lines marked E) and sixteen anti-node positions (lines marked A and I) which confirm that is is the eighth diametral mode.

In general all the above diametral modes which occur at frequencies below 12 kHz have equal spacing of nodes and anti-nodes ; this is a distinctive characteristic of a diametral mode.

4.4 Eigenvalue Analysis Of The Pad

4.4.1 Pad model definition

The brake pad modelled has the same dimensions as to the one used in the experiments by Fieldhouse and Newcomb [10]. The outer periphery of the brake pad follows very closely the circumference of the disc and covers a sector of 60 degrees. This reduces to 45 degrees at the inner periphery. The radial width of the pad is 40 mm at the backplate tapering to 36 mm at the friction face. The backplate is of mild steel (E=205 GPa , density = 7750 kg/m ^{3}) and 5 mm thickness and the friction material (E = 8 GPa , density = 2250 kg/m^3)is 12.5 mm thick. At both ends of the pad is a portion of the backplate known as the 'ears' where the pad is abutted to a machined groove in the caliper as shown in Chapter Three. A schematic diagram of the pad is shown in figure 4.8.

In order to take into account the thickness of the backplate and also that of the friction material , 8 noded isoparametric brick elements are used in the analysis as shell elements are not suitable for this relatively low aspect ratio (width/thickness) geometry.The resulting finite element model of the pad is shown in figure 4.9

The element definition of the pad has to follow closely that of the disc at the friction interface. This results in the pad model being defined using a cylindrical coordinate system with an angular definition around the circumference of 6 degrees as for the disc. This constraint is confined to the friction interface only as other parts of the pad can be defined independantly without affecting the interface. Master degrees of freedom are selected to take into account factors (a),(b) and (c) outlined in section 4.2.3.3. The reduced Householder method is again used to determine the eigenvalues and eigenvectors of the model in the frequency range of 1kHz - 14 kHz.

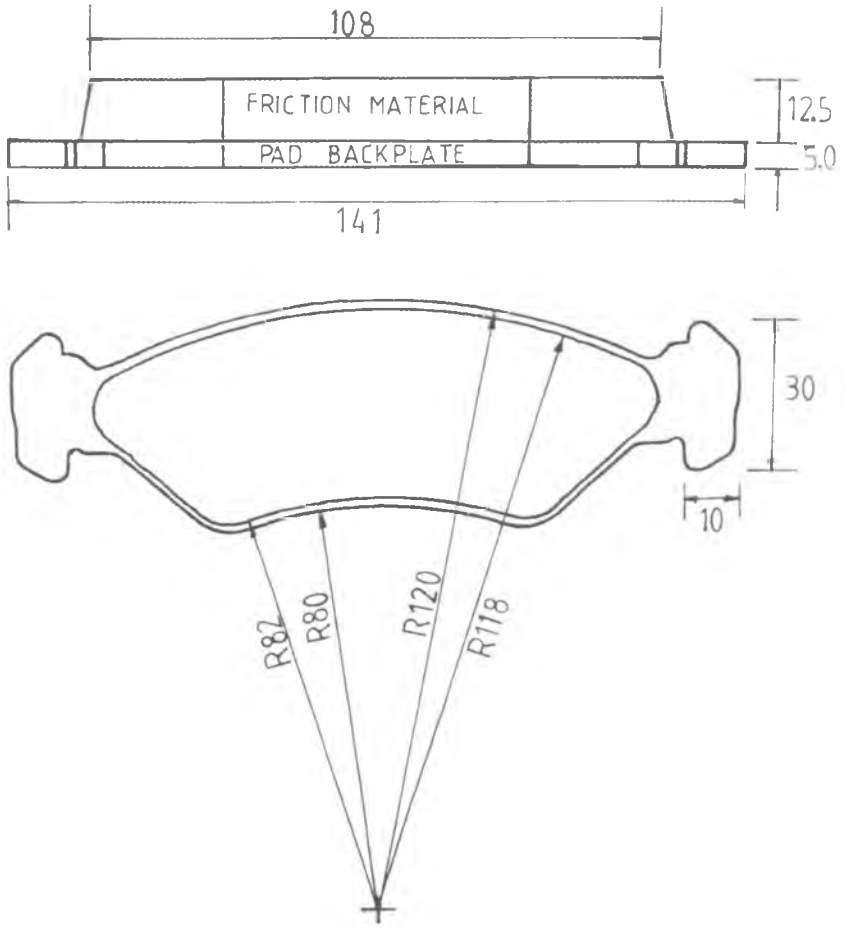

Figure 4.8 - Schematic diagram of the pad (all dimensions in mm)

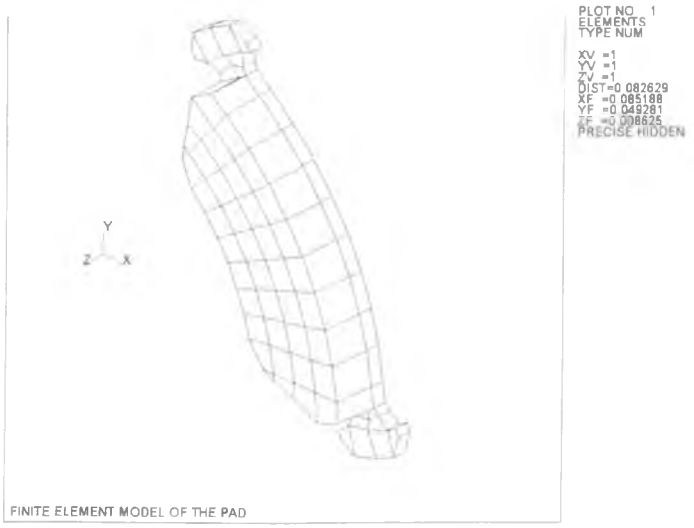

Figure 4.9 - Finite element model of the pad

Figure 4.10a - Pad mode shape and equal displacement contour plot at 2608 Hz

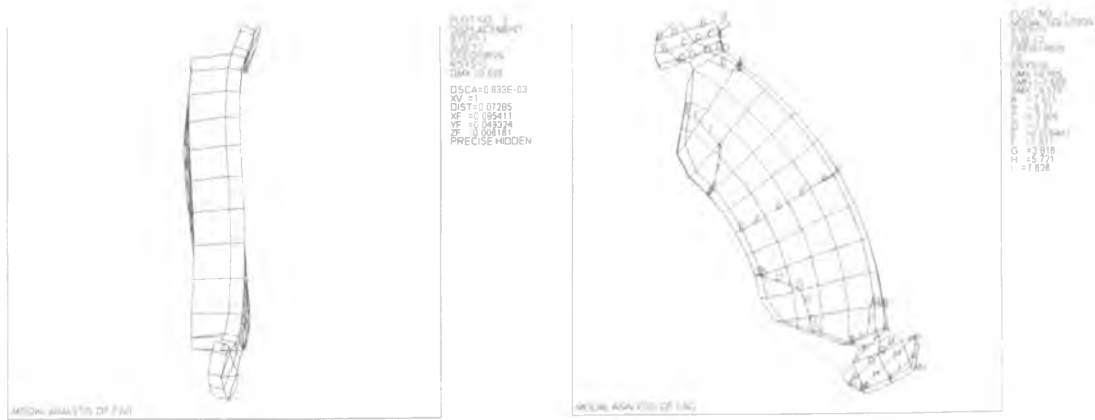

Figure 4.10b - Pad mode shape and equal displacement contour plot at 4625 Hz

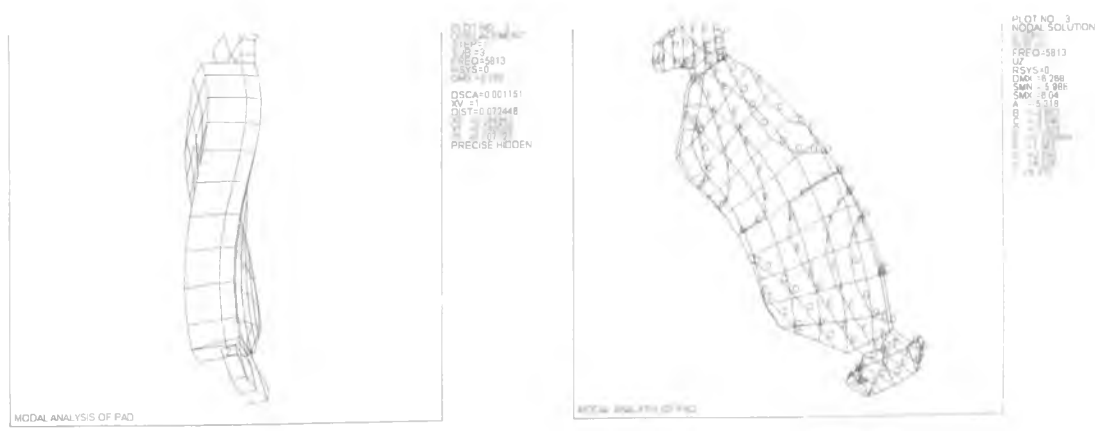

Figure 4.10c - Pad mode shape and equal displacement contour plot at 5813 Hz

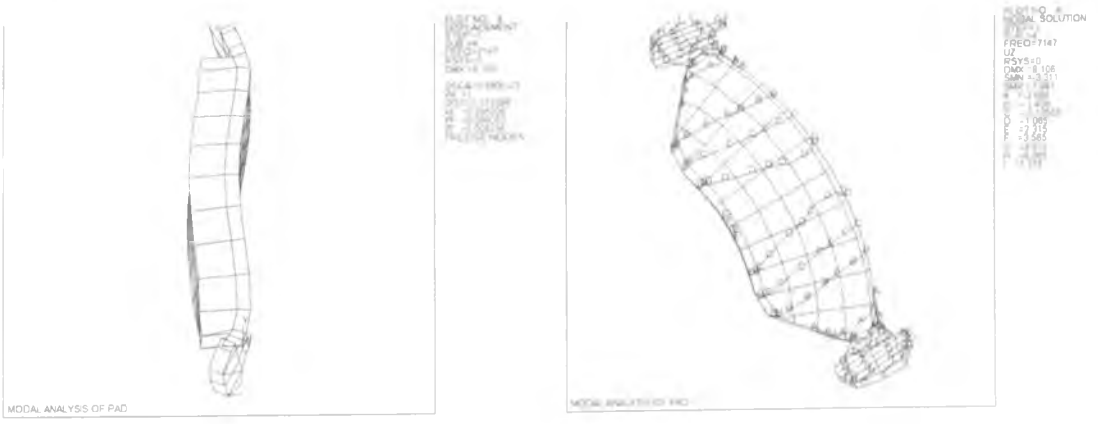

Figure 4.10d - Pad mode shape and equal displacement contour plot at 7147 Hz

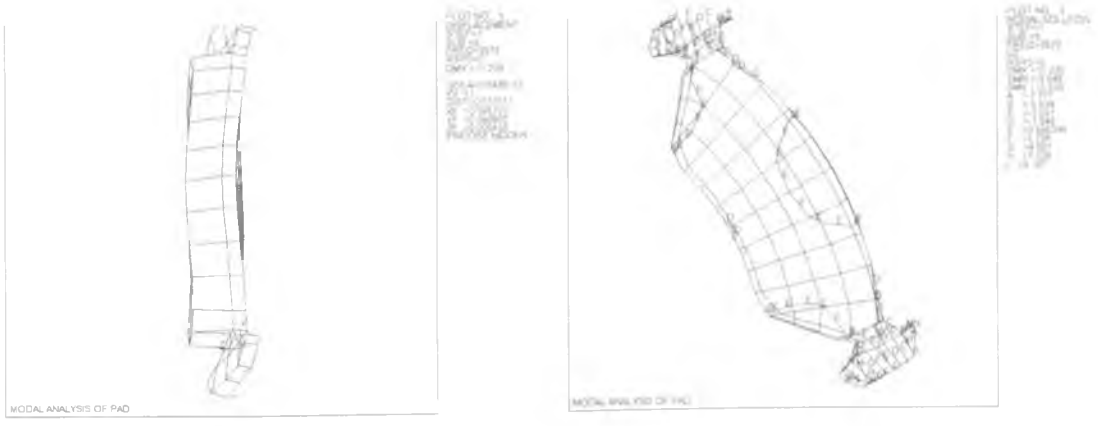

Figure 4.10e - Pad mode shape and equal displacement contour plot at 9579 Hz

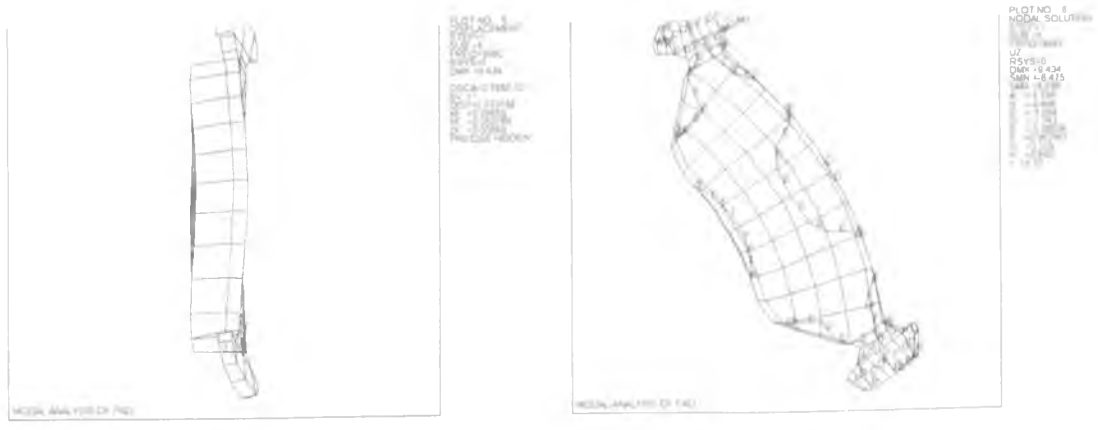

Figure 4.10f - Pad mode shape and equal displacement contour plot at 9992 Hz

Figure 4.10g - Pad mode shape and equal displacement contour plot at 10723 Hz

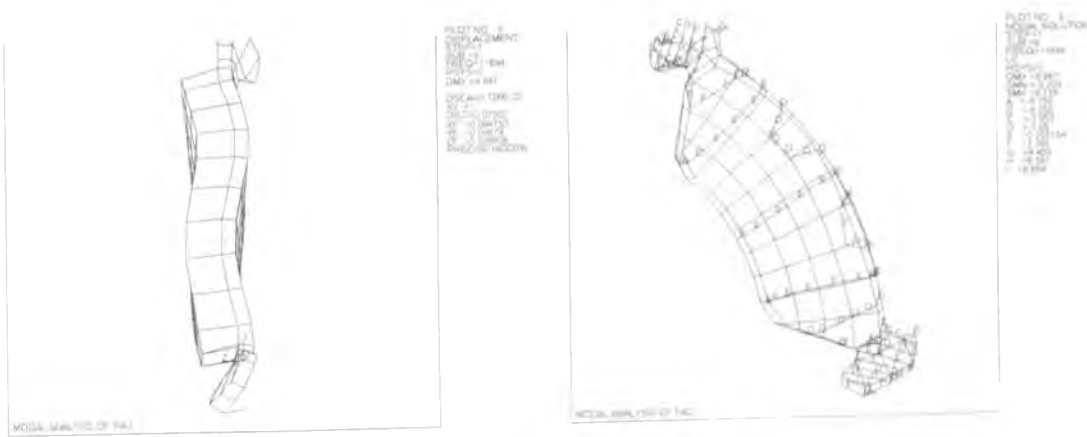

Figure 4.10h - Pad mode shape and equal displacement contour plot at 11693 Hz

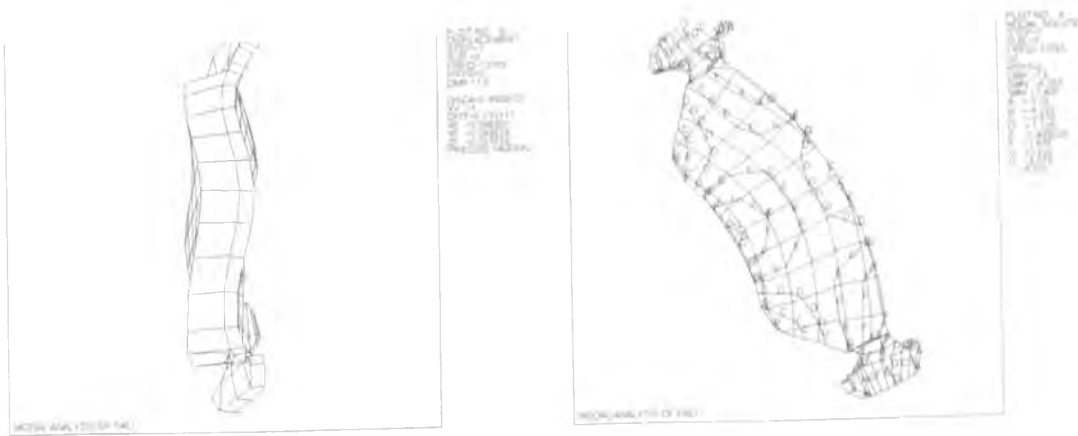

Figure 4.10i - Pad mode shape and equal displacement contour plot at 11765 Hz

4.4.2 Results

The eigenvalue analysis of the above pad model predicted a total of 9 modes within the frequency range 1 000 Hz - 14 000 Hz studied. From the results , the first mode occurring at a frequency of 2608 Hz is of the first bending type as clearly shown in the displaced shape plot of figure 4.10a. The figure also shows the mode shape in the form of equal displacement contours which indicate the minimum displacement occurring at the centre line of the pad i.e. this position is an anti-node. It can be seen that the contour lines are more closely spaced at the ends of the backplate indicating that the ears displace more relative to other parts of the brake pad (due to the lower stiffness in this region).This mode shape is hereafter termed the first bending mode designated mode (B1).

The second mode occurring at a frequency of 4625 Hz is also of the bending type as clearly shown in figure 4.10b. From the equal displacement contour plot, there are 3 nodes (shown as lines marked E with displacement contour value 0.0005) ; one of the nodes is situated at the pad centreline and the other two at either end of the friction face of the pad (the part connecting the ears to the pad). This mode shape is termed the second bending mode (B2) in the following discussion.

The third mode occurring at a frequency of 5813 Hz is not of the bending type shown in figures 4.10a-b. The mode shape shown in figure 4.10c could be more properly described as a twisting mode. The equal displacement contour plot indicates two nodal line running diagonally across the pad from the ears and curving to the pad centre. The fringe lines lying diagonally on the ears are of different orientation from those on the ears for the bending modes which lie horizontally. This mode shape is termed the first twisting mode (T1).

The fourth mode occurring at a frequency of 7147 Hz is again of the bending type as shown in the mode shape plot of figure 4.10d. The equal displacement contour plot shows four nodal lines on the pad , beginning with the one lying nearest to the ear (marked

C) and and another one on the pad quarter line repeated on the other half of the pad. There is an anti-node line (marked E) at the centre of the pad and other anti-nodes in between the nodes and the ends of the ears. This mode shape is termed the third bending mode (B3).

The fifth mode at a frequency of 9579 Hz and shown in figure 4.10e is of a similar twisting type to the one shown in figure 4.6c but of a different order. There are three node lines , one running across the central part of the pad and one running across the lower quarter of each half of the pad as shown in the equal displacement contour plot. This mode shape is termed the second twisting mode (T2).

The sixth mode shown in figure 4.10f is also of the twisting type and perhaps of similar order to the one discussed above but with the displacement of the lower portion of the middle of the pad more developed compared to figure 4.6e For the purpose of the discussion this mode shape is also termed the second twisting mode (T2b).

The seventh mode occurs at 10 723 Hz and cannot be clearly described as belonging to the either bending or twisting type. As shown in figure 4.10g , the ears are undergoing twisting motion with the equal displacement contour lines lying across the ear at both ends. This mode shape is termed the twisting ears mode (TE) in the discussion.

The eighth mode occurs at 11 693 Hz and is of the bending type as shown in the displaced shape plot of figure 4.10h. The equal displacement contour plot shows three node lines lying across the pad , one at the middle and one on either side, and there is also a node line at each ear making a total of 5 node lines on the pad This mode shape is termed the fourth bending mode (B4) in the discussion.

The ninth mode occurs at a frequency of 11 765 Hz and is of the twisting type as can be clearly seen in both the displaced shape and the equal displacement contour plots of figure 4.10i which show similar trends to those of figures 4.10c and 4.10f. This mode shape

which is one order higher than the one shown in figure 4.10f is termed the third twisting mode (T3).

To summarise , there are in general two major types of modes which are either of the bending or twisting variety with the mode order increasing with the frequency ; there is also one mode which does not fit neatly into either of these two categories since it involves a major movement of the pad ears only.

4.5 Comparison With Experiments

The experiments on disc brake noise using holographic interferometry by Fieldhouse and Newcomb [10] provide ample experiment evidence for comparison with the finite element results. The plain disc and brake pad modelled in the analysis are very similar to those used in the experiments therefore allowing for direct comparison. Due to the importance of understanding the reconstructed images , the basic mechanics of the holographic interferometry technique based on [61] are discussed here.

The interpretation of the results from the reconstructed holographic images are based on the fact that the minima of the superimposed waves seen as dark fringes occur at points where the displacement , d , satisfies the following equation:

$$d = (2n + 1)\lambda / (2(\cos\alpha + \cos\beta) \qquad (4.15)$$

where α is the angle of incident of the light wave from the normal plane to the object and β is the angle of reflection. If the light source could be made as perpendicular as possible to the object , both angles would be small , thus

$$d = (2n + 1)\lambda / 4 \qquad (4.18)$$

Therefore , the first minimum occurs at n=0 , d=λ/4 the following minimum at n=1,d=3λ/4 and so on. Thus, two neighbouring fringes have a displacement difference of half a wavelength. The relative vibration velocity of the points can be obtained by dividing the displacement difference by the pulse separation time Δt. The relative velocity is therefore proportional to the fringe density , the number of interference fringes per unit length.A high fringe density also indicates a node of the displaced shape [61]. These facts are used to interprete and translate the reconstructed holographic images into a more meaningful mode shape description.

4.5.1 The experimental results for the free-free disc

The reconstructed holographic images presented in [10] for the disc mode shapes are reproduced here in figure 4.11. As the images are of relatively difficult to understand the significance of the fringe lines of the images are discussed in here withsome detail. The region of high fringe density (nodes) and low fringe density (anti-nodes) for the diametral modes are distributed uniformly around the circumference of the disc and can be identified quite readily. There are other modes in addition to the diametral modes , amongst which are the circumferential modes (with the fringe lines in concentric circles about the disc centre). However as only the diametral modes are the only modes of interests in squeal problems , these are fully discussed here whilst other mode types are ignored.

In figure 4.11 the natural frequencies and the corresponding mode shapes of the disc in the free-free condition are shown in the form of reconstructed holographic images. The experimental results show that the first mode occurs at a frequency of 1100 Hz with the disc undergoing deformation with one end of the diametral up (maxima) and the opposite end of the diameter down (minima).This skew mode shape is not categorized as either diametral or circumferential mode.

The second mode occurs at a frequency of about 1400 Hz and shows part of the four nodal lines and and four anti-nodes position of the second diametral mode. The top hat portion of the disc does not show any fringe lines which indicates an undeformed shape.

The third mode occurs at a frequency of 2200 Hz. The fringe lines on the disc are in the form of several circular lines concentric about the disc centre. This is the first circumferential mode of the disc.

Following closely on the third mode is the fourth mode at 2280 Hz with the fringe lines clearly showing six node lines and six anti-nodes positions around the circumference which indicate that this is the third diametral mode.

The fifth mode is also a diametral mode occurring at 3400 Hz. The figure shows eight node lines and eight anti-nodes position around the circumference which indicates the fourth diametral mode.

The sixth mode occurs at a frequency of 4800 Hz. The figure showed ten node lines and ten anti-nodes positions around the circumference which indicates the fifth diametral mode.

The seventh mode occurs at a frequency of 6400 Hz. The fringe lines in the figure show twelve node lines and twelve anti-nodes position along the circumference indicating the sixth diametral mode.

The eighth mode occurs at a frequency of 6800 Hz and does not belong to either the circumferential or diametral mode groups. The ninth mode which also does not belong to either the diametral or circumferential mode classifications occurs at a frequency of 7400 Hz.

The tenth mode occurring at a frequency of 8400 Hz is a diametral mode. The fringe lines in the diagram show fourteen node lines and fourteen anti-nodes positions around the circumference indicating the seventh diametral mode.

The eleventh mode occurring at a frequency of 10 600 Hz is also a diametral mode. The fringe lines in the diagram show sixteen node lines and sixteen anti-node positions along the circumference indicating the eighth diametral mode.

The ninth diametral mode occurs at a frequency of 12 960 Hz with the fringe lines in the diagram clearly showing eighteen node lines and eighteen anti-node positions around the circumference.

Between the eighth diametral mode (10 600 Hz) and the ninth diametral mode (12 960 Hz), there are four other modes which do not belong to either the circumferential or diametral mode classifications and cannot be easily described. These modes occur at frequencies of 12 000 Hz , 12 450 Hz , 12 500 Hz and 12 700 Hz respectively.

Except for the eighth and ninth diametral modes , the top hat portion of the disc do not show any significant fringe line density relative to the friction face of the disc which indicates this is a relatively stationary part of the disc. This aspect of the experimental results supports the assumption that the top hat does not participate in the vibration at the natural frequencies of the diametral modes and therefore can be correctly omitted from the analysis.

There is a total of 16 elastic modes within the frequency range of 0 -13 000 Hz studied in the experiment and eight of which belong to the diametral mode category and only one mode to the circumferential mode category with the remaining seven modes belonging to neither classification. As the diametral modes are the only modes which participate during squeal, these are the most important and their frequencies are listed in table 4.2.

Table 4.2- Frequencies of the first eight diametral modes for the 'free-free' disc

Diametral Mode	**Frequency (Hz)**
2nd	1400
3rd	2280
4th	3400
5th	4810
6th	6450
7th	8410
8th	10640

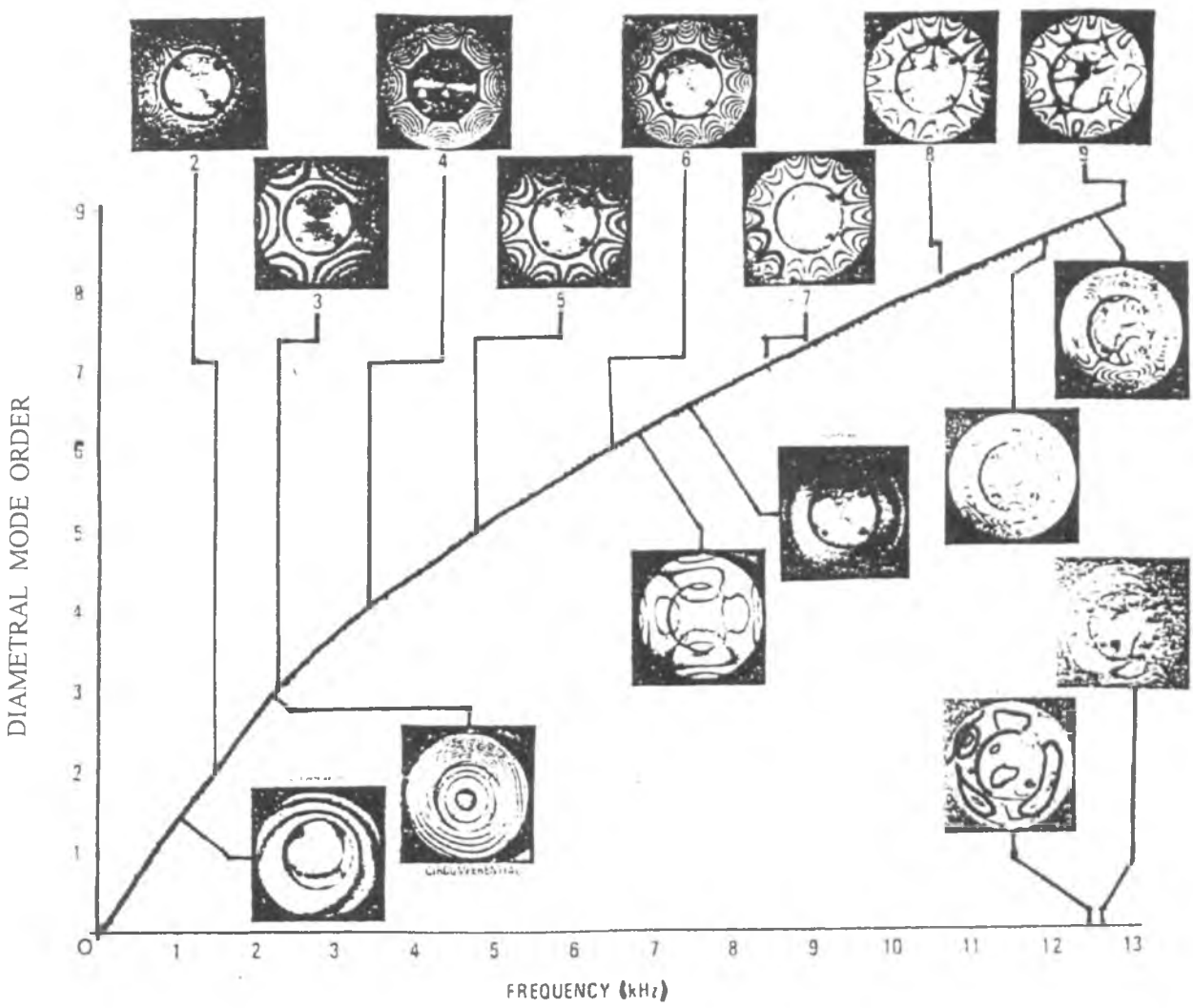

Figure 4.11 - Reconstructed holograms showing modes of vibration of the disc [10]

4.5.2 The experimental results for the free-free pad

In the experiments on the pad [10] , the piezo-electric crystal exciter was mounted at 45 degrees to the pad longitudinal axis. This fact is important because if the exciter lies at the node of any mode of the pad , then that particular mode cannot be excited. From figure 4.12 , the areas of high and low fringe density can be used to deduce the positions of the nodes and antinodes present in the reconstructed images of the pad.

From the experimental results in [10], it is apparent that there are other modes present above 11 kHz but , as all the squeal modes in the experiments occured at a frequency below 11 kHz, these higher frequency modes are not considered. Furthermore, as the boundary condition for the supported condition of the pad during squeal is stiffer than for the free-free condition, the natural frequencies associated with the pad during squeal must be higher than those occurring under free-free conditions. From inspection of the results published in [10], it is not easy to ascertain the position of the nodes and antinodes of the torsion modes and the mode shapes are deduced from the experimenters' observation that the torsion modes produce fringe lines running horizontally to the 'ears' of the pad rather than vertically as in the bending modes

The first mode occurs at a frequency of 2692 Hz and is of the first bending mode type (B1). There is a clear anti-node at the centre of the pad and two nodes equidistant from the pad centreline with the fringe lines on the pad ears showing maximum displacement. The fringe lines is indicate a similar trend to the finite element contour plot shown in figure 4.10a.

The second mode occurring at a frequency of 4231 Hz is of the second bending mode (B2) type and has a similar trend of fringe lines to the finite element contour plot of figure 4.10b. There is a clear node position at the centreline of the pad and two anti-nodes equidistant from this position which suggests a second bending type of mode.

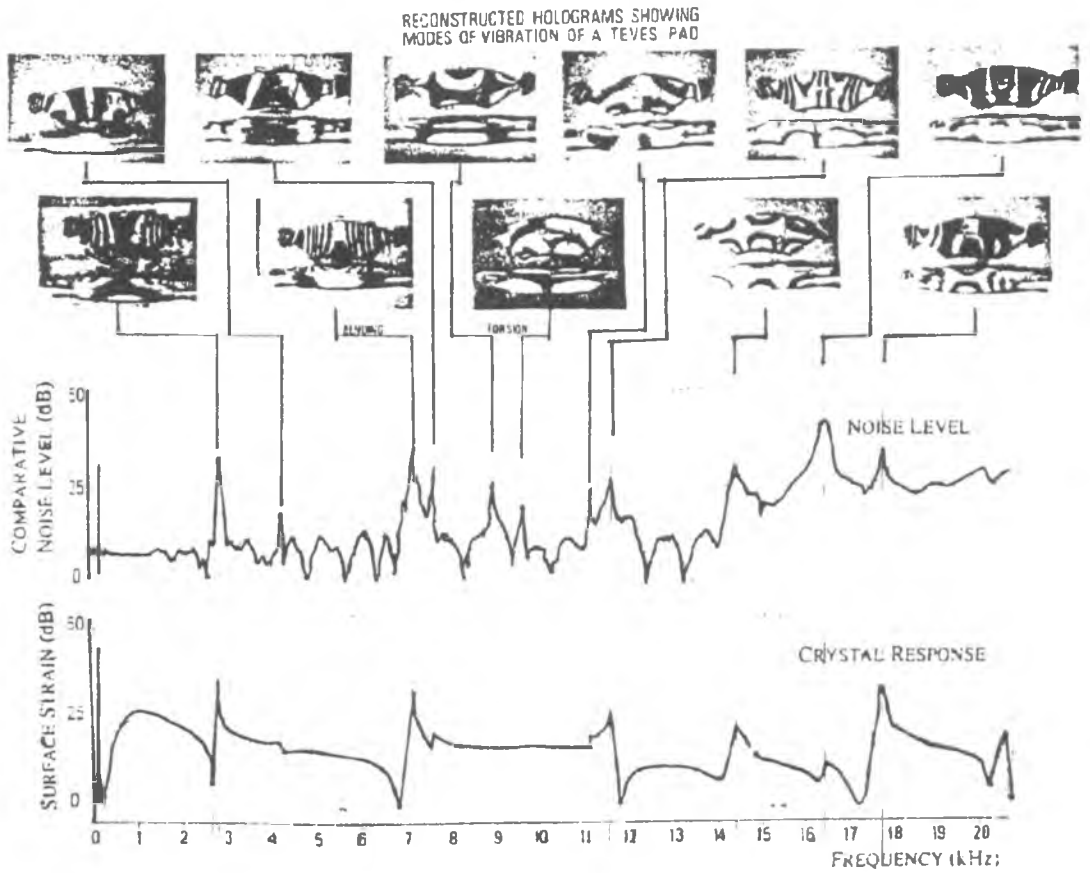

Figure 4.12 - Reconstructed holographic images for the free-free pad [10]

The third mode occurs at 7154 Hz and has 3 anti-nodes positioned across the pad friction surface suggesting the third bending mode (B3). Furthermore the fringe line trend is similar to that shown in figure 4.10d.

The fourth mode occurring at 7615 has a significant fringe density only at the ears of the pad. This suggests an almost flat pad and therefore a mode shape where only the ears bend i.e. the bent ears mode (BE). The fringe lines of this mode closely match the contour plot shown in figure 4.10g.

The fifth mode occurs at 8770 Hz and the image shows clearly fringe lines lying across the ears (parallel to the pad horizontal axis). Although the fringe formation across the friction face is not easily described, it is noted that there is only one curved fringe across this face and two small curved fringes at either end connected to the fringe lines on the ears.This is similar to the second twisting mode (T2a) of figure 4.10e.

The description is similar for the subsequent mode occurring at 10595 Hz which has two curved fringe lines across the friction face and one small curve fringe lines connected to the fringe lines on both ears. This mode is described as also the second twisting mode but labelled as mode T2b as it occur at higher frequency than the the second twisting mode described above and is similar to the mode T2b shown in figure 4 10f.

It should be noted that there was no indication of the first torsion mode in the reconstructed holographic images presented in [10]. The first torsion mode would have a node line running across the pad at approximately 45 degrees to the pad longitudinal axis. As such a node line may coincide with the position of the exciter crystals and as a mode cannot readily be excited at its node this particular mode was probably missed.The experimental results for the pad under free-free condition for frequencies less than 12 kHz are summarised in table 4.3.

Table 4.3 - The experimental mode shapes and natural frequencies for the brake pad

Number of nodes/antinodes	Mode shape description	Frequency (Hz)
Node=2,Antinode=1	First bending	2692
Node=3,Antinode=2	Second bending	4231
Node=4,Antinode=3	Third bending	7154
2 nodes at both ends	'Bent ears'	7615
	2nd twisting	8770
	2nd twisting	9667
	'Twisted ears'	11167
Node=5,Antinode=4	Fourth bending	11583

4.6 Discussion

The results obtained from the analysis and the experiments of [10] are compared on the basis of similar mode shapes. For the disc, only the diametral modes as shown in figures 4.7a-g are considered as it is only these which are involved in squeal. All the diametral mode shapes from the experiments are reproduced by the finite element model with close agreement. The frequencies from the simplified finite element model also generally follow closely those from the experiment as shown in figure 4.6. Relatively large discrepancies occur at both ends of the frequency range : at the lower end the maximum frequency difference between the experimental and model results for the second diametral mode (marked 2D) is 255 Hz (18.2 %) whilst at the higher end for the eighth diametral mode (marked 8D) the difference is 585 Hz (5.5%). In relative terms the errors are always less than 10% except for the second and third diametral modes (18.2% and 13.9% respectively). The experimental results of Fieldhouse and Newcomb [10] indicate that the second diametral mode is not involved with squeal and the third diametral mode is only involved for a trailing edge abutment. Therefore results for the second and third diametral mode are less important for the present analysis of squeal. The best correlation occurs for

the fifth , sixth ,seventh and eighth diametral mode where the errors are less than 5%. Therefore results involving these diametral modes can be treated with confidence and the finite element model of the disc is acceptable for the present purpose of squeal analysis.

In the case of the pad , frequencies for all the mode shapes which can be directly compared such as the bending and twisting modes are included in the comparative plot of figure 4.13. It can be seen that there is one mode from the experiment which has not been reproduced directly in the finite element analysis of the pad i.e. the bent ears mode marked BE in figure 4.13. Results from modal analysis of the pad model using the reduced Householder method is compared with the full subspace method. As discussed above the reduced Householder method allows reduction of the problem size with the selection of suitable masters whilst the full subspace method takes into account all degrees of freedom in the pad model.

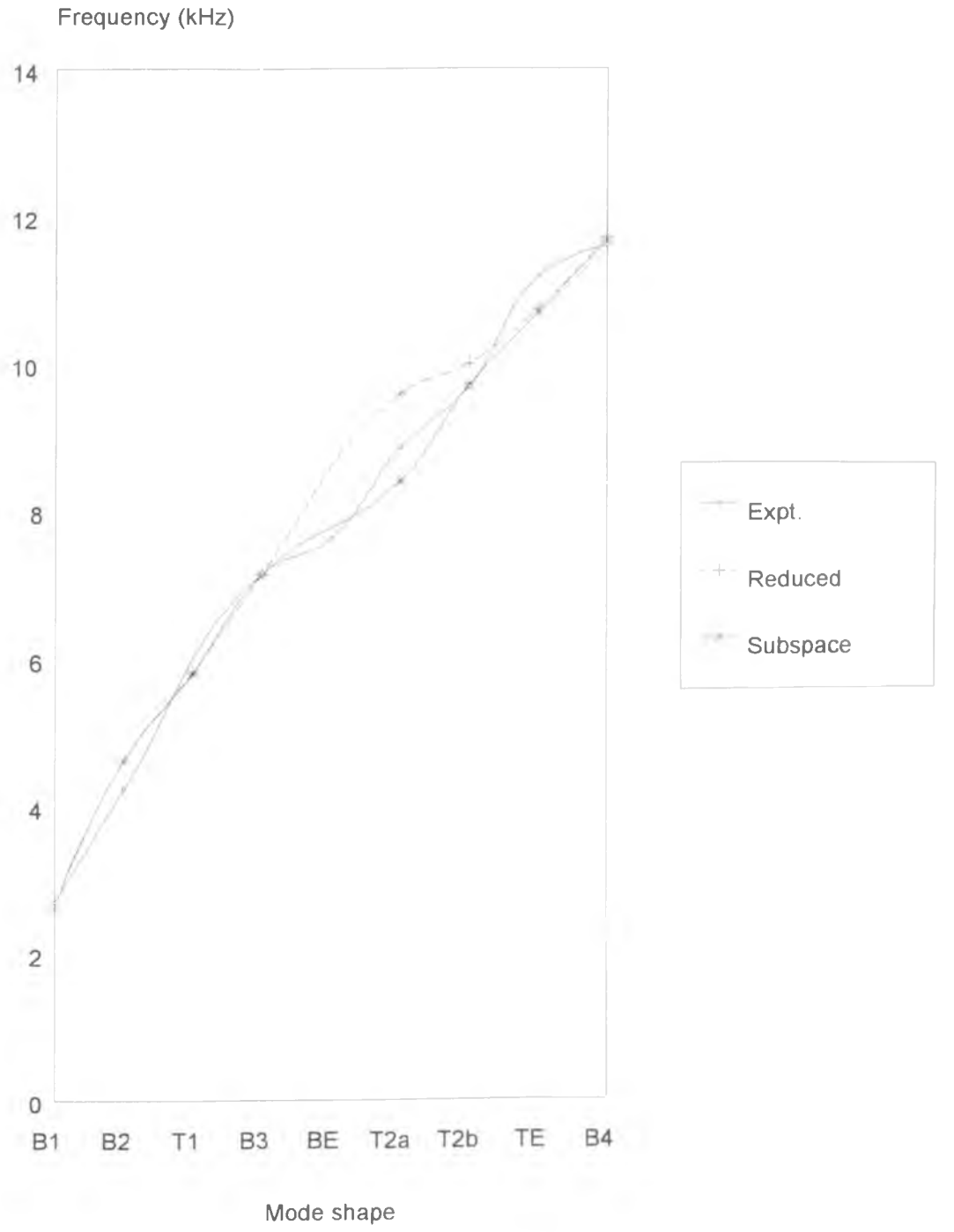

Figure 4.13 Comparison of experimental and finite element natural frequencies for the pad

Figure 4.13 shows that overall the pad finite element model achieves good agreement with the experimental results especially at the lower end of the frequency range. Relatively large differences occur for the higher frequency twisting mode of T2a for which the frequency of the reduced model is 529 Hz (5.90%) higher than the experiment whilst the full model gives a frequency of 8389 Hz which is 561 Hz (6.27%) lower than the experiment. All other modes gives relative differences of less than 5%. These differences can be attributed to the fact that the brake pad is a composite component made of two different materials and that in particular the friction material may have anisotropic material properties which can only be approximated. Further refinement of the pad model is limited by the finite element definition of the disc as the nodes on the pad friction surface need to have the same (r,θ) coordinates as the corresponding nodes of the disc to allow coupling at the later stage of stability analysis. However the maximum error from the pad model is only 6% and the model is therefore considered acceptable for the present purposes.

4.7 Summary

A finite element model of the simplified disc has been constructed and the results from free-free natural frequency analysis indicate that the predicted diametral modes of the disc compare well with the experimental results with differences in frequency of generally less than 10% (with the exception of the second and third diametral modes). The simplified shell element model of the disc (with an angular definition of 6 degrees) and the master degrees of freedom chosen (which are in the z-direction only) are adequate for dynamic analysis purposes. The pad finite element model also predicted mode shapes of very close similarity to the experimental results and the differences in frequency were less than 6% with master degrees of freedom chosen in the z-direction only (except for the abutment nodes). This study has shown that both the disc and pad models as well as the master degrees of freedom selected are adequate for the subsequent stability analysis.

CHAPTER FIVE

CONTACT PRESSURE ANALYSIS OF THE BRAKE PAD

5.1 Introduction

The disc brake assembly used in this study consists of three major components , the caliper , the disc and the pads. The caliper interacts with the inner pad via the piston and with the outer pad via the paw. Both pads are prevented from circumferential motion by the abutments which can operate either on the leading or trailing edge of the pad or on both. The contact at these external connections is modelled as stiff springs thus avoiding the need to include a caliper model in the stability analysis. The most active interactions occur between the pads and the disc and the pad-disc interface is of utmost importance because this is where the circumferential friction force excites the transverse motion of the disc and the pads. Therefore it is necessary to determine the contact area and pressure distribution between the pads and disc for various conditions in order to provide the information for calculation of the contact stiffness magnitude and distribution for the subsequent stability analysis.

In this chapter , the distribution of reaction force at the pad-disc interface under the applied load from the brake line pressure is studied using the finite element method. The study covers the effect of friction coefficient , the abutment arrangement , the form of loading (piston or paw) and the friction material Young's modulus.

5.2 Method of analysis

The finite element model of the pad used in this study is similar to the one derived for the natural frequency analysis reported in Chapter Four. However in order to carry out the contact analysis efficiently the specialised non-linear finite element package ABAQUS [10] was used for this stage of the work. The most suitable method of representing the contact effect at the interface in ABAQUS is the so-called interface gap element. This element models two surfaces which may maintain or lose physical contact and may also slide relative to one another with the option of specifying tangential stiffness for the stick condition. During application of the disc brake system, sliding is continuous and therefore no tangential stiffness was specified. The element has two degrees of freedom at each node, these being the displacements in the normal and tangential directions. A small initial gap is usually specified arbitrarily to provide an initial condition when there is no contact. As the nodes move closer towards one another the gap will become smaller until the displaced nodes touch at which point the contact becomes effective and a reaction force occurs. The gap element and the force-deflection relationship in the normal direction is shown in figure 5.1.

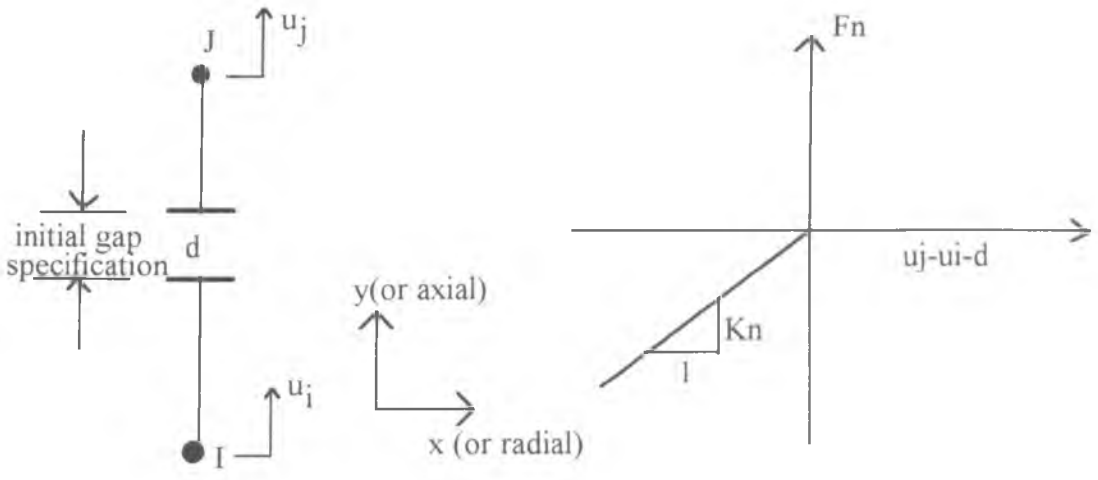

Figure 5.1 - Gap element and the normal force-deflection relationship

Notice from the force-deflection relationship that the reaction force is active only when the gap closure condition is met (i.e. uj-ui-d $\leq$ 0) and also that no tension force can be generated. The gap element is therefore non-linear and an iterative solution is necessary. In order to activate the circumferential friction force, one of the surfaces must be made to slide relative to each other; in the present work a small angle of rotation is specified for the rigid (in normal direction) disc surface.

5.2.3 Finite element models

The backplate hydraulic pressure applied to the brake system is transmitted through the paw onto the outboard pad and through the piston onto the inboard pad (figure 5.2). The pressure applied to the pad backplate is idealised as equal point forces acting on the nodes which are in contact with the piston for the inboard pad (figure 5.3a) and on the nodes which are in contact with the two fingers of the outboard pad (figure 5.3b). The pressure applied was varied from 0 to 10 bar (1 MPa) in 1 bar (0.1 MPa) steps.The Young's modulus of the mild steel back plate was taken as 207 GPa and the modulus of the friction material as 8 GPa. Poisson's ratio was assumed to be 0.25 in both materials. Constraints in the radial and circumferential directions were applied at both the leading and trailing abutments to prevent sliding. The disc surface was assumed to be rigid and flat and therefore is modelled using fully constrained

target nodes corresponding to the pad surface nodes. The analyses were initially performed both for zero friction (μ=0) and for a typical operating value (μ = 0.4).

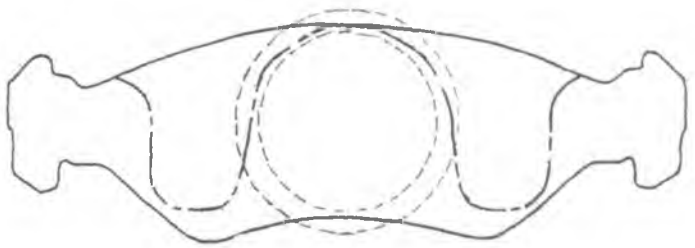

Figure 5.2 - Actual position of the paw (chain lines) and piston (dashed lines) relative to the pad

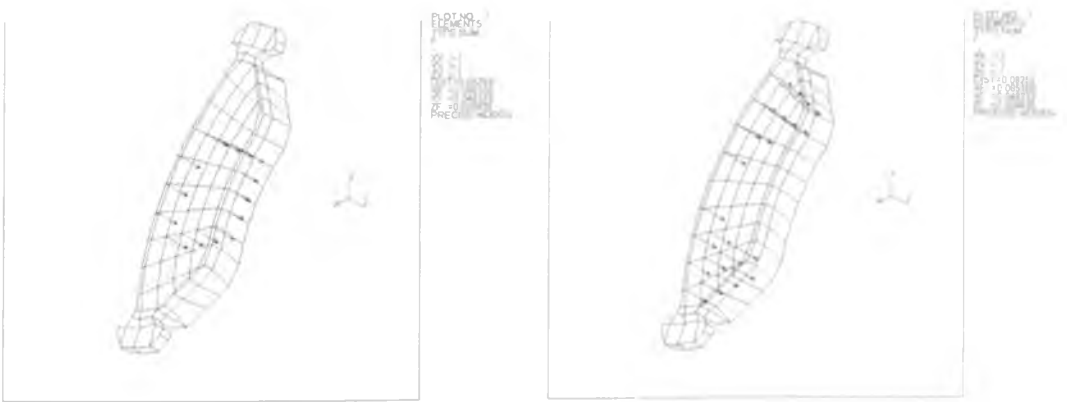

(a) Piston applied force (b) Paw applied force

Figure 5.3 - Idealised point forces acting on the pad finite element model

5.4 Results

5.4.1 Effect of circumferential friction

The important results from the present analysis are the nodal reaction forces at the pad friction interface which are used in the subsequent work for the determination of nodal contact stiffness. The nodal reaction force for each node is selected and displayed on a 3-dimensional graph showing the coordinates of the nodes (angle and

radius) and the magnitude of the reaction force for each pad friction interface node. The position of these nodes is defined in figure 5.4. The interface nodes which have angular coordinates of less than 6 degrees are considered the leading edge nodes whilst the nodes which have angular coordinates of more than 54 degrees are considered the trailing edge nodes.

Figures 5.5 and 5.6 show the effect of piston applied pressure and paw applied pressure respectively on the nodal reaction force at a line pressure of 10 bar. The nodal reaction force distribution in both cases is non-uniform , and for the zero friction condition (Fig. 5.5a & 5.6a) , the distribution is symmetrical about the centre line (30 degrees location). The effect of friction in both the piston and paw applied pressure cases is to shift the reaction force distribution towards the leading edge. In the case of the piston applied pressure , there is an increase in the number of nodes in contact when friction is included , with all the nodes forward of the centreline of the pad coming into contact as well as an additional node at the 48 degrees line (inner radius). Therefore the effect of friction for the piston applied pressure case is to spread the contact area further towards the leading edge whilst at the same time reducing the magnitude of the maximum reaction force from 114.9 N to 109.5 N. For the paw applied pressure case , all the nodes are in contact initially except for the 3 nodes across the centre line at the inner radius of the pad (due to the shape of the paw). When friction is included , the number of nodes in contact is reduced from 50 to 38 out of a total of 53 nodes at the model interface. This loss of contact results in an increased reaction force at the leading edge , thus making the reaction force distribution asymmetric.

In general , these analyses show that for a relatively concentrated load (as in the case of the piston applied pressure) the effect of friction is to increase the number of nodes in contact whilst for a more distributed load (as in the case of the paw applied pressure) the effect is to reduce the number of nodes in contact. In both cases, friction enhances the reaction force at the leading edge and reduces the reaction force at the trailing edge. Figure 5.7 illustrates the displaced shape of the pad under piston applied pressure and clearly show the lifting of the trailing edge of the pad.

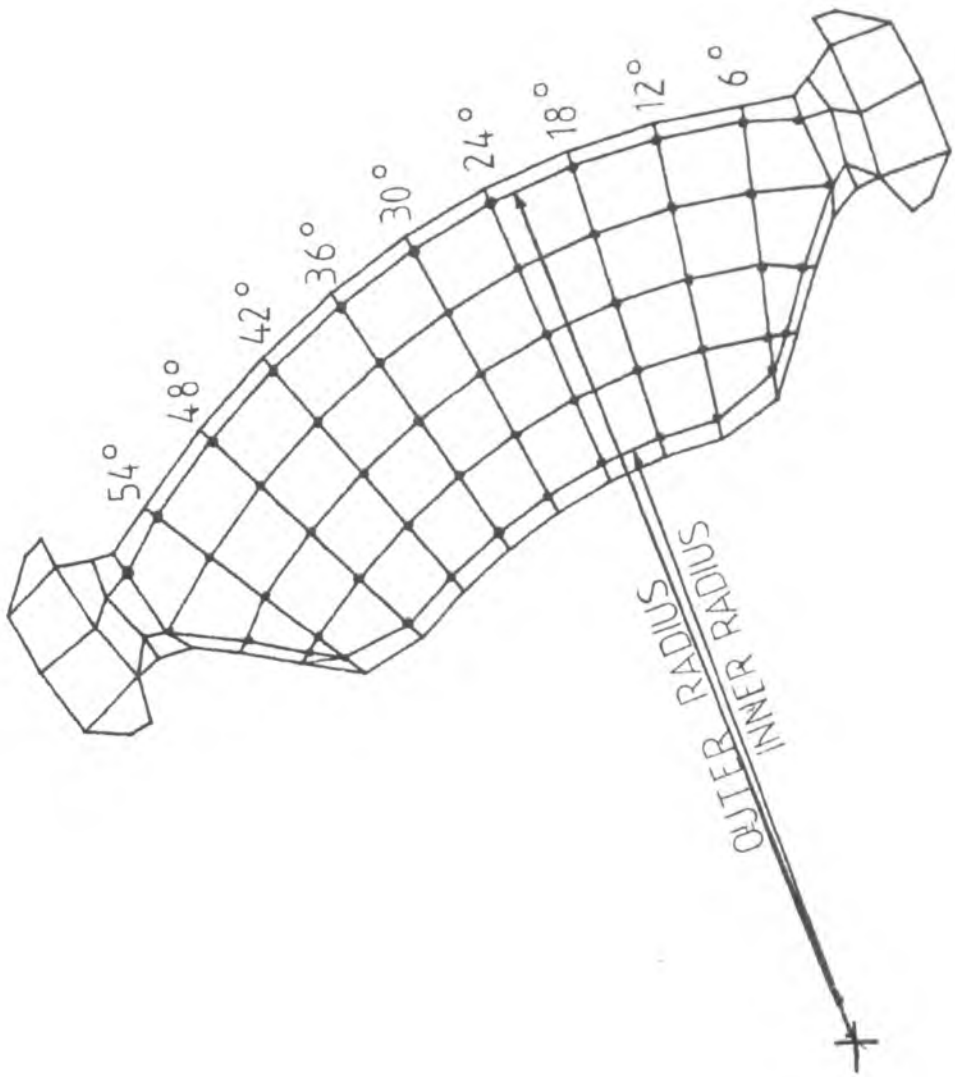

Figure 5.4 - Position of the interface nodes on the pad friction surface

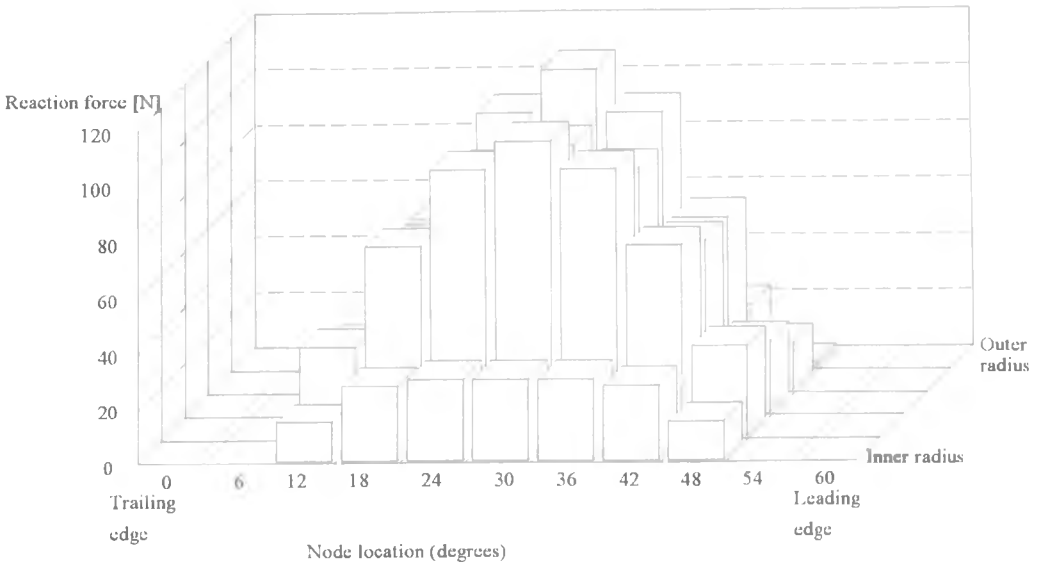

(a) μ=0

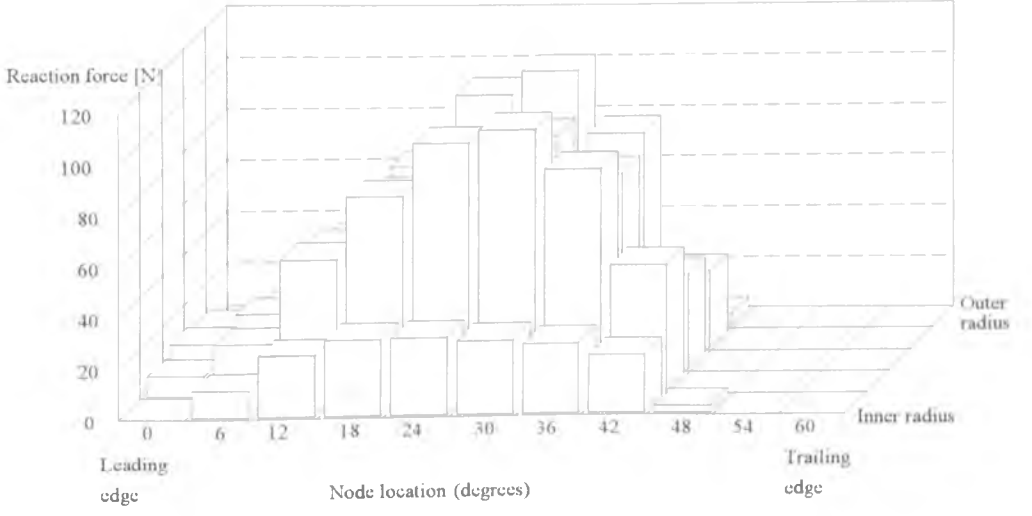

(b) μ=0.4

Figure 5.5- Nodal reaction force at the pad interface under piston applied pressure

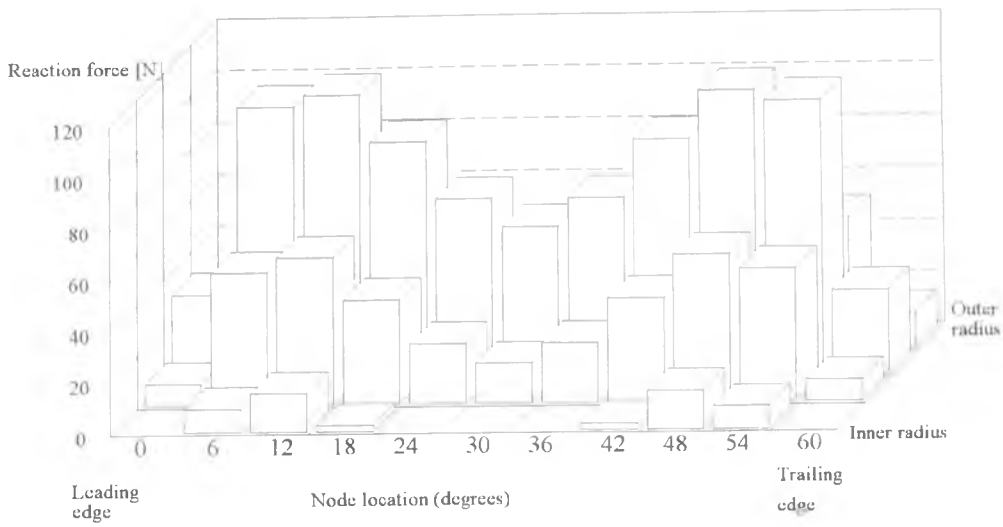

(a) μ=0.0

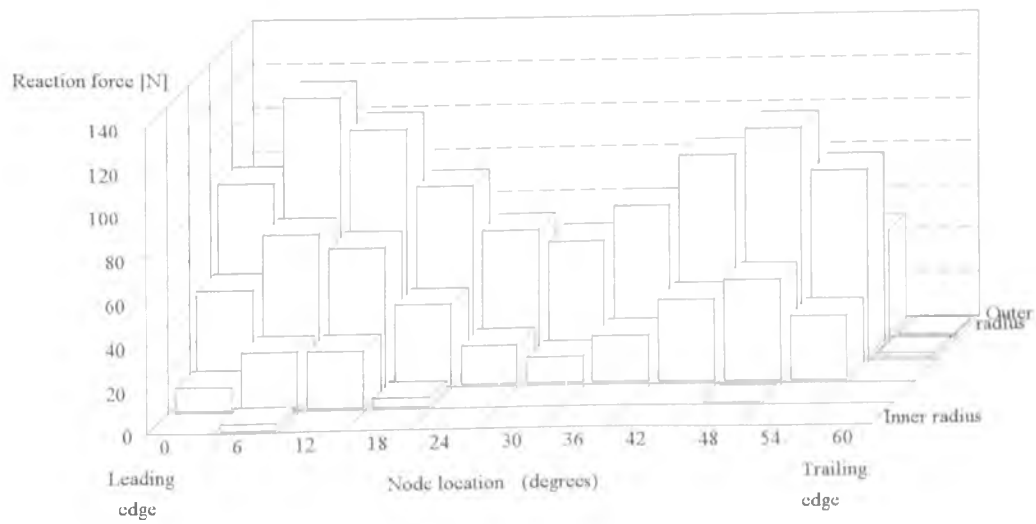

(b) μ=0.4

Figure 5.6 - Nodal reaction force at the pad interface under paw applied pressure

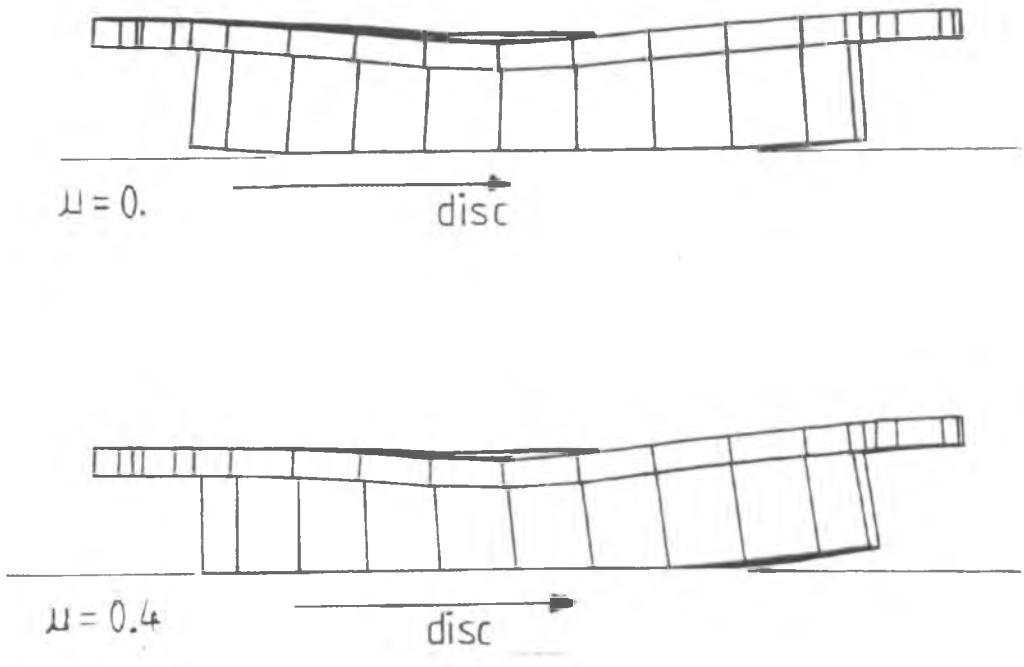

Figure 5.7 - The displacement of the pad under piston applied pressure and relative sliding.

5.4.2 Effect of magnitude of pressure

The effect of the magnitude of the applied pressure was also studied in order to determine whether the contact area changes with the load As the results for the paw applied pressure and piston applied pressure show similar trends, only the results for the piston applied pressure is discussed here in some detail. The load due to the piston applied pressure on the inboard pad was therefore applied in increments beginning from a load equivalent to a line pressure of 0.1 MPa (1 bar) up to a maximum of 1.0 MPa (10 bar) in steps of 0.1 MPa. The results for 3 different line pressures are shown in figure 5.8a for zero friction and figure 5.8b for a coefficient of friction of 0.4. For the purpose of this comparison the contact reaction forces at the nodes on the line of the outermost arc of the pad are taken. In order to allow comparison between the different pressure levels a continuous distribution is calculated from the discrete nodal

reaction forces. This is done by taking into account the distances between the neighbouring nodes resulting in specific reaction force as defined below:

$$\text{Specific reaction force} = \frac{\text{Average nodal reaction force between 2 nodes}}{\text{Distance between the 2 nodes}}$$

The area under the resulting curve (as shown in figures 5.8a and 5.8b) is the total nodal reaction force for the the line around the outermost arc considered. For zero friction coefficient , the specific pressure distribution is symmetrical for all pressure magnitudes and the effect of increasing pressure is to increase the reaction force magnitude in a linear manner as shown in figure 5.8a. It is is also apparent that the number of nodes in contact does not change with the pressure magnitude.

Figure 5.8b shows that the corresponding pressure distribution with friction included is shifted towards the leading edge and is no longer symmetric. However the effect of the pressure magnitude on the reaction force is still linear. Again there is no change in the number of nodes in contact as the pressure magnitude increases. Thus the linear relationship between the nodal reaction force and the applied pressure is maintained even when friction is present.

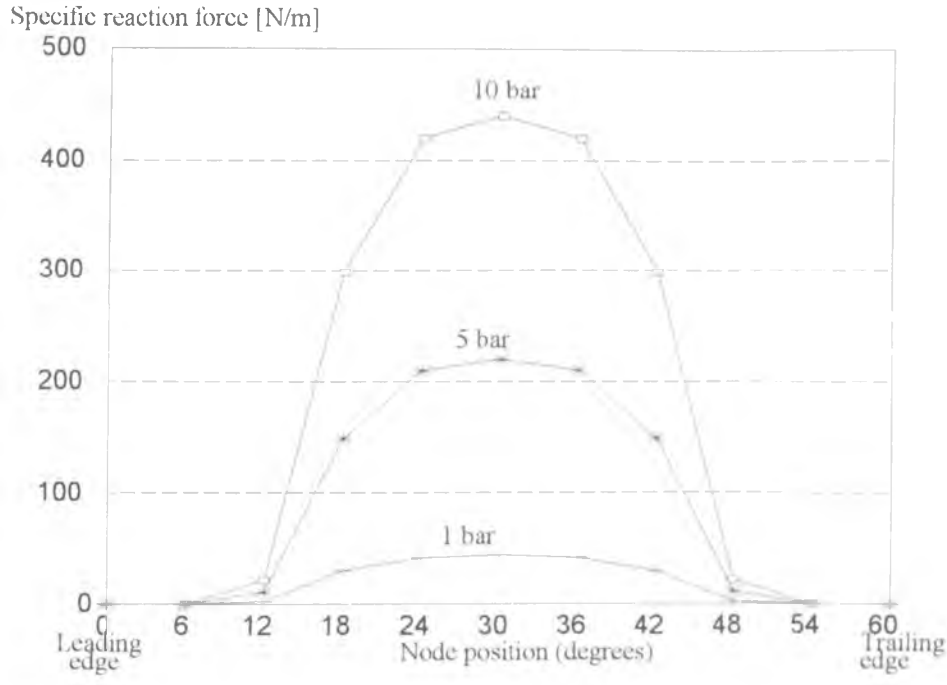

(a) μ=0

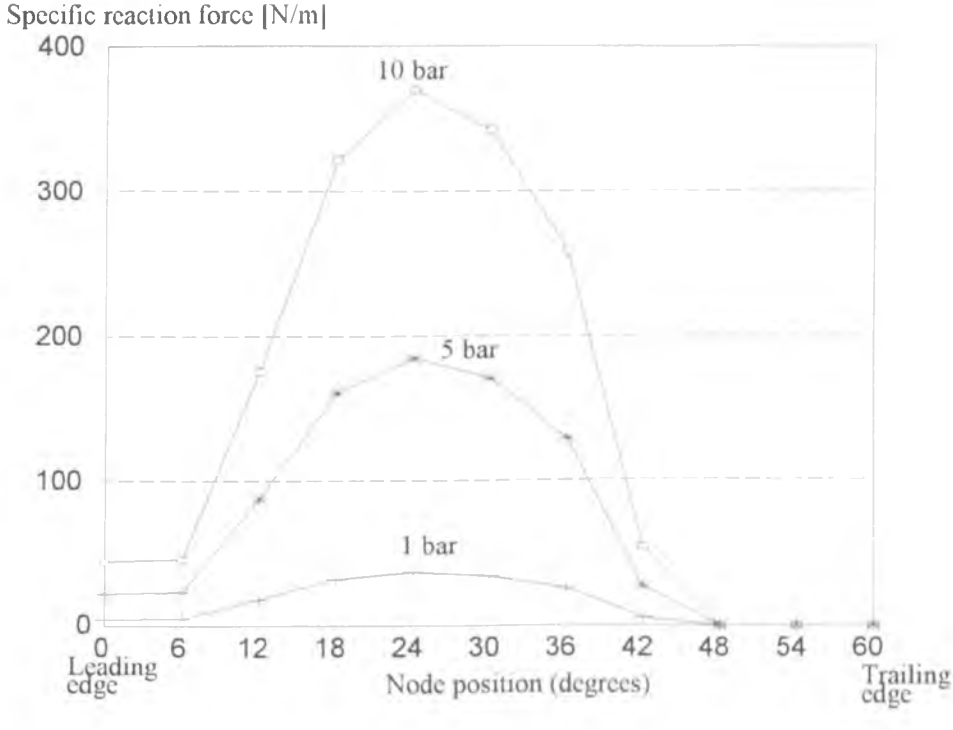

(b) μ=0.4

Figure 5.8 - Specific reaction force distribution for different magnitudes of line pressure (piston applied pressure)

5.4.3 Effect of abutment constraint

The effect of the nature of the circumferential restraint of the pad on the contact reaction force distribution was also studied. Three abutment arrangements were considered :-

a) leading edge abutment

b) trailing edge abutment

c) combined trailing and leading edge abutments.

The abutment effect was modelled as a constraint applied to the nodes on the pad back plate 'ears' in both the radial and circumferential direction. The results are shown in figures 5.9a -c.

It can be seen from the figures that the contact force distribution patterns are similar in all 3 cases and the number of nodes in contact does not change with the abutment arrangement. There is however a slight difference of the maximum nodal reaction force. For comparison , the standard deviation of the reaction force distribution for each abutment arrangement is also shown in Table 5.1. This parameter is sufficiently sensitive to detect any slight changes in the magnitude of the nodal reaction forces.

From Table 5.1 , the largest differences of the maximum reaction force occur between the leading and trailing edge abutment cases but the difference is only 3.4N (3.1%) whilst the respective standard deviations differ by only 1.307N (3.9%). From these results , it can safely be concluded that the abutment arrangement does not significantly alter the contact force distribution.

Table 5.1- Maximum reaction force and standard deviation for different abutment

a)Abutment type	**b)Maximum reaction force (N)**	**c)Standard deviation (N)**
Trailing edge	112.7	34.646
Leading edge	109.3	33.339
Trailing & Leading	109.5	33.902

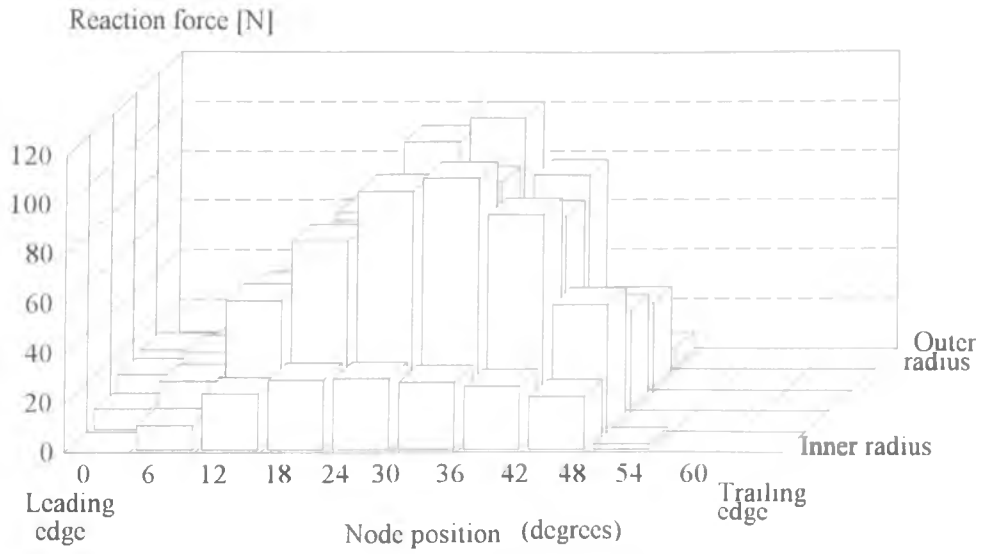

(a) leading edge abutment

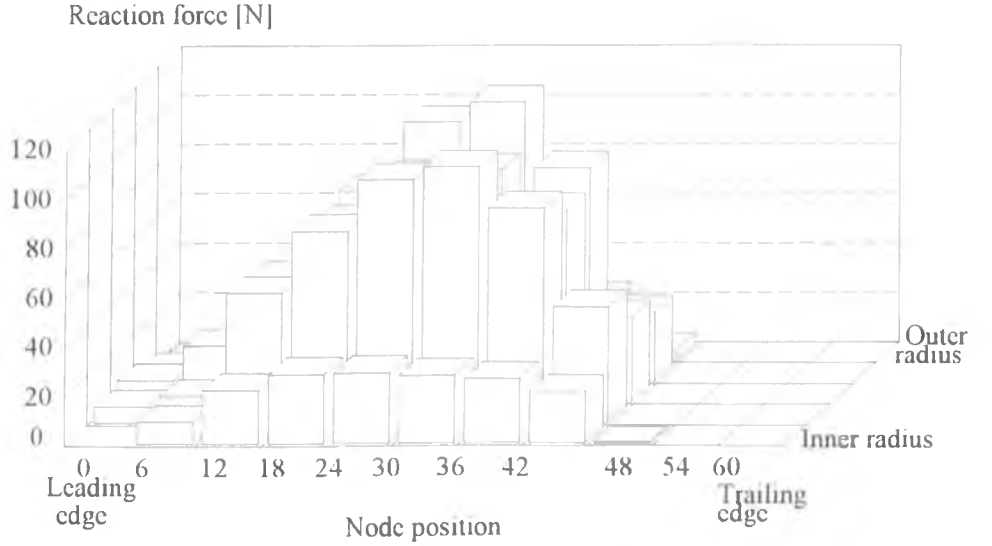

(b) trailing edge abutment

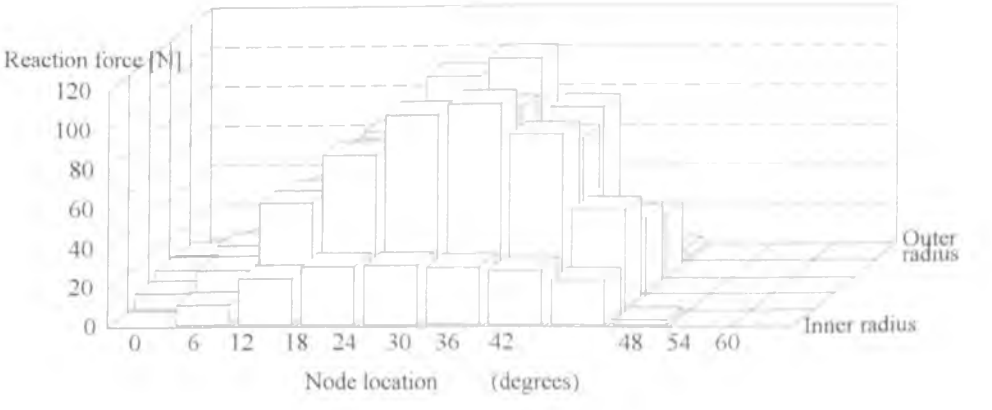

(c) combined leading and trailing edge abutments

Figure 5.9 - Nodal reaction force at the pad interface under piston applied pressure

5.4.4 Effect of friction material modulus

The effect of the Young's modulus of the friction material on the contact reaction force distribution was also studied. The baseline value for the study was taken as 8000 MPa representing a relatively 'hard' friction material , and alternative values of 18.75 %, 50% and 125% of this baseline material property were also studied. Only the piston applied pressure case with combined trailing and leading abutments is shown here as similar trends were found for the paw applied pressure case and other abutment arrangements. The results for the different friction material modulus values are shown in figures 5.10(a) - (d).

The results shown that the general pattern of contact force distribution does not change with the friction material modulus. The number of nodes in contact however does change , with increasing number of nodes in contact for lower modulus values. For the softest material considered (E=1500 MPa), the number of nodes in contact is 43 whilst for the hardest material (E=10000 MPa) the number of nodes in contact is 39.The standard deviation of the contact force distribution is again used as a measure of how the distribution pattern varies , with a lower standard deviation indicating a more uniform contact force distribution. The trend is shown in figure 5.11. It can be seen that the standard deviation of the nodal contact forces increases with the friction material modulus although not in a linear manner. A softer friction material allows more nodes to come into contact and simultaneously reduces the magnitude of the maximum reaction force. This also makes the contact force distribution more uniform as shown by the reducing standard deviation.

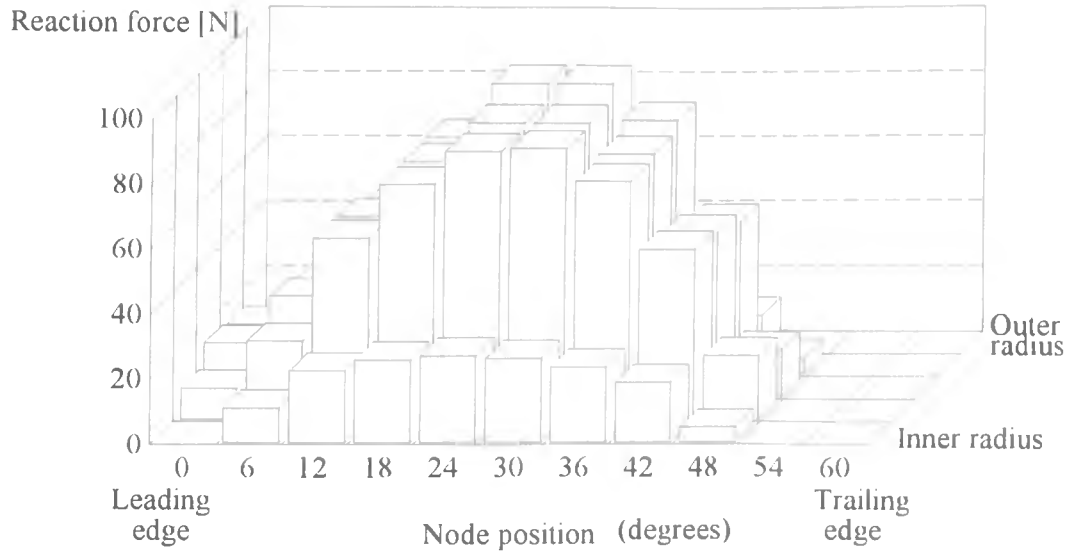

Figure 5.10a - Contact force distribution for friction material modulus of 1500 MPa

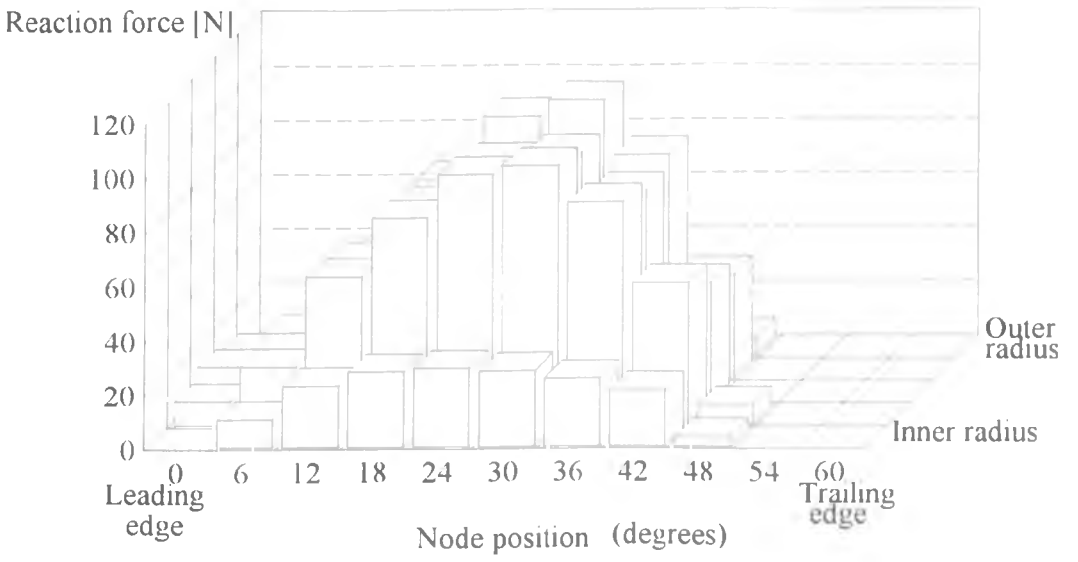

Figure 5.10b - Contact force distribution for friction material modulus of 4000 MPa

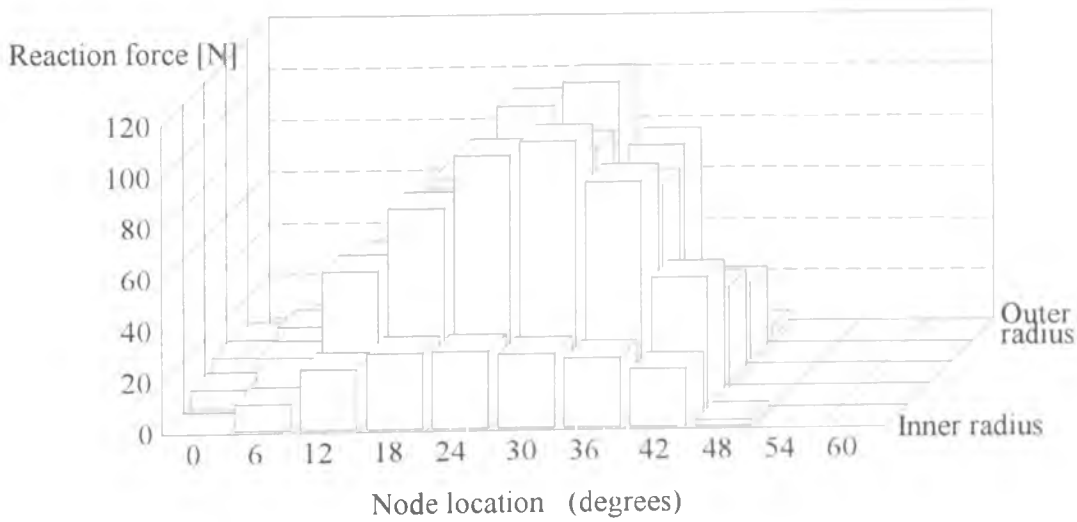

Figure 5.10c - Contact force distribution for friction material modulus of 8000 MPa

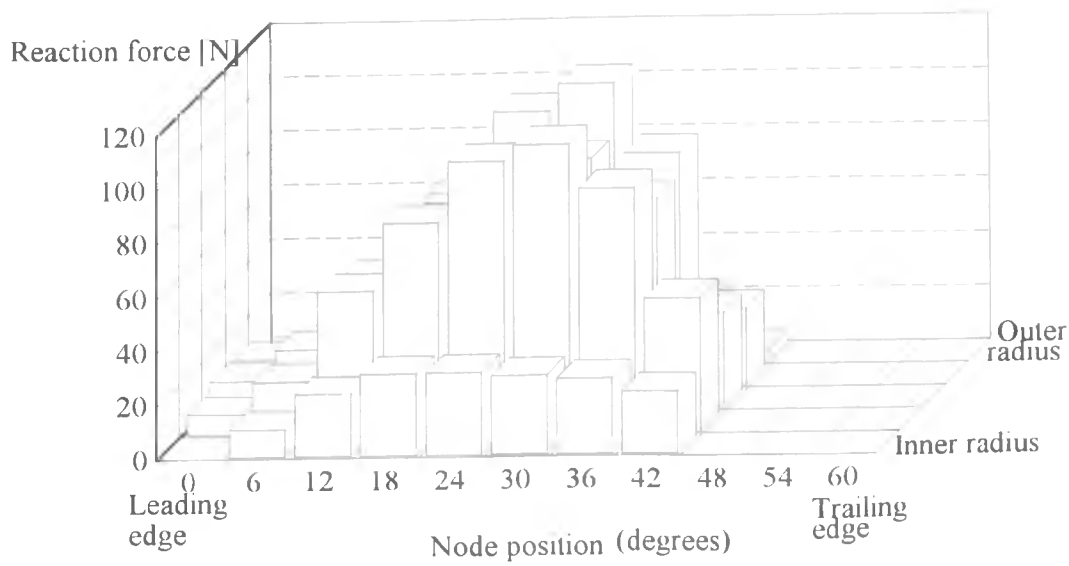

Figure 5.10d - Contact force distribution for friction material modulus of 10 000 MPa

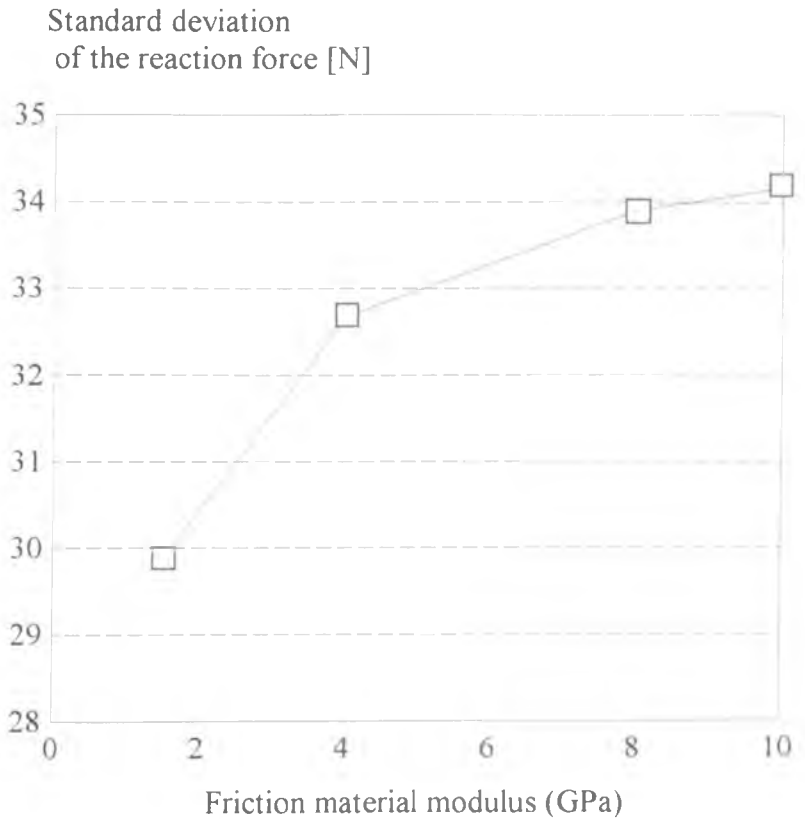

Figure 5.11 - Standard deviation of the contact force distribution for different friction material Young's modulus values.

5.5 Discussion

The contact reaction force analysis described above was carried out with the intention that the results could be used in the determination of contact stiffness. Also the extent to which each parameter varied affected the magnitude and distribution of the nodal reaction forces was determined

In the first study described in section 5.3.1 the effect of both piston and paw applied pressure load were investigated.Overall the results match well with the load distribution for a different pad geometry as measured by Tumbrink [69] using the ball pressure method Both sets of results reported indicate that the nodal contact force

distribution is not uniform and that not all the interface area is in contact. Therefore, within the operating pressure range of the brake this non-uniformity has to be taken into account when determining the nodal contact stiffness at the interface. The effect of circumferential friction is to shift the reaction force distribution towards the leading edge in both cases. The results of section 5.3.1 also indicate that the nodal reaction force distribution is strongly affected by the method of the applying the force (i.e. the piston or the paw) with the distrribution for the outboard pad (under the paw applied force) more uniform and with more nodes in contact than that for the inboard pad. Therefore , the strength of the nodal coupling (which is assumed at this level to be proportional to the reaction force) for the inboard pad which is loaded by the piston has a distribution different from that for the outboard pad which is loaded by the paw and this effect should be included in the stability analysis to follow.

In section 5.3.2 , the effect of the magnitude of the pressure loading on the nodal contact force distribution is studied.The results highlight the fact that the nodal reaction forces vary linearly with the applied pressure and the number of nodes in contact is not affected by the pressure magnitude. This corresponds well with the findings of Harding [65] and Day [66]. Previous work on the stability of a disc brake carried out by Liles [6] assuming that the distribution of stiffness is uniform because of the low pressure cannot be justified according to these results.

In section 5.3.3 the effect of the abutment arrangement on the reaction force distribution was shown to be of little significance with the difference between the leading edge abutment and the trailing edge abutment cases both in terms of maximum reaction force and standard deviation of the contact force distribution less than 4%. The number of nodes in contact and the distribution pattern remain the same for different abutment arrangements. With this knowledge , the stability analysis for different abutment arrangements could be carried out by limiting the parameter changes to the abutment support position , and not changing the contact stiffness distribution or magnitude.

In section 5.3.4 the sensitivity of the nodal reaction force to the friction material modulus was considered. The general effect is that a softer friction material enables more nodes to come into contact giving a more uniform contact pressure distribution as indicated by the relatively low standard deviation for the nodal reaction force. This result correlates well with the brake pad contact analysis due to Day et al [66]. Therefore, study of the effect of friction material modulus in the stability analysis should take the correct contact force distribution into account , particularly when extremes of materials are to be compared (for example friction material moduli of 400 MPa and 10 000 MPa). Small changes of say about 20% of the friction material modulus however would not merit such approach.

All the above parameters were considered in order to provide some insight into the scope of the planned stability analysis when the pressure effect is considered. The results have shown that some parameters do significantly affect the static contact pressure distribution between the pad and disc, these being primarily friction coefficient, pressure applicator shape and friction material modulus. The effect of these parameters on the pressure distribution therefore has to be taken into account in the stability analysis. Other parameters such as the abutment arrangement do not significantly affect the contact pressure distribution and the baseline results can be used with confidence for other conditions in the stability analysis.

CHAPTER SIX

CONTACT STIFFNESS DETERMINATION

6.1 Introduction

One of the most important parameters in the proposed finite element modelling of disc brake squeal is the magnitude of the stiffness coupling the components at the sliding friction interface. As discussed in Chapter Two, the contact stiffness (also termed the coupling stiffness in some literature) needs to be within a certain range for instability to occur In the present chapter methods for the determination of contact stiffness are discussed and compared The most important criterion is the ability of the method to relate the contact stiffness to the magnitude of the load applied to the pad thus establishing a link between pressure and contact stiffness.

6.2 Methods for interface contact stiffness determination

There are several methods to determine contact stiffness including :

a) stress-strain relationship method

b) experimental method

c) random process approach

Method (a) has been used by Nishiiwaki [50]. Method (b) has been used by D'Souza and Dweib [27] and Sherif et al [56]. Method (c) has been used by Sherif [57]. Each method is discussed in turn below.

6.2.1 Stress-strain relationship method

In method (a) the stress-strain relationship for the pad friction material is used to determine the contact stiffness. Assume the pad is pressed with force F against the disc which is assumed to be a rigid surface as shown in figure 6.1.

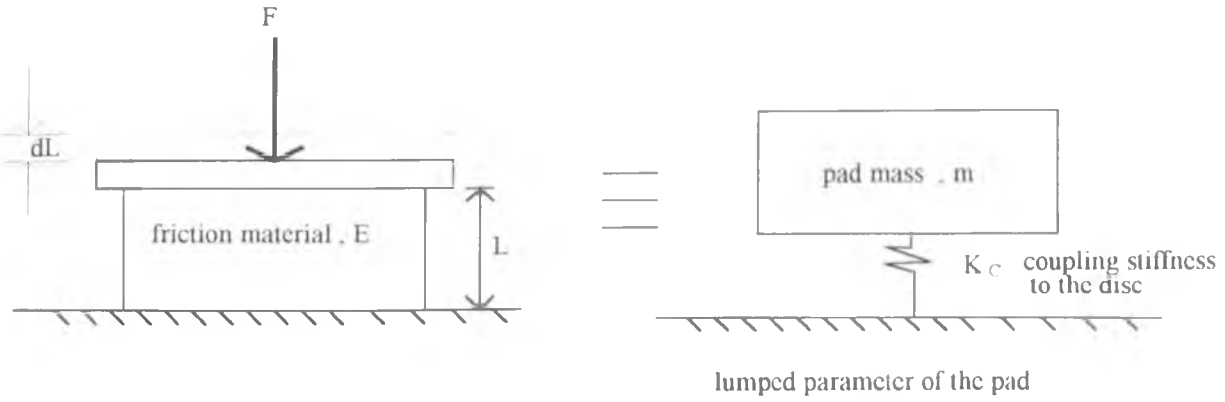

Figure 6.1 - Deformation of pad under normal load

The normal stress in the friction material is σ with resulting strain ε and the nominal contact area is A. From the elatic stress-strain relationship, the contact stiffness is :

$$K_C = F / dL = \sigma A / \varepsilon L = AE / L \qquad (6.1)$$

where dL is the change in L under load F.

In the above equation the contact stiffness is a function of contact area A, thickness of pad friction material L and the friction material modulus E. Therefore, there is no

effect of pressure on the contact stiffness which is the major drawback of this approach. Furthermore the stiffness of the friction material is already accounted for in the finite element model of the brake pad and therefore in the global stiffness matrix. It is clear from the above that this approach is suitable only in lumped parameter models in which the pad is assumed to be rigid.

6.2.2 Experimental method

In various experiments on friction-excited vibration using a pin-on-disc apparatus [27], the contact stiffness was derived from the equations of motion of the system for which the mass, acceleration,velocity, displacement and force were measured. The basis for this method is that the contact generates stiffness and damping which add to the existing structural and damping forces in the system An algorithm based on an experimental method to determine contact stiffness is an extension to the one used by Raguskis and Yurkauskas [76] in the determination of the stiffness of a radial thrust bearing assembly. The approach will be discussed here in some detail using a model of a beam mounted on ball bearings at each end which are idealised as springs of unknown stiffness.

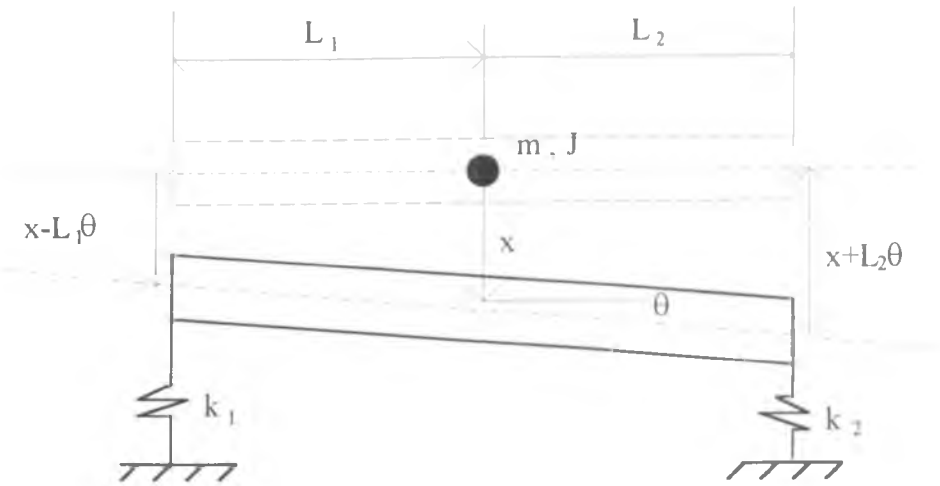

Figure 6.2 - Schematic diagram for computing unknown support stiffness [76]

The equations of motion of the system are :

$$m\ddot{x} + (k_1 + k_2)x - (x_1L_1 - k_2L_2)\theta = 0 \qquad (6.2a)$$

$$-(k_1L_1 - k_2L_2)x + J\ddot{\theta} + (k_1L_1^2 + k_2L_2^2)\theta = 0 \qquad (6.2b)$$

Equations (6.2) are linear differential equations with constant coefficients. Therefore the solution can be written in the form of :

$$x = A_1 \sin(\omega t + f) \qquad (6.3a)$$

$$\theta = A \sin(\omega t + f) \qquad (6.3b)$$

Substitute equations (6.3) into (6.2) and after algebraic transformation a quadratic equation in terms of ω^2 will be formed By solving the quadratic equation, the first and second natural frequencies can be found in terms of the system parameters. At resonance the modes of vibration would be analogous to the principal modes acting at the natural frequencies of the system. Therefore a search can be made for the values of k_1 and k_2 to give the correct predicted natural frequencies ω_i. Assuming that each stiffness is bounded between two values, k-high and k-low, a closeness function C, could be used for assessment of the search accuracy :

$$C = \sum_{i=1}^{n} (\omega_i - \omega_i')^2 \qquad (6.4)$$

where ω_i' is the experimental value obtained from modal analysis. For this example (n=2), the closeness function would be :

$$C = (\omega_1 - \omega_1')^2 + (\omega_2 - \omega_2')^2 \qquad (6.5)$$

The stiffness coefficients k_1 and k_2 are selected to minimise the closeness function.

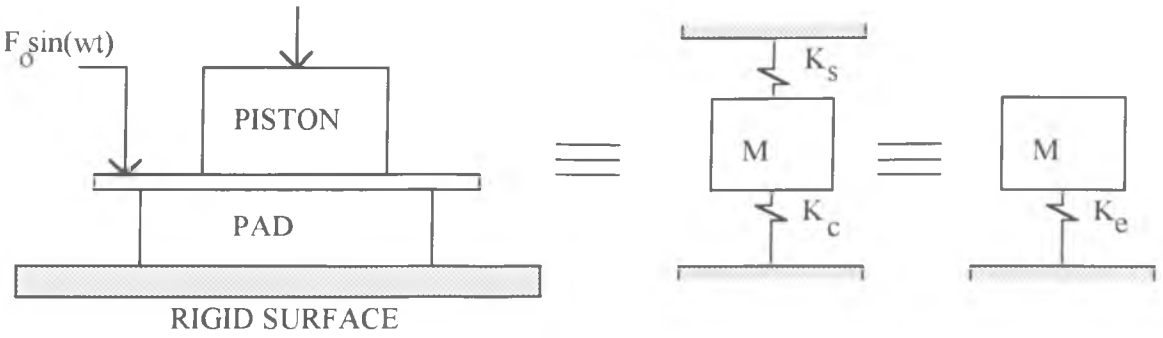

Figure 6.3 - Simplified model illustrating the experimental approach

In the present finite element model of the pad-disc system , contact is idealised as equivalent springs distributed throughout the interface connecting the surface nodes on the disc with the adjacent nodes on the pad as discussed in Chapter Three. The above method could be used to determine the effective overall stiffness of the pad (including the stiffness of the piston-backplate contact) idealised as shown in figure 6.3. The response of the clamped pad could be determined by forced vibration experiments for varying piston loads and, as in equation (6.3), the closeness function could be made to approach zero from which the effective overall stiffness K_e could be determined relatively easily as a function of load. However a major shortcoming of this approach is the need to establish a relationship between the support stiffness at the piston-backplate interface (K_S) and the desired contact stiffness (K_C). This requires predetermined values of the support stiffness (K_S).

6.2.3 Random process approach

The determination of contact stiffness by the random process approach is based on the culmination of several studies by Greenwood and Williamson [77], Greenwood and Tripp [78], Nayak [79] and Thomas and Sayles [80]. This approach was used by Sherif [57] in his analysis of the longitudinal vibration of a brake pad. The method emanated from the need to determine the joint stiffness of machine tools, for example between the saddle and the bed of a lathe. It is based on the definition of a band of wavelengths relevant to the surface interactions (plane-plane) and using them to obtain

working expressions for stiffness in terms of measured surface parameters. As the approach is very relevant to the problem of flat surface interactions such as between the disc and the pad, it is discussed below in some detail.

6.2.3.1 Theory of random process approach

Greenwood and Williamson [77] used the random process approach to explain the behaviour of two surfaces in contact, one of which is rough and the other perfectly smooth as shown in figure 6.4. The rough surface is assumed to be covered with a large number of asperities of random height which at least near their summits are all spherical with the same radius β as shown in figure 6.5. The probability of a particular asperity having a height between z and z + dz above some reference plane will be $\phi(z)dz$ where ϕ is the probability density function.

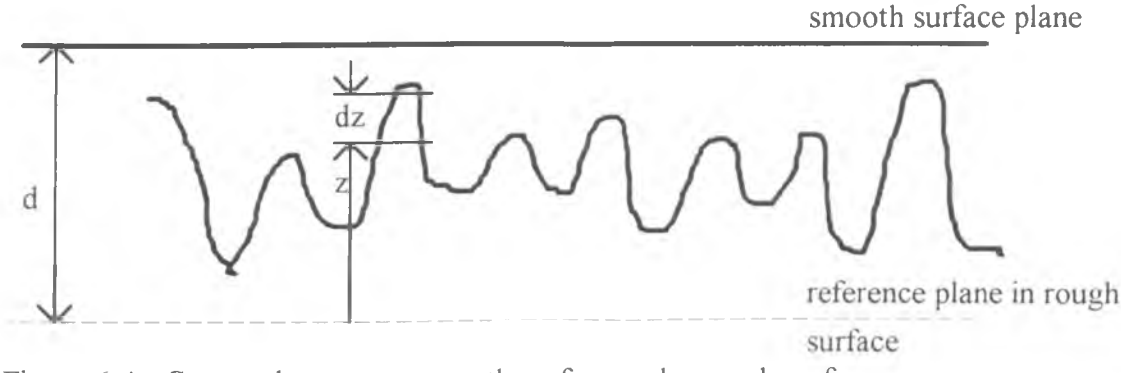

Figure 6.4 - Contact between a smooth surface and a rough surface

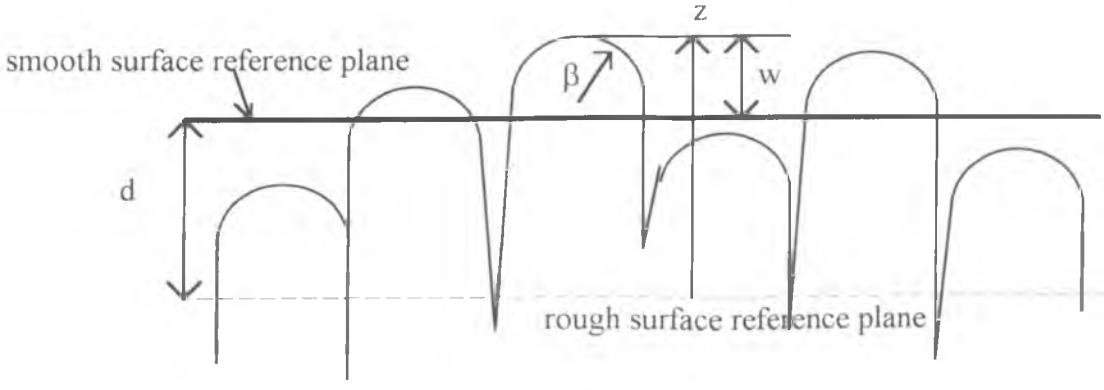

Figure 6.5 - Idealised rough surface with each peak having a spherical top with radius β, differing only in height.

The standard Hertzian contact equations can be used to determine the individual asperity behaviour. The contact radius a_1, contact area A_1 and load P_1 for each asperity in contact can be expressed in terms of the normal compression or compliance w defining the amount by which the points outside the deforming zone move together during the deformation, thus :

$$a_1 = \beta^{1/2} w^{1/2} \tag{6.6}$$

$$A_1 = \pi \beta w \tag{6.7}$$

$$P_1 = (4/3) E' \beta^{1/2} w^{3/2} \tag{6.8}$$

where

$$\frac{1}{E'} = \frac{1-\nu_1^2}{E_1} + \frac{1-\nu_2^2}{E_2} \tag{6.9}$$

and E_1, E_2 are the Young's moduli of surfaces 1 and 2 respectively, ν_1, ν_2 the corresponding Poisson's ratios and β the asperity radius. In the case of very different material moduli such as those of the friction material of the brake pad and the cast iron rotor, E' is simply the plane stress modulus of the softer material.

If the two surfaces come together so that their reference planes are separated by a distance d , then there will be contact at any asperity whose height was originally greater than d. Therefore the probability of contact at any given asperity of height z is given by

$$\text{prob}\,(z > d) = \int_d^{\infty} \phi(z)\,dz \tag{6.10}$$

For N number of asperities, the expected number of contacts n will be

$$n = N \int_d^{\infty} \phi(z)\,dz \tag{6.11}$$

Also, since for any asperity in contact $w = (z - d)$ (see figure 6.5) and therefore $A_1 = \pi\beta w(z - d)$ from equation 6.7, then the mean asperity contact area is given by

$$\bar{A}_1 = \int_d^\infty \pi\beta(z-d)\phi(z)dz \tag{6.12}$$

and the expected total area in contact is

$$A = \bar{A}_1 n = \pi n\beta \int_d^\infty (z-d)\phi(z)dz \tag{6.13}$$

Equally from equation (6.8) the expected total load is

$$P = \bar{P}_1 n = \frac{4}{3}E'\beta^{1/2} n \int_d^\infty (z-d)^{3/2}\phi(z)dz \tag{6.14}$$

where $\bar{P}_1$ is the mean asperity load.

Thus, from the probability of asperities being in contact, Greenwood and Williamson [77] managed to establish a relationship between the total load P and the separation of the mean (or reference) planes d as shown in equation 6.14. For convenience, they used standardized variables and described the asperity heights in terms of the standard deviation σ of the height distribution and the surface density of the asperities η defined by $N=\eta A_o$ where A_o is the nominal contact area. This gives :

$$n = \eta A_o F_0(h) \tag{6.15}$$

$$A = \pi\eta A_o \beta\sigma F_1(h) \tag{6.16}$$

$$P = \frac{4}{3}\eta A_o E'\beta^{1/2}\sigma^{3/2} F_{3/2}(h) \tag{6.17}$$

where the standardized separation is given by $h=\left(\frac{d}{\sigma}\right)$

and the function $$F_n(h)=\int_h^{\infty}(s-h)^n\phi\ (s)ds \tag{6.18}$$

where ϕ (s)ds is the probability of finding an asperity tip at a dimensionless height s (i.e. $s=\frac{z}{\sigma}$) above the mean plane of the rough surface.

Greenwood and Williamson [77] argued that most engineering surfaces have height distributions which can be approximated by a Gaussian distribution. Therefore the height distribution is given by

$$\phi(s)=\frac{1}{\sqrt{2\pi}}e^{-\left(\frac{s^2}{2}\right)} \tag{6.19}$$

from which $$F_n(h)=\frac{1}{\sqrt{2\pi}}\int_h^{\infty}(s-h)^n e^{-\left(\frac{s^2}{2}\right)}ds \tag{6.20}$$

The above function was tabulated for different values of n by Greenwood and Tripp[78]. Equation (6.17) was simplified by Greenwood and Williamson [77] to the form below

$$P=c\ F_{3/2}(h) \tag{6.21}$$

where $$c=\frac{4}{3}E'\beta^{1/2}\eta A_o\sigma^{3/2} \tag{6.22}$$

The variation of the ratio (P/c) with h based on equation 6.21 is shown in figure 6.6.

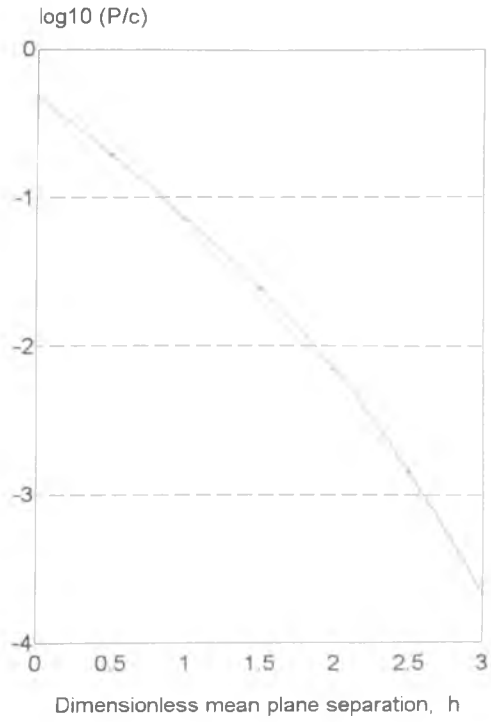

Figure 6.6 - Variation of dimensionless load (P/c) with dimensionless mean plane separation h according to equation (6.21) after [80].

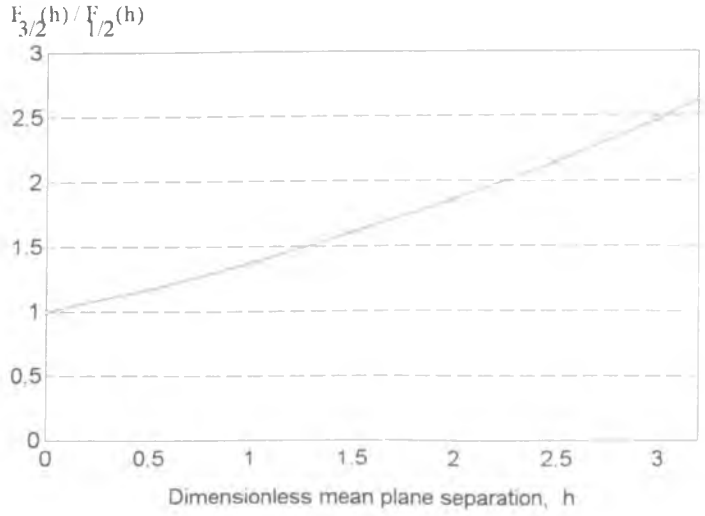

Figure 6.7 - Variation of the ratio $\frac{F_{1/2}(h)}{F_{3/2}(h)}$ with dimensonless mean plane separation after [80].

The stiffness resulting from the interaction of the two planes is defined as the load P necessary to produce unit displacement of the mean plane separation and for the purpose of the present study can be taken as the contact stiffness value , K_C:

$$K_C = \frac{dP}{dd} = \frac{dP}{dh}\cdot\frac{dh}{dd} \tag{6.23}$$

Now $\frac{dh}{dd} = \frac{1}{\sigma}$ and by differentiating equation (6.21) with respect to h and rearranging to include the load P rather than the constant c :

$$K_C = \left(\frac{3}{2\sigma}\right)\frac{F_{1/2}(h)}{F_{3/2}(h)}P \tag{6.24}$$

Equation (6.24) provides an expression whereby the contact stiffness of the surfaces can be related to the applied load by the standard deviation of the height distribution σ and the ratio $\frac{F_{1/2}(h)}{F_{3/2}(h)}$. This ratio has been determined by Greenwood and Tripp [78] and plotted by Thomas and Sayles [80] against h as shown in figure 6.7.

Upto this point it is still not possible to apply equation (6.24) as some of the terms needed to calculate $F_{3/2}(h)$ from equations (6.21) and (6.22) such as the asperity radius β and the surface density of asperities η cannot be measured directly. Nayak [79] promoted a way of statistically relating the asperity radius and surface density using a random process model whereby the rough isotropic surface is characterised by its autocorrelation R and power spectral density (PSD). He was thus able to derive several important characteristics of a surface using the random process such as the surface asperity density:

$$\eta = \frac{1}{6\pi\sqrt{3}}\left\{\frac{m_4}{m_2}\right\} \tag{6.25}$$

where m_2= 2nd moment of the PSD

m_4=4th moment of the PSD.

Nayak [79] also proved from his analysis that the surface gradient could be expressed as follows :

$$\theta^2 = \left(\frac{\pi m_2}{2}\right) \tag{6.26}$$

and that the mean asperity radius β can be approximated by the following equation.

$$\frac{1}{\beta\sqrt{m_4}} = \frac{8}{3\sqrt{\pi}} \approx 1.50 \tag{6.27}$$

Thomas and Sayles [80] proposed that the surface gradient could be related to the mean absolute profile slope, $\tan\theta$ by the following expression :

$$\left(\frac{H}{E\tan\theta}\right) \geq 3 \tag{6.28}$$

where H is the hardness of the material and E is the Young's modulus. By assuming in general that the hardness is three times the yield strength Y, we obtain

$$\tan\theta \leq \left(\frac{Y}{E}\right) \tag{6.29}$$

For most materials the ratio $\left(\frac{Y}{E}\right)$ is very small. Thus to a good approximation

$$\tan\theta \approx \theta = \left(\frac{Y}{E}\right)$$

Equation (6.28) can be related to equation (6.26), thus

$$m_2 = \frac{2}{\pi}\left(\frac{Y}{E}\right)^2 \tag{6.30}$$

which enables m_2 to be calculated from the assumed material properties of the surfaces.

Thomas and Sayles [80] proposed further that the first three even moments of the PSD curve are given as follows :

$$m_0 = 4\sigma^2 \tan^{-1}\Omega \tag{6.31}$$

$$m_2 = 4a^2\sigma^2(\Omega - \tan^{-1}\Omega) \tag{6.32}$$

$$m_4 = 4a^4\sigma^2(\frac{\Omega^3}{3} - \Omega + \tan^{-1}\Omega) \tag{6.33}$$

where a is the auto-correlation decay function of the height distribution , $\Omega = \frac{\omega_2}{a}$ and ω_2 is the cut-off wavelength for the high pass filter (i.e. an upper frequency limit for the analysis).

Therefore, knowing m_2 from equation (6.30), equation (6.32) can be solved for Ω in terms of material properties and measured surface profiles which enables m_0 and m_4 to be calculated. Knowing the first three even moments of the PSD and surface roughness properties a and σ, all other properties such as the mean asperity radius β and the mean asperity density η (from equations (6.27) and (6.25) respectively) can then be calculated. Thus, in order to use the random process approach, the main parameters required from the measurement of the surface profiles are the rms value of the roughness σ and the auto-correlation decay function of the height distribution a.

The main assumptions of this method can be listed as below :

a) the distribution of surface heights is Gaussian

b) the upper frequency limit is set by the onset of plasticity, the condition for which can be expressed in terms of the mean absolute profile slope related to the ratio of hardness to the Young's modulus

c) the surfaces are considered to have exponentially decaying autocorrelation functions

d) hardness is assumed to be three times the yield strength.

The random process asperity approach applied to the modelling of surface roughness has one major limitation [78]. When the load applied is sufficiently large, the mean planes will tend to overlap and the mean plane separation d becomes negative. This may suggest that the real area of contact becomes larger than the apparent area which cannot be true. Thus a limit of positive d must be imposed.

The implementation of the random process approach in the present work is discussed in in more detail in section 6.4.

6.3 Comparison of the three methods

In order to determine the most suitable method for the present purposes comparison has to be made between the three methods discussed above which all take into account the material properties and the contact area.

In the first method, the contact stiffness derived is not related to the applied load. The only way for the contact stiffness of a constant modulus material to change is by reducing the thickness and even then only one value of stiffness is obtained for any load magnitude. In a lumped parameter model the contact stiffness (or coupling stiffness) derived using this method is valid as the material stiffness is not represented directly in the model. However in the finite element method the stiffness matrix has already taken into account the elastic properties of the friction material. Therefore this method is not suitable for the present analysis of the effect of pressure on disc brake squeal.

In the second method, the contact stiffness calculated does change with the applied applied as shown by Bracken and Sakioka [51] with a higher load causing the natural frequency of the system to increase. This method however includes the cumulative effect of the surface roughness and the pressure at all joints. It is difficult therefore to establish a relationship between the support stiffness at the piston-pad backplate interface and the pad-disc contact stiffness as only the cumulative effect of

theoretical calculation of its stiffness). To allow for a non-uniform stiffness distribution, the distribution would have to be pre-determined and the closeness function calculated to allow for this. Further difficulties lie in introducing friction at the interface (in order to represent the sliding condition) as the analysis presented in Chapter Five shows that friction causes the contact force distribution (and hence the stiffness) to be biased towards the leading edge which may change the dynamic response of the system.

In the random process approach , the contact stiffness is a function of the applied load. The relationship also includes the surface properties of the interface (experimental work by Sherif et. al. [56] showed that a glazed disc surface is a necessary condition for squeal to occur). With this approach the effect of pressure can be isolated from the surface properties and analysed independently. As the contact stiffness is related to the applied load, the contact stiffness for each node pair at the disc-pad interface can be directly related to the nodal contact reaction force. Thus high reaction force will give high contact stiffness and the distribution of contact stiffness will follow exactly that of contact reaction force. This is very much in accordance with the requirements of the present analysis as discussed in Chapter Three.

It should be noted however that all the approaches described above can only approximate the actual contact stiffness as other operating factors unaccounted for such as disc run-out , thermal distortion of the pad and uneven wear of the mating surfaces can all affect the force distribution and the stiffness resulting from the contact.

From the above discussion, the random process approach has distinct advantages over the two other methods, namely the ability to relate contact stiffness to the load and the consideration of surface roughness in the calculation.Therefore the random process approach is used to determine the contact stiffness in the present study as described in the following section

6.4 Contact Stiffness Determination by The Random Process Approach

The steps for implementing the random process approach for contact stiffness determination in the present work can be summarised as below :

a) Measurement of the surface roughness of both the pad and the disc surface using a Talysurf 5 surface profile measuring machine. As the machine does not calculate the autocorrelation function, the roughness heights were digitised from the printout of the surface profiles for use in further computations.

b) Calculation of the autocorrelation function (section 6.4.2) for each surface. The delay length was limited to 10% of the record length to reduce error.

c) Calculation of the relevant parameters of the surfaces as discussed in section 6.3. A programme was written in C (see Appendix I for the programme listing)to calculate the stiffness for each load condition (0.1 - 1 MPa line pressure in steps of 0.1 MPa), the results from which were used to produce the contact stiffness versus load curves.

d) Calculation of the contact stiffness for different surface and material properties to determine the sensitivity of contact stiffness to various parameters.

6.4.1 Measurement of surface roughness of the disc and the pad

Measurement of the surface roughness of an unworn disc and a new pad was carried out using a Talysurf 5 profile meter . The longest measured length from this profile meter is 100 mm. The measurement was carried out in a tangential straight line across the face of the disc and the pad through the pad centroid (it was not feasible with the available equipment to measure along a circumferential arc to more closely follow the circular interaction between the disc and the pad). The printed surface profiles were then digitised and the data used for the calculation of the variance and root mean square value of the roughness and the decay constant of the autocorrelation function. These parameters are the necessary input for the contact stiffness determination.

6.4.2 Calculation of the autocorrelation function

One of the requirements in the implementation of the random process approach in determining contact stiffness is the calculation of the autocorrelation function of the surfaces. In this section the definition of the autocorrelation function and its importance is discussed based on the work of Halling [81]. The autocorrelation function for a single profile is obtained by delaying the profile relative to itself by some fixed interval, then multiplying the original profile by the delayed one and averaging the product values over a representative length of the profile. Thus

$$R(l) = E\,[\, z(x)\, z(x+l)] \tag{6.46}$$

where E expected (average) value

z(x) height of the profile at a given coordinate x along the mean line z(x)=0

z(x + *l*) height at an adjacent coordinate (x + *l*) taken at an interval *l* from the previous one

If the values of the ordinates at discrete intervals *l* are known this may be interpreted as

$$R(l) = \frac{1}{N-l}\sum_{x=1}^{N-l} z(x)z(x+l) \tag{6.47}$$

where N is the total number of ordinates in a sample length L It can be clearly seen that when the interval length *l*=0, R(*l*) reduces to the variance σ^2 or the root mean square value σ of the profile. The autocorrelation function is therefore usually plotted in standardised form r(*l*) where

$$r(l) = \frac{R(l)}{R(0)} = \frac{R(l)}{\sigma^2} \tag{6.48}$$

The general decay of the function indicates a decrease of correlation as *l* increases and is an indication of the random component of the surface profile while the oscillatory

component of the function indicates any inherent periodicity of the profile. Detail discussion and examples of various engineering surfaces and their autocorrelation functions can be found in [81].

6.4.3 Results from the autocorrelation function of the disc and pad surfaces

Figures 6.9 and 6.11 show the calculated autocorrelation functions of the disc and pad surface profiles for different delay lengths upto 11 mm and 10 mm respectively. These functions can be approximated by an exponential function as shown in the $\log_e R(l)/R(0)$ versus l plots of figures 6.10 and 6.12 which indicates that the height distribution are Gaussian. The best fit straight lines drawn through the experimental points on these plots give the decay constant in the equation $R(l) = Ae^{-a|l|}$. An non-Gaussian surface (such as a perfectly sinusoidal topography) would have a non-exponential decay function for its autocorrelation function There are indeed small oscillations about the best fit straight line as shown in figures 6.10 and 6.12 indicating some small inherent periodicity in the surfaces. For Hertzian dry contact applications (for which the random process approach is derived), the periodic component of the profile can be negelected as it is the random component (i.e the exponential decay term) which is of primary importance. Therefore the small periodicity is ignored in the following calculations. The present results also fulfill two of the criteria (section 6.2.3.1) for the implementation of the random process approach namely that the surface is Gaussian and its autocorrelation function decays exponentially. The statistical parameters of both surfaces are shown in table 6.1

From table 6.1, the root mean square roughness from the measurement of the disc surface is 11.38 μm which is five times smaller than the value for the pad which is 51.78 μm. This is due to the better surface finish of the disc which is machined compared to the relatively rough surface of the pad which consists of embedded particles in a polymer matrix. Consequently the autocorrelation function decay constant reflects the fact that the variation of the height distribution on the disc surface is less than that on the pad surface (a perfectly constant amplitude sinusoidal surface has a zero decay constant)

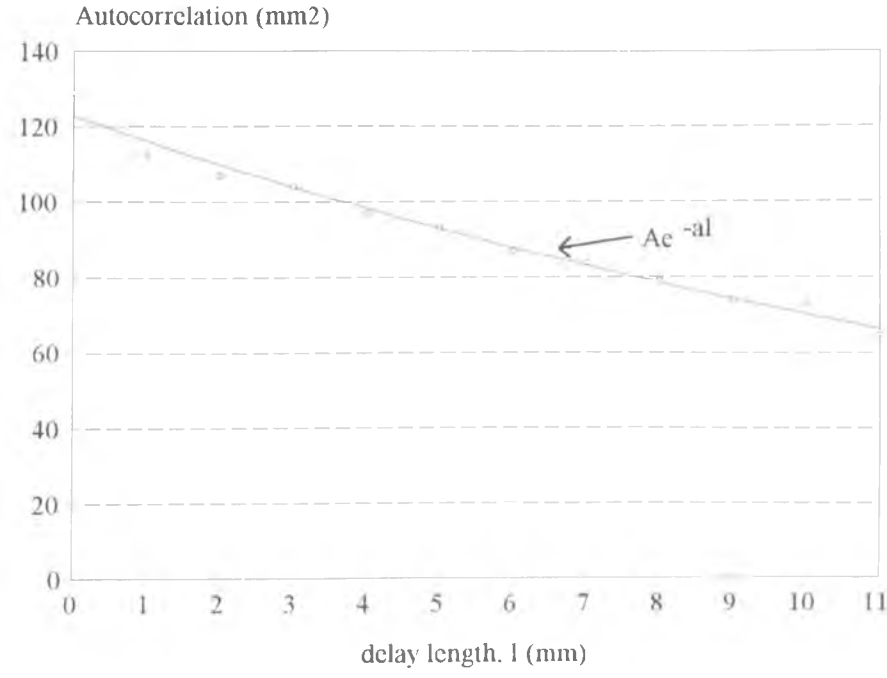

Figure 6.8 - Autocorrelation function of the disc surface roughness profile

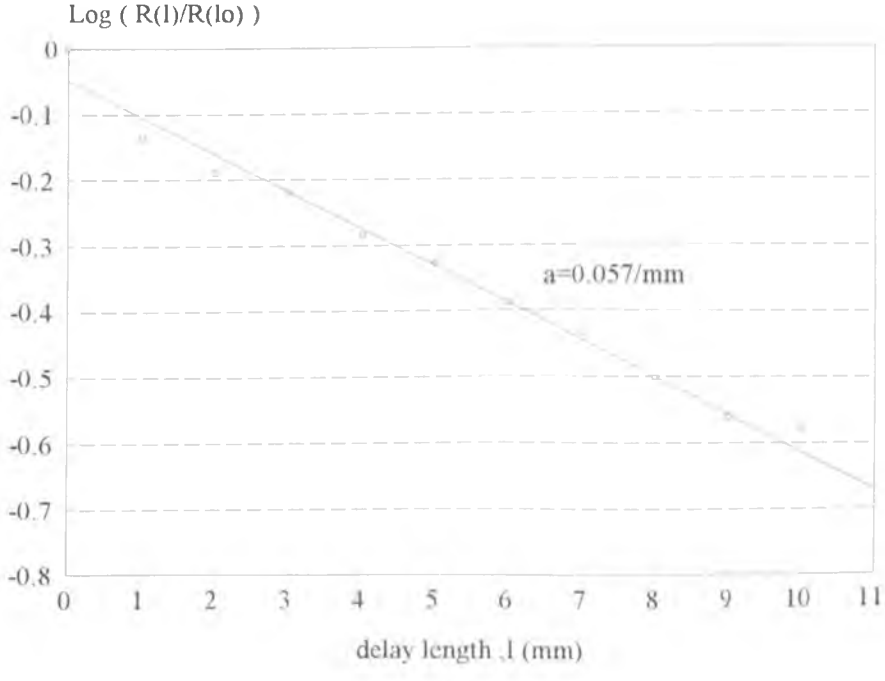

Figure 6.9 - Decay constant of specific autocorrelation function of the disc

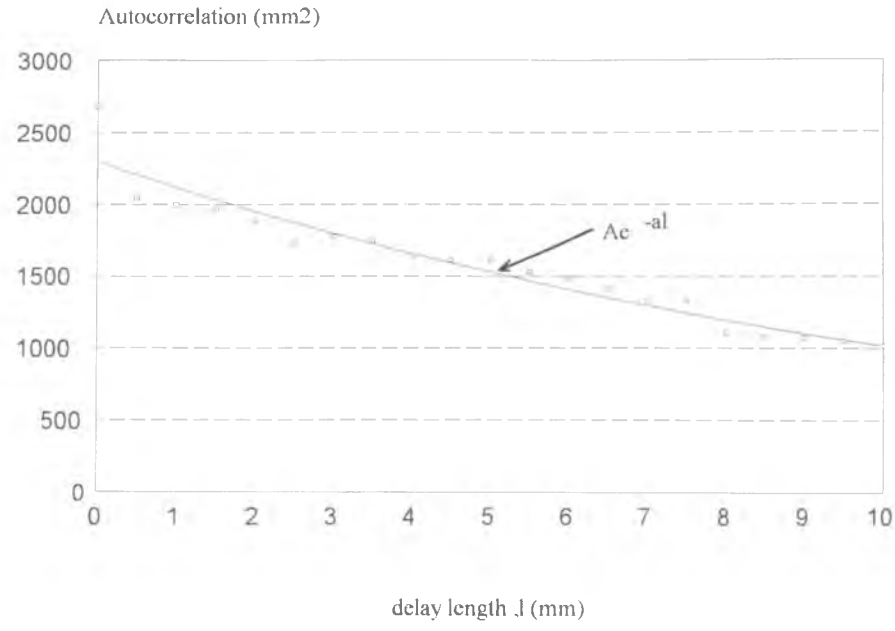

Figure 6.10 - Autocorrelation function of the pad surface.

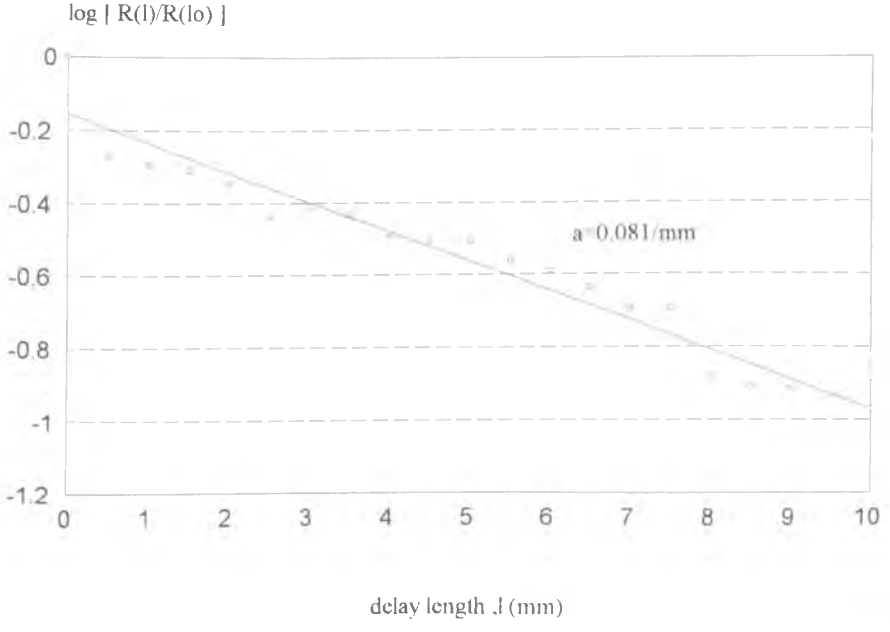

Figure 6.11 - Decay constant of specific auto correlation function of the pad surface.

Table 6.1 - Results from the roughness measurement of the disc and pad

Component	Root mean square roughness, σ (μm)	Auto correlation function decay constant,a (mm^{-1})
Disc	11.38	0.057
Pad	51.78	0.081

6.4.4 Results of the contact stiffness calculation

Using the available material data and the surface roughness properties measured for both the disc and the pad, the contact stiffness for the initial baseline system was calculated for each load condition. The data and results from the calculations are listed in table 6.2. The calculation of the effective modulus according to equation 6.2 gives a value which at 8.000 GPa is identical to that of the pad friction material (since this has a very much lower Young's modulus than that of the disc). In other words, in terms of this calculation the disc can be regarded as effectively rigid.

Table 6.2 - Material data and results from calculation

	Disc	**Pad**
Young's modulus E (GPa)	120	8
Poisson ratio, ν	0.25	0.25
Asperity radius β (mm)	0.4348	14.35
Asperity density (mm^{-2})	39.34	0.0415

The results shown in table 6.2 indicate that the asperity radius of the pad is comparatively very large and the asperity density very low. This is because equation 6.32 used in the calculation of the even moments produces a very small value of Ω =24.148 for the pad since both the surface roughness rms σ and the decay constant a are large. In comparison the low rms value and the low decay constant of the disc surface roughness produce a relatively large value of Ω = 1088.3 which results in a

small predicted asperity radius and relatively high asperity density. Physically this result is believable as a relatively smooth surface with small asperity radii such as that of the disc is expected to have higher asperity density than a relatively rough surface with large asperity radii such as the pad.

In the random process approach, the ratio of the load P to the constant c is required to be less than 0.4 in order to obtain a dimensionless mean plane separation greater than zero. For the pad friction material surface measured in the present case the ratio P/c for a load of 173N (equivalent to 1 bar line pressure) is 1.59×10^{-2}. In contrast for the disc surface at the same load level, the ratio $P/c = 2 \times 10^{-4}$ which is two orders of magnitude smaller. Selection of the ratio P/c (as per equation 6.21) is based on the fact that the results show that the pad asperity radius is thirty-three times larger than the disc asperity radius, indicating that it is a 'rough' disc acting on the 'flat and smooth' pad (in the sense that the smaller asperities on the disc are acting against the relatively flat and large asperities on the pad). A further consideration is that the approach is based on the Hertzian equations for asperity contact and it is therefore the smaller asperity radius which strongly influences the effective radius of the contact. Therefore a surface profile with a much smaller rms and a value will much more greatly influence the final outcome than the surface profile with the larger rms and a value (i.e. the rougher surface). These factors indicate that it is ratio P/c for the disc only which needs to be used in the determination of contact stiffness and reduce the problem to that of essentially normally distributed spherical asperities on a rigid disc acting against a flat elastic pad. Therefore for all further calculations the disc surface rms value alone is used in equation (6.24) even though the effective or composite radius is still used in equation (6.22).

For the measured value of the disc roughness and the material properties listed above, the contact stiffness is calculated for load steps of 0.1 MPa (1 bar) upto 1.1 MPa (11 bar) line pressure.

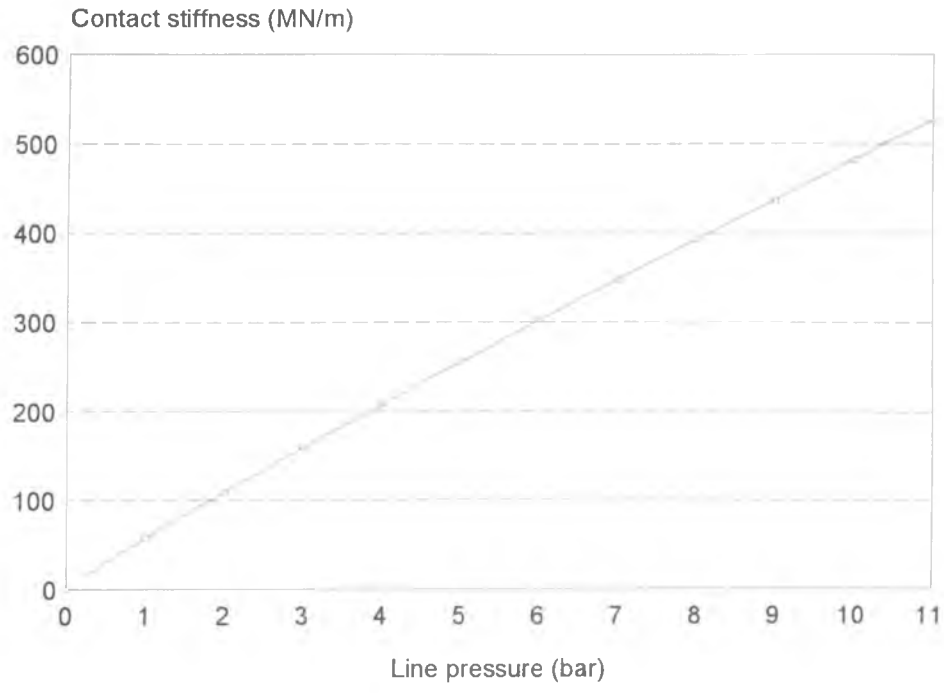

Figure 6.12 - Calculated contact stiffness for the pad-disc interface

The results shown in figure 6.12 indicate that the contact stiffness, K_C (N/m) for the condition described can be approximated as a linear function of the line pressure P (in bar) as follows :

$$K_C = 47221P \tag{6.49}$$

For comparison Sherif [57] predicted a similar linear curve from his data which for a load of 1 kN gave a contact stiffness of 38 MN/m. This is one order of magnitude less than the stiffness under a similar load (279.90 MN/m at 5.7 bar) in figure 6.16. The difference can however be attributed to the softer pad used by Sherif (E pad = 1 GPa) and the fact that his measurements were restricted to the pad surface only whereas in the present work the disc surface roughness is dominant as discussed above.

6.4.4.1 Effect of friction material properties on contact stiffness

The effect of friction material property on the contact stiffness was studied by varying the Young's modulus and the yield strength of the friction material simultaneously to give a constant ratio of $\frac{E}{\sigma_y} = 40$ (recall that a yield strength of 20 MPa was taken as the baseline value corresponding to the 8 000 MPa modulus).

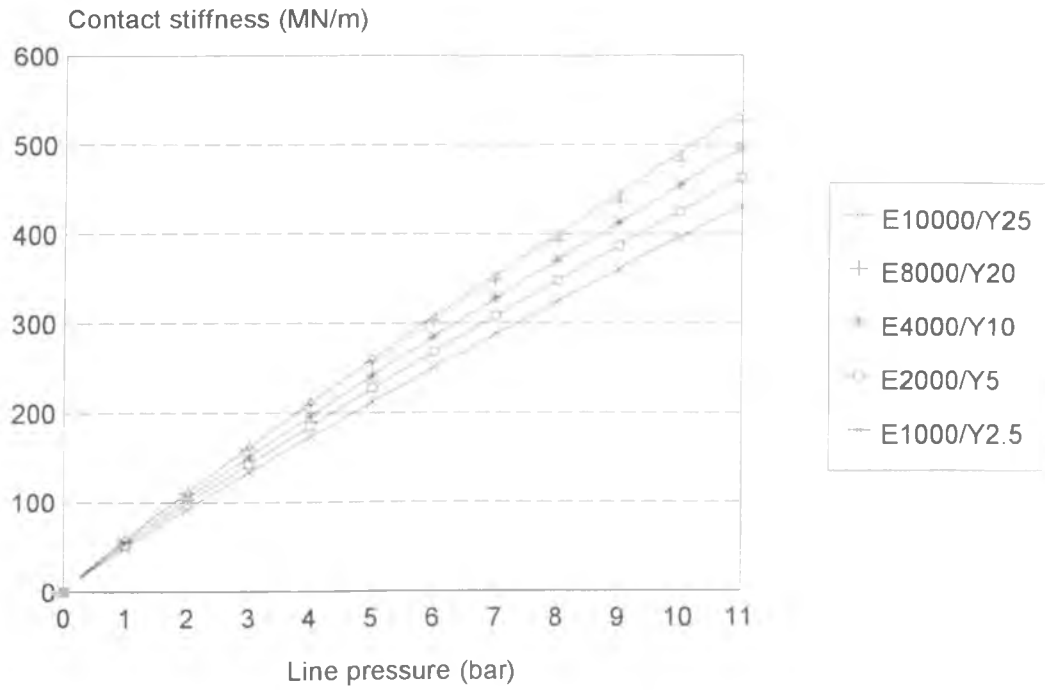

Figure 6.13 - Effect of friction material modulus on the contact stiffness

The results shown in figure 6.13 indicate that the contact stiffness does not vary greatly with changes in the friction material properties. This is due to the fact that the surface interactions are still between the relatively flat asperities of the pad and the small radius of the disc asperities. For a modulus of 10 000 MPa, the calculated pad asperity radius is 14.33 mm whilst for a modulus of 2000 MPa it is still 14.33 due to the constant ratio $\frac{E}{\sigma_y}$ used in the calculation. The differences in the calculated values

of contact stiffness arise simply from the effect of different E values on the effective modulus. The general trend as expected is that a friction material with low modulus results in a lower contact stiffness value than for a higher modulus pad material. For a tenfold reduction of the friction material modulus from 10 000 MPa to 1 000 MPa, the corresponding contact stiffnesses at 10 bar line pressure differ only by 104 MN/m, a change of about 20%.

6.4.4.2 Effect of disc material on contact stiffness

To study the effect of disc material on the contact stiffness, different disc materials are modelled including aluminum alloy, aluminum metal matrix composite, mild steel, magnesium metal matrix composite in addition to the baseline material of grey cast iron. The properties of the materials selected are shown in table 6.3. The surface topography was assumed to be as measured for the cast iron disc.

Table 6.3 - Material properties for the disc

Material	Modulus, E (GPa)	Yield strength, σ_y (MPa)	$\frac{E}{\sigma_y}$
Cast iron	120	345	348
Aluminum alloy	76	505	150
Aluminum MMC	100	215	465
Mild steel	205	304	674
Magnesium MMC	63	220	286

The results shown in figure 6.14 indicate that the contact stiffness for the different disc materials does not differ very much. In each case, material with a lower ratio of $\frac{E}{\sigma_y}$ gives higher contact stiffness as expected since σ_y is a hardness indicator (based on the assumption that the hardness of the material is three times the yield strength). A high disc modulus does not significantly affect the contact stiffness calculation as it is the

friction material modulus (which is two orders of magnitude smaller) which dominates the effective modulus in the calculation.

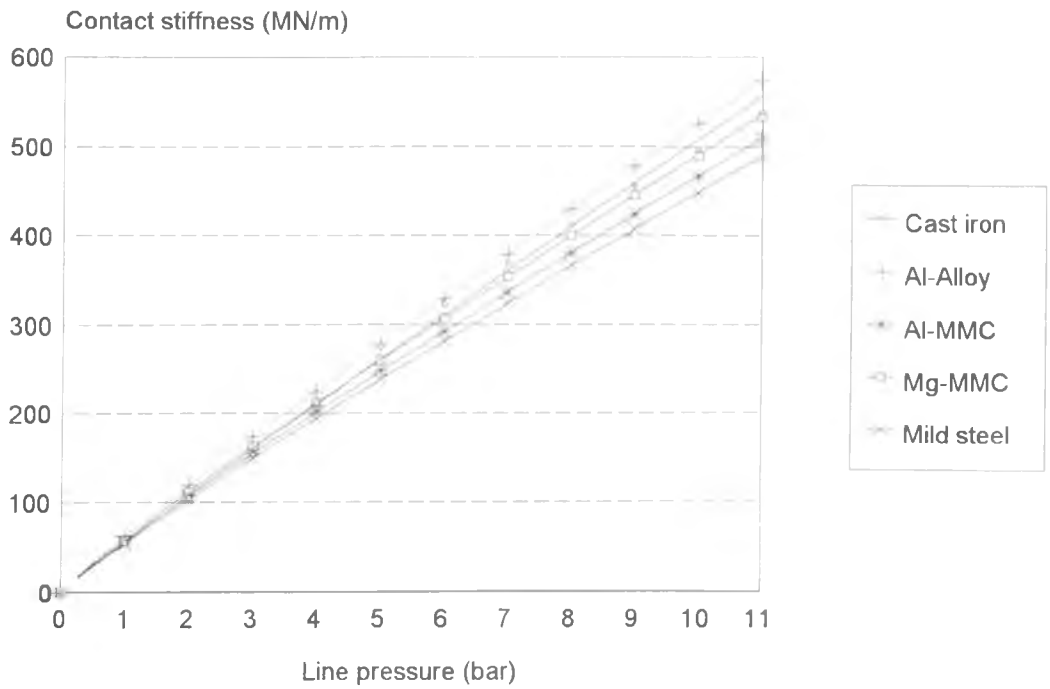

Figure 6.14 - Effect of disc modulus on contact stiffness

6.4.4.3 Effect of disc rms roughness on contact stiffness

To study this effect three alternative roughness rms values for the disc surface of 15μm, 10μm and 7.5μm are considered in addition to the baseline value (11.38 μm). The results shown in figure 6.15 indicate that contact stiffness increases significantly with decrease in the rms surface roughness of the disc. This is as expected since contact stiffness is inversely proportional to the disc rms surface roughness as shown by equation (6.24). Furthermore the calculated asperity radius increases with the rms surface roughness of the disc (which leads to a reduction in the asperity density). The cumulative effect is to increase the contact stiffness as rms surface roughness decreases.

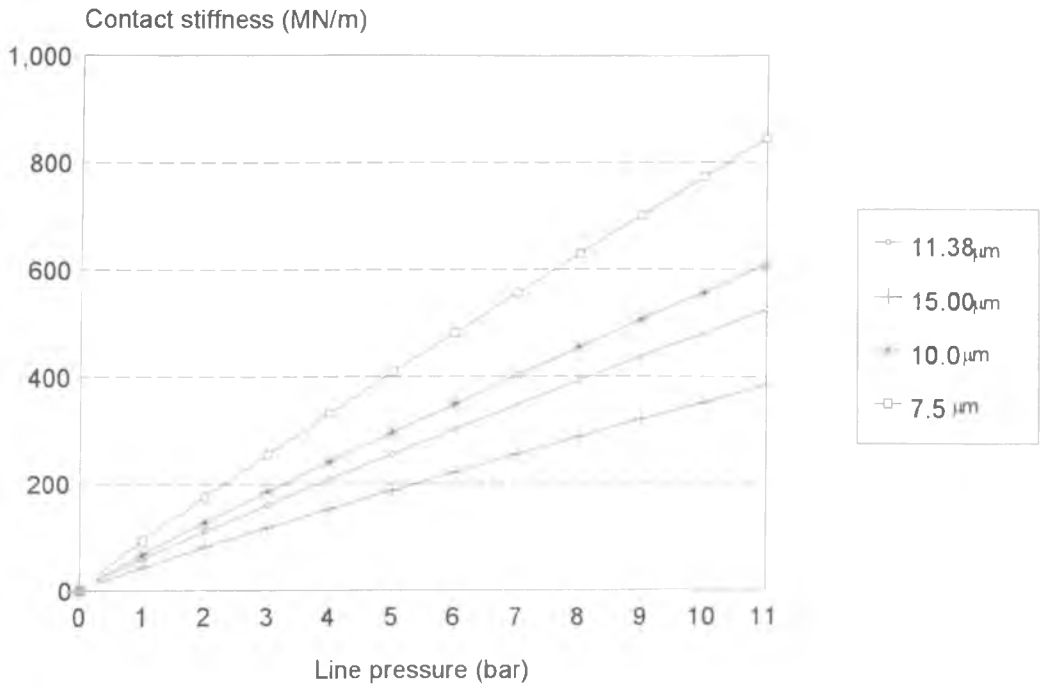

Figure 6.15 - Effect of disc surface rms surface roughness on contact stiffness

6.4.4.4 Effect of brake pad surface roughness on contact stiffness

In the calculation of the effect of the brake pad surface, two different cases are considered in addition to the baseline measured values. Firstly the rms roughness of the pad is reduced to 25μm (which is about half of the measured rms) with the decay constant unchanged at a = 0.081 mm $^{-1}$. The second case is where the rms roughness of the pad is unchanged at 51.74μm but the decay constant is reduced to 0.0415mm $^{-1}$. The results are shown in Table 6.4. It is clear that as the rms roughness of the pad is decreased the pad asperity radius β also decreases whilst the asperity density η increases. This in turn reduces the effective radius of the asperity at the pad-disc interface. However, as the constant c and the area density η used in the calculation (as per equation 6.22) are effectively those of the disc, the effect on contact stiffness is minimal.

Table 6.4 - Calculated parameters for different pad surfaces rms value

Parameters	rms=25 μm a=0.081 mm^{-1}	52 μm (measured) a=0.081 mm^{-1}	rms=52 μm a=0.0415 mm^{-1}
β pad (mm)	3.59	14.35	7.68
β disc (mm)	0.4348	0.4348	0.4348
β effective (mm)	0.3878	0.4220	0.4115
η pad (mm^{-2})	0.6614	0.415	0.1446
η disc (mm^{-2})	39.34	39.34	39.34
c pad (eqn. 6.22)	55786	10883	37423
c disc (eqn. 6.22)	1019727	1063627	1050325
Contact stiffness at line pressure of 10 bar (MN/m)	479.7	481.4	480.9

However as the pad becomes smoother the decay constant a cannot be expected to remain unchanged and as shown in the final column of table 6.3 the effective radius is also reduced for smaller a. Nevertheless the pad surface needs to have even smaller rms and a values than those shown in table 6.4 in order to significantly reduce the contact stiffness. The last row of table 6.3 shows that there is only a very small difference in contact stiffness for the different pad surface roughness parameters considered.

6.4.5 Example of nodal contact stiffness calculation.

The objective of estimating the total interface contact stiffness is to determine a suitable value for the nodal contact stiffness value for use in the friction matrix in the stability analysis. An example is now given of how the nodal contact stiffness is calculated for the pad-disc interface, assuming a friction material modulus of 8000 MPa, the measured roughness properties of the pad, equal trailing and leading edge

abutments, friction coefficient of 0.4 and line pressure of 10 bar. The node chosen is the one for which the maximum reaction force is predicted (109.5 N) which has coordinates of (R = 110mm, θ = 30 degrees) on the pad model definition (see figures 5.4 and 5.5a).

Piston diameter = 46.84 mm

The total force applied to the pad = Pressure at 10 bar X piston area

$$= (0.1\ \text{N}) \times \left(\frac{\pi}{4} \times 46.84^2\right) = 1735\text{N}$$

Total contact stiffness (from figure 6.12) = 496 MN/m

Nodal reaction force (from figure 5.6c) = 109.5 N

Nodal contact stiffness = (Nodal reaction force /Total force)*(Total stiffness)

= 31.3 MN/m

The calculation is repeated for all other node pairs on the pad-disc interface to determine the individual node contact stiffness for use in the friction matrix in the stability analysis.

6.5 Discussion

The random process approach to contact stiffness calculation takes account of both the material and surface properties at the interface. For the baseline parameters studied, the calculated contact stiffness varies in direct proportion to the applied pressure. In section 6.4.4.1, the effect of friction material properties on contact stiffness was studied. From the results, a stiffer friction material gives a higher contact stiffness for the same applied pressure as expected but the proportional change of contact stiffness is much less than that of the friction material modulus.

The effect of the disc material studied in section 6.4.4.2 showed that for the five different materials considered the contact stiffness does not vary very much.

Generally harder materials as indicated by the ratio $\frac{E}{\sigma_y}$ give higher contact stiffness as expected.

In section 6.4.4.3 the effect of the disc surface rms roughness on the contact stiffness was investigated. The results indicate that contact stiffness is sensitive to the disc surface roughness and in particular that a reduction in surface roughness increases the contact stiffness. Therefore the effect of wear on brake squeal could be analysed indirectly by considering the effect of rms roughness on the contact stiffness. The curves presented in figure 6.15 could be used to determine the operating roughness domain over which the contact stiffness may vary throughout the life of the disc, for example by taking the measured rms value of 11.38 μm as being for a new and unworn disc. Then, by assuming that the surface roughness is decreased by wear, the contact stiffness would progressively increase even though the line pressure remains the same. The effect of disc surface roughness has been demonstrated in the experimental work of Sherif et al [57] in which the disc surface had to be glazed (i.e smooth) for squeal to occur - a neccessary but not sufficient condition. The results shown in section 6.4.3.3 together with those from the stability analysis reported in Chapter Seven below may help explain these effects.

Section 6.4.4.4 shows that pad surface roughness has little effect on the contact stiffness. This is due to fact that the pad asperity is large and therefore has little influence on the effective radius compared to the effect of the much smaller disc asperity. However if the pad surface was sufficiently reduced in its rms roughness and decay constant, the effect would then be significant.

The sample calculation given in section 6.4.5 demonstrates how the nodal contact stiffness is derived. It gives a distribution pattern identical to that of the nodal reaction force as the predetermined total force and total stiffness do not vary for a given pressure. Using this method force equilibrium is maintained and the sum of the distributed nodal stiffness equates to the current total stiffness at the interface.

In all, the approach used to calculate the nodal contact stiffness in this thesis has taken into account both the partial contact state at the pad-disc interface and the material and surface properties of the interface thereby providing the necessary link between applied pressure and contact stiffness.

CHAPTER SEVEN

STABILITY ANALYSIS OF THE COUPLED PAD-DISC SYSTEM

7.1 Introduction

The individual finite element models of the pad and the disc (free-free modal analysis of which has been compared with experimental results in Chapter Four) can be coupled for stability analysis in order to predict squeal taking into account the contact pressure distribution at the interface as discussed in Chapter Five. By using an unsymmetric eigenvalue solver, the resulting eigenvalues are complex numbers in which the sign and the magnitude of the real part indicates the relative stability and the imaginary part estimates the frequency of the resulting modes.

In the present chapter , the stability of the coupled pad-disc system is discussed in terms of the unstable modes of interest and their evolution with parameters such as contact stiffness. The complex eigenvectors which describe the asynchronous motion of the modes are studied and these modes are compared with experimental squeal mode shapes [10] for validation of the approach. Additional

sensitivity studies are also carried out in order to investigate the effect of certain parameters on the stability of the coupled pad-disc system

7.2 Methodology

The individual finite element models of the disc and the pad are validated for dynamic analysis in Chapter Four. The reduced (substructured) models of the pads and the disc are now to be coupled using the interface matrix derived in Chapter Three. External connections to the pads where the inboard pad makes contact with the piston and the outboard pad with the paw are modelled using stiff springs connected to rigid points as schematically shown in figure 7.1. The finite element model of the coupled pad-disc system is shown in figure 7.2. The baseline condition is taken as a combined trailing and leading edge abutment with the friction coefficient set at $\mu = 0.4$ and a support stiffness of 24 MN/m for both the pad backplate -piston and also the backplate-paw external connections.

The distribution of the contact stiffness at the nodes on the pad-disc interface is determined by the magnitude of the nodal reaction force predicted by a non-linear finite element contact analysis , the results of which are presented in Chapter Five

Complex eigenvalue analysis is carried out for different values of contact stiffness in order to observe the system behaviour throughout for the range of typical line pressures. The analysis is carried out in steps of 50 MN/m upto 600 MN/m starting from a contact stiffness of 50 MN/m, representing line pressure in the range 0.1 - 1.2 MPa (1-12 bar).

In order to determine the effect of operating pressure two parameters in particular are considered:

i) interface contact stiffness , K_C

ii) external support stiffness , K_S

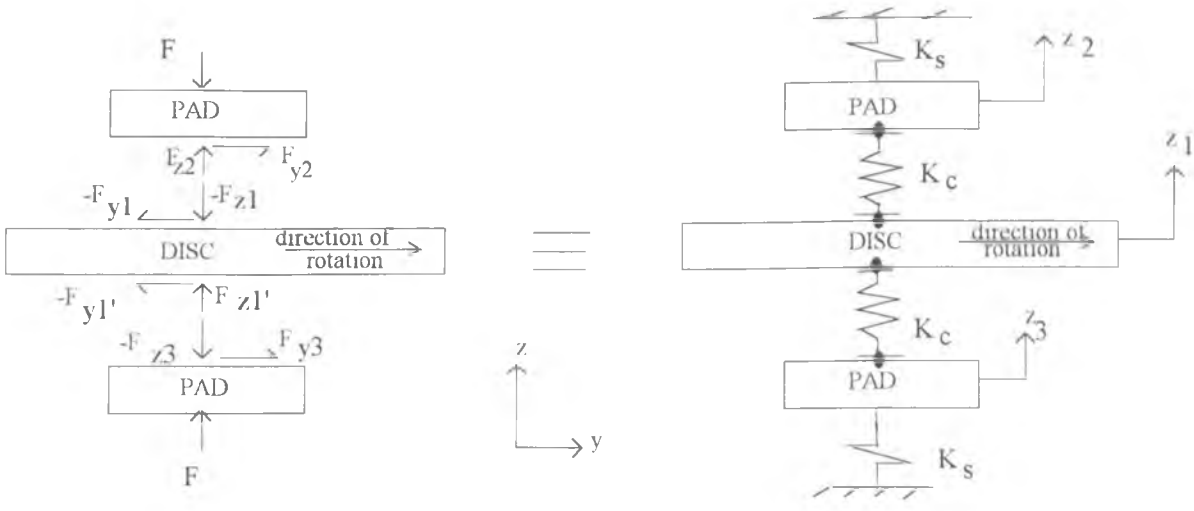

Figure 7.1 - Active forces acting at the sliding interface and the schematic diagram of the coupled pad-disc model

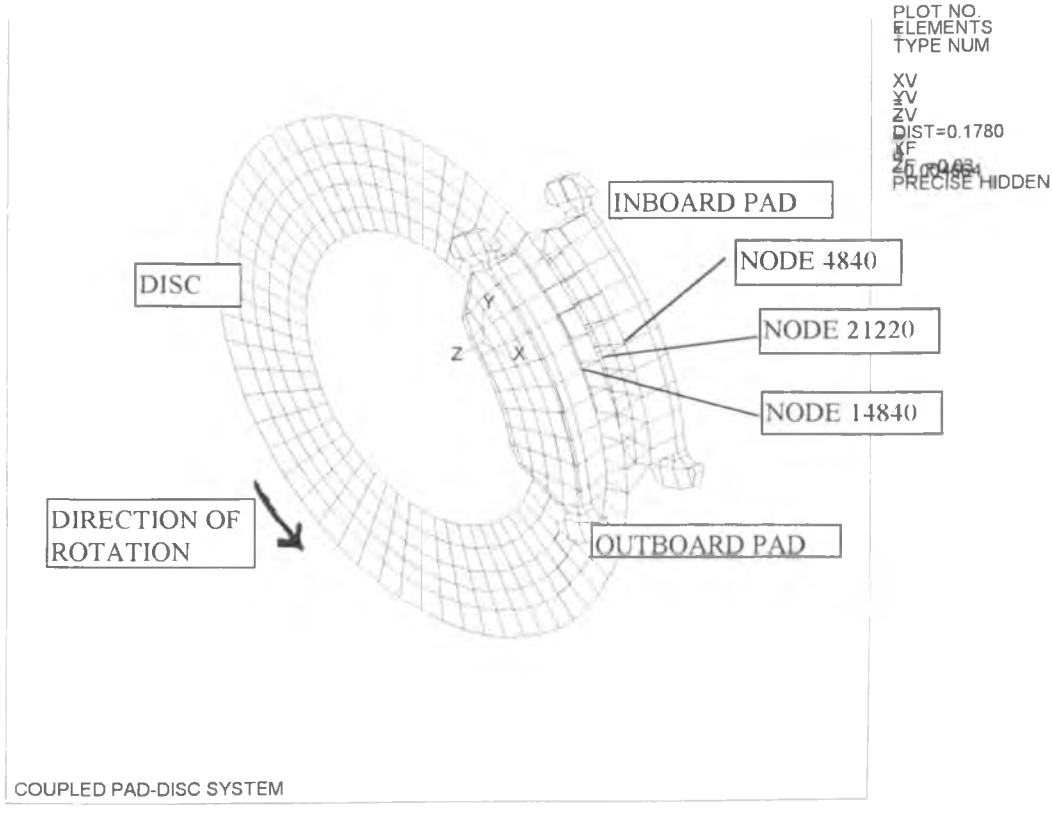

Figure 7.2 - The finite element model of the coupled pad-disc system.

In this study the parameters are varied independently so that the effect of each can be isolated. A full listing of the input data for the stability analysis can be found in Appendix II.

For each complex eigenvalue problem the solution takes over 60 hours on a standalone Apollo Domain Series 4500 computer. Using a Sun GPSB computer which is a general purpose server the solution takes about 6 - 12 hours depending on the number of users on the computer. It is therefore essential to reduce the problem size as discussed in Chapter Four.

7.2.1 Interpretation of complex eigenvalues

As the approach adopted in this chapter relies heavily on the evaluation of complex eigenvalues, their meaning is explained here based on the work of Newland [82]. For the i-th eigenvalue the complex eigenvalue s_i is written as

$$s_i = \sigma_i + j\omega_i \tag{7.1}$$

In control literature the complex eigenvalues are plotted on the complex number plane (commonly known as the s-plane) as shown in figure 7.3. For an eigenvalues which is complex , s its complex conjugate , $s_i^* = \sigma_i - j\omega_i$ must also exist. For these eigenvalues there will be a corresponding pair of complex conjugate eigenvectors , U_i and U_i^*.

In stability assessment it is the real part of the eigenvalue which is of importance. Thus for complex eigenvalues all the necessary information relating to the stability of the system is adequately represented by the first and second quarters of the s-plane with unstable modes lying in the first quarter and stable modes lying in the second quarter.

The displacement response for free vibration in any mode can be written as

$$u(t) = c_1 e^{s_i} U_1 + c_1^* e^{s_i^*} U_1^* \tag{7.3}$$

where c_1 and c_i^* are arbitrary constants. By selecting $c_1 = c_i^* = 1$ then ,

$$u(t) = e^{s_1} U_1 + e^{s_i^*} U_i^* \tag{7.4}$$

The displacement response for a mode with complex eigenvalues is the combination of the separate responses of the two eigenvectors (the complex eigenvector and its conjugate). Thus for an eigenvalue of $s = \sigma + j\omega$ and its complex conjugate of $s = \sigma - j\omega$ the displacement response can be rewritten as:

$$u(t) = e^{\sigma t}(e^{i\omega t} U + e^{-i\omega t} U^*) \tag{7.5}$$

Using the Argand diagram , the contribution from each eigenvector to the mode shape can be represented by two counter-rotating vectors of increasing magnitude (for an unstable mode as the real part σ is positive) as shown in figure 7.4. The sign of the imaginary part will determine the direction of rotation of the vector , positive is counter-clockwise and negative is clockwise.

The response u(t) is the addition of these two complex quantities which rotate in opposite directions at angular rate ω multiplied by the increasing exponential $e^{\sigma t}$.These rotating complex quantities are sometimes described as phasors and the addition of the two phasors is twice the projection onto the real axis of either of them. Therefore the displacement response for each mode can be written as :

$$u(t) = 2e^{\sigma t}|U|\cos(\omega t + \phi) \tag{7.6}$$

where the phase angle ϕ is given by:

$$\tan \phi = \mathrm{Im}\{U\}/\mathrm{Re}\{U\} \tag{7.7}$$

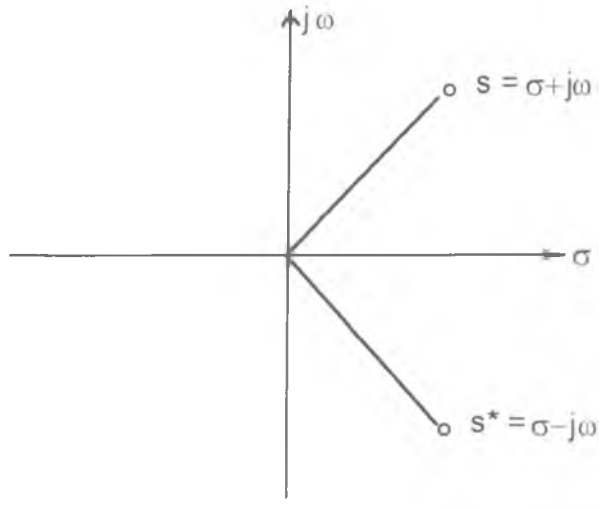

Figure 7.3 - Complex eigenvalue and its conjugate on the s-plane

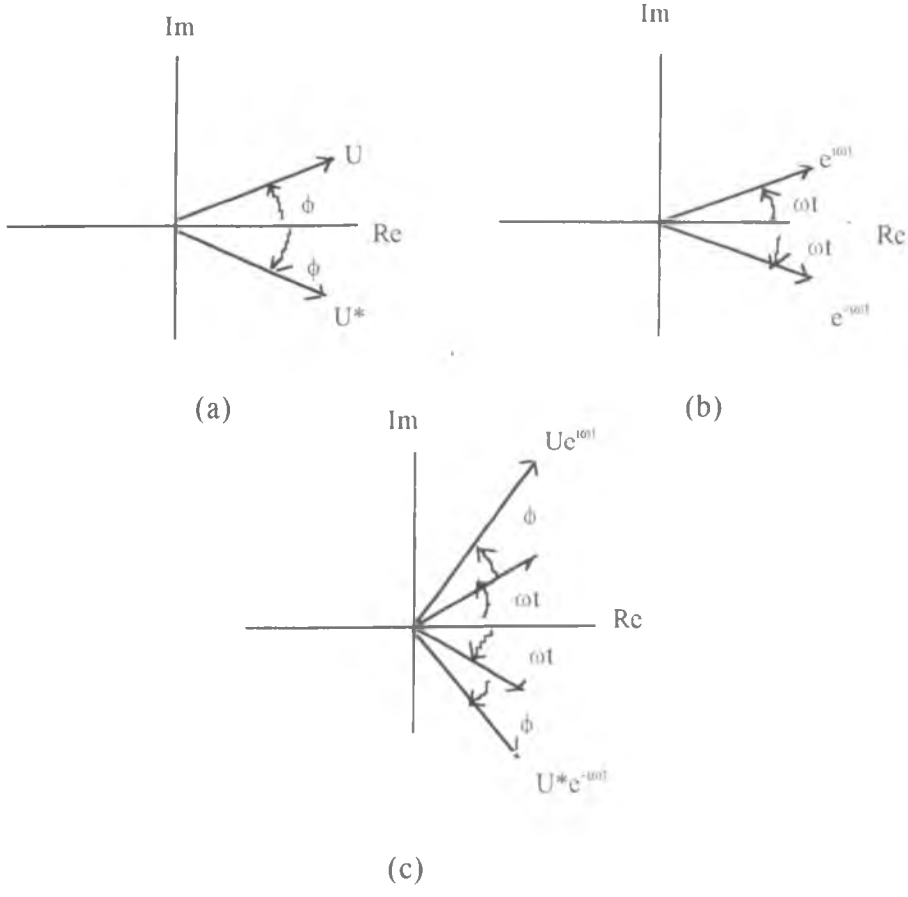

Figure 7.4 - Argand diagram for (a) complex-conjugate eigenvector pair (b)counter rotating phasors of unit length (c) the results of multiplying complex quantites in (a) and (b) [82]

From equations (7.6) and (7.7) , it is no longer adequate to represent the mode shape for a complex mode with complex eigenvectors in a single mode shape diagram as for the free-free response in Chapter Four as the individual mode coordinates in general no longer moves in phase or out of phase together.The notion of fixed nodes and anti-nodes can no longer apply as there exists a non-zero phase relationship between the coordinates. The exception would be when the imaginary part of the eigenvector is very small compared to the real part thus making the phase difference calculated from equation 7.7 insignificant.

In order to interpret a complex mode shape , it is necessary to calculate the position of each point on the model over a cycle and present the mode shape as an evolution in time as it repeats itself over each cycle (although for an unstable mode the amplitude also grows with time). These changes over a cycle are not easily presented for a very large degree of freedom model as used in the present study. Therefore only the real parts of the eigenvectors are displayed (which is equivalent to the displaced shape of the mode when $\omega t = 2\pi , 4\pi..$ as per equation 7.6). However one particular unstable mode is selected and the evolution of the phase angle of its complex eigenvector between the coupled nodes of the finite element is studied as the mode moves in and out of the unstable region.

7.3 Results

7.3.1 Effect of contact stiffness , K_C

For the baseline condition defined above , the effect of contact stiffness is studied by changing the stiffness in steps of 50 MN/m between 50 and 600 MN/m and determining the complex eigenvalues for each case using the unsymmetric eigenvalue solver in ANSYS [8]. The results obtained indicate that lowest contact stiffness for instability is 100 MN/m. Therefore complex eigenvalues for this condition are shown in the s-plane plot of figure 7.5 from which it can be seen only one unstable mode (7.5 + 8917j) is evident. For the purpose of the following discussion this mode is

referred to as mode A. This unstable mode is paired with a stable mode of the same frequency (-7.5 + 8917j) as also observed in other published results [6,43].

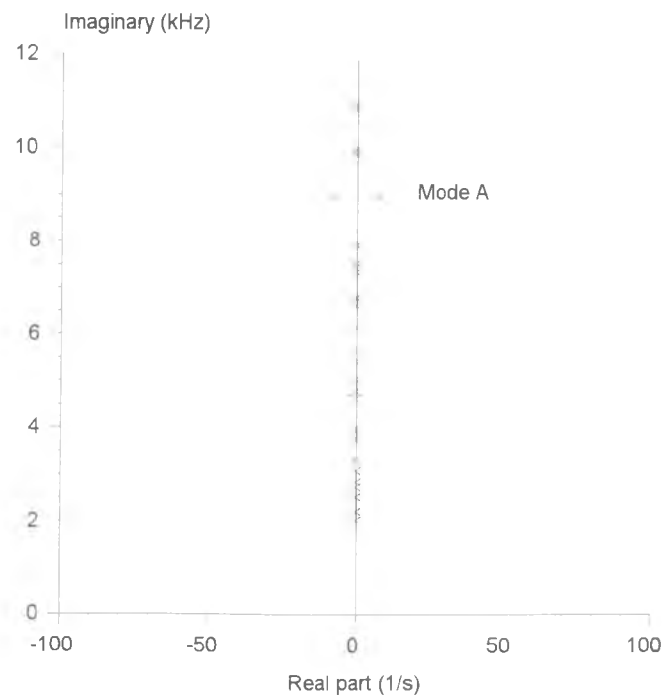

Figure 7.5 - Eigenvalue plot for contact stiffness of 100 MN/m

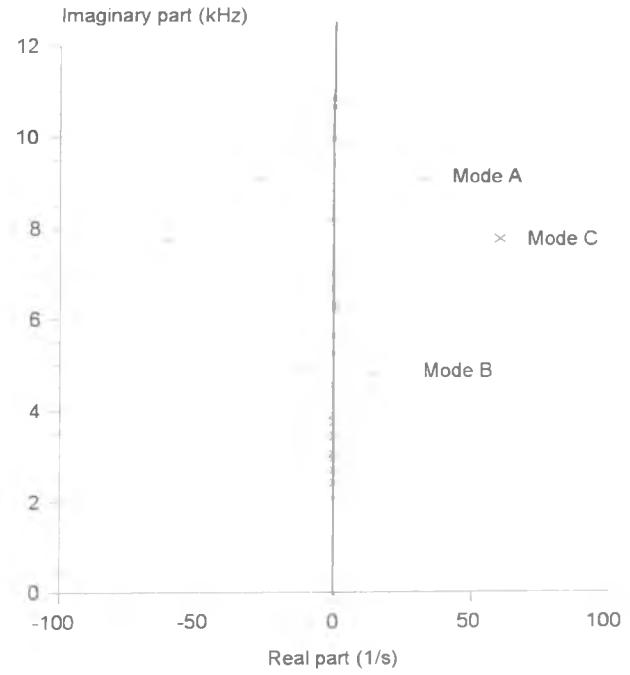

Figure 7.6a - Eigenvalues for contact stiffness of 150 MN/m

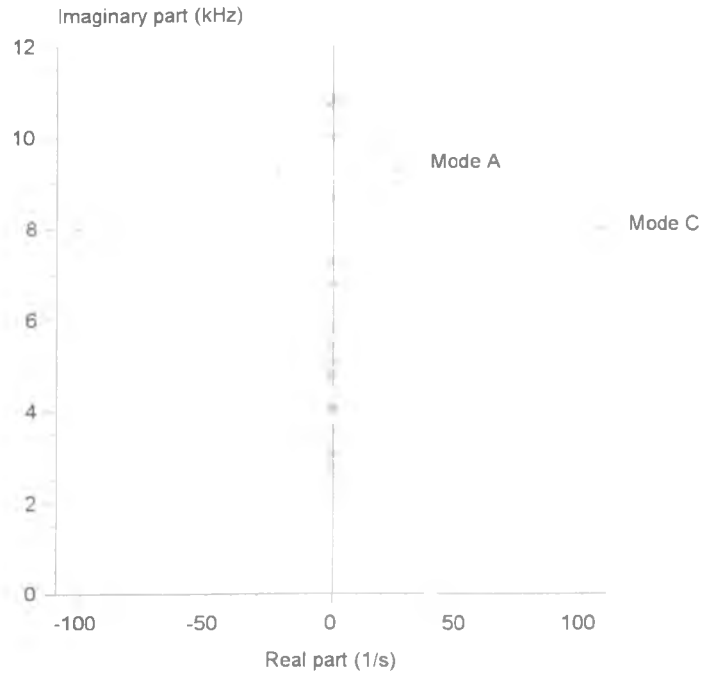

Figure 7.6b - Eigenvalues for contact stiffness of 200 MN/m

Increasing the contact stiffness to 150 MN/m causes two new unstable modes to emerge as shown in figure 7.6a. The first of these (termed mode B) has an eigenvalue of (13 + 4799j) and is also paired with a stable mode with eigenvalue of (14 + 4765j). The other new unstable mode has an eigenvalue of (60 + 7753j) and is termed mode C. This unstable mode is also paired with a stable mode with eigenvalue of (-60 + 7753j). The unstable mode A detected at K_C=100 MN/m as shown in figure 7.5 has now increased its real part and frequency to (32 + 9063j).

As the contact stiffness is further increased to 200 MN/m (figure 7.6b),unstable mode B which was unstable at contact stiffnesses of 100 and 150 MN/m has now become stable with eigenvalue of (0 + 4802j) compared with its stable pair at (0 + 4975j). For the remaining unstable modes , mode A has decrease its real part with an eigenvalue of (26 + 9241 j) and mode C has increased its real part with eigenvalue of (100 + 7954j).

The results indicate that for contact stiffnesses of 100 MN/m and above there are one or more unstable modes and that as the contact stiffness is increased the modes may become more or less unstable. By presenting the eigenvalues on an s-plot , all the eigenvalues associated with a particular value of contact stiffness can be observed. However the resulting figures are cluttered and it is not an efficient way to see the effect of contact stiffness on the overall stability of the system. What is important is to isolate each unstable mode and study its development with changes in the contact stiffness.

Therefore, in order to more efficiently track the effect of contact stiffness on instability , the evolution of both the real part and imaginary part of the complex eigenvalues for each unstable mode is studied. It is also necessary at the same time to consider the stable mode which occurs at the same frequency in order to study any specific behaviour resulting from the evolution of the mode pair with contact stiffness. Therefore for each unstable mode, the frequency and real part of the unstable eigenvalue and the frequency of its stable pair are plot against contact stiffness on the same graph as shown in figure 7.7. Unstable mode B is omitted from this exercise as it

occurs only for one contact stiffness value of 150 MN/m and is also considered less important as the real part is relatively small.

The results in figure 7.7 show that throughout the contact stiffness range studied there are five significant unstable modes occuring at different frequencies (shown as solid lines) and over different ranges of contact stiffness. These modes are marked A,C,D,E and F respectively. It is important to note that in each case the real part (shown as dashed lines) becomes positive as two modes of different frequencies converge ; also that the real part develops until it reaches a maximum and then reduces back to zero as the frequencies of the modes again diverge. This type of behaviour is typical of complex eigenvalue instability analysis [45].

Mode A has an unstable frequency range of 8917 - 9236 Hz. This frequency range lies between the frequencies of the 7th diametral (8708 Hz) and 8th diametral (11225 Hz) modes of the disc model under free-free conditions. Since frequency must increase as a result of contact (since the restraint stiffness increases) it is expected that the disc diametral mode order for mode A should be 7. This effect can be seen even at a low contact stiffness of 100 MN/m where the frequency is 8.92 kHz is 209 Hz higher (4.1% higher) than for the free-free condition. The displaced shape for mode A is shown in figure 7.10. from which the seventh diametral mode of the disc can indeed clearly be seen.

Mode C has an unstable frequency range of 7753 - 8301 Hz which lies between the frequencies of the 6th diametral mode (6578 Hz) and 7th diametral mode (8708 Hz) of the free-free disc. However the initial of unstable frequency of 7753 Hz is 1175 Hz higher (17.9% higher) than the 6th diametral mode frequency under free-free conditions. The frequency increase is too high to suggest that the diametral mode order of the disc is six. This aspect of the results for mode C is discussed in more detail in section 7.4.1

Mode D has an unstable frequency range of 6166 - 6316 Hz occuring between contact stiffnesses of 350 - 400 MN/m. The lower end of this unstable frequency is 412

Hz less (6.4% lower) than the sixth diametral mode of the disc under free-free conditions.

Mode E has an unstable frequency range of 6667 - 6736 Hz occuring between contact stiffnesses of 450 - 550 MN/m. The lower end of this unstable range is 89 Hz greater (1.4% higher) than the sixth diametral mode of the disc under free-free conditions.

Mode F becomes unstable at a contact stiffness of 400 MN/m with the real part reaching its maximum at a contact stiffness of 500 MN/m after which the mode becomes more stable with the real part reducing as contact stiffness is increased. The unstable frequency range of mode F is between 10151 - 10394 Hz. The minimum unstable frequency is 1741 Hz more (20.7% higher) than the seventh diametral mode under free-free conditions.

These results show that the unstable modes do not possess higher frequencies as contact stiffness is increased ; in other words a low contact stiffness does not restrict an unstable mode to be of low frequency (as shown by mode A) and indeed , even at relatively high values of contact stiffness , modes of relatively low frequency still exist (as shown by mode D and E).

From figure 7.7 , the contact stiffness ranges over which particular modes become unstable are different and in some cases overlap (for example modes C and D). This indicates that for a particular value of contact stiffness several unstable modes may occur. The magnitude of the real part as discussed in Section 7.2.1 above does not predict the relative amplitude (or strength) of each mode ; it only reveals how fast the mode is growing and is thus only a relative measure of squeal propensity in the sense that a mode with large real part is more likely to manifest itself as squeal. From Table 7.1 which compares the maximum real part which occurs throughout the contact stiffness range, mode C has the highest maximum real part followed by mode F. Interestingly these modes occur over different ranges of contact stiffness , mode C at the lower range and mode F at the higher end.

Table 7.1- Contact stiffness and frequency range of the unstable modes (K_S=24 MN/m)

Mode	Contact Stiffness range (MN/m)	Frequency range (Hz)	Maximum real part (1/s)
A	100 - 250	8917 - 9236	32.1
B	150	4799	13
C	150 - 350	7753 - 8301	107
D	350 - 400	6166 - 6316	88.5
E	450 - 550	6667 - 6736	64.3
F	400 - 600	10151 - 10394	101

7.3.2 Effect of support stiffness , K_S

The contacts between the pad backplate and the piston or paw are modelled as stiff springs of total stiffness K_S connecting to ground those nodes on the pad backplate to which point forces are applied to model the piston or paw applied force as defined in Chapter Five (figures 5.3 a-b). Results of the stability analysis for the baseline values of support stiffness K_S=24 MN/m are discussed in section 7.3.1 above. The complex eigenvalue analysis is now repeated for two alternative values of support stiffness:

i) K_S = 2.4 MN/m

ii) K_S = 240 MN/m

The stability analysis was again carried out over a contact stiffness range of 50 - 600 MN/m in each case.

The results for a support stiffness of 2.4 MN/m presented in figure 7.8 indicate three unstable modes within the range of contact stiffness and frequency studied. The first unstable mode (labelled A) first appears at a contact stiffness of 125 MN/m with frequency of 8977 Hz and dies out at a contact stiffness of 250 MN/m with frequency of 9394 Hz. The second unstable mode (labelled C) occurs at a contact

stiffness of 200 MN/m and frequency of 7833 Hz and persists upto the maximum contact stiffness modelled. The third unstable mode (labelled F) occurs at a contact stiffness of 350 MN/m with frequency of 10053 Hz and also continues upto the end of the contact stiffness range studied. The contact stiffness range for the first unstable mode (mode A) is quite narrow compared to the other two. Furthermore the appearance of these unstable modes level as the contact stiffness is increased is not in the same order as their respective frequencies. In each case (as before), the instability is signalled by the convergence of two different modes initially at different frequencies whereupon the real part of one mode becomes positive whilst stability is achieved when the frequencies of the two modes diverge.

The results shown in figure 7.7 for a support stiffness of Ks=24 MN/m are revisited in order to discuss the support stiffness effect. Comparison of figure 7.7 and 7.8 shows that, a support stiffness is increased tenfold from initially 2.4 MN/m to 24 MN/m , two additional unstable modes appear (modes D and E). Furthermore mode C which initially covered a wide range of contact stiffness 175 - 600 MN/m (figure 7.8) has now been reduced to a range of 150 - 350 MN/m (figure 7.7). More importantly the critical value of contact stiffness at which the modes converge has been shifted to a lower value. Mode F which first becomes unstable at contact stiffness of 350 MN/m in figure 7.8 now begins at a contact stiffness of 400 MN/m (figure 7.7).

When the support stiffness is further increased to K_S = 240 MN/m , a very different trend to figure 7.7 and 7.8 is seen as shown in figure 7.9. There are now only two unstable modes which occur near the extreme ends of the frequency range. The first unstable mode (mode G) occurs within a contact stiffness range of 200 - 250 MN/m with a frequency range of 3500 -3600 Hz whilst the second (mode F) occurs within a contact stiffness range of 400 - 600 MN/m with a frequency range of 9262 - 9496 Hz. Compared to the two other values of support stifffness , the real part in this case is much reduced (40.0 maximum) and the unstable modes A,B,C,D and E occuring for K_S=24 MN/m have now disappeared.

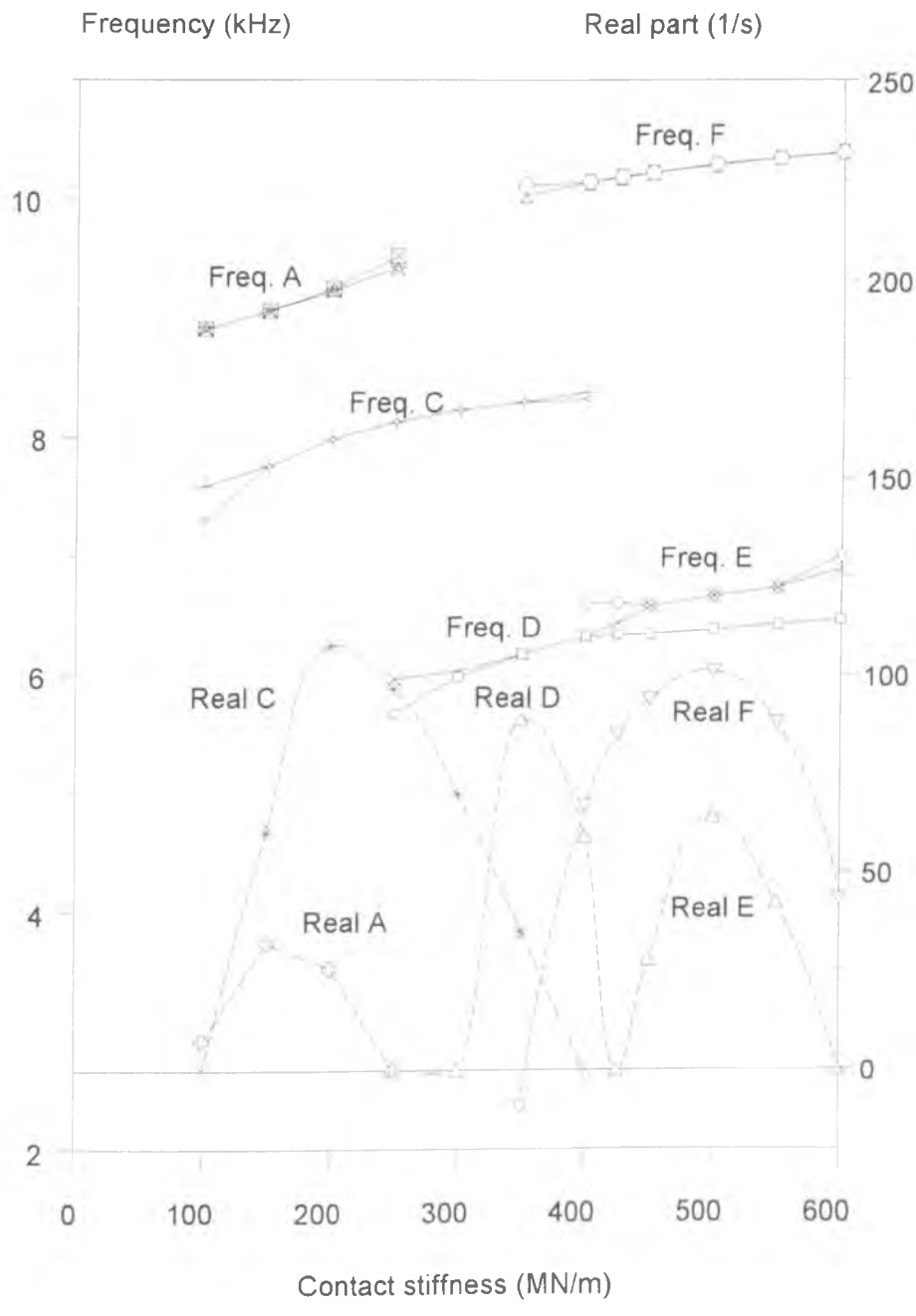

Figure 7.7 - The evolution of the frequency and real part of unstable modes (baseline condition , support stiffness K_S= 24 MN/m)

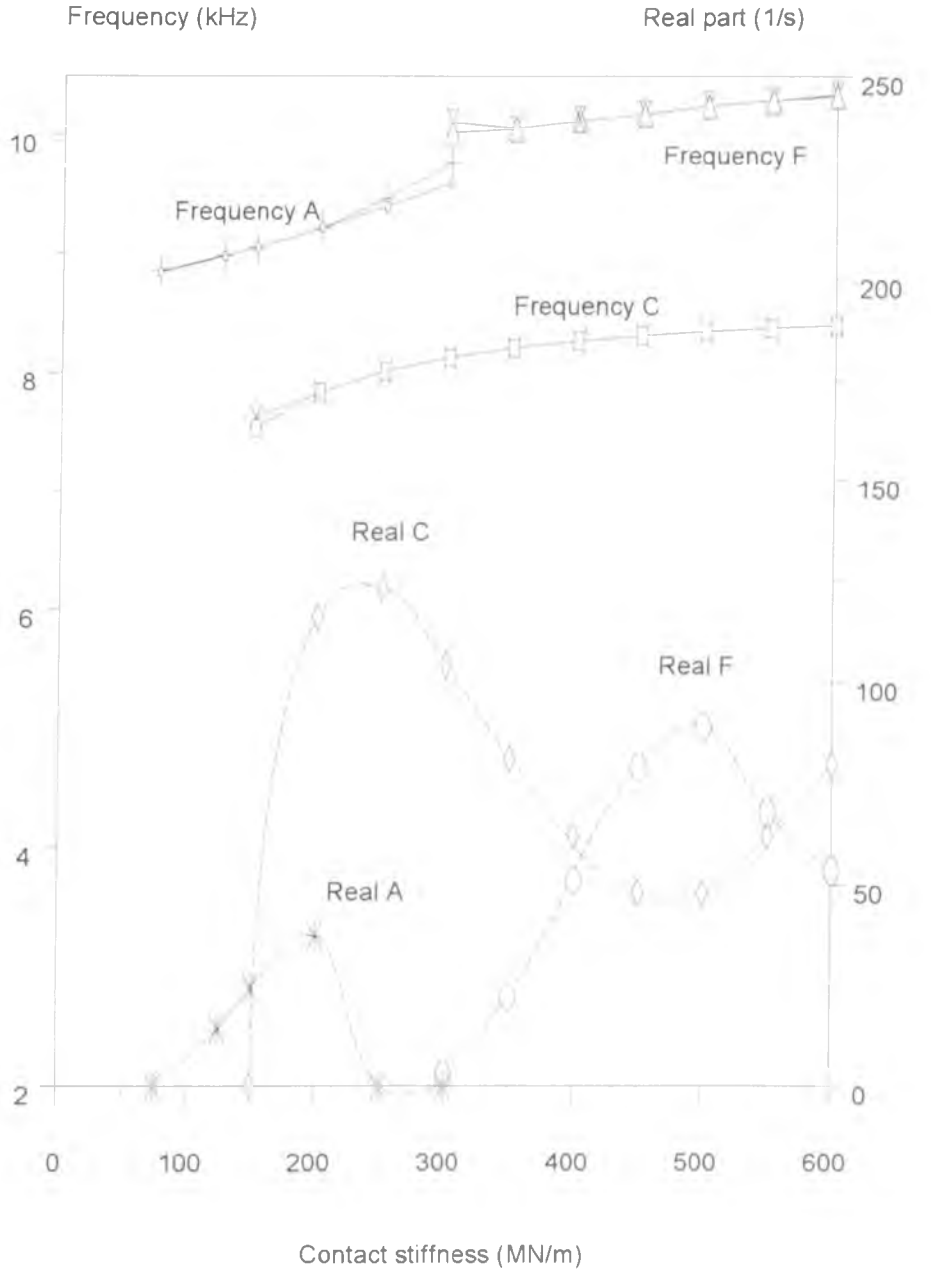

Figure 7.8 - Unstable modes evolution with contact stiffness (support stiffness K_s= 2.4 MN/m)

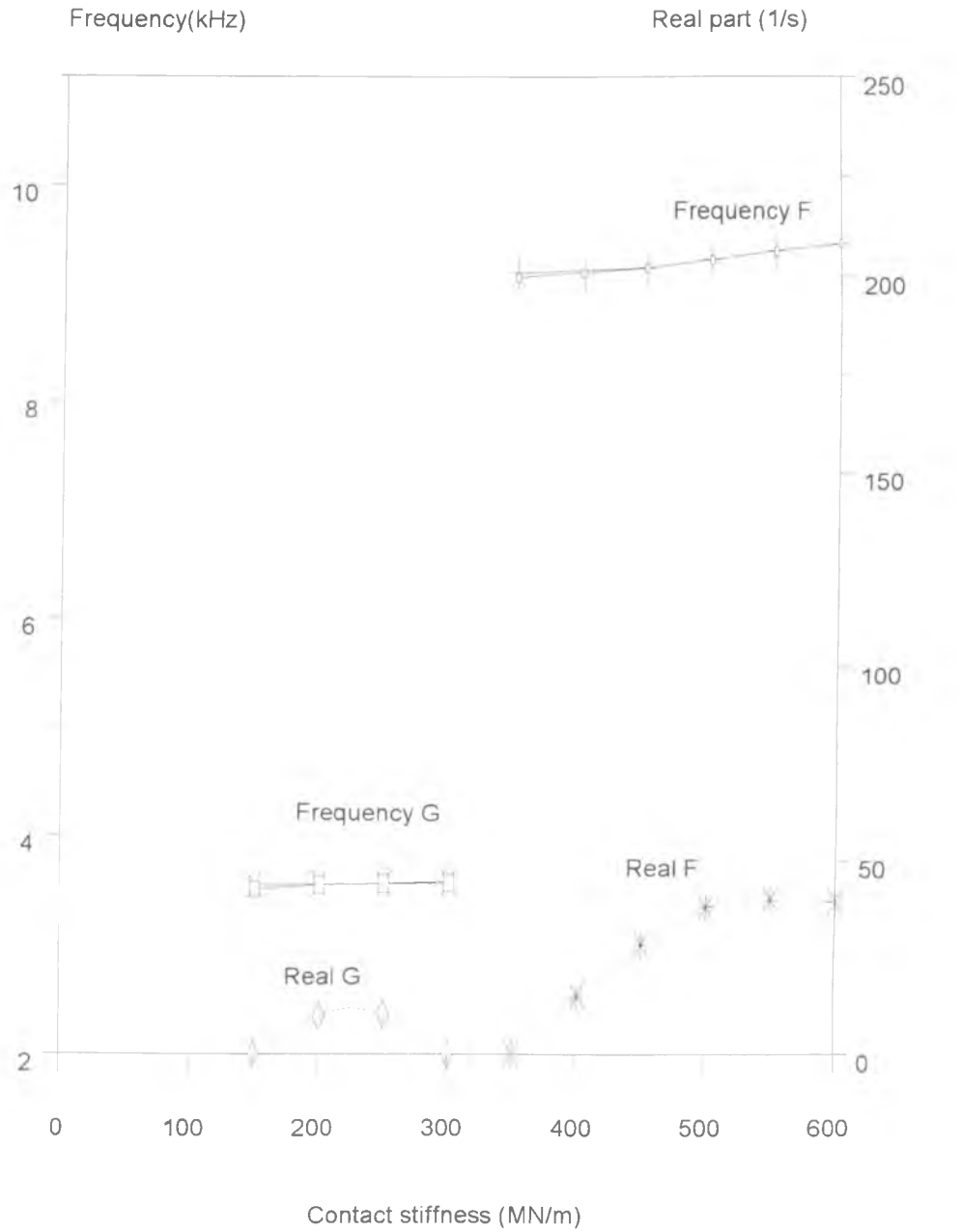

Figure 7.9 - Evolution of unstable modes with contact stiffness (support stiffness K_s =240 MN/m)

7.3.3 Mode shapes

The unstable modes discussed in Section 7.3.1 and 7.3.2 above were only labelled in alphabetical order to allow for comparison and reference purposes. In this section the mode shape for each unstable mode is presented in figures 7.11 - 7.15 It must be stressed that, although the eigenvector from the analysis is complex, only the real part is shown in these figures. Therefore these can be said to represent the mode shape when $\omega t = 2\pi , 4\pi , 6\pi...$ (as per equation 7.6). For comparison the undisplaced shape of the model and the relative positions of the components are shown in figure 7.2.

Mode A (figure 7.10) involves the disc undergoing displacements similar to those of the 7th diametral mode. The inboard pad (operated on by the piston) is moving in a 'bent ears' mode whilst the outboard pad (pressed by the paw) is in its second twisting mode.

Mode B (figure 7.11) involves the disc undergoing its fifth diametral mode even though the displacements are not very pronouced relative to those of the pad. The inboard and outboard pads both undergo their second bending mode of deformation.

The mode shape of the disc in mode C (figure 7.12) is discussed in more detail in section 7.4 below. The inboard pad clearly undergoes the third bending mode whilst the outboard pad undergoes a combination of bending at the leading end and twisting at the trailing end.

Mode D (figure 7.13) involves the disc moving in the sixth diametral mode. The inboard pad appears undeformed with only the leading ear undergoing bending. The outboard pad clearly experiences the first twisting mode Mode E (figure 7.14) which is a progression of mode D as the contact stiffness increases also has the disc deforming in the sixth diametral mode. The inboard pad, which for mode D is relatively immotive, now experiences deformation of the trailing ear. The outboard pad is no longer twisting but possesses an almost similar mode shape to that of the inboard pad

In mode F (figure 7.15) the disc undergoes the seventh diametral mode. The inboard pad does not experience significant deformation whilst the outboard pad is clearly undergoing the second twisting mode.

Mode G which occurs only for a very high value of support stiffness (K_S= 240 MN/m) and with a narrow range of contact stiffness and relatively low maximum real part of 15 is not considered important and is therefore omitted from discussion.

All the unstable modes described above involve diametral deformation of the disc. In all cases it is the outboard pad which has a more pronounced displaced shape compared to that of the inboard pad. In addition the mode of deformation of the outboard pad is different from that of the inboard pad except for mode B. This can be attributed to the way the support stiffness is distributed at the backplate and the resulting contact stiffness distribution at the pad-disc interface.

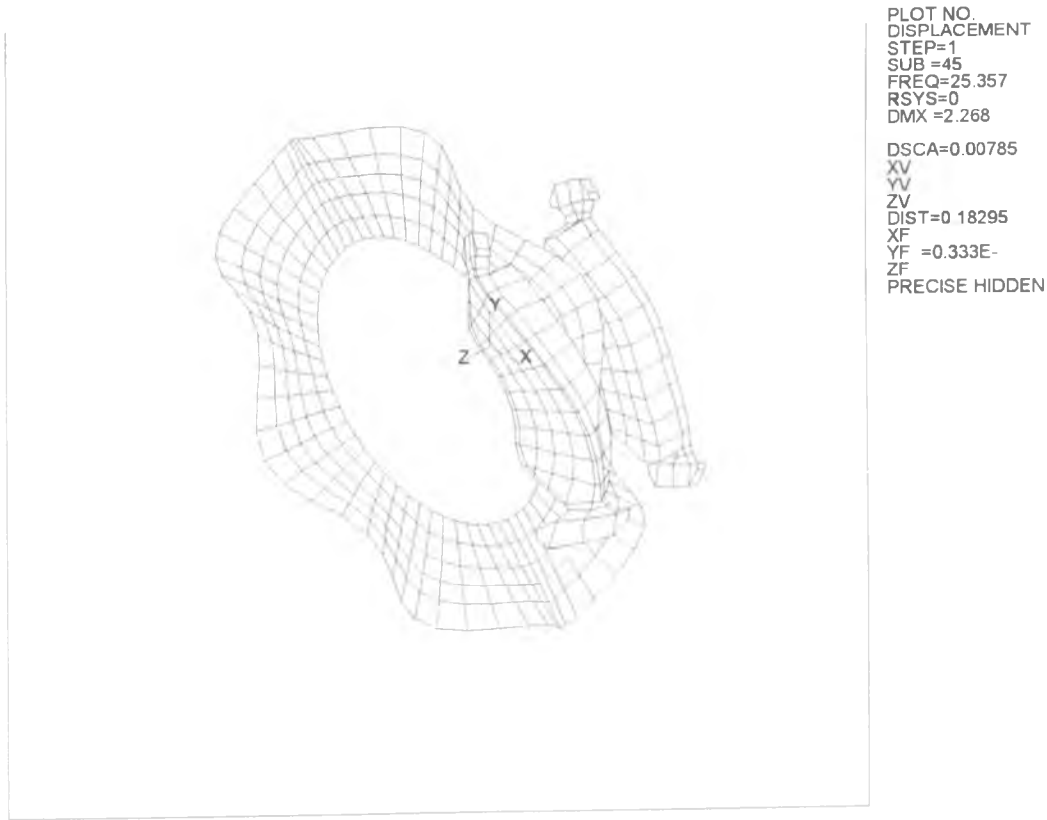

Figure 7.10 - Mode shape for unstable mode A (K_C = 150 MN/m , K_S = 24 MN/m)

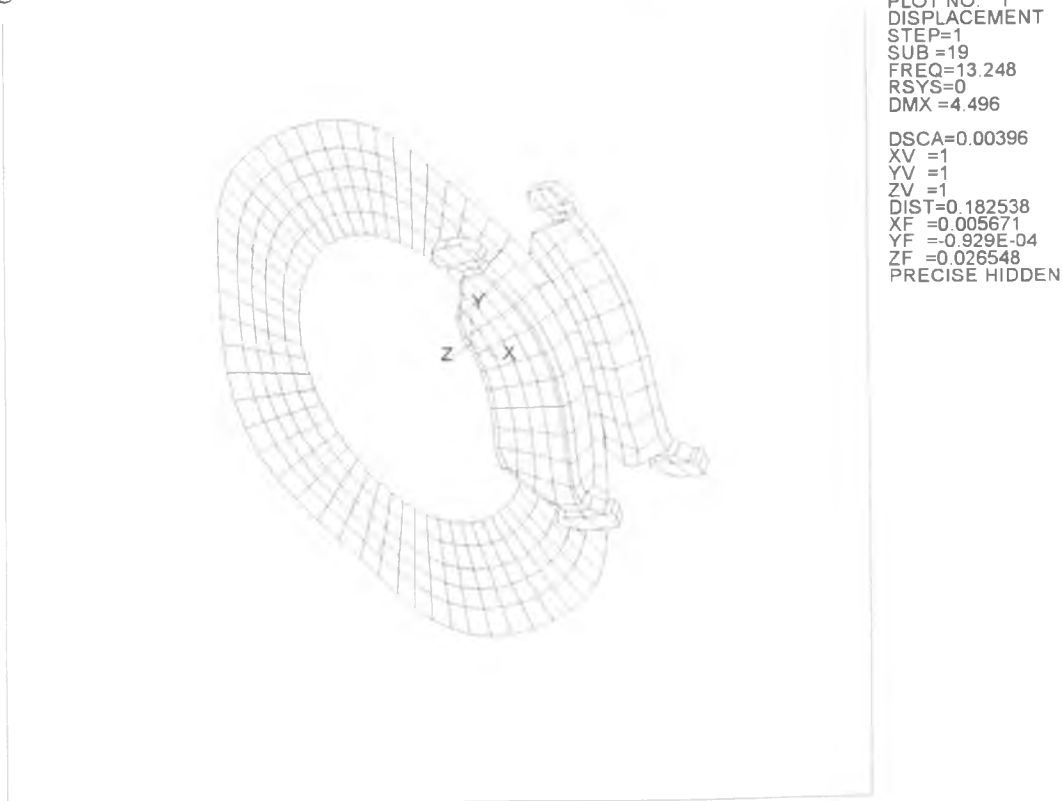

Figure 7.11 - Mode shape for unstable mode B (K_C = 150 MN/m , K_S = 24 MN/m)

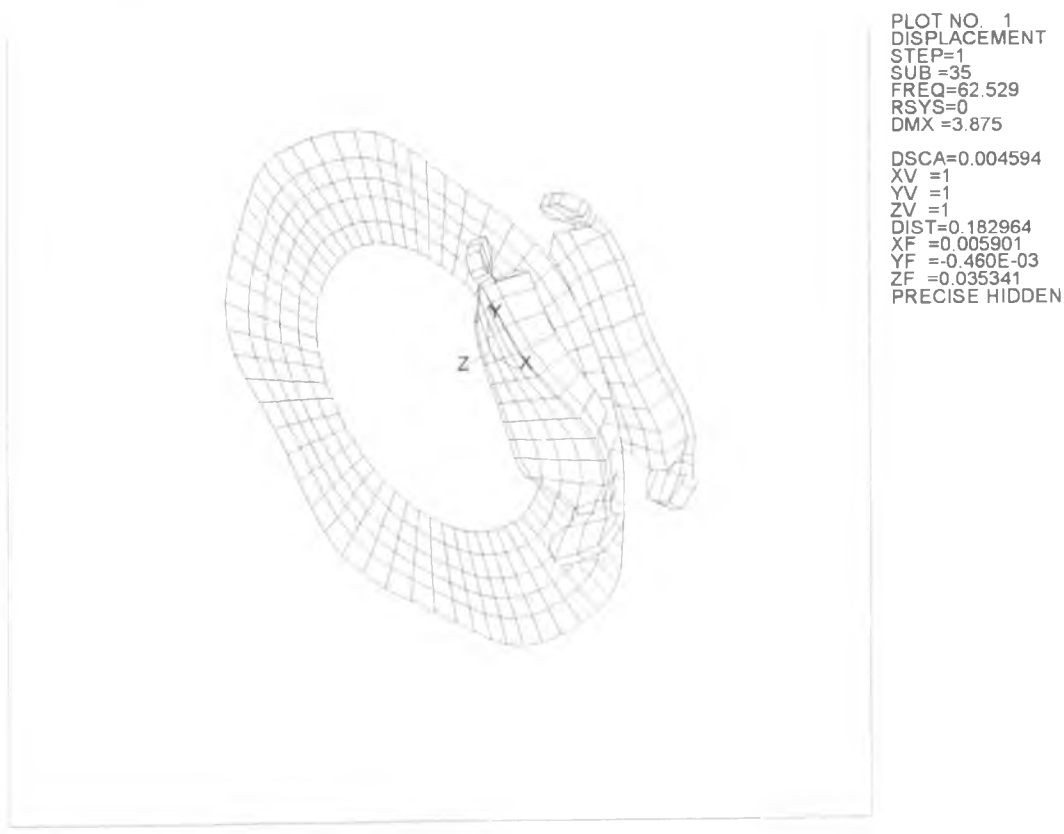

Figure 7.12 - Mode shape for unstable mode C (K_C = 150 MN/m , K_S = 24 MN/m)

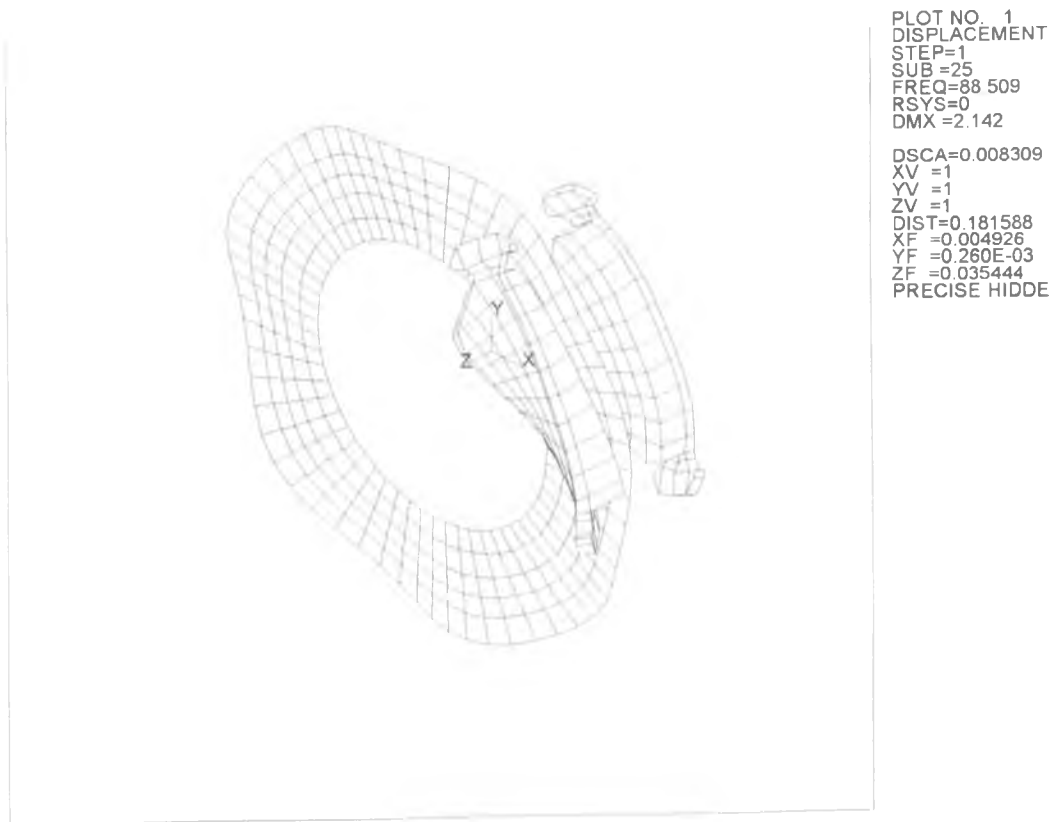

Figure 7.13 - Mode shape for unstable mode D (K_C = 350 MN/m , K_S = 24 MN/m)

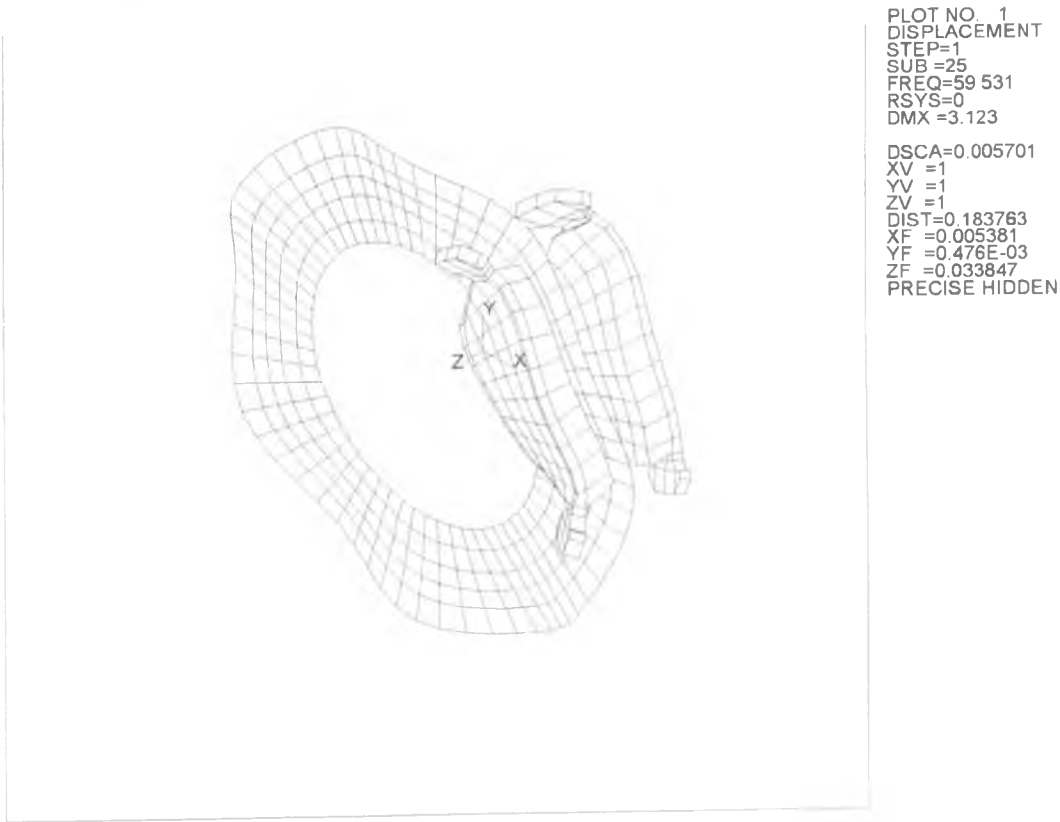

Figure 7.14 - Mode shape for unstable mode E (K_C = 500 MN/m , K_S = 24 MN/m)

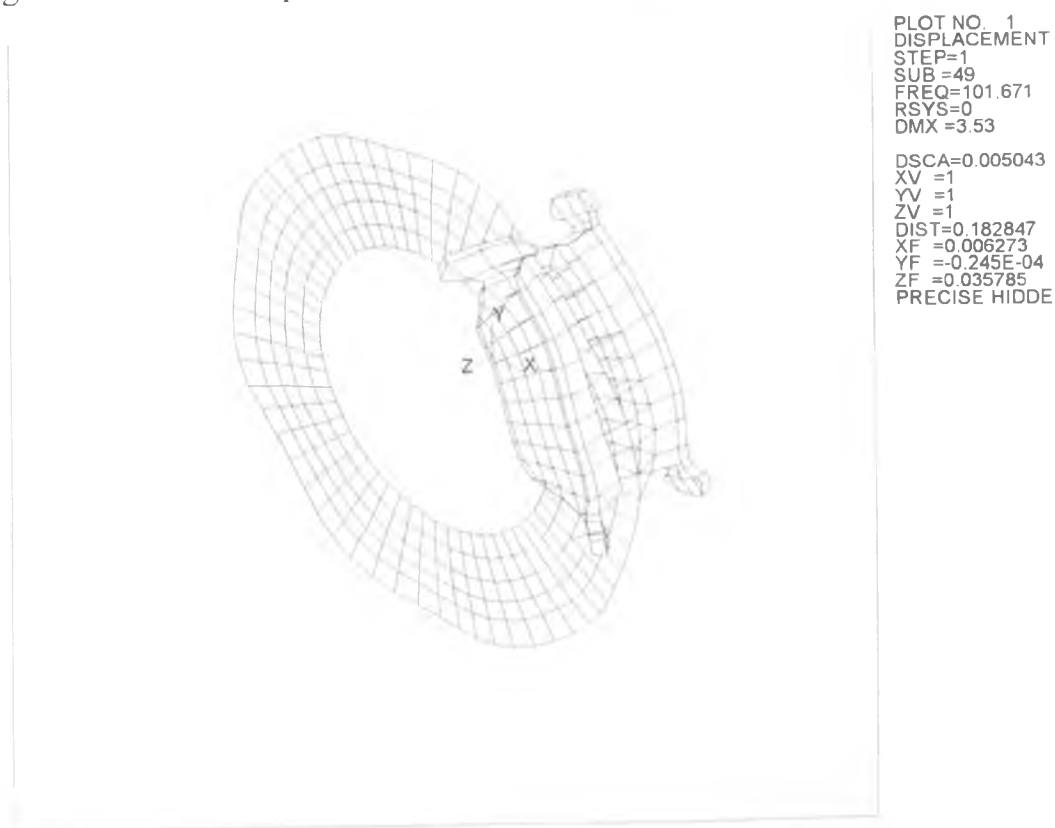

Figure 7.15 - Mode shape for unstable mode F (K_C =500 MN/m , K_S = 24 MN/m)

7.3.4 Variation of phase angle with contact stiffness.

It is of interest to investigate the evolution of the phase difference between the normal displacements at the interface between the principal components (the disc and the pads) as a function of contact stiffness. Unstable mode C (for K_c= 100 - 425 MN/m and K_S= 24 MN/m as in figure 7.7) was selected for this study. It is not feasible to compare all the coupled nodes at the interface at once and therefore a representative node is selected for each component: one node located on the centre of the outer circumference on the friction face of each of the outboard (node 14480) and inboard pads (node 4480) as well as the adjacent node on the disc (node 21220) as shown in figure 7.2. These nodes are selected as they lie on the pad centreline plane and in any diametral mode of the disc it is the outermost node (i.e. at the disc circumference) which undergoes maximum displacement. Within the formulation of the interface element it is the interaction between the nodes on the pad and the disc represented by their normal (axial) displacements which generates the contact force as indicated in figure 7.1. Therefore the phase angle of the normal displacement at each node selected was calculated using equation 7.7 and the results together with the components of the complex eigenvectors for these displacements are listed in Table 7.2. It can be seen that the phase difference is effectively zero for the stable condition (i.e. K_c = 100 MN/m and K_c = 425 MN/m). In all other cases the phase angles are not zero. The phase differences between the normal displacements of the pad nodes and that of the disc together with the real part of the unstable mode eigenvalue are plotted against contact stiffness in figure 7.16.

The results in figure 7.16 show that the phase difference for both the inboard pad-disc and outboard pad-disc normal displacements follow closely the trend of the real part of the eigenvalue. The maximum real part coincides with the phase difference value closest to 180 degrees and the real part becomes zero as the phase difference also tends to zero. This aspect can be explained by considering the interface element matrix used to couple the nodes for which maximum variation of normal force implies a phase difference of 180 degrees between the normal displacements of the node pair. Thus the maximum real part of the unstable mode C coincides with the maximum

phase difference between the pads and disc as the pads effectively 'hammer' the disc. It is expected that this same relationship between phase difference and positive real part would apply to other modes. It is also interesting to note that the inboard pad leads the outboard pad by 43 degrees within the unstable range of contact stiffness and the phase difference remains relatively constant at about 43 degrees ($\approx \pi/4$ radian) except when K_C = 350 MN/m where the phase difference between the outboard pad and the inboard pad is 33.44 degrees. This imply that the inboard pad hammers the disc first followed by the outboard pad thus allowing for energy transfer between the pads and the disc.

Table 7.2 - The components of the eigenvector and phase angle of the selected normal displacements for different values of contact stiffness

Contact stiffness K_C (MN/m)		Inboard pad node	Disc node	Outboard pad node
100	Eigenvector (Re) (Im) Phase angle , ϕ	1.6137 + 0.3462E-4j 0.00°	-0.5233 - 0.9428E-4j 0.01°	0.2008 + 0.6917E-4j 0.02°
150	Eigenvector (Re) (Im) Phase angle , ϕ	0.5597 - 0.6530j 310.60°	-0.0293 + 0.2856j 95.87°	-0.0299 - 0.2351j 277.24°
200	Eigenvector (Re) (Im) Phase angle , ϕ	-0.0494 - 0.7270j 224.03°	0.1583 + 0.2045j 52.26°	-0.3667 - 0.3545j 266.11°
250	Eigenvector (Re) (Im) Phase angle , ϕ	0.3326 + 0.4431j 53.11°	-0.1136 - 0.0115j 185.79°	0.5501 + 0.1016j 10.46°
300	Eigenvector (Re) (Im) Phase angle , ϕ	0.2668 + 0.2958j 47.95°	-0.0275 + 0.0296j 132.92°	0.5784 + 0.0623j 6.14°
350	Eigenvector (Re) (Im) Phase angle , ϕ	0.2123 + 0.1546j 36.05°	0.0237 + 0.0440j 61.67°	0.5944 + 0.0273j 2.61°
425	Eigenvector (Re) (Im) Phase angle , ϕ	0.3152 - 0.2663E-4j 0.00°	0.1429 - 0.2868E-5j 0.00°	0.6801 - 0.5486E-5j 0.00°

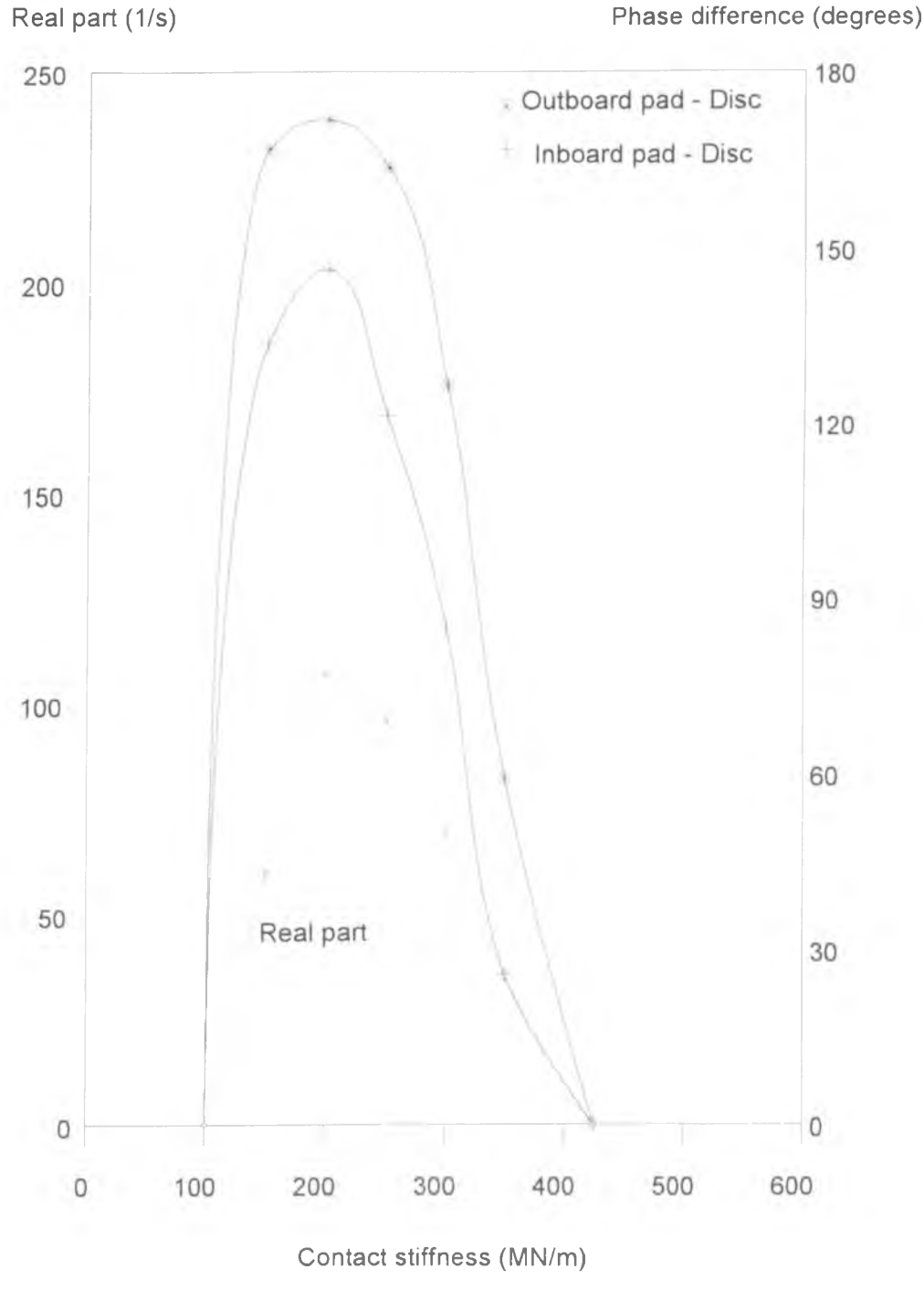

Figure 7.16 - The real part of the eigenvalue and the phase difference between normal dispalcements of the outboard and inboard pad nodes and the disc node for mode C (support stiffness $K_S = 24$ MN/m)

7.4 Discussion

The results from the complex eigenvalue analysis suggest that for different values of support stiffness there are different unstable modes. Instability occurs in each case as a result of two modes initially of different frequencies coming together to form an unstable mode (with a corresponding stable mode with real part of equal magnitude but negative sign) at a certain value of contact stiffness. This instability continues upto a higher value of contact stiffness whereupon the mode frequencies diverge resulting in both modes becoming stable again.

Beginning from a very low value of backplate support stiffness of 2.4 MN/m, there are initially three unstable modes which occur over a relatively wide range of contact stiffness. As the support stiffness is increased to K_S=24 MN/m one of these unstable mode vanishes but a new unstable mode appears and the two other unstable modes seen at K_S = 2.4 MN/m now occur over a narrower range of contact stiffness. As the support stiffness is further increased to K_S=240 MN/m, only one significant unstable mode from the previous condition remains but with very much reduced real part and lower frequency.

The effect of applied pressure on disc brake squeal problem can now be explained using the results from the analysis for both varying contact stiffness K_C and support stiffness K_S. In the contact stiffness determination discussed in Chapter Six , the effect of increasing applied pressure is to increase the contact stiffness linearly. Based on this result, an assumption can be made that the same trend applies to the pad backplate interface i.e. the support stiffness also increases linearly with the applied pressure (although the exact relationship is not determined). As the pressure is increased on the pad backplate , the contact stiffness increases causing some modes to converge to form unstable modes and this instability continues upto a certain value of stiffness when the modes diverge to become two separate stable modes. At the same time the support stiffness also increases with increasing applied pressure and this forces the unstable modes to occur within a narrower band of contact stiffness. This translates in practice to the range of applied pressure over which squeal occurs as shown by

Fieldhouse and Newcomb [10]. As the pressure increases further new unstable modes arise with the same convergence-divergence phenomenon. However the corresponding increase in the support stiffness finally suppresses these modes and squeal therefore dies out above a certain value of applied pressure. The stabilising effect of increased support stiffness also compares well with the experimental finding by Sherif et al [56] that increased support stiffness (achieved by using a steel ball pressing on the pad and also by having a grooved backplate) reduces squeal noise. It also compares well with the analytical work of Ghesquirre [46] whereby increasing the caliper normal stiffness (equivalent to the support stiffness of the model used in the present study) caused one of the modes to become stable.

For comparison with the experimental results the two modes with the highest maximum real part are selected from the analytical results for a support stiffness of 24 MN/m. It may be judged that these modes have the highest squeal propensity compared to the other modes and furthermore they occur over a wide range of contact stiffness and also a relatively wide range of support stiffness. The values of the contact stiffness used in the analysis is converted to equivalent line pressure according to the results of the interface contact stiffness calculation shown in figure 6.12 of Chapter Six. The unstable frequency range from the analysis for these two modes is compared with the squeal frequency range of the experiment [10] in figure 7.17

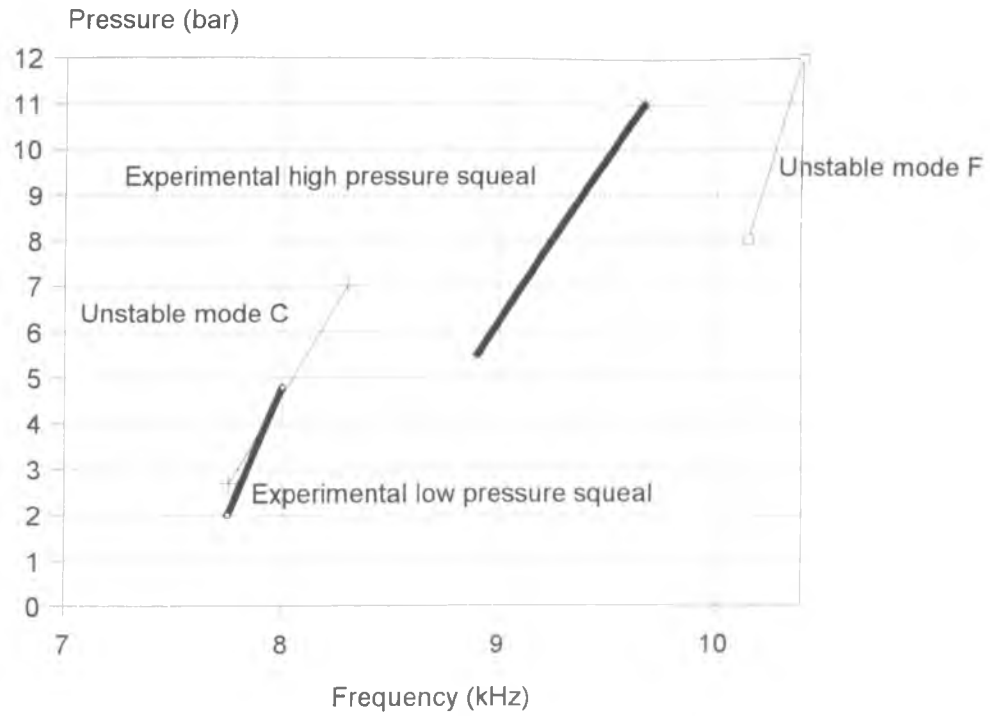

Figure 7.17 - The line pressure-frequency relationship for both experimental and analytical squeal modes

The results in figure 7.17 indicate that the first unstable frequency range from the analysis compares very well with the experiment whilst the second unstable frequency range from the analysis is somewhat higher. The discrepancy for the higher frequency range may be due to the fact that, as stated in Chapter Four, the pad finite element model under free-free condition compares well with experimental results only for frequencies below 8 kHz (figure 4.13). The discrepancy could also be reduced by increasing the support stiffness which would result in a lowering of the second unstable frequency range as shown by comparison of figure 7.9 and 7.7. Bearing in mind these observations, it is fair to conclude that the approach has been successful in predicting the correct range of line pressure and frequency over which squeal occurs.

In order to compare the predicted unstable mode shapes with experiment, only the most significant unstable modes are selected which as discussed above are modes C

and F. The unstable mode C is compared to the low pressure range from the experiment [10] whilst, for the high pressure range , unstable mode F is selected for comparison. The analytical unstable mode is displayed as an equal displacement contour plot which allows for direct comparison with the reconstructed holographic image from the experiment. It is important to note that the analysis does not directly model the caliper. On the other hand in the actual brake system the caliper forms an arc of 93 degrees covering the disc and therefore only the fringes outside the caliper arc can be revealed in the reconstructed holographic image. The results from the finite element analysis can however reveal the equal displacement contours under the pad which provides a distinct advantage in the analysis of the mode shape. In addition the construction of the actual brake system is such that the outboard pad is partially obscured by the caliper paw while the inboard pad is totally hidden. Therefore comparison of the pad mode shapes can only be made for the outboard pad (with the limitation mentioned above) whilst for the inboard pad only the analytical mode shape is available.

7.4.1 Low pressure range squeal

In order to allow for comparison of the mode shape from the analysis with experiment, the equal displacement contour plots of the disc and the pads from the analysis are shown separately in figures 7.19a-c in order to allow the contour plot of the disc under the pad to be displayed.

The disc mode shape from experiment (figure 7.18) is evidently diametral with a uniform node spacing outside the pad-disc contact area. A total of 11 antinodes and 10 nodes can be counted outside the caliper arc. Measurement between two successive nodes reveals an angle of 27 degrees. Similarly the mode shape from the analysis (figure 7.19a) reveals 11 nodes and 10 antinodes outside the 92 degrees arc representing the pad and caliper shown by the two bold lines in the figure Measuring the angle between the nodes outside the caliper arc again reveals an angle of 27 degrees. Thus the nodal spacings of the experimental and analytical modes outside the caliper arc are the same. If one assumes that the disc nodal spacing under the pad and

caliper remains similar to that elsewhere on the disc, this condition implies a diametral mode order of 6.67 (360°/(27°x 2)). In order for the disc mode shape to be purely of sixth diametral mode, the nodal spacing need to be 30 degrees (360°/12) and uniformly spaced both in and out of the contact area (for comparison free-free sixth diametral mode shape can be found figure 4.6e of Chapter Four). However the equal displacement plot (figure 7.19a) shows that there are 4 nodes and 3 antinodes under the pad with the angle between the nodes no longer uniform. At the leading edge the angle between the nodes is 32 degrees which is 5 degrees more than that between the nodes outside the caliper arc. Furthermore by closely inspecting the displacement contours there are 6 maxima (lines marked I) and 7 minima (6 lines marked A and a single line marked C) and 13 node clusters (lines marked E) around the disc circumference. The diametral mode order is defined by the (even) number of nodes (or antinodes) divided by two. This shows that the mode shape occuring under the coupled condition is not the sixth diametral mode of the disc and therefore cannot be detected in advance by natural frequency analysis of the free-free disc.

This conclusion provides an added explanation to the hypothesis of Fieldhouse and Newcomb [10] that the source of excitation for low pressure squeal is the pad rather than the disc due to the large difference in the natural frequency of the disc sixth diametral mode (6450 Hz) and the squeal frequency (7850 Hz). As the coupled diametral mode of the disc does not exist naturally, it must therefore be excited at this mode shape and frequency by interaction with the pad.

It is difficult to compare the predicted mode shape of the outboard pad with experiment as in the latter a large proportion of the pad is covered by the caliper paw The equal displacement contour plot on the outboard pad model (fig. 7.19b) shows a bending deformation of the trailing end indicated by the curved contours whilst the leading end is undergoing some form of twisting indicate by the horizontal contour lines. In the experiment , the pad trailing end also undergoes a relatively large bending deformation as shown by the closely spaced vertical (relative to the pad longest dimension) fringe lines whilst the leading end has two widely spaced vertical fringe lines indicating a relatively small bending displacement. The similarity of the mode

shapes for the pad therefore is limited to the trailing end of the pad as the leading end in the finite element analysis displays a twisting mode whilst in the experiment it undergoes a small degree of bending.

For the inboard pad no comparison can be made as the inboard pad is hidden in the experiment by the caliper housing. However the mode shape of the coupled system (figure 7.12) shows that the pad is only undergoing small displacements relative to the outboard pad. The finite element contour plot (figure 7.19c) indicates the inboard pad to have a displaced shape similar to that of the first bending mode.

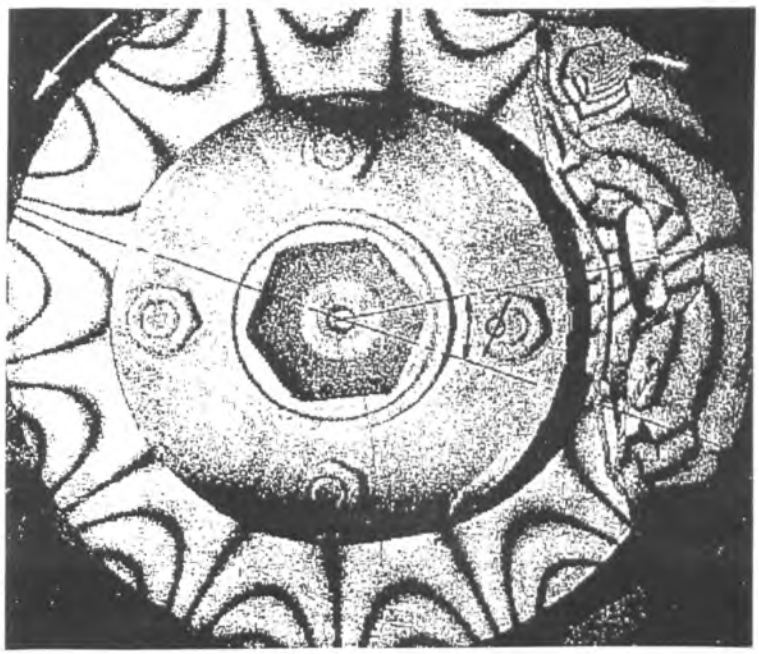

Figure 7.18 - Reconstructed holographic image for low pressure squeal mode [10]

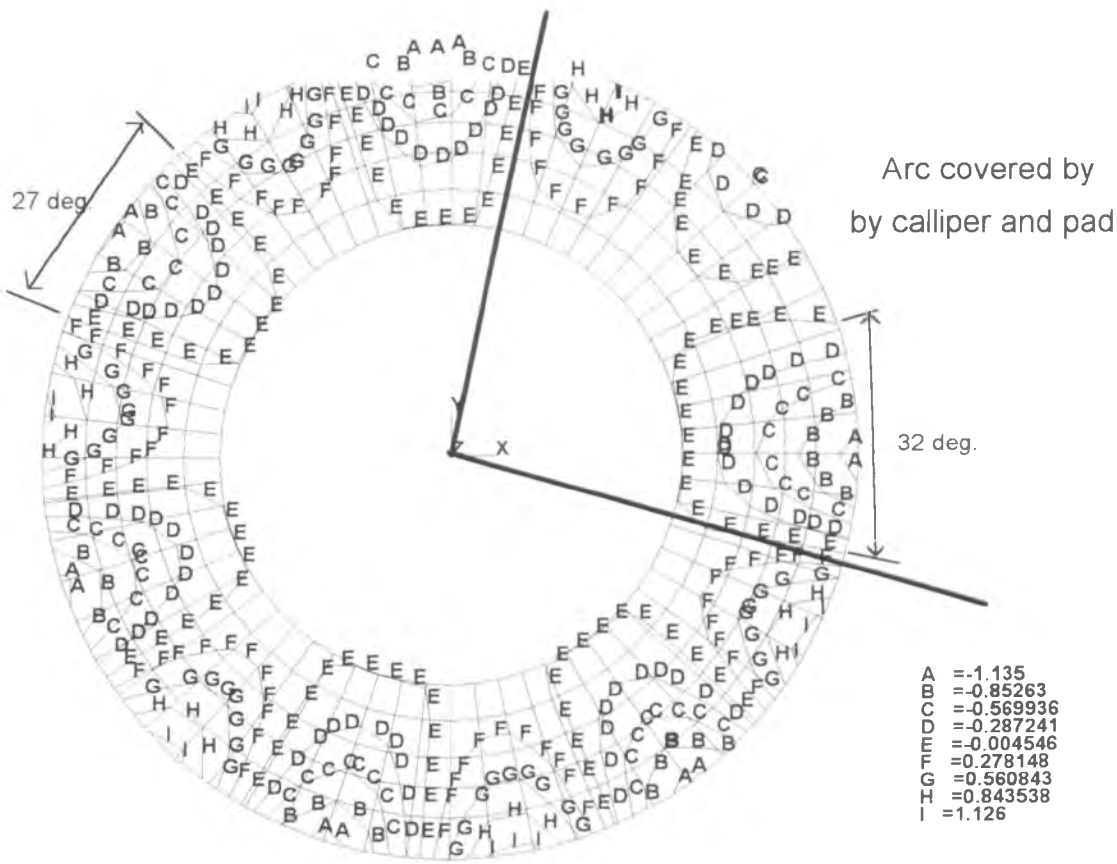

Figure 7.19a - Equal displacement contours on the disc for unstable mode C (K_C=150 MN/m , K_S = 24 MN/m)

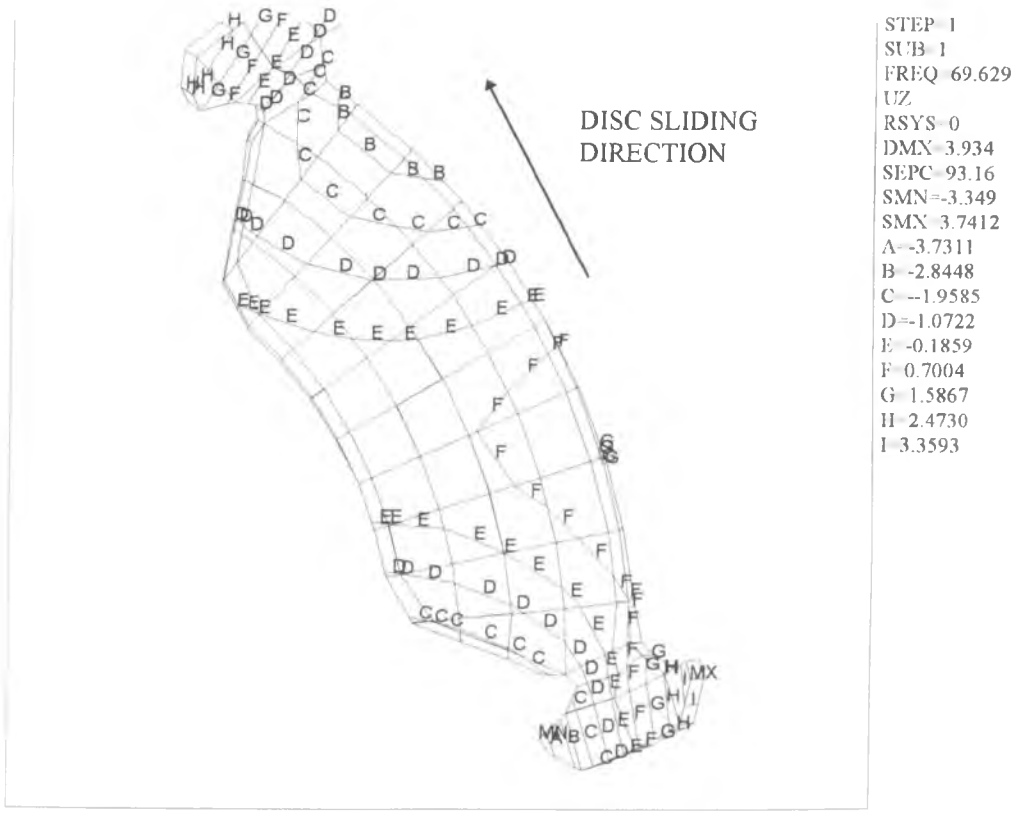

Figure 7.19b - Equal displacement contours on the outboard pad for unstable mode C (K_C=150 MN/m , K_S=24 MN/m)

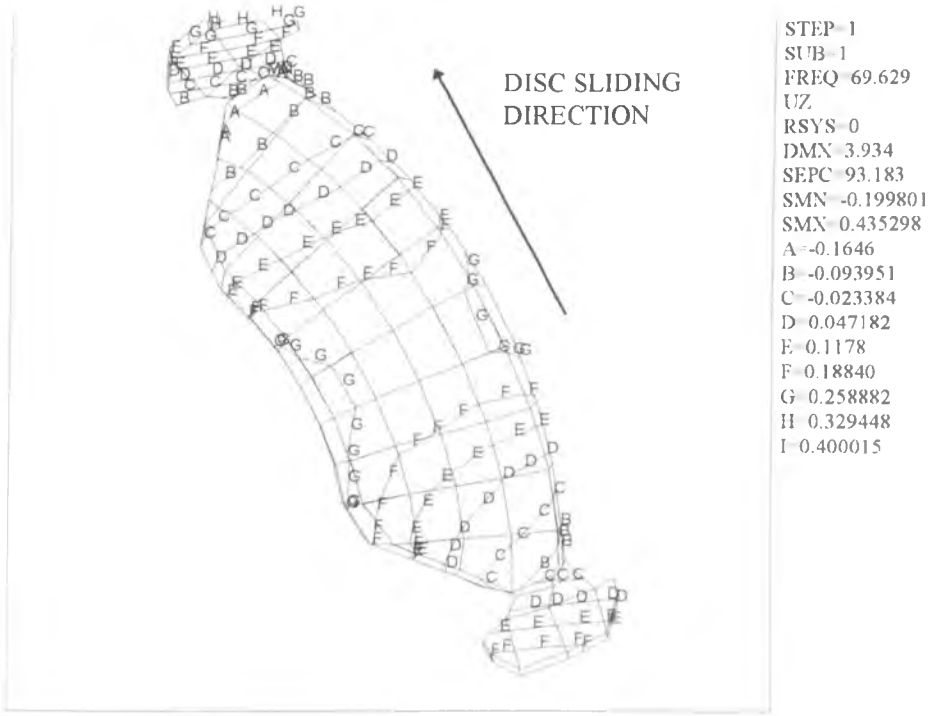

Figure 7.19c - Equal displacement contours on the inboard pad for unstable mode C (K_C=150 MN/m , K_S = 24 MN/m)

7.4.2 High pressure range squeal

The equal displacement contour plot from the analysis (figure 7.21a) shows that the disc has a total of 12 antinodes (lines marked A and H) and 11 nodes (lines marked E) outside the caliper arc with an average nodal angular spacing of 23 degrees. Inside the caliper arc, the contour lines are very much distorted with 2 antinodes and 3 nodes detected whilst the nodal spacing is much larger with 35 degrees between those under the leading edge part of the pad and 37 degrees between those nodes under the trailing edge. Since there are 14 nodes and 14 antinodes around the disc circumference in total the mode can be defined as the seventh diametral mode. The reconstructed holographic image of the disc brake during squeal in the high pressure range (figure 7.20) shows that outside the caliper arc there are a total of 11 nodes and 12 antinodes with an angular nodal spacings of 24 degrees. Therefore the nodal spacing of the disc from the analysis and experiment is very similar whilst the numbers of nodes and antinodes outside the caliper arc are identical.

The holographic image for the outboard pad (figure 7.20) is covered by the caliper and only the fringe lines on the ears can be clearly seen These reveal the pad ears at both leading and trailing edges to be undergoing twisting. Although the trailing ear has higher fringe density than the leading ear. The results from the analysis (figure 7.20c) also reveal the trailing pad ears to have a twisting deformation indicated by the one horizontal (relative to the pad longest dimension) contour line. The leading edge of the pad has similar horizontal contour lines but with higher density which indicates larger deformation as shown in the mode shape plot for mode F (figure 7.15). As both ends of the pad undergo twisting in the analysis and in the experiment in can confidently be stated that the outboard pad mode shape from the analysis compares well with experiment for the high pressure range.

The results from the analysis (figure 7.21c) show horizontal lines on the trailing edge of the inboard pad indicating a twisting motion whilst the leading edge has diagonal lines bending indicating with slight twisting. Again it is not possible to compare those predicted motions with experiments.

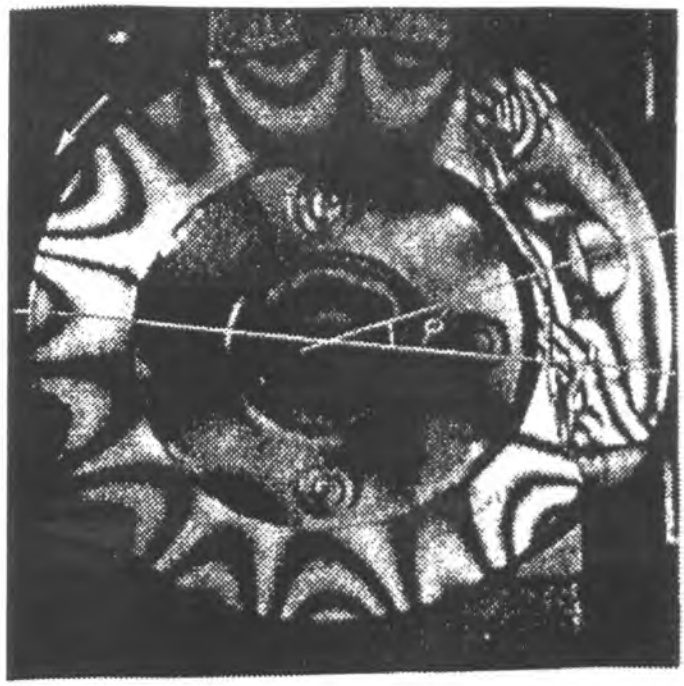

Figure 7.20 - Reconstructed holographic image for the high pressure range squeal [10]

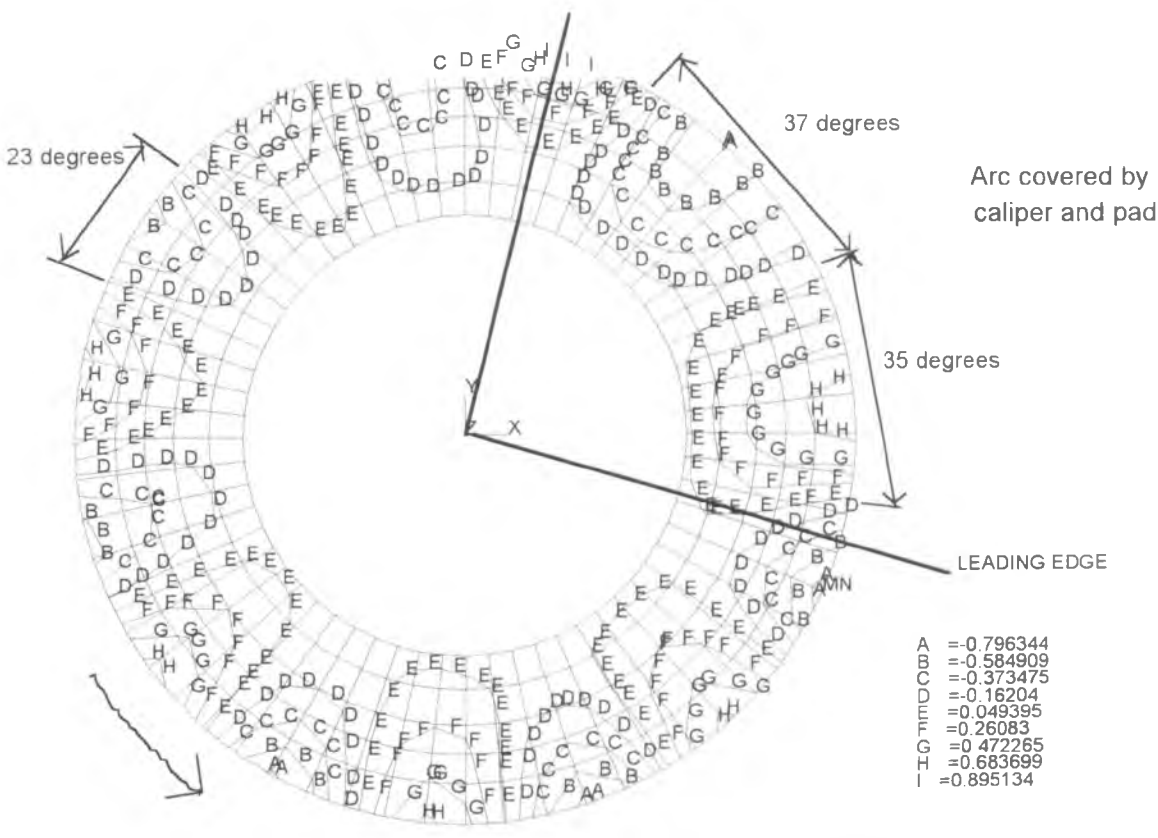

Figure 7.21a - Equal displacement contours on the disc for unstable mode F

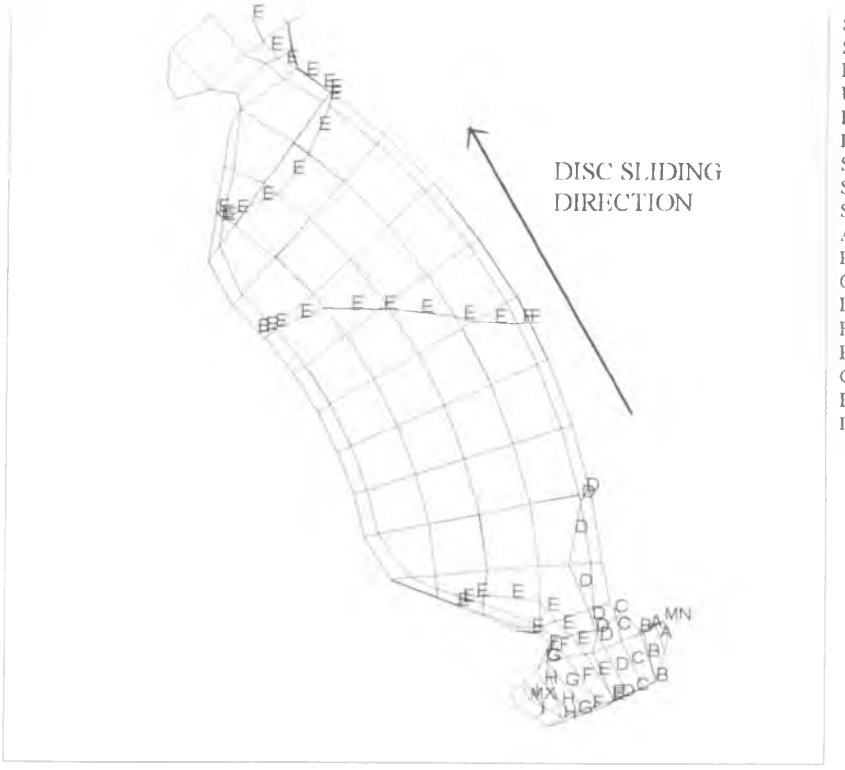

Figure 7.21b - Displacement contours on the outboard pad for unstable mode F (K_C =500 MN/m , K_S = 24 MN/m)

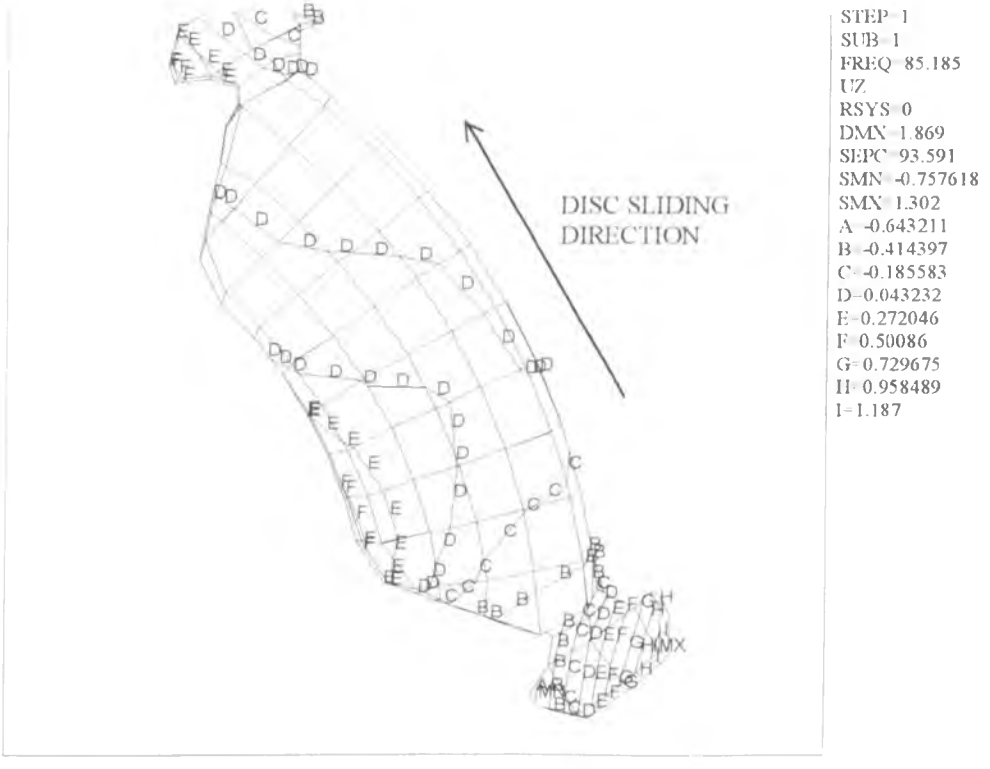

Figure 7.21c - Displacement contours on the inboard pad for unstable mode F (K_C =500 MN/m, K_S = 24 MN/m)

For both the low and high pressure range squeal, the disc mode shape is somewhat distorted compared to the free-free condition. In both cases it has been shown that the angular spacing of the nodes is regular away from the caliper but very much changed under the pad. This suggests that modal analysis of disc under free-free conditions would not indicate the squeal mode shape or frequency. Similarly the pad mode shapes from the coupled analysis do not show much similarity with those under free-free conditions as described in Chapter Four. Therefore a coupled pad-disc analysis is necessary to correctly predict the mode shape and frequency of the unstable modes which can be related to squeal and provide the necessary information for squeal abatement. It has been shown by Hoffman [54] that for damping layer on the pad backplate to be effective it must undergo relatively large displacements as in a bending mode. The results presented in figure 7.19b show the pad undergoing bending and the leading part of the outboard pad also undergoing bending which indicates the suitability of the damping layer approach to moderate unstable mode C.

The diametral modes of the disc for the unstable modes as described above no longer takes the form of a pure diametral mode (i.e uniform node spacing). This suggests that modification to the disc would not have much effect on the stability of the coupled pad-disc system as diametral mode separation would be effective only for diametral modes which have uniform nodal spacing. The effect of mode separation on the stability of the coupled pad-disc system is further considered in Chapter Eight.

The results from the analysis revealed some unstable modes which were not apparent in the experiment. However the unstable modes with a relatively high real part in their complex eigenvalue compare well with experimentally observed squeal modes. This indicates that the order of magnitude of the contact stiffness derived in Chapter Six has produced results in terms frequency and pressure range for the major unstable modes that compare reasonably with the experimental results of Fieldhouse and Newcomb [10].

The good correlation between the results from the finite element analysis and the experiments in terms of instability frequency and the associated mode shapes within the right range of applied pressure have shown that squeal can be successfully

modelled using the finite element method. This also demonstrate that the magnitude of contact stiffness assumed is correct in the sense that it produces unstable modes which resemble experimental squeal modes. Thus the general effect of pressure on disc brake squeal has been explained taking account of both interface contact stiffness and support stiffness. The coupled finite element model and the complex eigenvalue solution technique can now be applied to investigate the effect of parametric changes (from the baseline values) on the propensity for disc brake squeal as explained in Chapter Eight below.

CHAPTER EIGHT

PARAMETRIC STUDIES OF THE COUPLED PAD-DISC SYSTEM

8.1 Introduction

The coupled pad-disc model used in Chapter Seven for the complex eigenvalue stability analysis has predicted a number of unstable modes, several of which show good correlation with experimental squeal evidence. The conditions for which the results from the model compare well with experiment are selected as baseline values and the sensitivity of the results to variations in these baseline parameters is studied in this chapter.

There are several reasons why sensitivity studies are needed. Firstly there is a desire to determine parameters which lead to improved stability of the system thus helping designers to eliminate squeal by changing those parameters. Secondly there is the need to compare variations from the present approach with other variations carried out experimentally and analytically, thereby further validating the present modelling

approach for squeal related work. The parameters studied here are open to physical interpretation and, as much as possible , related experimental work is used to verify the trend of the results.

8.2 Methodology

The baseline condition selected for this sensitivity analysis is of a combined trailing and leading edge abutment with a friction coefficient of 0.4. The contact stiffness distributions are the same as in Section 6.3.1 i.e. leading edge biased for both inboard and outboard pads. The backplate connection stiffness is taken as 24 MN/m and the abutment stiffness is taken as 1.2 MN/m.

The parameters studied in this exercise include:

a) friction coefficient , μ

b) stiffness of the abutment

c) contact stiffness distribution

d) Young's modulus of the disc material

e) Young's modulus of the pad material

f) effect of disc asymmetry.

8.3 Effect of Friction Coefficient

Friction coefficient which is one of the most important factors in any friction brake design is governed by controlling the composition of the friction material and also proper matching of the friction pair. As economic factors begin to make downsizing of components more attractive , the use of a higher friction coefficient to achieve similar braking performance for a smaller rotor diameter is encouraged. In this study the squeal propensity of the coupled pad-disc system is estimated for different friction coefficients in the range of 0.1 to 0.7 in steps of 0.1 Only one value of contact stiffness of 300 MN/m is used for the analysis as, at this value, the resulting unstable modes compare well with experiment as reported in Chapter Six.

There are three unstable modes detected within the range of friction coefficient studied. The first unstable mode begins at a friction coefficient of between 0.4 and 0.5 (as at μ=0.5 the real part is already 30) as shown in figure 8.1. It comes about as a result of two different modes at an initially different frequencies (5970 Hz , 6090 Hz) coming together at a common frequency of 5975 Hz. After the modes converge, the real part grows with increasing friction coefficient whilst the frequency continues to fall. The real part reaches a maximum at μ= 0.6 after which it reduces with increasing μ

The second unstable mode first occurs at a friction coefficient of 0.5 as shown in figure 8.2 as two different modes at different frequencies (6530 Hz , 6709 Hz) coalesce at a common frequency of 6551 Hz. After this, the real part increases with increasing friction coefficient whilst the frequency remains relatively unchanged.

Figure 8.3 shows the third unstable mode first occurring at a friction coefficient of 0.35 when two separate modes at different frequencies (8120 Hz , 8340 Hz) coalesce at a common frequency of 8231 Hz. Again the real part increases monotonically with the friction coefficient whilst the frequency remains relatively unchanged.

To give an overall picture , the evolution of the frequency for all three unstable modes is shown in figure 8.4. It can be seen that there are different critical friction coefficients at which the modes converge. For modes A and B, the critical friction coefficient is about 0.5 whereby the critical friction coefficient for mode C is 0.35. The lower the critical friction coefficient the easier the mode will become unstable. Also the real part (which indicates the instability) tends to grow with increasing friction coefficient (with the exception of mode A which reaches a maximum at μ=0.6 as shown in figure 8.1). In general higher friction coefficient therefore results in a less stable system as the system can accommodate more unstable modes. This is in agreement with all other published results [6,7,43,47].

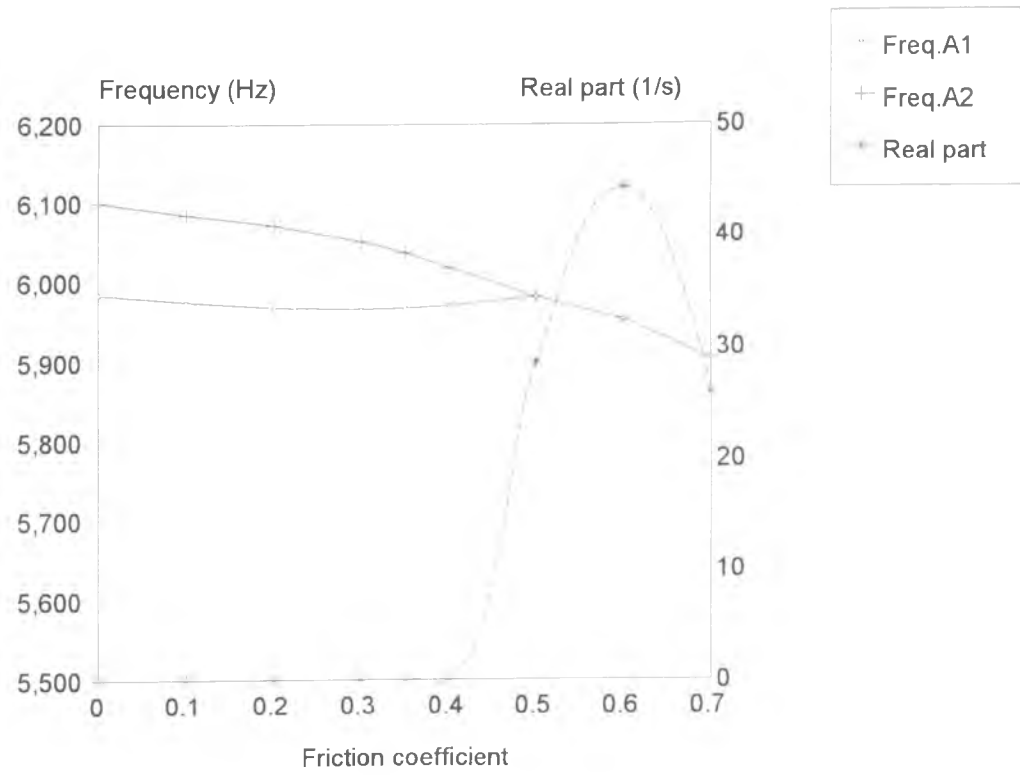

Figure 8.1 - Unstable mode A

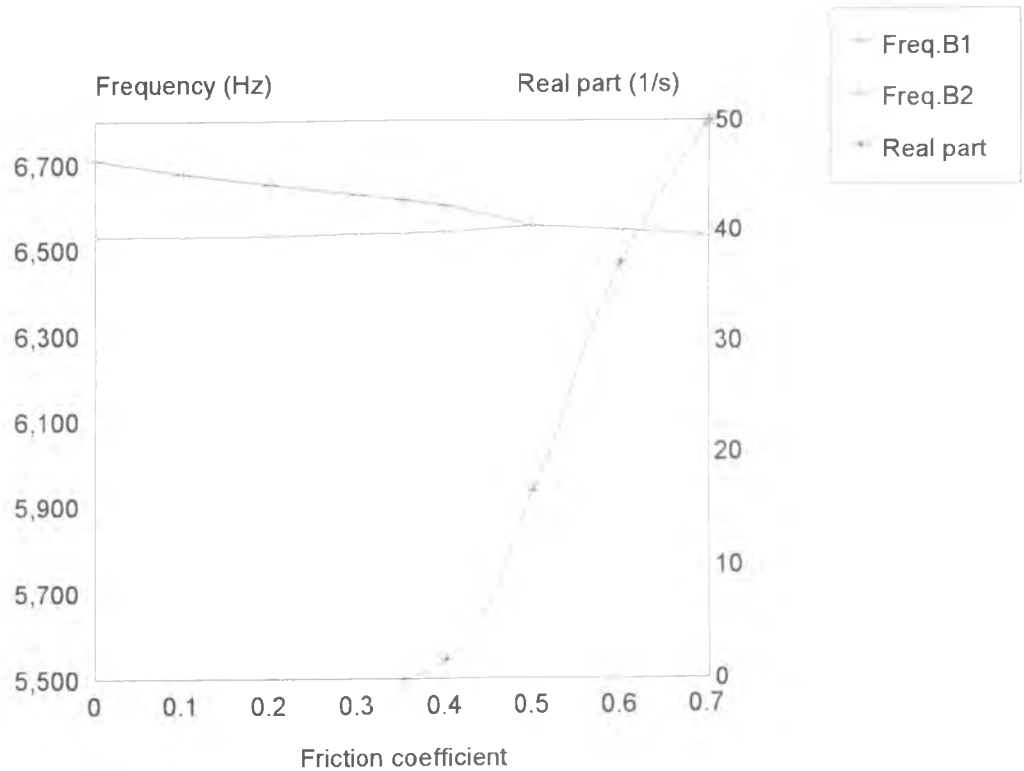

Figure 8.2 - Unstable mode B

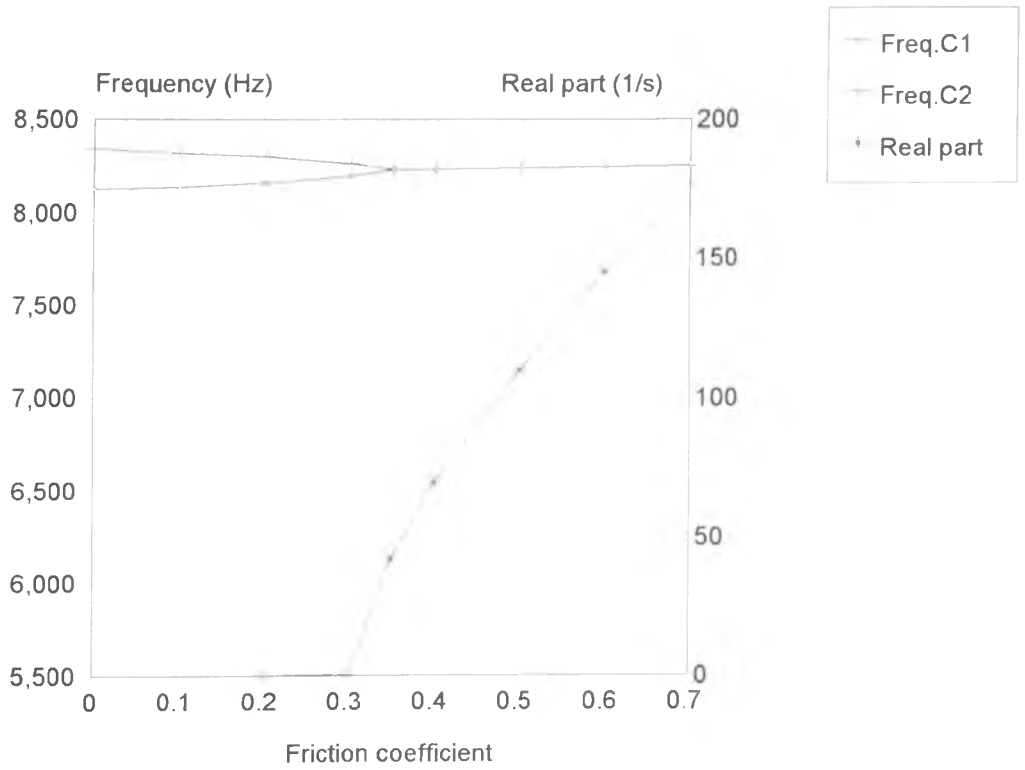

Figure 8.3 Unstable mode C

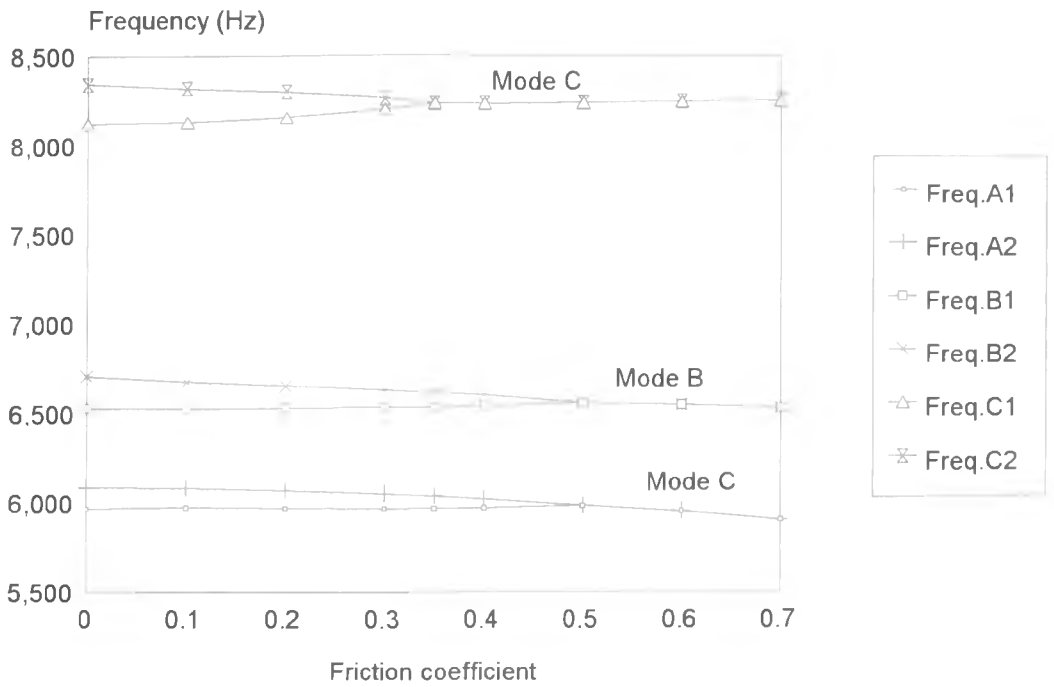

Figure 8.4 - The overall unstable modes

8.4 Effect of Abutment Stiffness

The pad abutments are modelled as stiff springs connecting two nodes at each of the pad ears to ground. The baseline stiffness is 2.4 MN/m at each end. Two additional values are used to study the sensitivity of the model to the abutment stiffness:

i) 0.0024 MN/m

ii) 2400 MN/m

The results for the abutment stiffness of 0.0024 MN/m shown in figure 8.5 indicate five unstable modes within different ranges of contact stiffness. All the unstable modes occur at frequencies above 5 kHz.

Comparing the results for abutment stiffnesses of 0.0024 MN/m (figure 8.5) and 2.4 MN/m (figure 7.7), the trends and the frequency range over which the modes are unstable remain essentially the same. There is one exception to this observation in that the mode with the highest frequency range (10.1 - 10.6 kHz) has increased its maximum real part from 71 to 102 as the abutment stiffness is increased. However, when the abutment stiffness is further increased to 2400 MN/m (about an order of magnitude greater than the pad-disc contact stiffness), there are some major changes to the unstable modes indicated in figure 8.6 including:

a) a reduction of the contact stiffness range over which the modes are unstable

b) significant increase in the maximum real part of the complex eigenvalues.

Therefore the effect of abutment stiffness is mode-specific in the sense that different modes are influenced in a different manner by the magnitude of the abutment stiffness. An increase in abutment stiffness tends to stabilise modes which are unstable over a relatively narrow range of contact stiffness by reducing further the unstable contact stiffness range and the magnitude of the maximum real part. For modes which are unstable over a relatively wide range of contact stiffness, an increase in abutment stiffness from the baseline value increases the magnitude of the real part and hence reduces the stability. There is also a downward shift of the critical contact stiffness for the higher frequency unstable modes, in particular mode F for which the critical contact stiffness value is reduced from 400 MN/m to 300 MN/m.

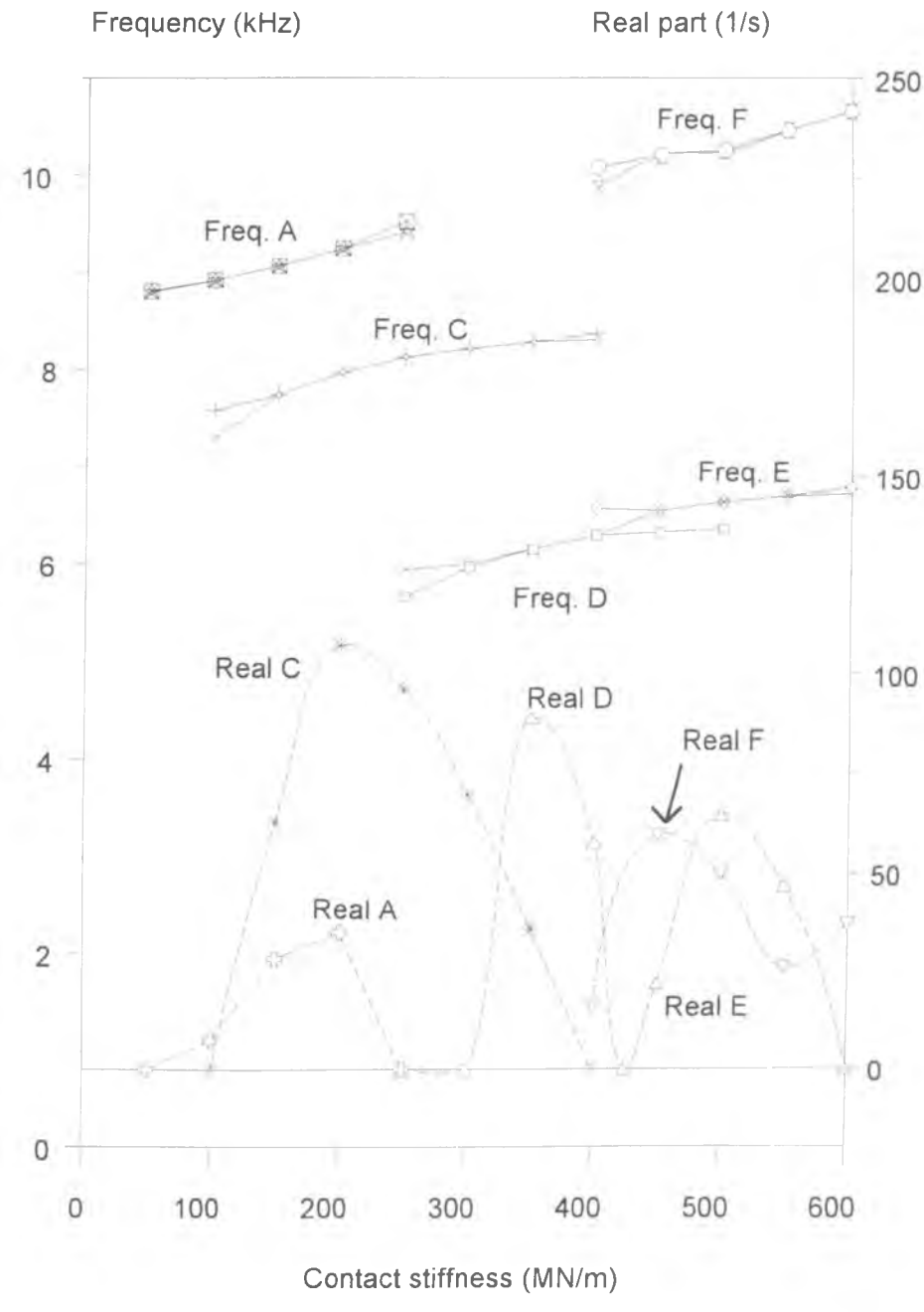

Figure 8.5 - Unstable modes for abutment stiffness of 2.4 kN/m

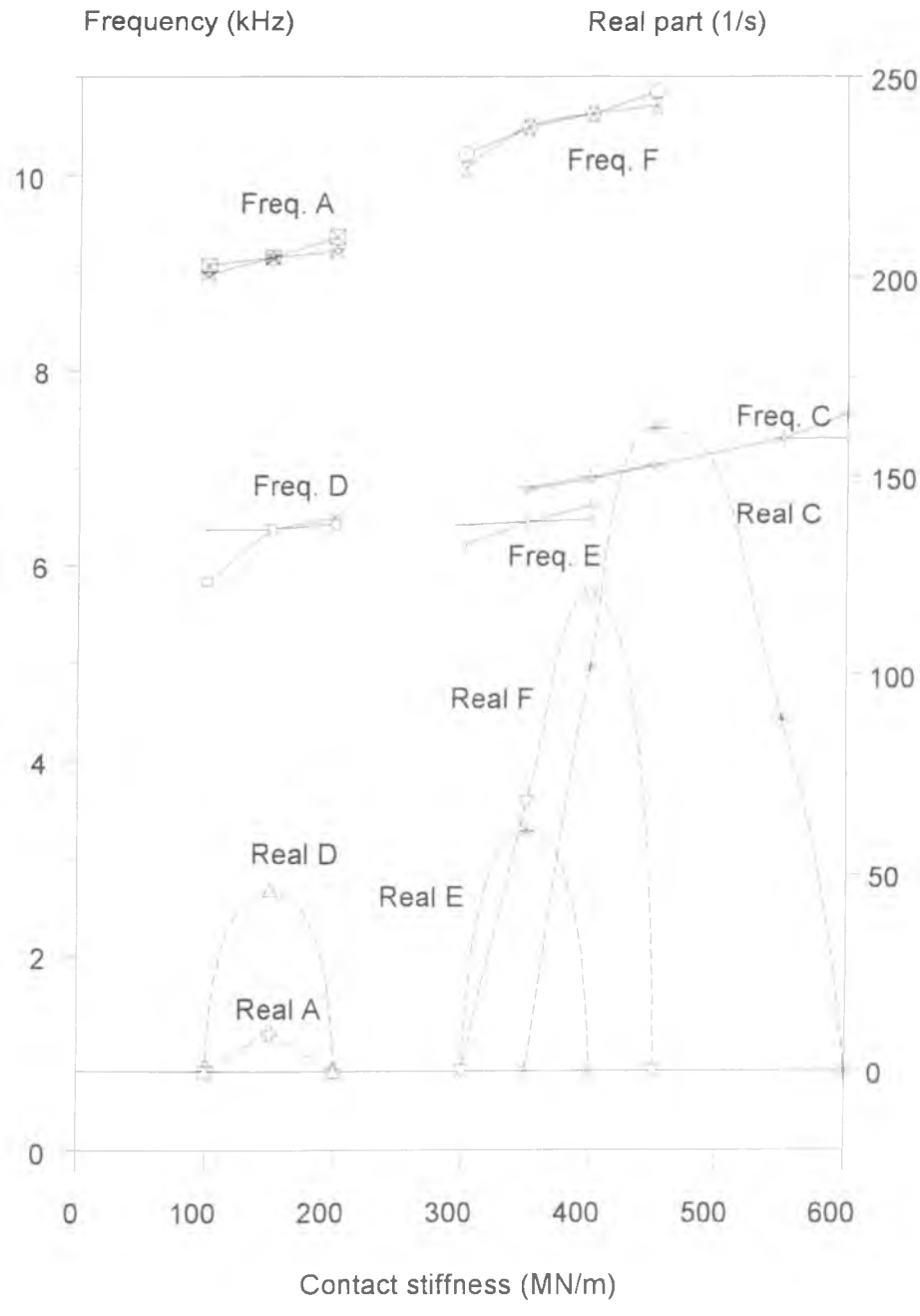

Figure 8.6 - Unstable modes for abutment stiffness 2 400 MN/m

8.5 Effect of Contact Stiffness Distribution

Three different contact stiffness distributions are considered in this study namely:

i) leading edge biased
ii) uniform
iii) trailing edge biased.

The leading edge biased distribution is the baseline condition from the contact analysis described in Chapter Five which showed that the distribution tends to be biased towards the leading edge for both inboard and outboard pads due to the friction effect. The uniform contact stiffness distribution is achieved by specifying the same contact stiffness for all the node pairs at the pad-disc interface. This in practice could be achieved (to a certain extent) by using softer friction material and spreading out the force applied to the backplate as demonstrated in Chapter Five for the case of paw applied pressure. The trailing edge biased contact stiffness distributions are obtained by mirroring all the contact values for the leading edge biased distribution about the pad centreline (as the pad is symmetric about this line). This again result in partial contact but now the nodes at the trailing edge have higher contact stiffness values than those at the leading edge. In practice a very similar effect can be achieved for the inboard pad by moving the piston towards the trailing edge.

All the analyses are carried out for a combined trailing and leading edge abutment with friction coefficient of 0.4 and for a range of contact stiffnesses upto 600 MN/m Figure 7.7 shows the mode evolution for the baseline leading edge biased distribution which occurs under normal sliding As discussed in detail in Chapter Seven, there are five major unstable modes within the range all involving the sixth and seventh diametral modes of the disc.

Figure 8.7 shows the corresponding mode evolution for a uniform pressure distribution over both pads. A total of three unstable modes is indicated with the first mode (mode D) occurring over a very narrow contact stiffness range. In contrast mode

C occurs over a contact stiffness range of 250 - 400 MN/m and mode F occurs over a contact stiffness range of 300 - 450 MN/m. The maximum real part for this condition is 175 for unstable mode C compared with 107 for the same mode with the baseline contact stiffness distribution (figure 7.7).

Figure 8.8 shows the mode evolution for the trailing edge biased condition from which a total of three unstable modes can again be detected. The first unstable mode (mode D) occurs over a contact stiffness range of 350-450 MN/m , the second unstable mode (mode E) occurs over a contact stiffness range of 500 - 600 MN/m and the third unstable mode (mode C) occurs over a contact stiffness range of 550 - 600 MN/m. The maximum real part for this condition is now 70, again for mode C.

In general these results demonstrate that interface contact stiffness distribution does influence the stability of the coupled pad-disc system. Moreover a contact stiffness distribution biased towards the trailing edge results in unstable modes within a very narrow range of contact stiffness compared to the leading edge biased distribution. Furthermore the maximum real part of the complex eigenvalues for the trailing edge biased condition (73) is very much reduced from the leading edge biased condition (100) and the uniform contact pressure distribution (145). In addition unstable mode F which appears for both leading edge biased and uniform distribution no longer exists in the trailing edge biased distribution. The results also indirectly suggest that wear resulting in a reduction of the thickness of the friction material and (usually) a more uniform contact pressure distribution will affect the stability of the system and in particular the contact stiffness range over which modes become unstable.

Therefore two important trends can be detected from these results:

1) the leading edge biased and uniform contact stiffness distributions have similar unstable modes (at this level indicated by the frequency range over which they occur)

2) the trailing edge biased contact stiffness distribution tends to stabilise the system as indicated by the reduced range of contact stiffness for the unstable modes and the reduction in magnitude of the real part.

The above trends match well with the lumped parameter model results of Brooks et al [43] which predicted that moving the centre of pressure towards the leading edge creates a more unstable system and also the experimental results of Fieldhouse and Newcomb [10] which showed that when the pressure application point on the pad backplate is shifted towards the trailing edge the squeal noise level is much reduced.

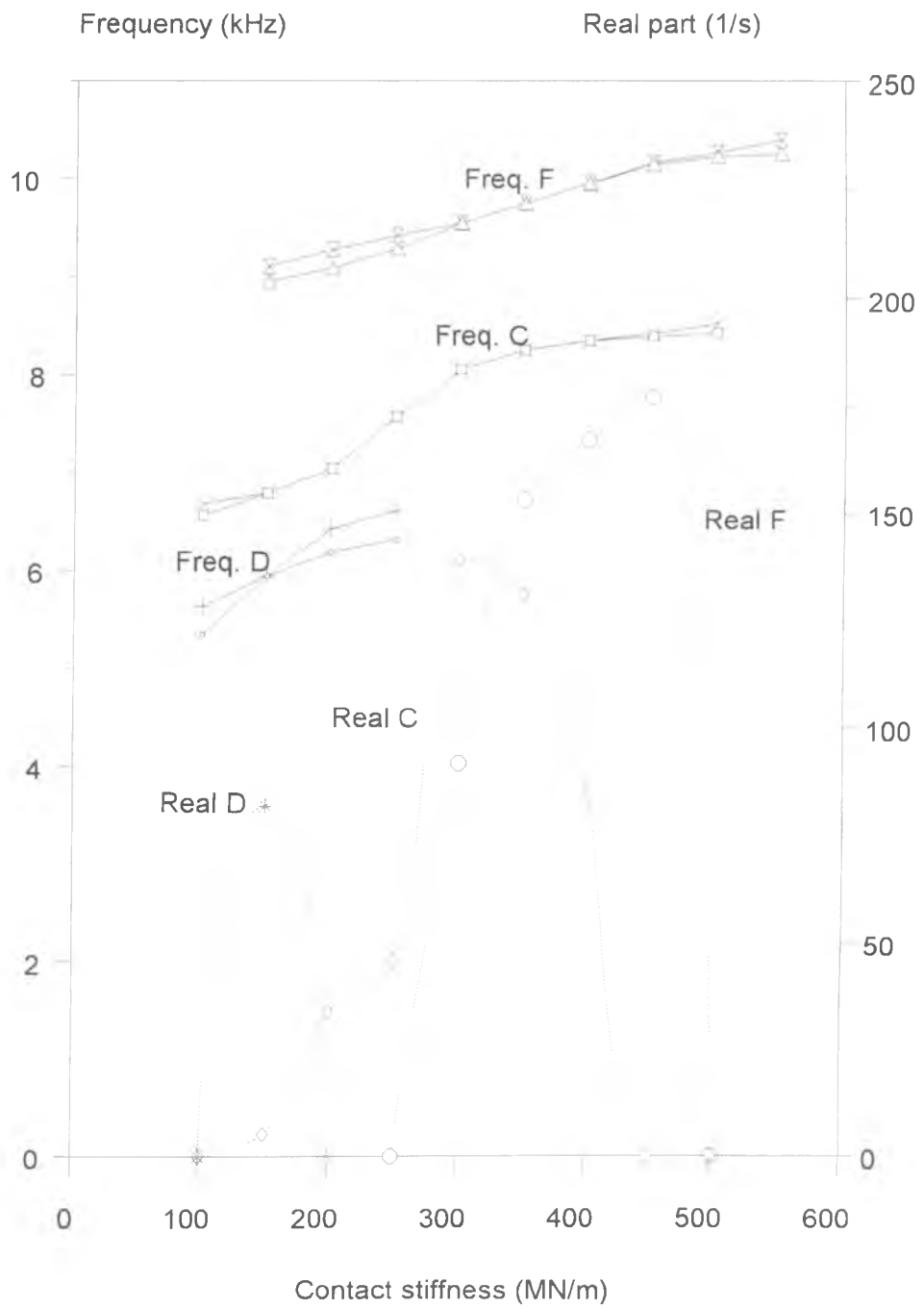

Figure 8.7 - Unstable modes for uniform contact stiffness distribution

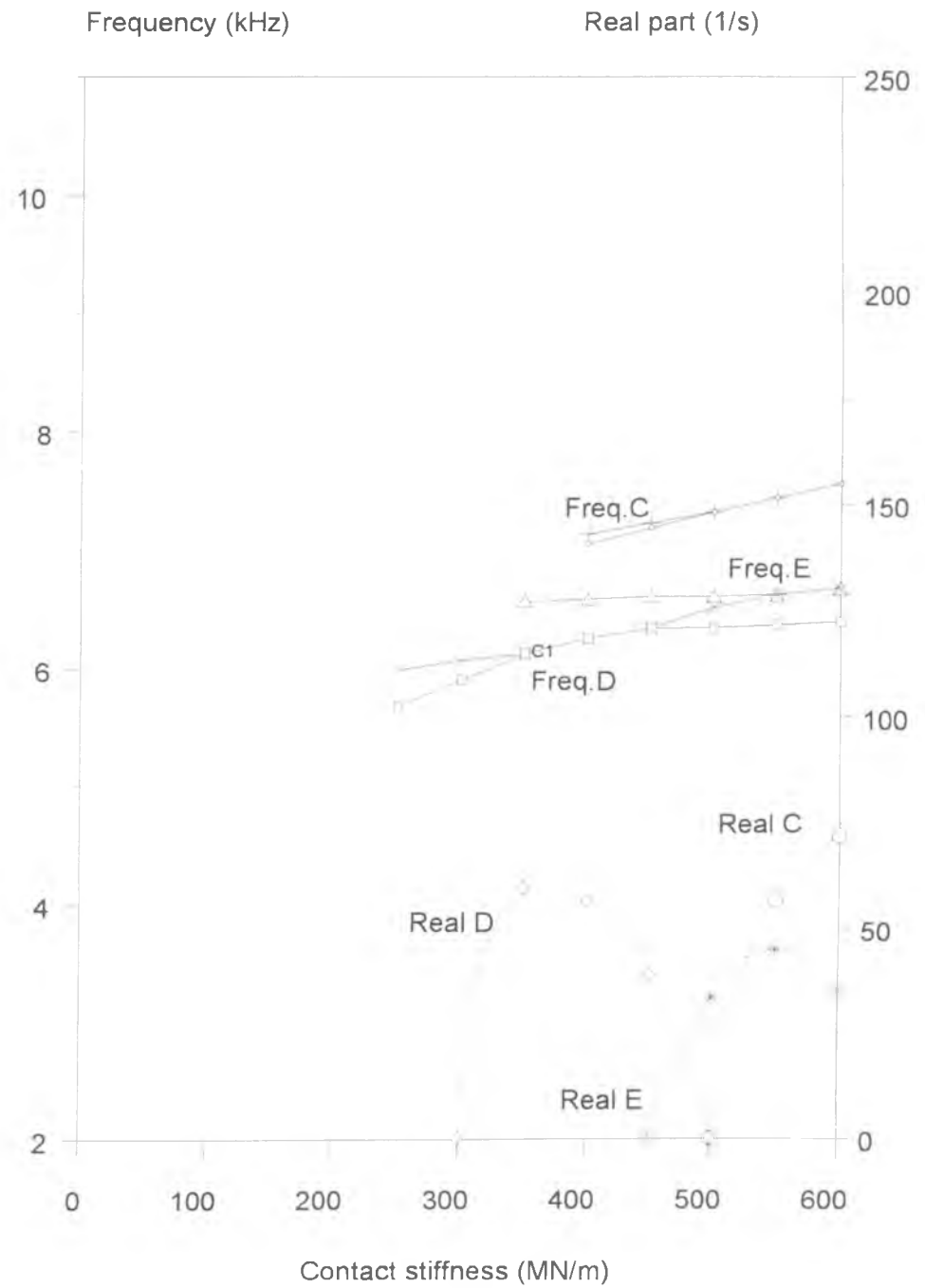

Figure 8.8 - Unstable modes for trailing edge biased contact stiffness distribution

8.6 Effect of The Pad Flexibilty

The effect of pad flexibility is studied here by setting the Young's moduli of the pad backplate and friction material at artificially high values (205 x 10^9 GPa and 8 x 10^9 GPa respectively) such that there are no flexible modes within the frequency range studied. The contact pressure distribution however is assumed to be unaffected (i.e. leading edge biased) in order to isolate the effect of pad flexibility.

The results shown in figure 8.9 indicate that there are only two unstable modes for a rigid pad. These occur at 4227 Hz and 6253 - 6387 Hz with maximum real parts of 42 and 26 respectively. The unstable frequency of 4227 Hz is very near to the pad first rigid body translation (transversely) frequency whilst the second unstable frequency is very near to the pad rotational frequency (about the pad longitudinal axis). Comparison of figure 8.9 with the baseline condition (figure 7.7) shows that flexibility of the pads is important in the generation of instability. Rigid pads still produce instability but with much reduced real part and within a narrower range of contact stiffness (less than 50 MN/m for both modes). These results suggest that rigid pads would improve the stability of the system. This aspect of the results compares well with the work of Liles [6] and Sherif [57] where shorter pads (i.e. less flexible) were found to improve stability. In practice, any change of the friction material stiffness (and possibly also of the backplate material) may effect the contact pressure distribution. However consideration of this additional effect of pad flexibility was not possible within the time constraints of the present study.

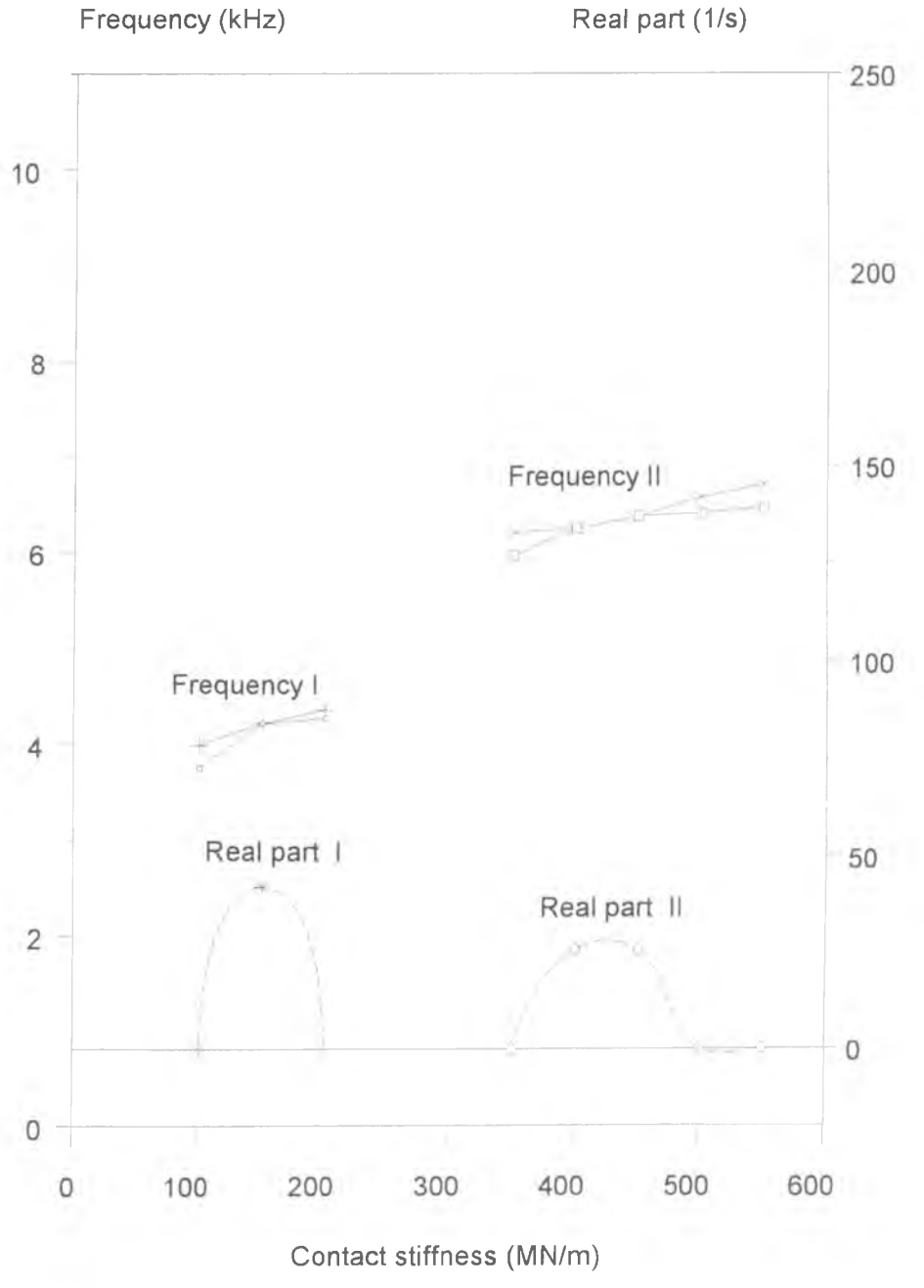

Figure 8.9 - Unstable modes for inflexible pads

8.7 Effect of Different Disc Material

The material properties of the disc are varied here to determine the effect of different disc material on the system stability. Both the density and Young's modulus are varied for each case as they are the most important from a dynamics point of view. The baseline properties are for the traditional grey cast disc with assumed modulus of E=120 GPa and density of ρ=7250 kg/m^3. Three other material property sets are considered :

i) E = 120 GPa and ρ=2250 kg/m^3

ii) E = 8000 GPa and ρ=7250 kg/m^3

iii) E = 120x10^3 GPa and ρ=7250 kg/m^3

The properties for material (i) are based on that of aluminum metal matrix composite (Al-MMC) [83]. Properties (ii) are for a hypothetical material with unrealistically high Young's modulus such that only one diametral mode (the second diametral) occurs within the frequency range studied. Material (iii) is also hypothetical with a Young's modulus which is made so high that there are no flexible modes within the frequency range studied in order to see whether flexible modes of the disc are essential for instability of the system.

For the baseline disc properties (figure 7.7), five unstable modes can be detected as discussed in detail in Chapter Seven. With disc material properties similar to those of Al-MMC, free-free modal analysis shows that diametral modes of order up to six exist under 12 kHz compared to eight for the baseline properties (Table 8.1). The stability results (figure 8.10) indicate that only one unstable mode exists at a contact stiffness of 100 MN/m and higher with the unstable frequency beginning at 7 kHz and increasing gradually with the contact stiffness. The real part also generally increases with the contact stiffness. These results indicate that an Al-MMC disc may well be less prone to squeal as there are only one unstable mode compared to five for the grey cast iron equivalent.

When the Young's modulus of the disc is increased to 8000 GPa, free-free modal analysis of the disc revealed the natural modes listed in Table 8.2. With only one free-free diametral mode within the frequency range studied, the number of unstable modes is reduced from five to three as shown in figure 8.11, all which have frequencies below that of the second diametral mode. As the Young's modulus of the disc is further increased to 120×10^3 GPa , the first mode occurs at 18473 Hz as shwon in Table 8.3 which is outside the frequency range of interests (1 - 11 kHz).

Table 8.1 - Free-free modes for the Al-MMC disc

Frequency (Hz)	Mode description
1068	1st circumferential
1287	Not diametral or circumferential
2094	2nd diametral
3585	3rd diametral
5734	4th diametral
8517	5th diametral
11917	6th diametral

Table 8.2 - Free-free modes for the disc with E=8000 GPa

Frequency (Hz)	Mode description
4769	Circumferential
5748	Circumferential
9352	2nd diametral

Table 8.3 - Free-free modes for the disc with E= 120×10^3 GPa

Frequency (Hz)	Mode description
18 473	Circumferential

However increasing the Young's modulus further to an essentially rigid disc does not remove the instability. As shown in figure 8.12, there are still three unstable frequency bands of 5680 -6609 Hz , 6975 - 7370 Hz and 8676 - 9419 Hz with maximum real parts of 179, 145 and 245 respectively which are significantly higher than for the disc with E=8000 GPa. A detail study of the mode shape for each of these unstable modes does not show any diametral modes of the disc. The disc mode shape in each case shows an upward deflection for the half of the disc in which contact occurs whilst the other half remains flat.

These results demonstrate that raising the disc natural frequencies by increasing the Young's modulus is not necessarily beneficial in reducing squeal propensity. There seems to be one band of unstable frequency in the range 5-9 kHz which occurs for all the disc material properties studied. It would appear that this unstable frequency band has little relation with the disc dynamic characteristics suggesting the pad to be the principal source of instability in this case.

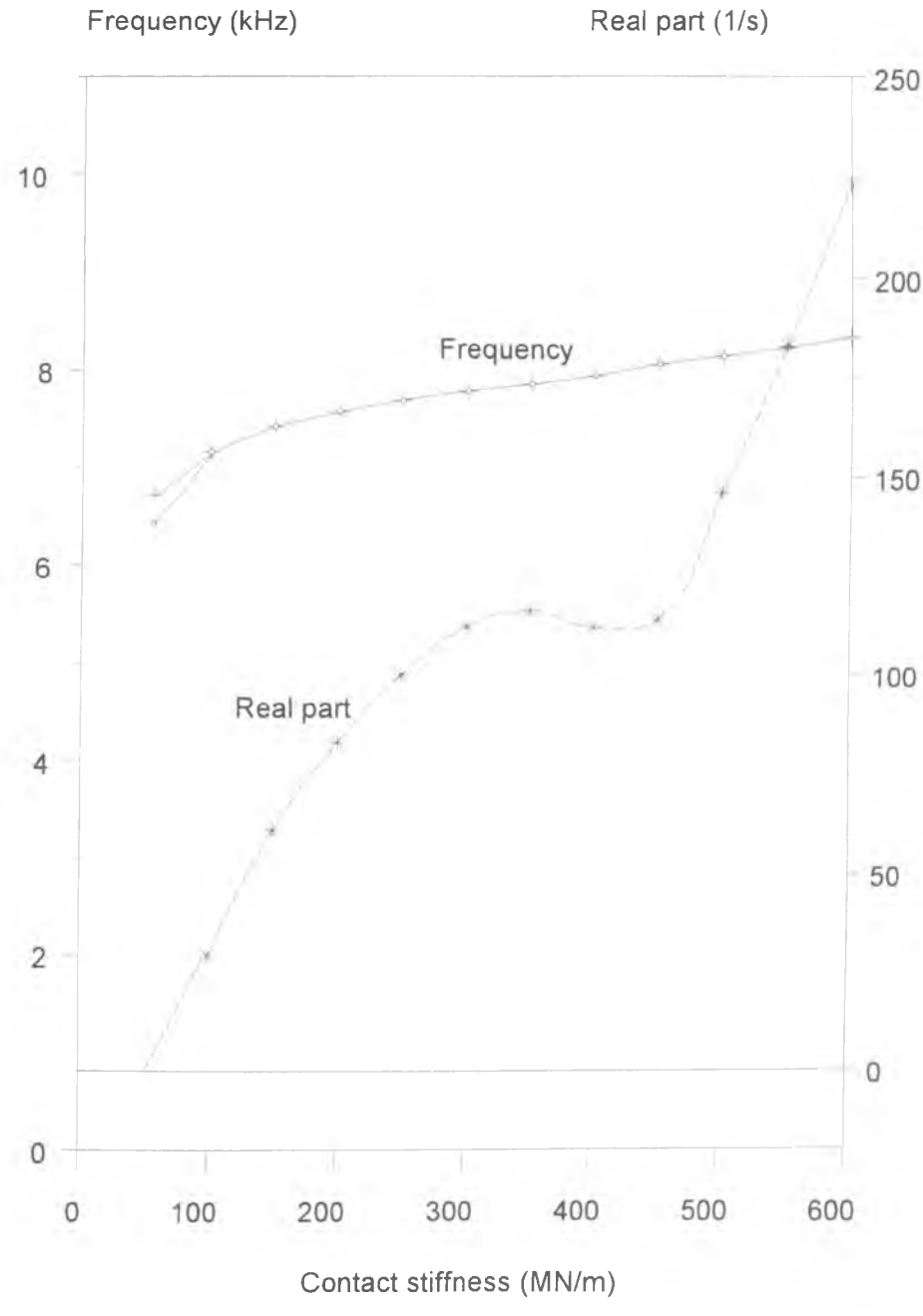

Figure 8 10- Unstable modes for aluminum metal matrix composite disc (E=120 GPa , ρ=2250 kg/m3)

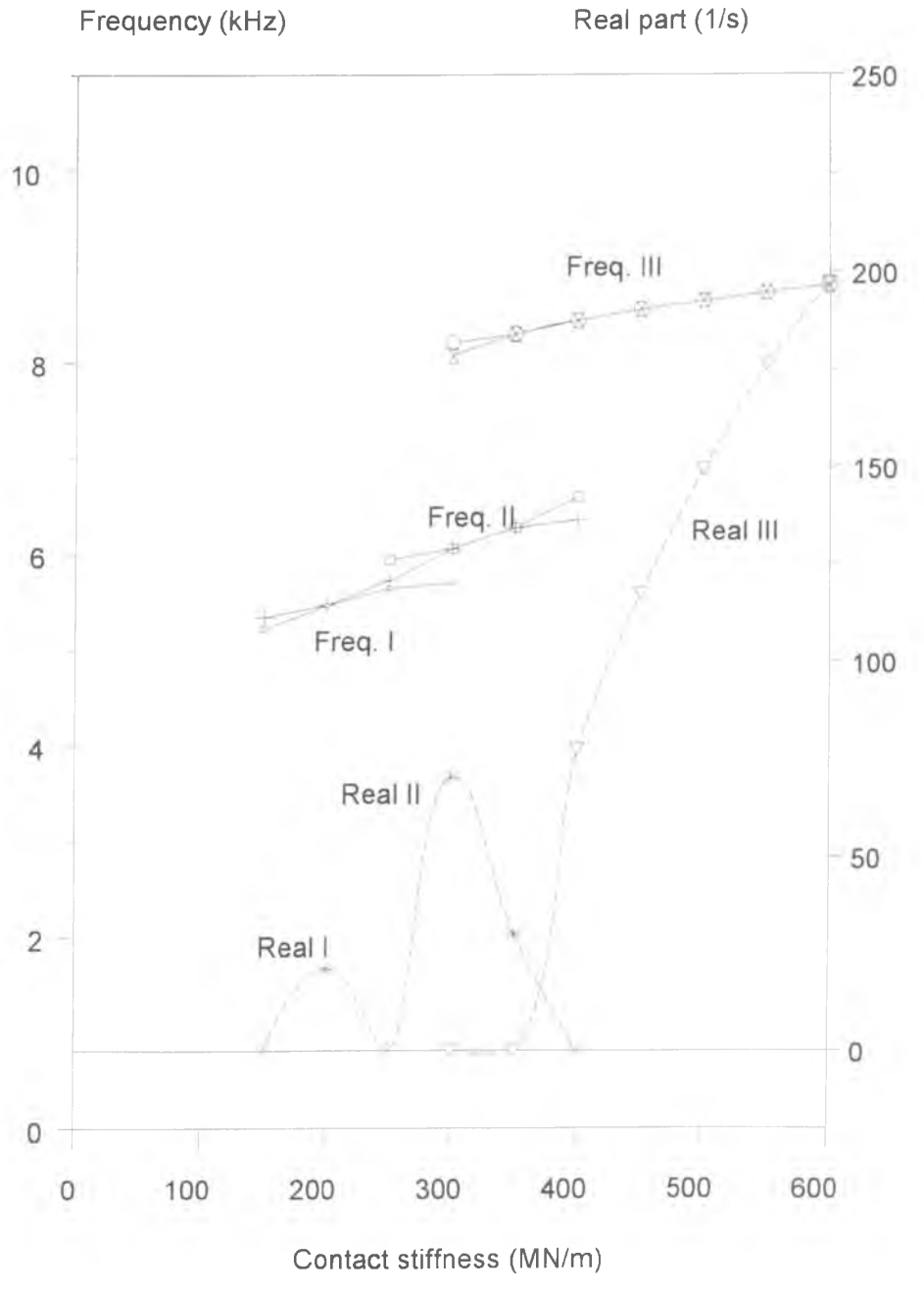

Figure 8.11 - Unstable modes for a disc with very high Young's modulus (E=8000 GPa)

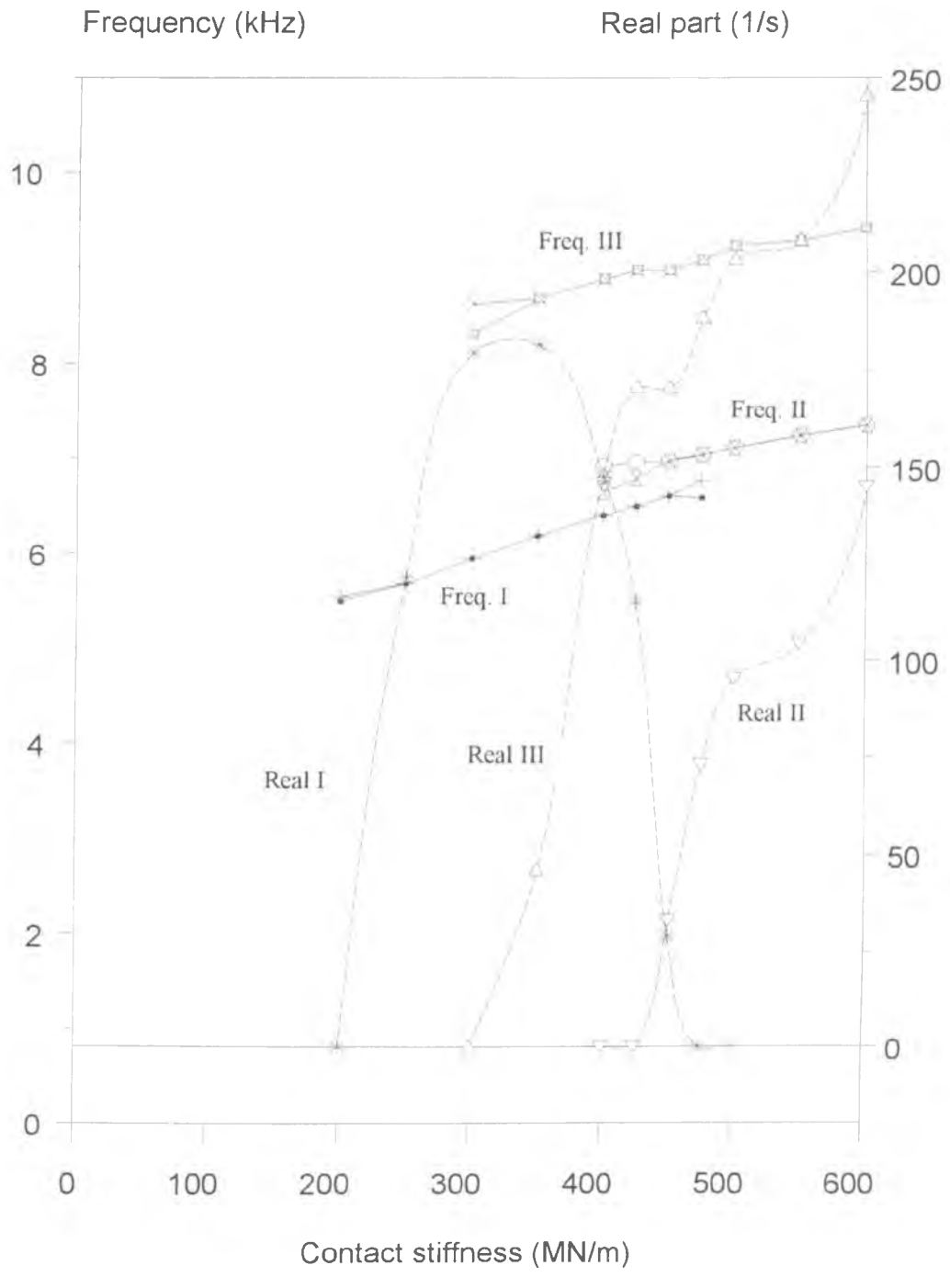

Figure 8.12 - Unstable modes for an inflexible disc.

8.7 Effect of Disc Symmetry

One suggested method to stabilise a squeal mode is to separate the doublet modes of the disc. The term 'doublet mode' is used to describe diametral modes of the disc which have the same diametral mode order and same frequency but have a relative phase difference of 90 degrees in the free-free condition. The basic idea that stability can be achieved by separating these modes is based on the fact that unstable squeal modes occur when two stable modes converge at particular values of certain parameters (friction coefficient , contact stiffness). These two modes are usually of the same diametral mode order but are initially separated in frequency by the coupling between the pad and the disc under the applied pressure. Figures 8.1 - 8.3 show clear examples of this convergence effect.

There are several ways of separating the diametral modes all based on modifying the stiffness or mass distribution around the circumference of the rotor. Lang et al [59] used a technique of adding mass along the outer circumference of a drum brake in order to separate the doublet modes. Nishiiwaki et al [58] varied the number of stiffeners on a ventilated disc to achieve the same effect. For a plain disc as assumed in this analysis, a practical way to achieve the separation of the doublet modes is by machining slots in the disc. In the finite element model , this can be simulated by simply reducing the thickness of the disc shell elements in certain areas. The slot angular width in the model is limited to multiples of 6 degrees as the constraint that the disc mesh must be compatible with the pad model still applies. Obviously in practice the width of slots would not be limited by this constraint. In the present analysis the number of slots modelled is 4 , 5 , 6 , 10 and 12.The depth of the slot in each case is 5.5mm compared with the total thickness of the disc 10.25 mm and the slot is assumed to be symmetrical about the disc mid-plane. The circumferential symmetry of the disc however must also be maintained by regularly spacing the slots in order to preserve disc balance. The effect of the slots therefore is primarily to reduce the infinite symmetry of the disc to an order of symmetry equivalent to the number of slots.

Table 8.3 - Frequencies of the free-free diametral modes for a slotted disc

Number of slots	Frequency	2nd diam. mode	3rd diam. mode	4th diam. mode	5th diam. mode	6th diam. mode	7th diam. mode	8th diam. mode
0 (PLAIN)	**f1 (Hz)**	1145	1961	3137	4659	6578	8708	11225
	f2 (Hz)	1145	1961	3137	4659	6578	8708	11225
4	**f1 (Hz)**	1092	1916	3029	4478	6148	8324	10859
	f2 (Hz)	1171	1916	3037	4478	6345	8324	10908
5	**f1 (Hz)**	1125	1906	3008	4377	6181	8223	10560
	f2 (Hz)	1125	1906	3008	4497	6181	8223	10560
6	**f1(Hz)**	1123	1845	2984	4392	5979	8153	10444
	f2(Hz)	1123	1937	2984	4392	6262	8153	10444
10	**f1 (Hz)**	1112	1847	2879	4107	5867	7791	9875
	f2 (Hz)	1112	1847	2879	4336	5867	7791	9875
12	**f1 (Hz)**	1106	1827	2830	4120	5470	7647	9773
	f2 (Hz)	1106	1827	2830	4120	6006	7647	9773

The results from free-free modal analysis of the slotted disc are shown in Table 8.4 in which f1 indicates the frequency of the lower diametral mode of the doublet pair and f2 the frequency of the higher mode. It is clear that the number of slots does alter the frequency of the diametral modes but this effect is limited to certain modes for which the mode diametral order is a simple multiple of the number of the slots. For example the results for the disc with four slots show that the second , fourth and eighth diametral modes are all affected (the sixth diametral mode being affected the most with a frequency separation of 197 Hz) whilst for five slots, it is only the fifth diametral mode which shows any separation. Another important trend is that increasing the number of slots increases the frequency separation as shown in figure 8.13. For the

present numbers of slots studied , the sixth diametral mode is most affected and, as the number of slots is increased from 6 to 12 , the frequency separation for this mode is increased from 283 Hz to 536 Hz

In order to investigate the effect of separated doublet modes on the system stability , an unstable mode is selected for which the disc mode is clearly pure diametral in that the nodal distance remains constant for the disc both in and out of the contact area and the coupled frequency is relatively close to that of the free-free diametral mode of the disc. This unstable mode involves the disc sixth diametral mode as shown in figure 7.20. Separation of the sixth diametral doublet modes can be achieved with 4 , 6 or 12 slots as indicated in figure 8.13. However, in order to reduce the problem to a manageable size , only a disc with six slots giving a frequency separation of 283 Hz under free-free conditions is selected to study the effect of mode separation on the stability of the system. An end view of the finite element model of the disc with six slots is shown in figure 8.14 in which the slots are shown blank and the circumferential angle is measured from the global x-axis. Equal displacement contour plots of the sixth diametral doublet modes for the disc model with six slots are shown in figures 8.15 and 8.16 respectively

Figure 8.15 shows the lower of the sixth diametral doublet modes which occurs at a frequency of 5979 Hz. It is clear that the x-axis in the diagram represents one of the node lines of the disc. In figure 8 16 the contour plot of the other sixth diametral mode which occurs at a frequency of 6263 Hz is shown and this time the x-axis coincides with one of the anti-node lines (marked E). It is therefore clear that the sixth diametral doublet mode pair has now been separated in frequency terms by 284 Hz whilst the mode shape is different only in the relative phase angle of 90 degrees. The lower frequency mode occurs when the anti-node is positioned over the slots in the disc where the stiffness is lower due to the reduction in thickness whilst the higher frequency mode occurs when the node is positioned over the slots which therefore have a less significant effect on the frequency (the corresponding frequency for the unslotted disc is 6578 Hz).

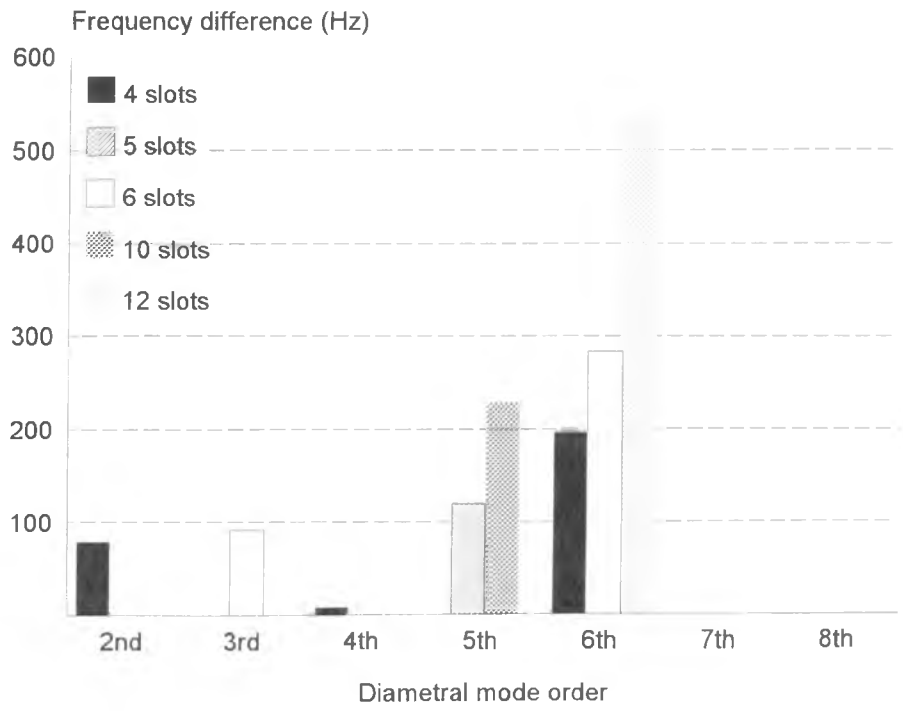

Figure 8.13 - Effect of number of slots on the frequency difference of the disc diametral modes

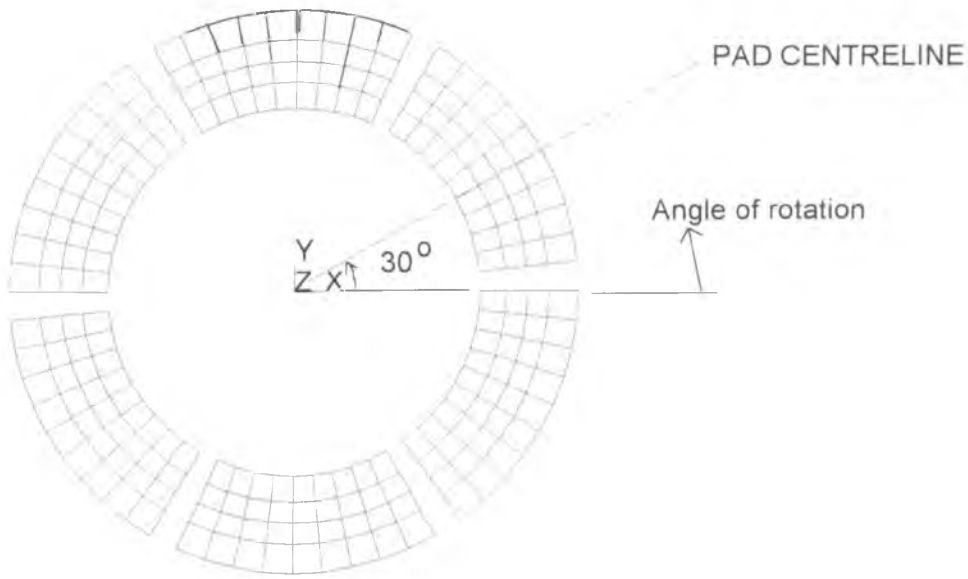

Figure 8.14 - The finite element model of the slotted disc showing the slot position (blank)

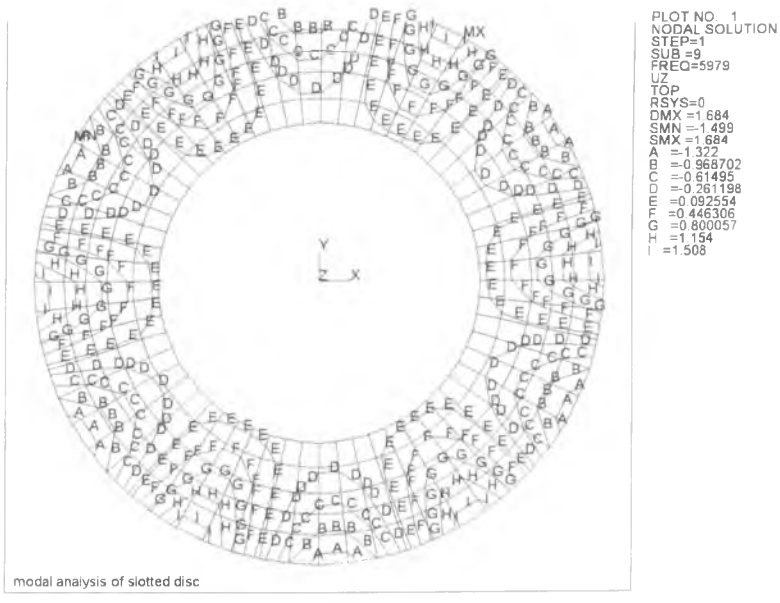

Figure 8.15 - Displacement contour plot of the lower sixth diametral mode for a six slot disc (for position of slot refer to figure 8.14).

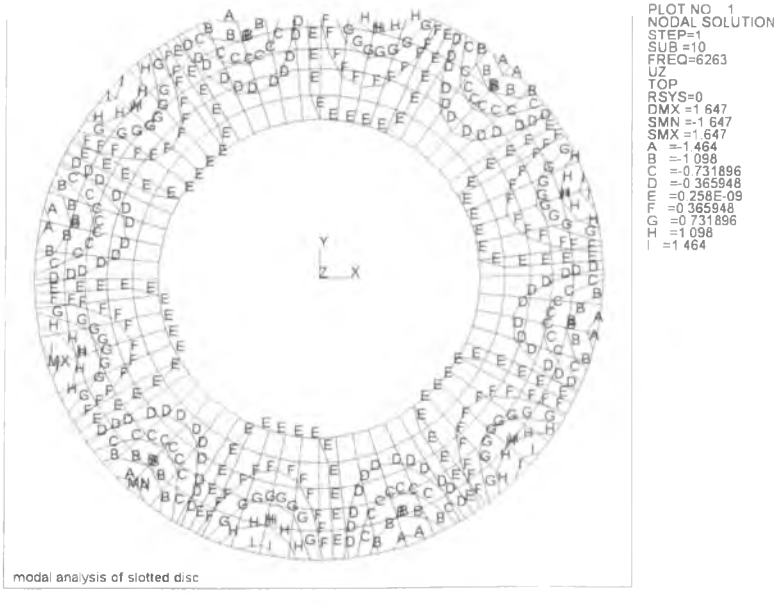

Figure 8.16 -Displacement contour plot of the upper sixth diametral mode for a six slot disc (for relative position of slots refer to figure 8.14).

As the slotted disc rotates, the position of the disc asymmetry changes with respect to the pad. This effect was taken into account in the stability analysis by rotating the disc (with respect to the pads) by successive angular interval of 6 degrees and determining complex eigenvalues at each angular position for a contact stiffness range of 50 - 600 MN/m. The leading edge biased contact pressure distribution is assumed throughout. The angle of rotation is measured relative to the pad centreline as shown in figure 8.14. The results for an angular position of zero degrees (i.e. when the axis of one of the slots is 30 degrees forward of the pad centreline) as shown in figure 8.17 indicate that there are several unstable modes within the contact stiffness range studied. Detail investigation of the mode shape plots show that these modes involve the sixth , seventh and eighth diametral modes of the disc. Of these there are two unstable modes both involving the sixth diametral disc mode which occur at different frequencies and ranges of contact stiffness. The low contact stiffness range mode (referred as mode M) is unstable for contact stiffnesses of 250 - 350 MN/m whilst the high contact stiffness range mode (referred to as mode N) occurs for contact stiffnesses of 375 - 450 MN/m.The range of contact stiffness for these two modes to be unstable was found to vary slightly with the relative angle of rotation. The remaining two unstable modes involve the seventh diametral disc mode (mode O) which occurs at a contact stiffness of 200 MN/m and above and the eighth diametral mode (mode P) which occurs at a contact stiffness of 500 MN/m and above. The contact stiffness ranges of these two modes however were found not to vary with the angle of rotation.

In order to study the effect of rotation angle on the stability of the system, the maximum real part for modes M and N throughout the unstable contact stiffness range is plotted against the angle of rotation in figure 8.18a whilst for modes O and P the corresponding values at a contact stiffness of 550 MN/m are shown in figure 8.18b. In both cases the range of angle of rotation shown is only from 0 - 60 degrees as the cycle repeats itself every 60 degrees of rotation. For modes M and N (figure 8.18a) which involve the sixth diametral modes of the disc the real part varies greatly with the rotation angle. For mode M which involves the lower frequency sixth diametral mode the maximum real part peaks at relative angular positions of 0 , 30 and 60 degrees whilst for mode N which involves the higher frequency sixth diametral mode the

maximum real part peaks at angular positions of 18 and 48 degrees. Furthermore the peak positions for mode M coincide with the trough positions for mode N. This variation in real part indicates cyclic instability for each of these mode as the disc rotates.

For modes O and P the results (figure 8.18b) show little variation of the real part ($\pm$ 8) with the angle of rotation. Detail studies of the disc contour plots show that the nodal spacing is not uniform particularly for the disc contact area under the pads.

The above results show that limiting the symmetry of the disc is only effective for certain modes, in particular those modes for which the disc diametral deformation coincides with the symmetry of the slotted disc (in this case the sixth diametral mode). For unstable modes which involve the disc seventh and eight diametral modes the effect is minimal. Thus it can be said that the strategy of separating a disc doublet mode of a certain diametral order is effective for reducing squeal propensity involving that same diametral mode order only. In the present case it is also interesting to note that the real part for the unstable mode involving the disc sixth diametral mode (mode M) reduces to zero (i.e. completely stable) at certain angles of disc rotation. However, for the mode in the higher contact stiffness range (mode N), the real part only reduces to a minimum of 15. This suggests further that the separation of the doublet modes is more effective for low applied pressures.

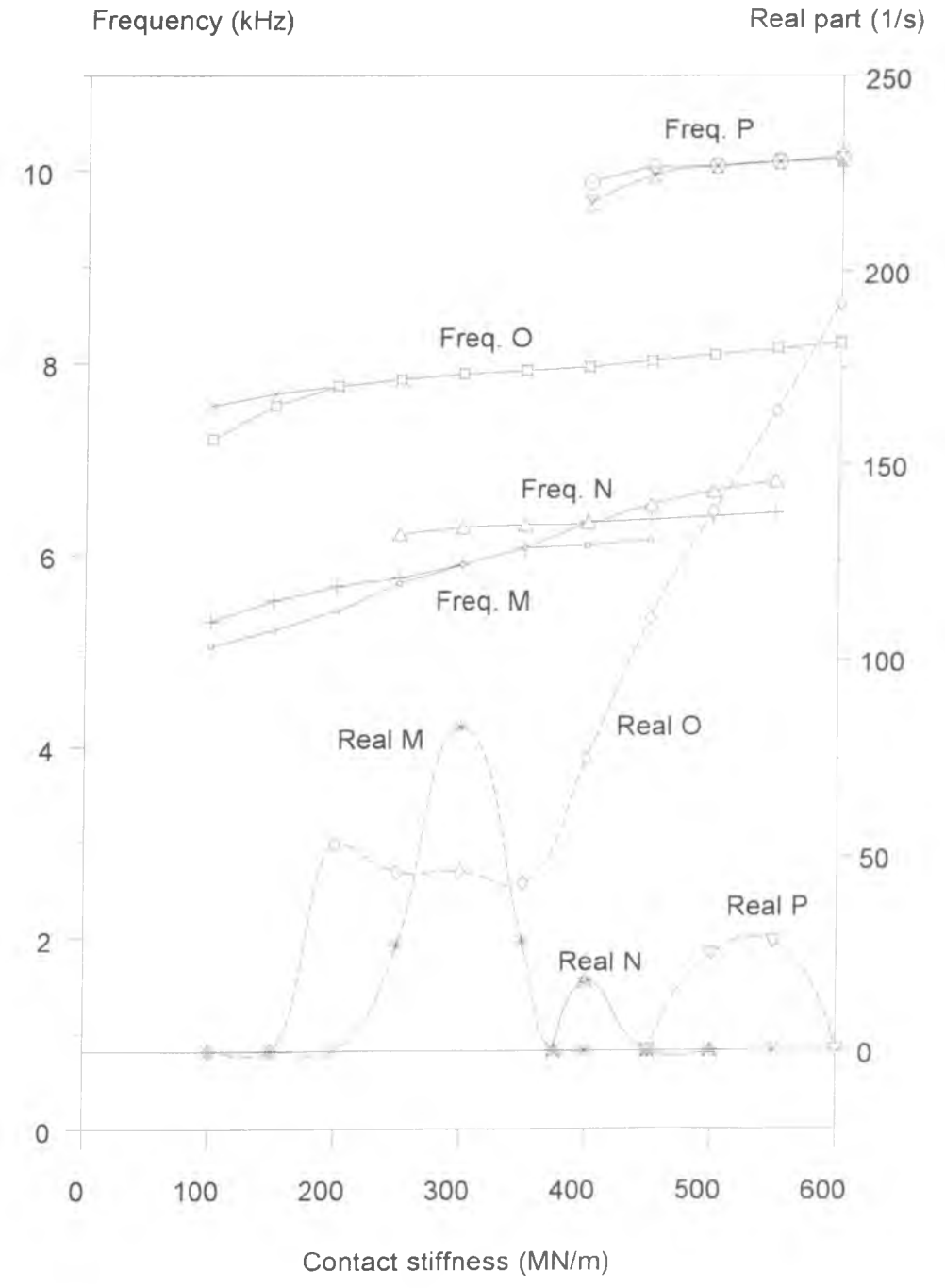

Figure 8.17 - Unstable modes evolution for zero angle of relative rotation

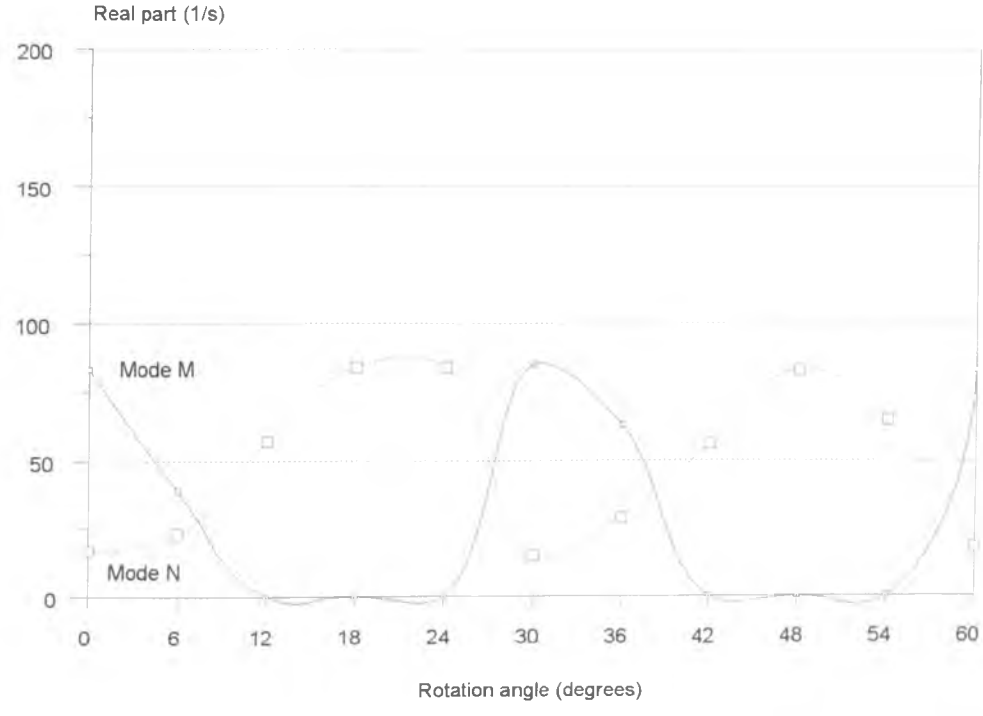

Figure 8.18a - Variation of maximum real part of mode M and N with relative angle of rotation.

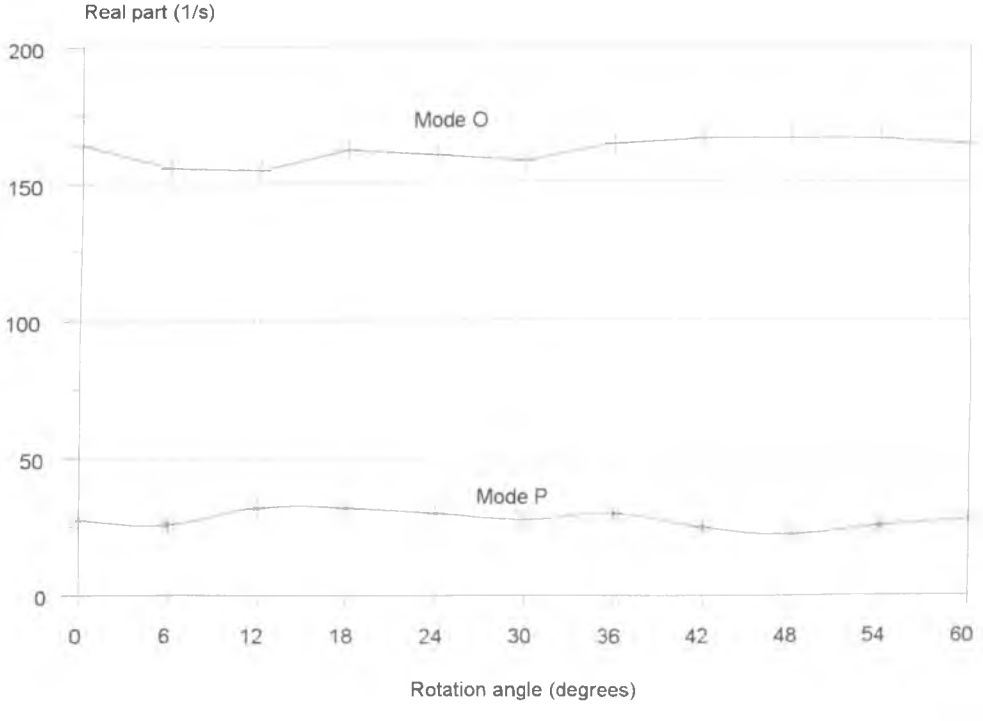

Figure 8.18b - Variation of maximum real part of mode O and P with relative angle of rotation.

8.9 Discussion

The parametric studies described above have shown several important trends. The study on the effect of friction coefficient (section 8.3) has shown that there is a critical friction coefficient to initiate instability the value of which is mode dependant. The minimum critical coefficient of friction for the instability with the present configuration is 0.35. Increasing the friction coefficient has the effect of increasing the magnitude of the real part which can be interpreted as an increase in squeal propensity. A similar effect was reported by Liles [6].

The abutment stiffness (section 8.4) does not have a great effect on the system stability except when the stiffness is about one order of magnitude larger than the pad-disc contact stiffness in which case the tendency is to make the unstable contact stiffness range narrower and to cause certain modes to become unstable at a lower value of contact stiffness (e.g. mode F). Another effect of increasing abutment stiffness is to increase the magnitude of the real part of the unstable modes. All these effects are however mode specific.

The pad-disc contact stiffness distribution (section 8.5) greatly affects the stability of the system by varying the contact stiffness range over which a mode becomes unstable and by changing the magnitude of the real part of the complex eigenvalue. A uniform stiffness distribution is the most unstable whilst a trailing edge biased distribution is the least unstable

Making the pad inflexible within the frequency range studied (section 8.6) causes the magnitude of the real part of the unstable modes to be very much reduced (a maximum real part of 42) and a very narrow unstable contact stiffness range of 100 MN/m or less. A rigid pad therefore significantly improves the system stability.

Varying the properties of the disc (section 8.7) changes the natural frequencies of the disc and the stability behaviour. For a disc having properties similar to Al-MMC, there is only one unstable mode with the real part in general increasing with the contact stiffness. With an artificially high Young's modulus in which the flexible modes of the

disc (under 11 kHz) are limited to the second diametral mode, instability still occurs within frequency ranges of 5.5 - 6.5 kHz and 8 -9 kHz. For a disc with no flexible modes at all (i.e. a rigid disc), the coupled system remains unstable within the same frequency range and the eigenvector plots show that the pads have similar displaced shape in both cases. This aspect of the results supports the prediction of Hulten [49] that instability still occurs even when the pad is pressed against a rigid surface.

Reducing the symmetry of the disc by machining six equispaced slots and thereby separating the sixth diametral mode pair by 283 Hz under free-free conditions (section 8.8) produces cyclic instability for unstable modes in which the sixth diametral mode of the disc is involved. Other modes however are not affected. This result compares well with the experimental observation of Lang et al [59] that modifying the symmetry of a drum brake rotor by adding mass caused cyclic squeal. Moreover Niishiwaki [58] showed that separating the diametral mode pair is only effective under low applied pressures. This is confirmed by the present analysis in which the stability of the low contact stiffness unstable mode is more greatly improved with the real part reducing to zero during the cycle whilst the real part for the high contact stiffness unstable mode only reduces to a minimum of 15.

The results from the current modelling approach show that instability of the coupled system consists of several unstable modes. Studies in which the disc properties were varied (section 8.7 and 8.8) show that the influence of the disc is limited to certain modes only which are characterised by a relatively uniform nodal spacing. These results confirm the hypothesis advanced in Chapter Seven that unstable modes in which the disc diametral mode is no longer pure (in the sense that the nodal spacing is no longer uniform) will not be affected by changes to the disc. This therefore excludes any unstable modes occurring at high contact stiffness (i.e. high pressure application) as such modes are greatly affected by the strong coupling between the pads and the disc. Indeed all the changes to the disc considered above only affect unstable modes which can in terms of frequency be related to modes D , E and F (of the baseline case) whilst the unstable modes with frequency range between 7-9 kHz (i.e. mode C) remain relatively unchanged.

These results suggest that much of the instability can be traced to the pad as also suggested by the fact that when parameters directly linked to the pad (abutment stiffness, support stiffness, contact pressure distribution , pad flexibility) are varied, the stability of the system is greatly affected. Therefore the present parametric studies are similar to the experimental results of Lewis and Shah [54] which showed that the natural frequencies of the pad clamped under pressure to the complete disc and those when it is clamped to a portion of the disc only were both close to the squeal frequency.This therefore largely excludes the disc from the instability process. Indeed the present analysis for an inflexible pad gave a much reduced magnitude for the real part of the complex eigenvalues which suggests that stability of the system can be improved by moving to a stiffer pad.

In the results discussed above, instabilities can be linked to both the pad and disc depending on the unstable modes considered. This aspect of the results explains and supports both arguments as to the cause of the disc brake instability. On the one hand many researchers have argued that instability is caused by the coalescence of disc diametral modes [48,58,59,60] with the resulting suggestion that stability can be achieved by separating these mode pairs. At the other extreme of opinion, it is shown that a model in which the disc is represented as a rigid surface can still generate instability [49] and therefore the proponents suggest that modifying the pad will improve stability. This latter hypothesis is supported by the experimental work of Lewis and Shah [54] in which the stability was improved by adding mass to the pad Both ideas as to the origin of instability are therefore supported by experimental evidence and also now by the results from the present analysis. Some unstable modes are indeed caused by the diametral mode pairs of the disc converging and the analysis showed that changing the disc modulus (and thus the disc natural frequencies) can reduce the instability. Also separating the diametral mode pair of concern by destroying the axial symmetry produces cyclic instability. However there are other unstable modes which are insensitive to the disc parameters and the analysis shows that even with a rigid disc instabilities can still occur. Furthermore these instabilities were shown to be sensitive to modification of the pad only. It is therefore imperative that instability be explained from both points of view thus allowing for modification of both the pad and disc in order to achieve better stability. Any generalisation that squeal

can be eliminated or reduced by carrying out modifications exclusively to one or other of the components must be treated with caution.

The results also further highlight the many parameters affecting squeal. For example it is likely that the effect of pad wear is to make the contact pressure distribution at the pad-disc interface more uniform such that the system becomes less stable and more prone to squeal. The many and various parameters affecting the stability of the system could well explain the fugitive nature of squeal. By taking account of all these parameters, the problem of squeal could be made more deterministic than at present but a limitation would be the enormous size and complexity of the required analysis.

At the present state of knowledge, it is suggested that an approach to reduce squeal propensity at the design stage using the finite element method should consist of the following stages:

1) From stability analysis using complex eigenvalues, the unstable modes which occur over a wide range of interface contact stiffness and have a relatively large positive real part should be targeted.

2) Detailed analysis of the disc diametral modes involved will reveal whether any particular unstable mode can be stabilised by carrying out changes to the disc in terms of its natural frequencies or limiting its symmetry thus separating the diametral mode pairs.

3) The effectiveness of (2) can be confirmed by varying the disc properties. Persistent instability with near constant unstable frequency range would indicate that the pad should be targeted.

4) If the pad is indeed responsible for the instability, parameter changes to the pad affecting the natural frequencies or contact pressure distribution will improve the stability of the system. A stiff pad has been shown to encourage stability in the present study.

CHAPTER NINE

CONCLUSIONS AND RECOMMENDATION

9.1 Conclusions

These can be summarised as follows:

(i) Careful consideration of the available literature has indicated that a complex eigenvalue approach together with an accurate finite element representation of the coupled pad-disc system offers a potential means of predicting disc brake squeal taking full account of the flexibilities of the major components and their interaction at the friction interface. To yield the unsymmetric stiffness matrix necessary for complex eigenvalue analysis to be meaningful, the interface contact model must involve the effect of circumferential friction. To account for the effect of varying brake applied pressure, a relationship between applied pressure and interface contact stiffness is required.

(ii) Finite element models of the pad and disc for a typical disc brake installation have been developed. Free-free modal analysis has shown that both these finite element models are adequate to describe the dynamic properties of the components with a maximum frequency difference from experimental results of 10%.

(ii) A non-linear contact pressure analysis of the pad pressed against a rigid surface has shown that contact is partial but that the contact reaction force at the pad interface varies linearly with the applied pressure because the contact area does not change. Introduction of friction due to circumferential sliding causes the contact pressure distribution to become asymmetric with the distribution biased towards the leading edge for both the piston and paw applied pressure cases. This is manifested in increased contact reaction force at the leading edge and lifting of the trailing edge of the pad. The abutment arrangement (leading, trailing and combined) has only a small effect on the distribution pattern and the magnitude of the contact reaction force at any position is changed by less than 4%. A softer friction material causes a larger contact area and a more uniform pressure distribution.

(iii) The interface contact stiffness between the pad and the disc has been calculated using a random process approach, the results of which show a linear relationship between contact stiffness and applied pressure. The contact stiffness calculated using this approach is most sensitive to the measured disc surface roughness whilst the effect of pad surface roughness is negligible. This is due to the relatively large pad mean asperity radius (thirty times larger than the disc mean asperity radius) calculated using the measured pad surface profile data. Therefore the pad surface roughness can be ignored in the contact stiffness calculation and the pad surface can safely be assumed to be flat. On the other hand , the Young's modulus of the friction material is so much lower than that of the disc that the latter can be effectively regarded as rigid in the calculations.

(iv) A stability analysis of the coupled pad-disc system using complex eigenvalues identifies a minimum contact stiffness for instability to occur, the value of which is mode specific. Instability occurs as the frequencies of two different modes converge at

a critical contact stiffness value; one mode then becomes very stable with a large negative real part whilst the other is very unstable with a relatively large positive real part. The instability continues until a certain maximum contact stiffness at which point the two modes diverge to be at different frequencies with the real part reducing to zero or less in both cases.

(v) The effect of increasing the external support stiffness K_S on the pad backplate is to stabilise the system in terms of reducing the number of unstable modes and the magnitude of the positive real part.

(vi) Arising from (iv) and (v) , the effect of brake applied pressure on squeal can be explained by the fact that at low pressures there is a certain range of contact stiffness (translated in practice as a range of line pressure) within which unstable modes occur. Increasing the contact stiffness beyond this range causes the instability of these particular modes to cease with other unstable modes emerging. However a parallel increase in the external support stiffness as a result of the increasing pressure tends to suppress these new instabilities. This therefore explains why squeal tends to occur at low applied pressures.

(vii) The trends from the analysis match those from the experiment in terms of frequency and mode shapes of unstable modes and the pressure range over which they occur. This correlation validates the approach used in the present work for squeal analysis

(viii) The magnitude of the real part of an unstable mode is directly related to the phase difference between the pad and the disc motions. The maximum real part occurs when the phase difference approaches 180^0 . Instability ceases when the phase difference is zero.

(ix) Instability occurs above a critical friction coefficient, the value of which is mode specific. For the baseline conditions studied (K_C =250 MN/m and K_S =24 MN/m), the

critical coefficient of friction is 0.35 . Instability increases with increasing friction coefficient beyond this value.

(x) A contact pressure distribution at the pad-disc interface which is uniform is most unstable and a distribution pattern biased towards the trailing edge of the pad is least unstable. The actual contact pressure distribution predicted by the finite element analysis is leading edge biased which gives intermediate instability.

(xi) Instability of the coupled pad-disc system is not very sensitive to the abutment stiffness. Only when the magnitude of the abutment stiffness is one order higher that the pad-disc contact stiffness is the stability affected , increasing the real part but reducing the range of contact stiffness over which instability occurs.

(xii) An inflexible pad reduces the system instability. This suggests that a short ,stiff pad would be less prone to squeal.

(xiii) Variation of the disc Young's modulus affects the number of unstable modes. However, even with an effectively rigid disc, instability still occurs. For all values of disc Young's modulus studied , instability occurs within the 7- 9 kHz range. This suggests that the pad is mostly responsible for the instability within this frequency range.

(xiv) Reducing the disc symmetry to lie on six diametral axes by introducing six equispaced slots in the disc surface only affects instability involving the sixth diametral mode of the disc. As the modified disc rotates , the real part fluctuates with the angle of rotation. This in practice can be related to cyclic squeal which has been shown to occur for a modified drum rotor with mass added to limit the axial symmetry.

(xv) The results suggest that instability can be explained by both the effect of disc doublet modes and pad instability depending on the mode. Unstable disc diametral modes with relatively uniform nodal spacing around the disc circumference can be stabilised by limiting the symmetry of the disc. This can be achieved practically by

machining slots in a plain disc or by a systematic arrangement of stiffeners in a ventilated disc. Unstable modes involving non-uniform nodal spacing in the disc are not affected by limiting the disc symmetry. Modification of the pad is the most effective strategy to stabilise these modes.

(xvi) The approach outlined in this thesis therefore unifies the two schools of thought on the origin of instability in a disc brake system. The results also suggest methods by which squeal can be systematically reduced at the design stage by targeting the most appropriate component as outlined in (xv) above.

9.2 Recommendations for Future Work

The following suggestions are made for future work :

(i) The present work does not take into account the effect of damping. Damping is one of the most important factors influencing stability of any system. Future work therefore should take this into account.

(ii) Inclusion of a caliper model will make the present approach more complete and enabled the effect of support stiffness to be more accurately modelled. A coupled caliper-pad-disc system may further enable the instability arising at lower frequency such as judder to be combined with the high frequency squeal as studied in the present work.

(iii) The present model assumes a variable friction force in direct proportion to the variable normal force based on Amonton's Law. Implementation of the Oden-Martin friction model might provide a more complete and realistic representation of friction.

References

1. Crolla, D.A. and Lang, A.M. "Brake Noise and Vibration - The State of the Art" , Vehicle Tribology , Leeds-Lyon 17, Tribology Series 18, (Dowson, D. ; Taylor, C M. and Godet, M. , ed.) Elsevier Science Pub., Sept. 1991, pp. 165 -174.

2. 'Case For Support" Internal Report of Mechanical Engineering Department , Leeds University , Sept. 1990.

3. 'WHICH? CAR-Guide to New and Used Cars 1995',Consumer Association, London 1995.

4. 'Lexus Brake Squeal Problem and Prevention of Recurrence' , Lecture given by personnel of Toyota Motor Corporation (Europe) Ltd. at the Mechanical Engineering Department ,Leeds University, 30th of December 1993.

5. Smales, H "Friction Materials - Black Art or Science" , Proc. I.Mech.E. ,Vol. 209, No. D3 , Part D : Journal of Automotive Engineering, 1995, pp. 151 -157.

6. Liles , G.D. "Analysis of Disc Brake Squeal Using Finite Element Method" , SAE Paper 891150.

7. Murakami, H.; Tsunada, N.;Kitamura, M. "A Study Concerned With Mechanism of Disc brake Squeal", SAE Paper 841233.

8. Oden, J.T. and Martins, J.A.C. "Models and Computational Methods for Dynamic Friction Phenomena", Computational Method in Applied Mechanics and Engineering., Vol. 52 , 1985 , pp.527 - 634.

9. ANSYS User's Manual , Revision 5.0A (Vol I-IV), Swanson Analysis Inc., Houston, USA, 1992.

10. Fieldhouse, J.D. and Newcomb, T.P. "An Investigation Into Disc Brake Squeal Using Hologrpahic Interferometry", 3rd Int'l EAEC Conference on Vehicle Dynamics and Powertrain Engineering - EAEC Paper No. 91084, Strasbourg , June 1991

11 ABAQUS User's Manual (Vol. I-IV) , Hibbit, Karlsson and Sorenson Inc.,Pawtucket ,USA, 1993.

12. Lang, A.M. and Smales, H. "An Approach to the Solution of Disc Brake Vibration Problems" , Proc. I. Mech. E. Conf. on "Braking of Road Vehicles", Paper C37/83 Loughborough , 1983.

13. Lamarque, P.V. "Brake Squeak: The Experience of Manufacturers and Operators: Report No. 8500B" Inst. Auto. Engrs. Research and Standardisation Comittee 1935.

14. Fosberry, R.A.C. and Holubecki, Z. "An Investigation of the Causes and Nature of Brake Squeal" , MIRA Report 1955/2.

15. Fosberry, R.A.C. and Holubecki, Z. "Some Experiments on the Prevention of Brake Squeal" , MIRA Report 1957/1.

16. Fosberry, R.A.C. and Holubecki, Z. "Third Report on Squeal of Drum Brakes" , MIRA Report 1957/3.

17. Fosberry, R.A.C. and Holubecki, Z. "Disc Brake Squeal : Its Mechanism and Suppression" , MIRA Report 1961/2.

18.Sinclair, D. "Frictional Vibrations" , Journal of Applied Mechanics , 1955 , pp 207 -214.

19. Basford, P.R. and Twiss, S.B. "Properties of Friction Materials. I - Experiments on Variables Affecting Noise: II- Theory of Vibrations in Brakes", Trans. ASME, 1958, Vol. 80 pp. 402-406 and pp. 407-410.

20. Wagenfuhrer, H. "Bremsgerausche" (Noises from Brakes), A.T.Z Augusts 1964, Vol. 66 , No. 8 , pp. 217 - 222.

21. Spurr, R.T. "A Theory of Brake Squeal", I.Mech. E. Auto Div. Proc. No. 1, 1961/62, pp. 33-40.

22. Lienkewicz, W. "The Sliding Friction Process - Effect of External Vibrations" , Wear , Vol. 13, 1969 , pp. 99-108.

23. Ko, P.L. & Brockeley, C.A. "The Measurement of Friction and Friction-Induced Vibration", Journal of Lubrication Technology , Trans. ASME , Vol. 92 , 1970 , pp 543 -549.

24. Aronov, V. ; A.F. , D'Souza ; Kalpakijan, S. and Shareef, I. "Experimental Investigation of the Effect of System Rigidity on Wear and Friction-Induced Vibrations" , Journal of Tribology , Trans. ASME , Vol. 105 , 1983 , pp. 206 -211

25. Soom, A. and Kim, C. "Interactions Between Dynamic Normal and Frictional Forces During Unlubricated Sliding", Journal of Lubrication Technology, Trans. ASME , Vol. 105 , April 1983, pp. 221-229.

26. Soom, A. and Kim, C. "Roughness-Induced Dynamic Loading at Dry and Boundary-Lubricated Sliding Contacts", Journal of Lubrication Technology, Trans. ASME , Vol. 105 , October 1983 , pp. 514-517

27. Dweib, A.H. and D'Souza, A.F. "Self-Excited Vibrations Induced by Dry Friction, Part 1 - Experimental Study" , Journal of Sound and Vibration, Vol. 137 (2), 1990 , pp. 163 -175.

28. D'Souza, A.F. and Dweib, A.H. "Self-Excited Vibrations Induced by Dry Friction, Part 2 : Stability and Limit Cycle Analysis" , Journal of Sound and Vibration, Vol. 137 (2), 1990 , pp. 177-190.

29. Yokoi, M. and Nakai, M. "A Fundamental Study on Frictional Noise (1st Report, The generating mechanism of rubbing noise and squeal noise)", Bulletin of JSME , Vol.22, No. 173, November 1979 , pp. 1665-1671.

30. Yokoi, M. and Nakai, M. "A Fundamental Study on Frictional Noise (2nd Report, The generating mechanism of squeal noise of higher modes)", Bulletin of JSME , Vol.23, No. 186, December 1980 , pp. 2118-2124.

31. Yokoi, M. and Nakai, M. "A Fundamental Study on Frictional Noise (3rd Report, The influence of periodic surface roughness on frictional noise)", Bulletin of JSME , Vol. 24, No. 194, Augusts 1981 , pp. 1470 -1476.

32. Yokoi, M. and Nakai, M. "A Fundamental Study on Frictional Noise (4th Report, The influence of angle of inclination of the rod on frictional noise)", Bulletin of JSME , Vol.24 , No. 194, Augusts 1981 , pp. 1477 - 1483.

33. Tworzydlo, W.W. , Becker, E.E. and Oden, J.T. "Numerical Modelling of Friction-Induced Vibrations and Dynamic Instabilities", Friction-Induced Vibration, Chatter, Squeal and Chaos , (Ibrahim , R.A. and Soom, A. ed.) , ASME Pub. 1992 . pp 87-97.

34. Swayze, J.L. and Akay, H. "Stability of Friction-Induced Vibrations in Multi-Degree-of-Freedom System" , Friction-Induced Vibration, Chatter, Squeal and Chaos , (Ibrahim , R.A. and Soom, A. ed.) , ASME Pub. 1992 , pp. 49 -56.

35. Jarvis, R.P. and Mills, B. "Vibrations Induced by Dry Friction", Proc. I Mech E., Vol.178 , Pt. 1 No. 32 1963/54 , pp. 847 -857.

36. Hales F.D. Communications in Reference [35].

37. Earles, S.W.E. and Soar, G.B. "Squeal Noise in Disc Brakes", Paper C100/71, Proc. I. Mech. E. Conf. on "Vibration and Noise in Motor Vehicles", 1971 , pp. 61-69.

38. Earles, S.W.E. and Soar, G.B. "A Vibrational Analysis of a Pin-Disc System with Particular Reference to Squeal Noise in Disc Brakes", Stress, Vibration and Noise Analysis In Vehicles (Gibbss, G.H. and Richards, T.H. ed.) , Applied Science Pub., London , 1975 pp 237 -251.

39. Earles, S.W.E. and Lee, C.K. "Instabilities Arising From the Frictional Interaction of a Pin-Disk System Resulting in Noise Generation", Journal of Engineering for Industry , Trans. ASME , Feb.1976 , pp 81 - 86.

40. Earles, S.W.E. and Badi, M.N.M. "Oscillatory Instabilities Generated In A Double-Pin and Disc Undamped System : A Mechanism of Disc Brake Squeal", Proc. I.Mech.E. , Vol. 198C , No. 4 ,1984 pp 43 -50.

41. North, M.R. "Frictionally Induced Self Excited Vibrations in a Disc Brake System" PhD Thesis , Loughborough University, 1972.

42. Millner, N. "An Analysis of Disc Brake Squeal", SAE Paper 780332.

43 Brooks, P.C. ;Crolla, D.A.;Lang , A.M.; Schafer, D.R "Eigenvalue Sensitivity Analysis Applied To Disc Brake Squeal" Proc. I. Mech. E. Conf. on "Braking of Road Vehicles", Paper C444/04/93 London 1993.

44. Berndt, P.J. and Schweiger, W. "Experimental and Theoretical Investigation of Brake Squeal Qith Disc Brakes Installed In Rail Vehicles", Wear , Vol. 113 ,1986 pp131 -142.

45. Ghesquire, H. and Castel, L. "High Frequency Vibration Coupling Between An Automobile Brake-Disc and Pads" , Proc. I.Mech.E. Conf. 'Autotech 1991' , I.Mech.E. Congress Seminar Paper C/472/11/021.

46. Ghesquire, H. and Castel, L. "Brake Squeal Noise Analysis and Prediction" , Proc. I.Mech.E. Conf. 'Autotech 1992' Paper C389/257.

47. Lee , A.C. "Study of Disc Brake Noise Using Multibody Mechanism With Friction Interface" , Friction-Induced Vibration, Chatter, Squeal and Chaos , (Ibrahim , R.A. and Soom, A. ed) ,ASME 1992, pp99-105.

48. Mottershead, J.E. and Chan,S.N. "Brake Squeal - An Analysis of Symmetry and Flutter Instability" , Friction-Induced Vibration, Chatter, Squeal and Chaos , (Ibrahim , R.A. and Soom, A. ed) ,ASME Pub. 1992 , pp87-97

49. Hulten , J. "Brake Squeal - A Self-Exciting Mechanism With Constant Friction" , Paper presented at SAE Truck and Bus Meeting, Detroit USA, November 1993.

50. Niishiwaki, M "Generalized Theory of Brake Noise" , Proc. I.Mech.E. ,Vol. 207, Part D : Journal of Automotive Engineering, 1993, pp.195- 202.

51 Bracken, W.J. and Sakioka, J.K. "A Methof For The Quantification of Disc Brake Squeal" , SAE Paper 820037.

52. Tarter, J.H. "Disc Brake Squeal" , SAE Paper 830530.

53. Schwartz, H.W.; Hays ,W.D. and Tarter , J.H. "A Systematic Approach To The Analysis of Brake Noise" , SAE Paper 850990.

54. Lewis, T.M. and Shah, P. "Analysis and Control of Brake Noise", SAE Paper 872240.

55. Hoffman , C.T. "Damper Design and Development for Use on Disc Brake Shoe and Lining Assemblies" , SAE Paper 880254.

56.Sherif , H.A.;Blouet, J.;Cretegny, J.F.;Gras, R. and Vialard, S. "Experimental Investigation of Self-Excited Squeal", SAE Paper 892451.

57. Sherif, H.A. "On the Design of Anti-Squeal Friction Pads for Disc Brakes", SAE Paper 910575.

58. Niishiwaki, M.;Harada. H.;Okamura, H. and Ikeuchi,T. "Study on Disc Brake Squeal" , SAE Paper 890864.

59. Lang, A.M. ; Schafer, D.R.;Newcomb, T.P. and Brooks, P C. "Brake Squeal - the Influence of Rotor Geometry" , Proc. I. Mech. E. Conf. on "Braking of Road Vehicles", Paper C444/016/93, London 1993.

60. Kim , S.Y. "S-Cam Brake Noise and Vibration Analysis" Lecture in Mechanical Engineering Dept. , Bradford University, 1993.

61. Felske, A. and Happe, A. "Vibration Analysis by Double Pulsed Laser Holography", SAE Paper 770030.

62. Felske, A. ; Hoppe, G. and Matthai, H. "Oscillations in Squealing Disk Brakes - Analysis of Vibration Modes by Holographic Interferometry" , SAE Paper 780333.

63. Felske, A. ; Hoppe, G. and Matthai, H. "A Study on Drum Brake Noise by Holographic Vibration ANalysis" , SAE Paper 800221.

64. Fieldhouse, J.D. and Newcomb, T.P. "An Experimental Investigation Into Disc Brake Noise" , Proc. I. Mech E. Conf. on "Braking of Road Vehicles", Paper C444/016/93 London 1993.

65. Harding, P.R.J. and Wintle, B.J. "Flexural Effects in Disc Brake Pads" , Proc I.Mech.E. ,Vol. 192 , Automobile Division, 1978 , pp. 1 - 7.

66. Tirovic, M. and Day, A.J. "Disc Brake Interface Pressure Distribution" , Proc. I.Mech.E. ,Vol. 205, Part D : J.o.Auto. Engrg. 1991 , pp. 137 - 146.

67. Day, A.J. ; Tirovic, M. and Newcomb, T.P. "Thermal effects and Pressure Distributions in Brakes" , Proc. I.Mech.E. ,Vol. 205, Part D : J.o.Auto. Engrg. ,1991 , pp. 199- 205.

68. Rendle, S. "Ford Sierra Owners Workshop Manual" , Haynes Pub., 1994 , pp 216-243.

69. Tumbrink, H.J. "Measurement of Load Distribution on Disc Brake Pads and Optimization of Disc Brakes Using the Ball Pressure Method" , SAE Paper 890863.

70. Kuo, B.C. "Automatic Control System" , Prentice-Hall Inc. , 1982 , pp. 362 -372.

71. Wilkinson, J.H. "The Algebraic Eigenvalue Problem" , Clarendon Press, Oxford , 1966 , pp 30 -38.

72. Kikuchi, N. "Finite Element Methods in Mechanics" , Cambridge University Press, 1986 , pp. 1 -22.

73. Chandrupatla, T.R. and Belegundu, A.D. "Introduction to Finite Elements in Engineering" , Prentice-Hall Int'l , 1991 , pp. 1-44.

74. Den Hartog "Mechanical Vibrations", McGraw Hill, 1956 , pp 90-101.

75. Guyan, R.J. "Reduction of Stiffness and Mass Matrices" , AIAA Journal , Vol. 3 , No. 2 , Feb. 1965 , pp. 380.

76. Ragulskis, K. and Yurkauskas "Vibration of bearings" , Hemisphere Pub. , New York , 1989 , pp. 102 -104.

77. Greenwood, J.A. and Williamson, J.B.P. "Contact of Nominally Flat Surfaces", Proc. of the Royal Society, Vol. A295 , 1966 , pp. 300-319.

78. Greenwood, J.A. and Tripp, J.H. "The Contact of Two Nominally Flat Rough Surfaces", Proc. I.Mech.E. ,Vol.185, 1971, pp. 625-633.

79. Nayak, P.R. "Random Process Model of Rough Surfaces", J o. Lubrication Technology, Trans. ASME, Series F, Vol. 93, No. 3, July 1971, pp. 398 -407.

80. Thomas, T.R. and Sayles, R.S. "Stiffness of Machine Tool Joints. A Random Process Approach" Journal of Engineering for Industry, Trans. ASME, Series F, Vol 99B, Feb. 1977, pp. 250 - 256.

81. Halling, J. "Principles of Tribology", MacMillan Press Ltd. , 1975 , pp. 16-38.

82. Newland, D.E. "Mechanical Vibration Analysis and Computation" , Longman Scientific & Technical Pub., 1989 pp.122-176.

83.Grieve, D.G. "The Design and Performance of Automotive Brakes in Advanced Composites : DTI-Link Structural Composites Project" Quarterly Progress Report , Mechanical Engineering Department , Leeds University , June 1995.

APPENDIX I

Programme Listings for the Calculation of Contact Stiffness Using The Random Process Approach In C++

```
#include <stdio.h>
#include <math.h>
#include <float.h>

/* comment : declaration of the parameters used in the calculation*/
/* comment : rms - roughness mm, a - autocorrelation decay constant ,*/
/* comment : e - modulus MPa, g - poisson ratio , r - effective radius of asperity mm*/
/* comment : y -yield strength  MPa*/
/* comment : 1 - friction material , 2 - disc */

double  pie,rms1,rms2,a1,a2,e,e1,e2,g1,g2,r1,r2,r;
double  p1,p2,xl,y01,y2,xr,xm,left,right,del,mid,aut[11];
double std1,std2,sig1,sig2,sig31,sig32,c1,c2,w,wi,sigt1,sigt2;
double area,d1,d2,t,ratf,sq,s[11],sig3_p1,sig3_p2;

int i,l;
double logauto;

main()
{
pie=3.141593;
rms1=51.78e-3;
rms2=11.384e-3;
a1=0.081;
a2=0.057;
e=0.;
e1=8.e3;
g1=0.25;
e2=120e3;
g2=0.25;
y01=20.00;
y2=345.0;
p1=0.;
p2=0.;
del=5.;
d1=0.;
d2=0.;
xl=0.;
xr=0.5;
xm=0.;
```

```
left=0.;
right=0.;
mid=0.5;
t=0.9558139;
std1=2681.46;
std2=129.60;

/* comment : to calculate effective modulus    */

e=1/((1-g1*g1)/e1 + (1-g2*g2)/e2);
printf("neff  :%5.2f",e);
getch();

/* Calculation of pad friction material surfaces */
/* to calculate sigma1 by iteration no 1  */

        p1=(1/(2*pie))*(y01/(e*a1*rms1))*(y01/(e*a1*rms1));
        del=5.;
        xl=p1-del;
        xr=p1+del;

/*      while((xr-xl)>0.0001 && mid>0.000001)  */
        for(i=0; i<=100; i++)
        {
        left=xl-atan(xl)-p1;
        right=xr-atan(xr)-p1;
        xm=(xr*left - xl*right)/(left - right);
        mid=xm - atan(xm) -p1;
        if(left*mid < 0.)
        xr=xm;
        if(left*mid > 0.)
        xl=xm;


        sig1=xm ;
        printf("\np1    :%2.8f",p1 );
        printf("\nleft  :%2.8f",left);
        printf("\nsigma1 :%2.5f",sig1);
        }

        sig31=sig1*sig1*sig1/3;

        sig3_p1=sig31 - p1;
        sq= sqrt((sig31 - p1));
        printf("\nsig3_p1 :%4.4f",sig3_p1);
        printf("\nsigma3 :%3.6f",sq);
        getch();

/* Calculation of asperity radius of the friction material surface*/
```

```
        r1=1./(3.*a1*a1*rms1*sqrt((sig3_p1 )));
        printf("\nr1 :%3.4f",r1);


/* Calculation of disc surface properties */
/* to calculate sigma2 by iteration no.2  */
/* sigma = asperity density */

        p2=(1/(2*pie))*(y2/(e*a2*rms2))*(y2/(e*a2*rms2));
        del=5.;
        xl=p2-del;
        xr=p2+del;

/*      while((xr-xl)>0.0001 && mid>0.000001)  */
        for(i=0; i<=10; i++)
        {
        left=xl-atan(xl)-p2;
        right=xr-atan(xr)-p2;
        xm=(xr*left - xl*right)/(left - right);
        mid=xm - atan(xm) -p2;
        if(left*mid < 0.)
        xr=xm;
        if(left*mid > 0.)
        xl=xm;
        sig2=xm ;
        printf("\np2    :%2.8f",p2 );
        printf("\nleft  :%2.8f",left);
        printf("\nsigma :%2.5f",sig2);
        }

        sig32=(sig2*sig2*sig2)/3;
        d1=((a1*a1)/(6*pie*sqrt(3))) *
          (sig31 - p1) /p1 ;
        d2=((a2*a2)/(6*pie*sqrt(3))) *
          (sig32 - p2) /p2 ;
        area=3212.0;
        sig3_p2=sig32 - p2;
        sq= sqrt((sig32 - p2));
        printf("\nsig3_p2 :%4.4f",sig3_p2);
        printf("\nsigma3 :%3.6f",sq);
        getch();

        /*Calculation of the asperity radius of the disc*/

        r2=1./(3.*a2*a2*rms2*sqrt((sig3_p2 )));
        printf("\nr2 :%3.4f",r2);

        /* Calculation of effective radius */
```

```
        r=(r1 * r2)/(r1 + r2);

/* Calculation of the constant c */

        c1=(4./3.)*d1*area*e*sqrt(r)*pow(rms1,1.5);
        c2=(4./3.)*d2*area*e*sqrt(r)*pow(rms2,1.5);

printf("\nd1  :%2.8f",d1);
printf("\nd2  :%4.4f",d2);
printf("\nr1 :%3.4f",r1);
printf("\nr2 :%3.4f",r2);
printf("\nsig1 :%3.4f",sig1);
printf("\nsig32 :%3.4f",sig32);
printf("\nr  :%6.9f",r);
printf("\nc1  :%6.6f",c1);
printf("\nc2  :%6.6f",c2);
getch();


/* Beginning of load calculation  */
/* One bar applied pressure = 173.5 N  , load = w */
/*  t= dimensionless mean plane separation*/

        for(i=1; i<=11; i++)
        {

        w=i*173.5;
        wi=w/c2;

        if( (log10( wi ) > (0.)) &  (log10( wi ) <= 2.5) )
        t = ( -log10(wi) +0.5) /(0.5)*(53./35.) - (73./35.);

        if( (log10( wi ) > (-0.5)) &  (log10( wi ) <= 0) )
        t = ( -log10(wi) - 0) /(0.5)*(28./35.) - (20./35.);

        if( (log10(wi) > -1) & (log10(wi) < -0.5 ))
        t=((-log10(wi) - 0.5) /0.5)*(22./35.) + (8 /35.);

        if(( log10(wi) > -1.5) & (log10(wi) < -1))
        t=((-log10(wi) - 1)/0.5)*(18 /35.) + (30 /35.);

        if(( log10(wi) > -2.0) & (log10(wi) < -1.5))
        t=((-log10(wi) - 1.5)/0.5)*(16.5/35.) + (48 /35.);

        if( (log10(wi) > -2.5) & (log10(wi) < -2.0))
        t=((-log10(wi) - 2.0)/0.5)*(14./35.) + (64.5/35.);

        if( (log10(wi) > -3.0) & (log10(wi) < -2.5))
```

```
t=((-log10(wi) - 2.5)/0.5)*(12.5/35.) + (78.5/35.);

if(( log10(wi) > -3.5) & (log10(wi) < -3.0))
t=((-log10(wi) - 3.0)/0.5)*(11./35.) + (91./35.);

if(( log10(wi) > -4.0) & (log10(wi) < -3.5))
t=((-log10(wi) - 3.5)/0.5)*(9.5/35.) + (102./35.);

if( (log10(wi) > -4.5) & (log10(wi) < -4.0))
t=((-log10(wi) - 4.0)/0.5)*(7./35.) + (111.5/35.);

if( (log10(wi) >= -5.0) & (log10(wi) < -4.5))
t=((-log10(wi) - 4.0)/0.5)*(5./35.) + (118.5/35.);

/* to calculate the value of ratio f, ratf by interpolation

if( t>= -3.0 && t < -2.5)
ratf = (12.5/17.8)*0.5 + (( t - (-3.0))/0.5)*0.5*((14. - 12.5)/17.8);

if( t>= -2.5 && t < -2.0)
ratf = (14./17.8)*0.5 + (( t - (-2.5))/0.5)*0.5*((16.5-14.)/17.8);

if( t>= -2.0 && t < -1.5)
ratf = (16.5/17.8)*0.5 + (( t - (-2.0))/0.5)*0.5*((20.5 - 16.5)/17.8);

if( t>= -1.5 && t < -1.0)
ratf = (20.5/17.8)*0.5 + (( t - (-1.5))/0.5)*0.5*((24.5 - 20.5)/17.8);

if( t>= -1.0 && t < -0.5)
ratf = (24.5/17.8)*0.5 + (( t - (-1.0))/0.5)*0.5*((29 -24.5)/17.8);

if( t>= -0.5 && t < 0.)
ratf = (29/17.8)*0.5 + (( t - (-0.5))/0.5)*0.5*((34.5 - 29)/17.8);

if( t>= 0. && t < 0.5)
ratf = (34.5/17.8)*0.5 + ( t /0.5)*0.5*((41.5 - 34.5)/17.8);

if( t>= 0.5 && t < 1.0)
ratf = (41.5/17.8)*0.5 + (( t - (0.5))/0.5)*0.5*((48.5 - 41.5)/17.8);

if( t>= 1.0 &&  t < 1.5)
ratf = (48.5/17.8)*0.5 + (( t - (1.0))/0.5)*0.5*((57 - 48.5)/17.8);

if( t>= 1.5 && t < 2.0)
ratf = (57/17.8)*0.5 + (( t - (1.5))/0.5)*0.5*((66-57)/17.8);

if( t>= 2.0 && t < 2.5)
ratf = (66/17.8)*0.5 + (( t - (2.0))/0.5)*0.5*((76-56)/17.8);
```

```
        if( t>= 2.5 &&  t < 3.0)
        ratf = (76/17.8)*0.5 + (( t - (2.5))/0.5)*0.5*((88-76)/17.8);

        if( t>= 3.0 &&  t < 3.5)
        ratf = (88/17.8)*0.5 + (( t - (3.0))/0.5)*0.5*((88-76)/17.8);

        if( t<= 0.0)
        ratf =0.9559787;

        printf("\nload      :%6.2f",w);
        printf("\nw/c       :%6.4f",wi);
        printf("\nlog10w/c2   :%2.6f",log10(w/c2));
        printf("\nthick      :%2.9f",t);
        printf("\nratioF     :%2.4f",ratf);

/* Calculation of the contact stiffness s[i] for each load condition */

        s[i] = 3*ratf*w/(2*rms2);
        printf("\n Stifness  :%6.6f",s[i]);
        getch();
}
}
```

APPENDIX II

Input Data For The Finite Element Analysis Using ANSYS REVISION 5.0A

```
/BATCH,LIST
/FILNAM,SUBDISC
/UNIT,S.I.
/TITLE, SUBSTRUCTURING OF THE SIMPLFIED DISC FINITE ELEMENT MODEL

/PREP7
!define element type
!coordinate system is cylindrical

CSYS,1
ET,1,63
ET,7,50

!material properties of grey cast iron
MP,EX,1,120E9
MP,DENS,1,7.520E3

!constants defining thickness of shell elements
R,13,8.3E-3
R,14,10.2E-3

!definition of disc
N,20010,68E-3,,5.255E-3
N,20012,78.5E-3,,5.255E-3
N,20014,89.5E-3,,5.255E-3
N,20016,98.5E-3,,5.255E-3
N,20018,107.5E-3,,5.255E-3
N,20020,120E-3,,5.255E-3
NGEN,60,100,20010,20020,2,,6,

MAT,1
TYPE,1
REAL,13
NUMSTR,ELEM,1001
E,20010,20012,20112,20110
REAL,14
E,20012,20014,20114,20112
E,20014,20016,20116,20114
E,20016,20018,20118,20116
E,20018,20020,20120,20118
EGEN,59,1001,1005,1
E,25910,25912,20012,20010
REAL,14
E,25912,25914,20014,20012
```

```
E,25914,25916,20016,20014
E,25916,25918,20018,20016
E,25918,25920,20020,20018

!constraint the inner periphery of the simplified disc\
D,20010,UZ,0.,,25910,100,UX,UY
NSEL,ALL
NROTAT,ALL

FINISH

!solution phase
/SOLU
ANTYPE,SUBSTR
SEOPT,SUBDISC,3

!define masters
M,20012,UZ,25912,100
M,20014,UZ,25914,100
M,20016,UZ,25916,100
M,20018,UZ,25918,100
M,20020,UZ,25920,100

SOLVE
SAVE
FINISH
/EXIT,ALL
!-----------------------------------------------------------------------------------------
!definition of the inboard pad and substructuring
!-----------------------------------------------------------------------------------------
/BATCH,LIST
/FILNAM,SUBPAD1
/TITLE,SUBSTRUCTURING OF THE INBOARD PAD
/UNITS,S.I.
/PREP7

CSYS,1
ET,2,14
ET,3,14,,3

!material properties of the mild steel backplate of the pad
MP,EX,2,207E9
MP,DENS,2,7.725E3

!material properties of the friction material
MP,EX,3,8E9
MP,DENS,3,2.5E3

!value of the nodal support stiffness
R,4,1.2E6

!definition of the pad finite element model
```

N,1,106.5E-3,-7.33
N,2,112E-3,-8.33
N,3,121E-3,-6
N,4,128E-3,-3.8
N,5,129.33E-3,-0.33

N,6,104.5E-3,-6
N,7,108.5E-3,-3.5
N,8,116.5E-3,-2
N,9,125E-3,0
N,10,128.5E-3,1

N,11,89.5E-3,3.5
N,12,89.5E-3,4.5
N,13,97.5E-3,1.5
N,14,97.5E-3,2.5
N,15,103.5E-3,0

N,16,107.5E-3,3
N,18,116E-3,2
N,19,119E-3,1.5

N,20,81.5E-3,6
N,22,85E-3,6
N,24,89.5E-3,6
N,26,98.5E-3,6
N,28,107.5E-3,6
N,30,116.5E-3,6
N,32,118.5E-3,6

N,120,78E-3,12
N,122,80.5E-3,12
N,124,89.5E-3,12
N,126,98.5E-3,12
N,128,107.5E-3,12
N,130,116.5E-3,12
N,132,118.5E-3,12

NGEN,7,100,120,132,,,6,

N,820,81.5E-3,54
N,822,85E-3,54
N,824,89.5E-3,54
N,826,98.5E-3,54
N,828,107.5E-3,54
N,830,116.5E-3,54
N,832,118.5E-3,54

N,834,89.5E-3,55.5
N,844,89.5E-3,56.5
N,846,97.5E-3,58.5
N,836,97.5E-3,57.5

N,848,103.5E-3,60

N,838,107.5E-3,60
N,840,116E-3,58
N,842,119E-3,57.5

N,940,104.5E-3,66
N,942,108.5E-3,63.5
N,944,116.5E-3,62
N,946,125E-3,60
N,948,128.5E-3,59

N,1040,106.5E-3,67.33
N,1042,112.5E-3,68.33
N,1044,121E-3,66
N,1046,128E-3,63.8
N,1048,129.33E-3,59

N,1115,107E-3,-1.8
N,1116,110E-3,-1
N,1118,117E-3,0
N,1119,121E-3,1.5

N,1138,110E-3,61
N,1140,117E-3,60
N,1142,121E-3,58.5
N,1148,107E-3,61.8

NGEN,2,200,1,1148,1,,,4.75E-3

!mild steel backplate
TYPE,6
MAT,2
E,1,2,7,6,2001,2002,2007,2006
EGEN,4,1,1

E,1115,7,1116,1116,3115,2007,3116,3116
E,1116,7,8,1118,3116,2007,2008,3118
E,1118,8,9,1119,3118,2008,2009,3119

E,1115,1116,16,15,3115,3116,2016,2015
E,1116,1118,18,16,3116,3118,2018,2016
E,1118,1119,19,18,3118,3119,2019,2018

E,20,11,12,22,2020,2011,2012,2022
E,11,13,14,12,2011,2013,2014,2012
E,13,15,16,14,2013,2015,2016,2014

E,22,12,24,24,2022,2012,2024,2024
E,12,14,26,24,2012,2014,2026,2024
EGEN,3,2,15
E,18,19,32,30,2018,2019,2032,2030

```
E,20,22,122,120,2020,2022,2122,2120
EGEN,6,2,19
EGEN,8,100,19,24,1

E,822,824,834,834,2822,2824,2834,2834
E,824,826,836,834,2824,2826,2836,2834
EGEN,4,2,68
E,822,834,844,820,2822,2834,2844,2820
E,834,836,846,844,2834,2836,2846,2844
EGEN,2,2,73

E,848,838,1138,1148,2848,2838,3138,3148
E,838,840,1140,1138,2838,2840,3140,3138
E,840,842,1142,1140,2840,2842,3142,3140

E,942,1148,1138,1138,2942,3148,3138,3138
E,942,1138,1140,944,2942,3138,3140,2944
E,944,1140,1142,946,2944,3140,3142,2946

E,1040,940,942,1042,3040,2940,2942,3042
EGEN,4,2,81

!friction material
TYPE,6
MAT,3
NGEN,2,2000,2011,2842,1,,,12.5E-3

NUMSTR,ELEM,101
E,2022,2012,2024,2024,4022,4012,4024,4024
E,2012,2014,2026,2024,4012,4014,4026,4024
EGEN,3,2,102

E,2022,2024,2124,2122,4022,4024,4124,4122
EGEN,4,2,105

EGEN,8,100,105,108,1
E,2822,2824,2834,2834,4822,4824,4834,4834

NUMSTR,ELEM,150
E,2824,2826,2836,2834,4824,4826,4836,4834
EGEN,3,2,150

NUMSTR,ELEM,201
E,2018,2019,4018,4018,2030,2032,4030,4030
E,2030,2032,4030,4030,2130,2132,4130,4130
EGEN,8,100,202
E,2830,2832,4830,4830,2840,2842,4840,4840

NUMSTR,ELEM,301
E,2020,2022,4022,4022,2120,2122,4122,4122
EGEN,8,100,301
```

E,2020,2022,4022,4022,2011,2012,4012,4012
E,2011,2012,4012,4012,2013,2014,4014,4014
E,2013,2014,4014,4014,2015,2016,4016,4016

E,2820,2822,4822,4822,2844,2834,4834,4834
E,2844,2834,4834,4834,2846,2836,4836,4836
E,2846,2836,4836,4836,2848,2838,4838,4838

!replacing portion of the mild steel on the backplate with friction material ('peg')

EDELE,17
EDELE,26
EDELE,56
EDELE,70

EDELE,5
EDELE,8
EDELE,75
EDELE,78

TYPE,6
MAT,2

E,16,18,30,28,2016,2018,2030,2028
E,122,124,224,222,2122,2124,2224,2222
E,622,624,724,722,2622,2624,2724,2722
E,828,830,840,838,2828,2830,2840,2838

!node generation to represent ground nodes for caliper support stiffness

NGEN,2,5000,1,1148,1,,,-1.75E-3

TYPE,4
REAL,10
NUMSTR,ELEM,401
E,5222,222
EGEN,4,2,401
E,5622,622
EGEN,4,2,405
E,5320,320
E,5322,322
E,5330,330
E,5332,332
E,5420,420
E,5422,422
E,5432,432
E,5520,520
E,5522,522
E,5530,530
E,5532,532

```
!constraint fully the ground nodes
NSEL,NODE,5001,5700
D,ALL,ALL,0.
NROTAT,ALL
NSEL,ALL

FINISH

!solution phase
/SOLU
ANTYPE,SUBSTR
SEOPT,SUBPAD1,3

!selecting masters
M,1,UZ,1148,1
M,1,UY,10,1,UX
M,940,UY,1046,1,UX

M,4012,UZ,4018,2,UY
M,4834,UZ,4840,2,UY
M,4022,UZ,4840,100,UY
M,4024,UZ,4822,100,UY
M,4026,UZ,4826,100,UY
M,4028,UZ,4828,100,UY
M,4030,UZ,4830,100,UY

SOLVE
SAVE
FINISH
/EXIT,ALL


!-----------------------------------------------------------------------------------------
definition of the outboard pad and substructuring
!-----------------------------------------------------------------------------------------

/BATCH,LIST
/FILNAM,SUBPAD2
/TITLE,SUBSTRUCTURING OF THE OUTBOARD PAD
/UNITS,S.I.
/PREP7

CSYS,1
ET,2,14
ET,3,14,,3

!material properties of the mild steel backplate of the pad
MP,EX,2,207E9
MP,DENS,2,7.725E3

!material properties of the friction material
MP,EX,3,8E9
```

```
MP,DENS,3,2.5E3

!value of the nodal support stiffness
R,4,1.2E6

!definition of the pad finite element model
!the outboard pad is position off zz above the inboard pad parallel to the z-axis
ZZ=60E-3

N,10001,106.5E-3,-7.33,ZZ
N,10002,112E-3,-8.33,ZZ
N,10003,121E-3,-6,ZZ
N,10004,128E-3,-3.8,ZZ
N,10005,129.33E-3,-0.33,ZZ

N,10006,104.5E-3,-6,ZZ
N,10007,108.5E-3,-3.5,ZZ
N,10008,116.5E-3,-2,ZZ
N,10009,125E-3,0,ZZ
N,10010,128.5E-3,1,ZZ

N,10011,89.5E-3,3.5,ZZ
N,10012,89.5E-3,4.5,ZZ
N,10013,97.5E-3,1.5,ZZ
N,10014,97.5E-3,2.5,ZZ
N,10015,103.5E-3,0,ZZ

N,10016,107.5E-3,3,ZZ
N,10018,116E-3,2,ZZ
N,10019,119E-3,1.5,ZZ

N,10020,81.5E-3,6,ZZ
N,10022,85E-3,6,ZZ
N,10024,89.5E-3,6,ZZ
N,10026,98.5E-3,6,ZZ
N,10028,107.5E-3,6,ZZ
N,10030,116.5E-3,6,ZZ
N,10032,118.5E-3,6,ZZ

N,10120,78E-3,12,ZZ
N,10122,80.5E-3,12,ZZ
N,10124,89.5E-3,12,ZZ
N,10126,98.5E-3,12,ZZ
N,10128,107.5E-3,12,ZZ
N,10130,116.5E-3,12,ZZ
N,10132,118.5E-3,12,ZZ

NGEN,7,100,10120,10132,,,6,

N,10820,81.5E-3,54,ZZ
N,10822,85E-3,54,ZZ
N,10824,89.5E-3,54,ZZ
```

N,10826,98.5E-3,54,ZZ
N,10828,107.5E-3,54,ZZ
N,10830,116.5E-3,54,ZZ
N,10832,118.5E-3,54,ZZ

N,10834,89.5E-3,55.5,ZZ
N,10844,89.5E-3,56.5,ZZ
N,10846,97.5E-3,58.5,ZZ
N,10836,97.5E-3,57.5,ZZ
N,10848,103.5E-3,60,ZZ

N,10838,107.5E-3,60,ZZ
N,10840,116E-3,58,ZZ
N,10842,119E-3,57.5,ZZ

N,10940,104.5E-3,66,ZZ
N,10942,108.5E-3,63.5,ZZ
N,10944,116.5E-3,62,ZZ
N,10946,125E-3,60,ZZ
N,10948,128.5E-3,59,ZZ

N,10040,106.5E-3,67.33,ZZ
N,10042,112.5E-3,68.33,ZZ
N,10044,121E-3,66,ZZ
N,10046,128E-3,63.8,ZZ
N,10048,129.33E-3,59,ZZ

N,11115,107E-3,-1.8,ZZ
N,11116,110E-3,-1,ZZ
N,11118,117E-3,0,ZZ
N,11119,121E-3,1.5,ZZ

N,11138,110E-3,61,ZZ
N,11140,117E-3,60,ZZ
N,11142,121E-3,58.5,ZZ
N,11148,107E-3,61.8,ZZ

NGEN,2,2000,10001,11148,1,,,-4.75E-3

!mild steel backplate
TYPE,6
MAT,2
NUMSTR,ELEM,1001
E,10001,10002,10007,10006,12001,12002,12007,12006
EGEN,4,1,1001

E,11115,10007,11116,11116,13115,12007,13116,13116
E,11116,10007,10008,11118,13116,12007,12008,13118
E,11118,10008,10009,11119,13118,12008,12009,13119

E,11115,11116,10016,10015,13115,13116,12016,12015
E,11116,11118,10018,10016,13116,13118,12018,12016

E,11118,11119,10019,10018,13118,13119,12019,12018

E,10020,10011,10012,10022,12020,12011,12012,12022
E,10011,10013,10014,10012,12011,12013,12014,12012
E,10013,10015,10016,10014,12013,12015,12016,12014

E,10022,10012,10024,10024,12022,2012,12024,12024
E,10012,10014,10026,10024,12012,12014,12026,12024
EGEN,3,2,1015
E,10018,10019,10032,10030,12018,12019,12032,12030

E,10020,10022,10122,10120,12020,12022,12122,12120
EGEN,6,2,1019
EGEN,8,100,1019,1024,1

E,10822,10824,10834,10834,12822,12824,12834,12834
E,10824,10826,10836,10834,12824,12826,12836,12834
EGEN,4,2,1068
E,10822,10834,10844,10820,12822,12834,12844,12820
E,10834,10836,10846,10844,12834,12836,12846,12844
EGEN,2,2,1073

E,10848,10838,11138,11148,12848,12838,13138,13148
E,10838,10840,11140,11138,12838,12840,13140,13138
E,10840,10842,11142,11140,12840,12842,13142,13140

E,10942,11148,11138,11138,12942,13148,13138,13138
E,10942,11138,11140,10944,12942,13138,13140,12944
E,10944,11140,11142,10946,12944,13140,13142,12946

E,11040,10940,10942,11042,13040,12940,12942,13042
EGEN,4,2,1081

!friction material
TYPE,6
MAT,3
NGEN,2,2000,12011,12842,1,,,-12.5E-3

NUMSTR,ELEM,1101
E,12022,12012,12024,12024,14022,14012,14024,14024
E,12012,12014,12026,12024,14012,14014,14026,14024
EGEN,3,2,1102

E,12022,12024,12124,12122,14022,14024,14124,14122
EGEN,4,2,1105

EGEN,8,100,1105,1108,1
E,12822,12824,12834,12834,14822,14824,14834,14834

NUMSTR,ELEM,1150
E,12824,12826,12836,12834,14824,14826,14836,14834
EGEN,3,2,1150

```
NUMSTR,ELEM,1201
E,12018,12019,14018,14018,12030,12032,14030,14030
E,12030,12032,14030,14030,12130,12132,14130,14130
EGEN,8,100,1202
E,12830,12832,14830,14830,12840,12842,14840,14840

NUMSTR,ELEM,1301
E,12020,12022,14022,14022,12120,12122,14122,14122
EGEN,8,100,1301

E,12020,12022,14022,14022,12011,12012,14012,14012
E,12011,12012,14012,14012,12013,12014,14014,14014
E,12013,12014,14014,14014,12015,12016,14016,14016

E,12820,12822,14822,14822,12844,12834,14834,14834
E,12844,12834,14834,14834,12846,12836,14836,14836
E,12846,12836,14836,14836,12848,12838,14838,14838

!replacing portion of the mild steel on the backplate with friction material ('peg')

EDELE,1017
EDELE,1026
EDELE,1056
EDELE,1070

EDELE,1005
EDELE,1008
EDELE,1075
EDELE,1078

TYPE,6
MAT,2

E,10016,10018,10030,10028,12016,12018,12030,12028
E,10122,10124,10224,10222,12122,12124,12224,12222
E,10622,10624,10724,10722,12622,12624,12724,12722
E,10828,10830,10840,10838,12828,12830,12840,12838

!node generation to represent ground nodes for caliper support stiffness

NGEN,2,5000,10001,11148,1,,,1.75E-3

TYPE,4
REAL,10
NUMSTR,ELEM,1401
E,15024,10024
EGEN,5,2,1401
E,15124,10124
EGEN,5,2,1406
E,15724,10724
EGEN,5,2,1411
```

```
E,15824,10824
EGEN,5,2,1416
E,15228,10228
EGEN,3,2,1421
E,15628,10628
EGEN,3,2,1424
E,15530,10530
E,15532,10532
E,15330,10330
E,15332,10332

!constraint fully the ground nodes
NSEL,NODE,15001,15900
D,ALL,ALL,0.
NROTAT,ALL
NSEL,ALL

FINISH

!solution phase
/SOLU
ANTYPE,SUBSTR
SEOPT,SUBPAD2,3

!selecting masters
M,10001,UZ,11148,1
M,10001,UY,10010,1,UX
M,10940,UY,11046,1,UX

M,14012,UZ,14018,2,UY
M,14834,UZ,14840,2,UY
M,14022,UZ,14840,100,UY
M,14024,UZ,14822,100,UY
M,14026,UZ,14826,100,UY
M,14028,UZ,14828,100,UY
M,14030,UZ,14830,100,UY

SOLVE
SAVE
FINISH
/EXIT,ALL

!-----------------------------------------------------------------------------------------
!coupling of the disc , inboard pad and outboard pad substructures using the interface
!elements with friction included , stiffness for each interface element is determined from
!the random process approach calculation
!-----------------------------------------------------------------------------------------

/BATCH,LIST
/FILNAM,STABILITY
/UNITS,SI
/TITLE, STABILITY ANALYSIS OF THE COUPLED PAD-DISC SYSTEM
```

```
/PREP7

CSYS,1
ET,1,63
ET,2,4,14,,3
ET,6,45
ET,7,50

!contact stiffness KC = 350 MN/m & and total force applied FTOT=1734.9 N(for !contact
pressure distribution purposes )
KC=350.0E6
FTOT=1734.9

!stiffness of the abutment to ground, KA=1.2MN/m
R,3,1.2E6

!determination of individual interface element contact stiffness
!based on the nodal contact reaction force on the pad from contact pressure analysis
!in Chapter Five - Figure 5.5b

*DIM,F,,800
*DIM,K,,800
*DIM,MUK,,800

!nodal reaction force for the inboard pad
F(201)=0
F(202)=11.96
F(203)=10.46
F(204)=3.855

F(205)=10.33
F(206)=20.01
F(207)=23.50
F(208)=17.39
F(209)=4.004

F(210)=23.62
F(211)=53.28
F(212)=50.02
F(213)=43.81
F(214)=15.32

F(215)=29.67
F(216)=77.67
F(217)=70.81
F(218)=72.37
F(219)=28.07

F(220)=30.20
F(221)=98.16
F(222)=88.96
F(223)=100.6
```

F(224)=32.23

F(225)=28.90
F(226)=103.4
F(227)=92.45
F(228)=109.5
F(229)=29.87

F(230)=27.31
F(231)=87.63
F(232)=77.32
F(233)=84.78
F(234)=22.55

F(235)=22.59
F(236)=49.82
F(237)=37.2
F(238)=30.26
F(239)=4.716

F(240)=2.433

!continue to define as F(241) - F(253) = 0

!nodal reaction for the outboard pad

F(301)=10.38
F(302)=44.88
F(303)=83.90
F(304)=32.85

F(305)=3.068
F(306)=25.85
F(307)=69.87
F(308)=123
F(309)=49.26

F(310)=0
F(311)=25.97
F(312)=63.45
F(313)=108
F(314)=46.49

F(315)=0
F(316)=3.863
F(317)=36.92
F(318)=81.33
F(319)=36.05

F(320)=0
F(321)=0
F(322)=17.62

```
F(323)=60.5
F(324)=28.78

F(325)=0
F(326)=0
F(327)=11.46
F(328)=54.89
F(329)=30.95

F(330)=0
F(331)=0
F(332)=20.91
F(333)=70.7
F(334)=38.23

F(335)=0
F(336)=0
F(337)=36.95
F(338)=93.50
F(339)=50.55

F(340)=0
F(341)=2.21e-3
F(342)=45.87
F(343)=105.6
F(344)=58.23

F(345)=0
F(346)=0
F(347)=29.1
F(348)=85.88
F(349)=47.71

F(350)=0
F(351)=0
F(352)=1.756
F(353)=0.783


*DO,I,1,53
        K(200+I)=KTOT(F(200+I)/FTOT))
        MUK(200+I)=MU*K(200+I)

!filling the matrix27 interface element (matrix 12 x 12) with individual contact stiffness
!to couple the inboard pad to the disc
        R,200+I
        RMORE
        RMORE,,-MUK(200+I)
        RMORE,,MUK(200+I),,,,K(200+I)
        RMORE,,,,,,-K(200+I)
        RMORE,
        RMORE,
```

```
        RMORE,
        RMORE,
        RMORE,
        RMORE,,,,,-MUK(200+I)
        RMORE,,,K(200+I)
        RMORE,
        RMORE,
        RMORE,
        RMORE,
        RMORE,,,,,,MUK(200+I)
        RMORE,-K(200+I)
*ENDDO

!repeat the above command exactly but with opposite sign i.e. + becomes + for MUK
!for the outboard pad as the direction of the normal forces changes relative to the !inboard pad
-- reactionary forces

!call the substructure files (or the superelement file , SE)
TYPE,7
SE,SUBDISC
SE,SUBPAD1
SE,SUBPAD2

!couple all the nodes on the pad friction face to the disc , for example
!for the inboard pad
TYPE,5
REAL,201
E,20014,4012
.....
E,21020,4840

!for the outboard pad
REAL,301
E,20014,14012
.....
E,21020,14840

!define ground nodes for the abutments and constraints use ux and uy dof springS
FINISH

!solution phase of modal analysis between 2-11 kHz
/SOLU
ANTYPE,MODAL
MODOPT,DAMP,100,2000,11000
SOLVE
SAVE
FINISH
/EXIT,ALL
```